Northumbria Research Link

Citation: Schwarz, Florian (2019) Pliocene vegetation and climate variability on the NE Tibetan Plateau (Qaidam and Kunlun Pass Basin) over glacial interglacial timescales. Doctoral thesis, Northumbria University.

Pliocene vegetation and climate variability on the NE Tibetan Plateau (Qaidam and Kunlun Pass Basin) over glacial-interglacial timescales

Florian Schwarz

PhD

2019

Pliocene vegetation and climate variability on the NE Tibetan Plateau (Qaidam and Kunlun Pass Basin) over glacial-interglacial timescales

Florian Schwarz

A thesis submitted in partial fulfilment of
the requirements of the
University of Northumbria at Newcastle
for the degree of
Doctor of Philosophy

Research undertaken in the Faculty of
Engineering and Environment

April 2019

Abstract

In recent years, high-resolution studies demonstrated that the climate during the mid-Piacenzian warm period (mPWP; 3.264 – 3.025 Ma) was characterized by high variability, but generally much warmer conditions in the northern high latitudes. Although warming is also expected to take place in the mid latitudes, there are contrasting modelling suggestions about precipitation changes and the extent of monsoonal influence in NW China. This study presents a high-resolution palynological record for the mPWP in the NW Qaidam Basin, which nowadays is located outside of the impact of the East Asian Summer Monsoon (EASM), and the first Plio-Pleistocene palynological record for the Kunlun Pass Basin, which during present-day receives precipitation from the EASM.

The high-resolution palynological record from the NW Qaidam Basin (SG-1b core) shows that between 3.495 – 3.011 Ma the vegetation was dominated by xerophytic shrublands in the basin, while the mountain slopes were covered by broadleaved and coniferous forests. High palaeoprecipitation estimates (MAP) indicate that the climate in the NW Qaidam Basin was much wetter (~120 – 400 mm) than present-day (~ 28 mm). The penetration of the EASM into the region was also recognised by the lithology and geochemistry of the SG-1b core, which demonstrate that a semi-deep and semi-large palaeolake existed in the basin during the Piacenzian. The *Artemisia*/Chenopodiaceae ratio shows that the moisture availability was not only controlled by orbital cycles, but also changed from Southern to Northern Hemisphere summer insolation dependence during the build-up of ice sheets in the Northern Hemisphere. The Kunlun Pass Basin record demonstrates that this study site on the northeastern Tibetan Plateau was affected by long-term climate cooling from the Early Pliocene to the mPWP and Plio-Pleistocene transition, which was characterised by a decline in coniferous and broadleaved patchy forest vegetation to xerophytic shrublands and steppes/meadows after the onset of the Northern Hemisphere glaciation (NHG). The palaeotemperature estimates show that the Kunlun Pass Basin was much warmer during the mPWP as suggested by a recently published modelling study. As a consequence, modelling studies (for future and past scenarios) should take into account that the NW Qaidam Basin likely becomes much wetter while the Kunlun Pass Basin becomes strongly warmer during times of global warmth.

Table of contents

List of Figures

List of Tables

List of Abbreviations

A/C = *Artemisia*/Chenopodiaceae
AAIW = Antarctic Intermediate Water
ACC = Antarctic Circumpolar Current
AMOC = Atlantic Meridional Overturning Circulation
C/N = carbon/nitrogen
CAS = Central American Seaway
CL = core lithology
CLP = Chinese Loess Plateau
CMT = temperature of the coldest month
comp = components
CS = core scan
CT = core texture
DSDP = Deep Sea Drilling Program
EAIS = East Antarctic ice sheet
EAM = East Asian Monsoon
EASM = East Asian Summer Monsoon
EAWM = East Asian Winter Monsoon
EEP = eastern equatorial Pacific
EITO = East Indian Tropical Ocean
ENSO = El Niño – Southern Oscillation
Eq. = Equation
EUC = Equatorial Undercurrent
Fig. = Figure
ITF = Indonesian Throughflow
IODP = Integrated Ocean Drilling Program
IRD = ice-rafted debris
ISM = Indian Summer Monsoon
ka = thousand years

m a.s.l. = meter above sea level
Ma = million years
MAP = mean annual precipitation
MAT = mean annual temperature
MIS = Marine Isotope Stage
MPdry = mean precipitation of the driest month
MPwarm = mean precipitation of the warmest month
MPwet = mean precipitation of the wettest month
mPWP = mid-Piacenzian Warm Period
MSP = mean summer precipitation
MST = mean summer temperature
MWP = mean winter precipitation
MWT = mean winter temperature
n.i. = not included
NADW = North Atlantic Deep Water
NGCUC = New Guinea Coastal Undercurrent
NHG = Northern Hemisphere glaciation
NLRS = nearest living relative species
NPDW = North Pacific Deep Water
NPIW = North Pacific Intermediate Water
ODP = Ocean Drilling Program
PAZ = pollen assemblage zone
PCA = Principle Component Analysis
pt. = point
RMSEP = root mean square error of prediction
SAMW = Subantarctic Mode Water
SST = sea-surface temperature
Tab. = Table
THC = thermohaline circulation
TOC = total organic carbon

WAIS = West Antarctic ice sheet

WA-PLS = weighted average partial least squares

WEP = western equatorial Pacific

WMT = temperature of the warmest month

wt % = weight percentage

XRF = X-ray fluorescence

Acknowledgements

First and foremost, I am very grateful to my supervisor Prof. Dr. Ulrich Salzmann for his immense support throughout my entire PhD, the numerous scientific discussions and the opportunity for fieldwork in China.

I would like to thank my second supervisor Prof. Dr. John Woodward for his helpful suggestions and scientific writing advice. Special thanks are given to Prof. Dr. Junsheng Nie (Lanzhou University, China) for the joint project and fieldwork in China as well as the numerous discussions that improved my understanding of proxies and climate processes significantly.

I am grateful to Prof. Dr. Erwin Appel (University of Tübingen, Germany), Prof. Dr. Jörg Pross (University of Heidelberg, Germany), Dr. Andreas Koutsodendris and his PhD student Martina Vannacci (University of Heidelberg, Germany), Prof. Dr. Xiaomin Fang (CAS, China) and Dr. Weilin Zhang (CAS, China) for providing access to the SG-1b core at Tübingen University, Germany. I would like to thank specifically Dr. Andreas Koutsodendris and his PhD student Martina Vannacci for sending additional samples from the SG-1b core, providing high-resolution images and XRF data from the core and having good discussions about the palaeovegetation in the Qaidam Basin.

For providing samples from the Kunlun Pass Basin and scientific discussions about palaeoelevation interpretations, I am thankful to Prof. Dr. Carmala N. Garzione and Dr. Feng Cheng (University of Rochester, USA).

Many thanks are given to Prof. Dr. Jian Ni (Zhejiang Normal University, China) for sharing his modern pollen dataset with me. Similarly, I am thankful for access to the NECLIME Palaeoflora dataset, which was provided by Dr. Torsten Utescher (University of Bonn, Germany). Without these two datasets, I could not have established the palaeoclimate estimates, which are an important part of my thesis.

I am grateful to the Graduate School of Northumbria University for providing me grants to visit the EPPC Conference (Dublin 2018), AASP Conference (Nottingham 2017) and PlioVAR workshop (Leeds 2016).

Furthermore, I would like to thank the lab technicians Lesley Dunlop and Dave Thomas for helping me out with lab processing of pollen samples, which can be time- and HF consuming when dealing with samples of low pollen concentration. I also want to thank Will Thomas for his support with the Element Analyser.

Many thanks are given to Dr. Sina Panitz who helped me a lot with the identification of palynomorphs when I started this research project.

Finally, I am grateful for the support of my parents and friends who helped me a lot throughout my PhD.

Declaration

I declare that the work contained in this thesis has not been submitted for any other award and that it is all my own work. I also conform that this work fully acknowledges opinions, ideas and contributions from the work of others.

Any ethical clearance for the research presented in this thesis has been approved. Approval has been sought and granted by the University Ethics Committee on the 15th of February 2016.

I declare that the Word Count of this Thesis is 43,609 words.

Name: Florian Schwarz

Signature:

Date: 12.04.2019

Chapter 1: Introduction

1.1 Rationale

The Pliocene was the last time interval that is characterised by significantly higher than pre-industrial atmospheric carbon dioxide concentrations (Pagani et al., 2010) and global temperatures that exceeded the modern average by 2 – 3 °C (Haywood et al., 2009; Haywood and Valdes, 2004; Martinez-Boti et al., 2015). Since these climatic conditions are projected to be within the low scenario for future global warming at the end of the 21st century (IPCC 2007), the Pliocene and more specifically the mid-Piacenzian warm period (mPWP) has attracted many data, modelling and data-model comparison studies to strengthen the understanding of this warm period (e.g. Andreev et al., 2014; Dolan et al., 2011; Dowsett et al., 2013; Feng et al., 2017; Haywood et al., 2013; Haywood et al., 2016; Kamae and Ueda, 2011; Li et al., 2018a; Lunt et al., 2012; Lutz, 2011; Panitz et al., 2016; Prescott et al., 2014; Salzmann et al., 2013; Seki et al., 2010). During the Pliocene, the distribution of landmasses was similar to the modern distribution although the closure of the Central American Seaway (CAS) and the Indonesian Throughflow (ITF) was not completed yet (Haug and Tiedemann, 1998; Karas et al., 2009). In the eastern equatorial Pacific (EEP), the gradual closure of the CAS caused the establishment of a strong upwelling zone as well as the initiation of a thermal gradient along the equatorial Pacific and shallowing of the EEP thermocline (Dekens et al., 2007; Lawrence et al., 2006; Steph et al., 2010). Since the modern thermal gradient across the equatorial Pacific was only established gradually during the Late Pliocene, several studies have discussed the possibility of a permanent El Niño like state in the Pacific Ocean during the Early Pliocene (Fedorov et al., 2006; Haywood et al., 2007; Ravelo et al., 2004; Steph et al., 2010; Wara et al., 2005), which could have had a profound impact on the climate in the circum Pacific regions similar to modern day El Niño occurrences (Cook et al., 2010; Kirono et al., 1999; Lau and Weng, 2001; McBride and Nicholls, 1983; Rodríguez et al., 2005; Wang and Hendon, 2007; Zhai et al., 2016).

Significant differences between present-day and the Pliocene exist in the scale of high latitude ice sheets, which can be traced using oxygen isotopes in benthic foraminifera from deep sea cores. Based on the level of these oxygen isotopes, deep sea temperatures and ice sheet extensions can be reconstructed and marine isotope stages (MIS) can be defined as either cold or warm periods. During the Late Pliocene, intervals of increased ice-rafted debris (IRD) suggest that glaciers were growing in the Northern Hemisphere during significant cooling events (such as MIS M2; 3.3 Ma), however, the build-up of the widespread permanent ice sheets did not take place until the Plio-Pleistocene transition (Jansen et al., 2000; Kleiven et al., 2002). In the Southern Hemisphere, the West Antarctic ice sheet (WAIS) and the East Antarctic ice sheet (EAIS) were reduced prior to 3.5 – 3.3 Ma due to warmer ocean water temperatures in the high latitudes (Naish et al., 2009; Patterson et al., 2014), but strengthened and stabilised afterwards (Patterson et al., 2014). The cooling trend during the Pliocene can also be observed in the benthic oxygen isotope records from Zachos et al. (2001) and Lisiecki and Raymo (2005), which show that ocean temperatures declined and high latitude ice sheets increased. Due to less extensive ice sheets, sea level may have been ~ 20 – 25 ± 10 m higher during the mPWP (e.g. Dowsett et al., 1999; Miller et al., 2012).

Although the warmer Pliocene world was characterised by ~ 2 - 3 °C higher global surface air temperatures (Haywood et al., 2009; Haywood and Valdes, 2004; Lunt et al., 2010; Martinez-Boti et al., 2015), the higher temperatures were not distributed homogenously over the planet, but amplified warming of up to 19°C occured in the high latitudes (Ballantyne et al., 2010; Panitz et al., 2016). Associated with higher temperatures was a northward migration of vegetation zones and reduction of tundras compared to modern-day as shown by a data-model hybrid reconstruction from Salzmann et al. (2008).

The response of mid-latitudinal areas to global warming though is less clear. Cook et al. (2014) suggested that the mid latitudes in the Northern Hemisphere would encounter increased aridity. Dai (2012) also suggested that most areas will dry in a global warming scenario, however, distinctly wetter conditions can be observed in the model in the Qaidam Basin area (NW China). Contrasting results can also be seen in Pliocene climate modelling scenarios. Yan et al. (2019) reconstructed a northwestward expansion of the East Asian Summer Monsoon

(EASM) on the Tibetan Plateau. However, in their modelling study, the climate of the Qaidam Basin remained hyperarid with no major changes in precipitation. In contrast, model simulations from Li et al. (2018a) suggest that the Qaidam Basin area (incl. the NW Qaidam Basin) received much higher mean annual precipitation (MAP) of up to 50 - 200 mm during the mPWP. Pollen records from the NW Qaidam Basin (Cai et al., 2012; Miao et al., 2011) show that there is a long-term aridification trend from the Early Miocene until Late Pleistocene, however, an age gap exists (~ 5.0 – 3.1 Ma) leading to the assumption that the palaeovegetation evolution was characterised by rather gradual drying during the Pliocene (incl. the mPWP) (Miao et al., 2013). Low variability and likely stable environmental conditions during the mPWP have also been suggested for other mPWP study sites (Willard, 1994). However, an increasing number of high-resolution studies with improved age control recently challenged these assumptions (Panitz et al., 2016) and demonstrated that climate during the mPWP was in fact highly variable (Andreev et al., 2014; Panitz et al., 2016) with frequent vegetation changes.

The NW Qaidam Basin is a prime study area for reconstructing past monsoonal extent and strength, as it is nowadays located just outside of the northwestward limit of the EASM. Despite the effort from many studies to reconstruct the Pliocene palaeovegetation history in the Qaidam Basin (Cai et al., 2012; Miao et al., 2011; Miao et al., 2013; Wang et al., 1999; Wu et al., 2011), a high-resolution reconstruction that could provide detailed information about vegetation changes on orbital timescales in this nowadays large hyperarid basin is missing. Pollen records indicate that a wetter climate persisted during the Pliocene (Miao et al., 2013; Wu et al., 2011). However, the source of precipitation in the NW Qaidam Basin is subject to controversy not only during the Pliocene, but also throughout the Neogene (Chen et al., 2009; Koutsodendris et al., 2018; Miao et al., 2013; Wei et al., 2015; Xu et al., 2011; Zhao et al., 2007).

Modern $\delta^{18}O$ and δD isotope analysis of precipitation suggest that the boundary between monsoonal and westerly moisture is located around ~ 34 – 35°N on the Tibetan Plateau (Tian et al., 2007). However, chironomid based salinity reconstructions at Lake Sugan (~ 38.9°N, 93.8°E) and tree ring growth in mountainous eastern Qaidam Basin (~ 37.3°N, 98.4°E) indicate that throughout the last millennium the boundary between the EASM and westerly dominated areas in the Qaidam Basin moved in east west direction (Chen et al., 2009; Xu et al., 2011). Wei et al. (2015) suggested that the EASM penetrated westwards towards Qarhan Salt Lake (~ 37.06°N, 94.7°E) during warm interglacials in the Late Pleistocene. A potential northwestwards expansion of the EASM into the NW Qaidam Basin during warmer intervals has also been suggested by Koutsodendris et al. (2018) for the Middle Pleistocene and Miao et al. (2013) for the Miocene. In contrast, based on carbonate isotope analysis, Caves et al. (2015) conclude that the westerlies were the main moisture source for Central Asia (including NW Qaidam Basin) during the Cenozoic. However, the EASM has been excluded in their reconstructions as the $\delta^{18}O_P$ signature of the EASM and the westerlies are similar and not enough data from lowland East China exists to model the Cenozoic EASM moisture flux (Caves et al., 2015).

The general long-term aridification of the Qaidam Basin has been linked to global climate cooling and the onset of the Northern Hemisphere glaciation (NHG), changes in atmospheric circulation and/or uplift of the Tibetan Plateau blocking moisture, which could enter the Qaidam Basin (Cai et al 2012, Miao et al 2016, Miao et al 2013, Wang et al 1999, Wu et al 2011).

An et al. (2001), Clemens et al. (2008) and Sun et al. (2010) suggested that the EASM and the East Asian Winter Monsoon (EAWM) were simultaneously strengthening in the time interval from 3.6 to 2.6 Ma. However, while An et al. (2001) indicates that uplift of Tibetan Plateau is responsible for this coeval evolution of summer and winter monsoon, Clemens et al. (2008) and Sun et al. (2010) connect the East Asian Monsoon (EAM) evolution to high latitude ice sheet variability. The onset of the NHG (~ 3.15 – 2.75 Ma) caused a change in the EAM system, which led to an anti-phased relationship of strong (weak) EASM during intervals of weak (strong) EAWM (Clemens et al., 2008; Sun et al., 2010).

Despite many studies proposing that uplift of the Tibetan Plateau could have contributed to Late Pliocene or Pleistocene aridification in the Asian interior (Cai et al., 2012; Wu et al., 2011), the timing history of Tibetan Plateau uplift phases during the Cenozoic remains controversial. While one theory suggests that most of the uplift had already taken place prior to the late Miocene (Garzione, 2008; Molnar et al., 1993; Quade et al., 2011; Tapponnier et al., 1986), others have suggested that main tectonic uplift movements occurred during Plio-Pleistocene times (An et al., 2001; Cui et al., 1998; Hsü, 1976; Li et al., 1981; Song et al., 2005a; Zheng et al., 2000). Since it is unclear whether the Pliocene palaeovegetation changes in the NW Qaidam Basin were primarily caused by changes in global climate or regional tectonic uplift, new high-resolution pollen records are necessary to facilitate a comprehensive understanding of the mechanisms that are responsible for the palaeovegetation variability in this nowadays hyperarid region.

Aridification is a severe problem, specifically for NW China, where the continued formation of deserts results in an economic loss of about 5.6 billion US Dollar per year (Tao, 2014). The ongoing desertification, which is partly caused by inappropriate land-use (e.g. overgrazing), is thought to be one reason for increased dust storm events affecting millions of people in eastern China (Tao, 2014). The Chinese government introduced the three-north shelterbelt project (North, Northeast and Northwest China) and other measurements in order to control the palaeoenvironmental problems and to reduce these wide-spread impacts on land and cities (Li et al., 2012). Understanding how vegetation and climate changes during the ongoing global warming is necessary to produce effective environmental policies.

This study will investigate the extent and strength of the EASM at the northwestern limit during the warm Pliocene by using two sediment records from the NW Qaidam Basin and the Kunlun Pass Basin. The two study sites are located either within (Kunlun Pass Basin) or outside (NW Qaidam Basin) the present-day limit of the EASM and therefore, offer a unique opportunity to examine palaeoclimate and -monsoonal variability.

The first high-resolution record from the Pliocene NW Qaidam Basin uses a multi-proxy approach of lithology, geochemistry and palynology data to reconstruct the palaeolake development, palaeovegetation and palaeoclimate evolution between 3.5 and 3.0 Ma. The lithology, X-ray fluorescence (XRF) core scanning and organic carbon/nitrogen (C/N) analysis conducted in this study will provide a detailed insight into the palaeolake variability on short timescales during the Late Pliocene, which has been previously described as a time interval of strong lake level and lake geochemistry changes (Fang et al., 2016; Lu et al., 2015). The palynological data will be used to reconstruct palaeovegetation variability and calculate palaeoclimate estimates by using pollen – climate transfer functions. Pollen – climate transfer functions are a common method to estimate the climate values for Holocene and Pleistocene records (Cao et al., 2014; Wen et al., 2013; Xu et al., 2010b). In this study, the potential of pollen-climate transfer functions to generate more accurate climate estimates for Pliocene pollen records from semi-arid regions will be explored for the first time. Previously used methods, such as the Coexistence Approach (Mosbrugger and Utescher, 1997), were focused on presence/absence of pollen taxa and have only limited success in semi-arid regions. Suitable palaeolake size proxies (e.g. lakeshore grasses) and moisture indicators (*Artemisia*/Chenopodiaceae ratio) will be compared to other regional and global high-resolution records, in order to identify the source of precipitation for the NW Qaidam Basin during the mPWP.

The study will also present the first long, well-dated pollen record from the Kunlun Pass Basin spanning a time interval from 4.314 to 0.853 Ma. Modelling approaches suggest that high mountain ranges would experience amplified temperature increases under a global warming scenario (Feng et al., 2014; Nogués-Bravo et al., 2007), which could lead to a replacement of tundras on plateau areas (Feng et al., 2014; Wang et al., 2011; Zhao et al., 2011). Thus, the palaeovegetation reconstruction of the Kunlun Pass Basin record will provide a unique view into high altitude palaeovegetation variability from the warm Early Pliocene until the onset of large scale NHG during and after the Plio-Pleistocene transition. Additionally, the pollen record from the Kunlun Pass Basin will be used to infer whether tectonic uplift on the northeastern Tibetan Plateau took place during Plio-Pleistocene times or not. Previous studies suggested that the altitude of the Kunlun Pass Basin ranged between 400 and 4200 m during the Late Pliocene (Cui et al., 1998; Wang and Chang, 2010; Wang et al., 2008b; Wu et al., 2001) which is below the modern height of 4700 – 5300 m.

Since the Kunlun Pass Basin record is located within the EASM boundary, a comparison of the overlapping interval with the NW Qaidam Basin (3.5 – 3.0 Ma) should reveal whether a northwestward migration of the EASM boundary is accompanied by stronger or weaker precipitation in the Kunlun Pass Basin area.

1.2 Research Questions

1. **How did the lake size and depth of the SG-1b palaeolake change during the time interval from 3.5 to 3.0 Ma and what palaeoenvironmental conclusions can be drawn from the palaeolake variability?**

2. **How did the vegetation change in the NW Qaidam Basin between 3.5 and 3.0 Ma?**

3. **Was the Late Pliocene precipitation in the NW Qaidam Basin controlled by the westerlies or the EASM?**

4. **How did the palaeovegetation and palaeoclimate change in the Kunlun Pass Basin area between the Early Pliocene and middle Pleistocene? Is there palynological evidence for tectonic uplift of the Kunlun Pass Basin after the Early Pliocene?**

5. **Does a northwestward migration of the EASM into the NW Qaidam Basin lead to enhanced precipitation in the Kunlun Pass Basin or does a larger extent of the EASM have an adverse effect on precipitation in the Kunlun Pass Basin?**

6. **How did the onset of glaciation in the Northern Hemisphere during the Late Pliocene and the full-scale glaciation during the Plio-Pleistocene transition affect the palaeovegetation in the NW Qaidam Basin and Kunlun Pass Basin?**

7. **What are the main forcing mechanisms of Late Pliocene climate variability in the NW Qaidam Basin and Kunlun Pass Basin?**

1.3 Thesis outline

This thesis is divided into six chapters. The first chapter outlines the rationale for conducting this thesis. The second chapter provides an overview of modern atmospheric circulations in East Asia and a brief summary of the most important Cenozoic geological developments controlling the palaeovegetation and palaeoclimate in the Asian interior. The study sites and methods are presented in Chapter 3. Chapter 4 examines the palaeovegetation and palaeoclimate evolution of the NW Qaidam Basin over the time interval from 3.5 to 3.0 Ma and addresses the question whether the EASM or the westerlies provided the main moisture source for this region during the mPWP. In Chapter 5, a new palynological record from the Kunlun Pass Basin, which spans a time interval from 4.314 to 0.853 Ma, will be presented and the question answered whether tectonic uplift of this part on the northeastern Tibetan Plateau still occurred post Early Pliocene. The main findings and conclusions of this thesis are summarised in Chapter 6.

Chapter 2: Literature review

2.1 The Northwest of China – present day

2.1.1 Geography

China's geography (Fig. 2 – 1) is characterised by a strong east-west altitudinal contrast. In East China, low-altitude plains exist in the north and northeastern parts, whereas the southern regions are influenced by the adjacent Tibetan Plateau resulting in a hilly landscape. The Tibetan Plateau dominates the landscape of the western and southwestern parts of China, with some of the highest mountains on Earth. As part of the Tibetan Plateau, the Kunlun Mountains and Qilian Mountains mark the border to the north and northeast. The Qaidam Basin, a large intramontane basin, is located in-between these two mountain ranges. North China is characterised by large deserts, such as the Taklamakan Desert in the Tarim Basin. The Tarim Basin is bordered to the north by the Tian Shan Mountains and to the south by the Kunlun Mountains. The Gobi Desert is located north of the Qilian Mountains. The Chinese Loess Plateau (CLP) is an intermediate topographical feature between the Qilian Mountains in the west and the plains in the east.

Temperatures in China follow two gradients; mean annual temperatures (MAT) increase in more southerly and easterly positions, while northerly and westerly parts have lower MAT (Fick and Hijmans, 2017). Temperatures on the Tibetan Plateau and other high mountain ranges have the lowest temperatures in China (Fig. 2 – 2). The MAT vary between 18 and 24°C in South China, 12 and 18°C in East China, -8 and 12°C in Northeast China, -10 and 8°C on the Tibetan Plateau, 4 and 12°C on the CLP and -10 and 12°C in the regions north of the Tibetan Plateau (Fick and Hijmans, 2017).

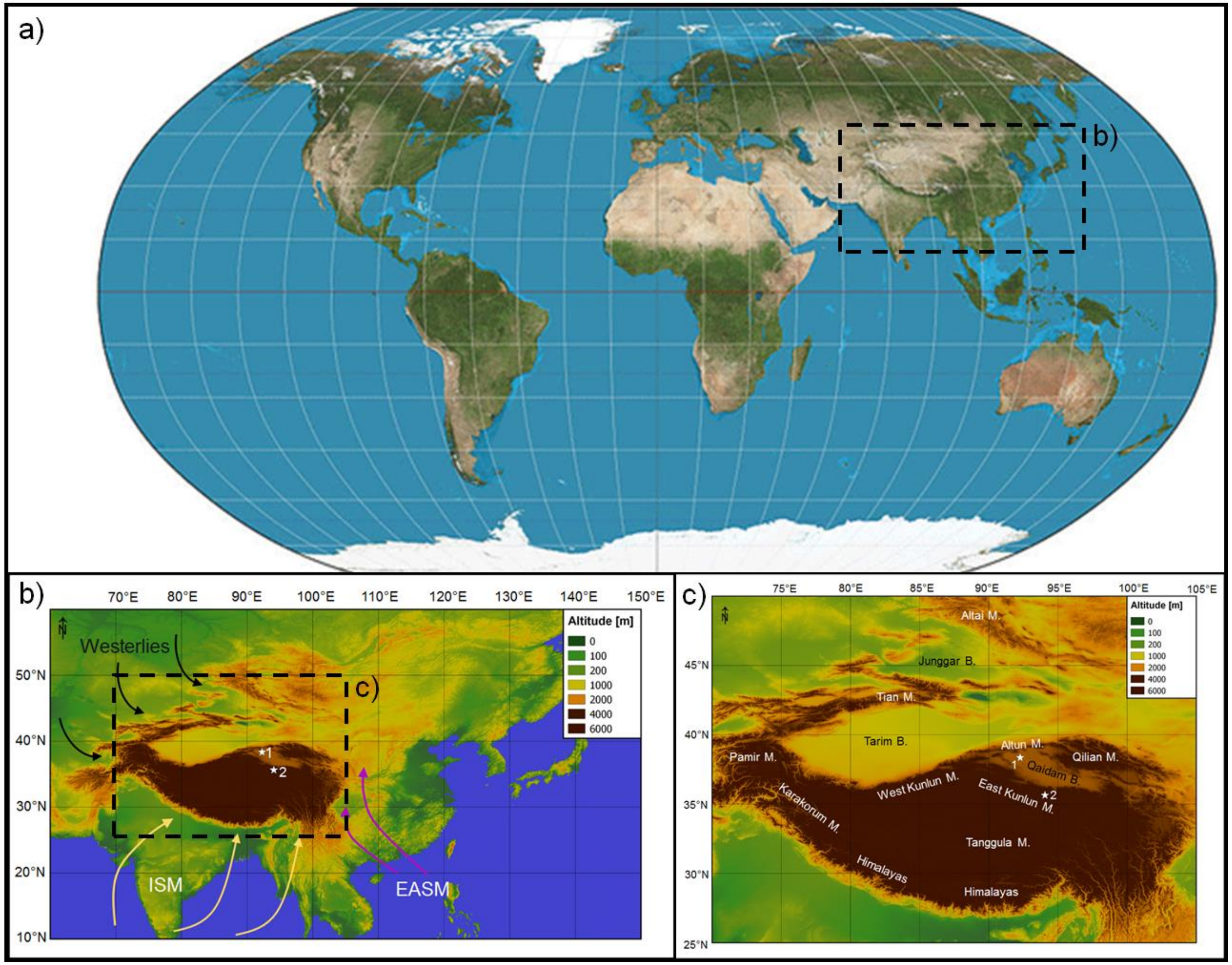

Fig. 2 – 1: A) Robinson projection of Earth (Snyder, 1997). B) Topography of East Asia. Arrows indicate the direction of major wind systems. C) Map of Northwest China. Mountains (M.) are shown in white, whereas basins (B.) are shown in black. Elevation in parts b) and c) is based on the Digital Elevation Model from NASA Shuttle Radar Topography Mission (SRTM). The map has been drawn using QGIS 2.18.4 (QGIS Development Team, 2016). Study sites in this thesis are indicated by 1 (SG-1b core) and 2 (Kunlun Pass Basin).

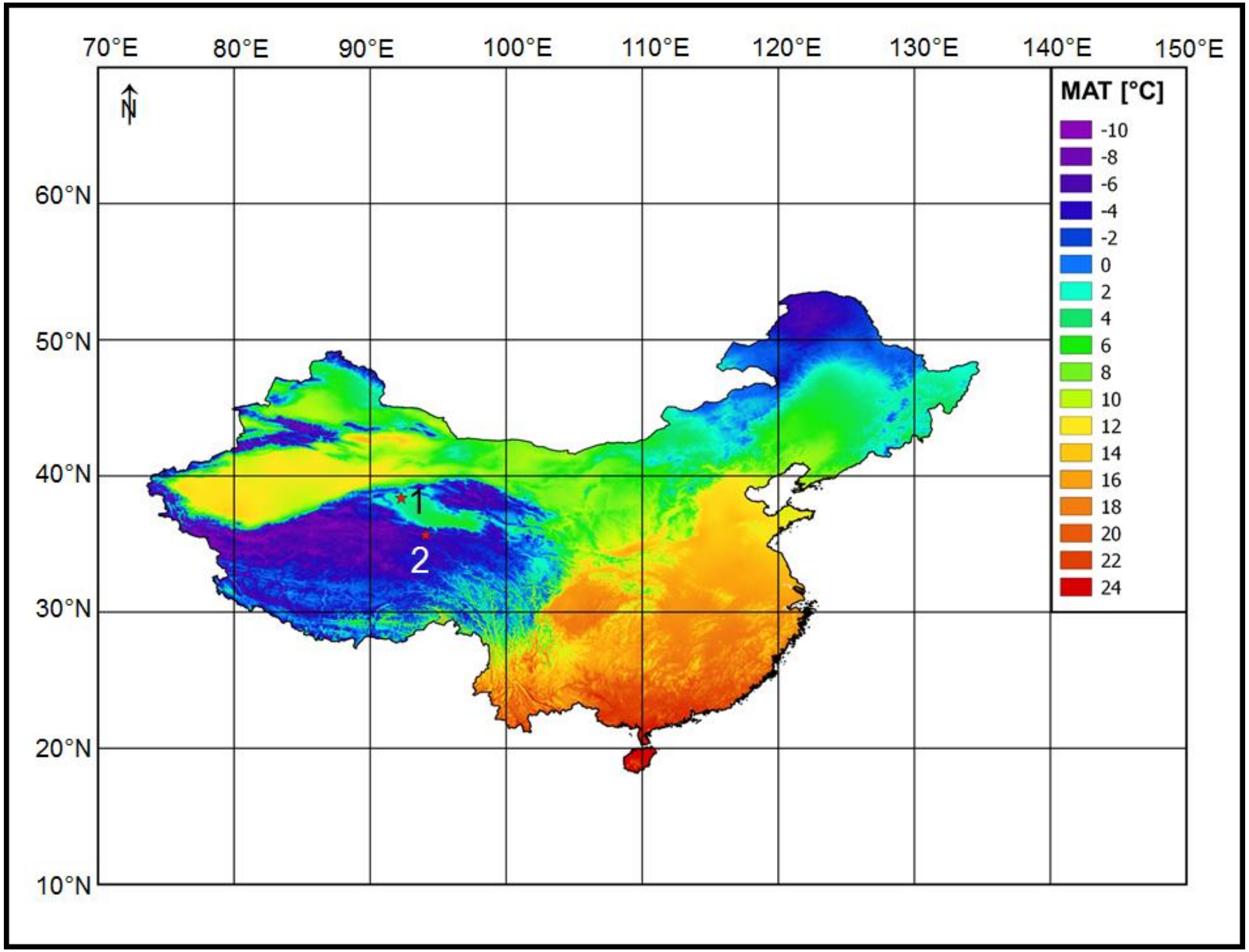

Fig. 2 – 2: MAT in China based on data from WorldClim (Fick and Hijmans, 2017; Hijmans et al., 2005). The map has been drawn using QGIS 2.18.4 (QGIS Development Team, 2016). Study sites in this thesis are indicated by 1 (SG-1b core) and 2 (Kunlun Pass Basin).

The precipitation distribution across China (Fig. 2 – 3) also follows a general southeast-northwest gradient with increasing precipitation in East China linked to the occurrence of the Indian Summer Monsoon (ISM) and EASM. The mean annual precipitation (MAP) varies between 1200 and over 2000 mm in Southeast China and decreases to 200 – 800 mm in Central China (Fick and Hijmans, 2017). In North China, the MAP does not exceed 200 mm in the basins, but can reach up to 800 mm on the mountain ranges (Fick and Hijmans, 2017). On the Tibetan Plateau, some of the southernmost parts can have a MAP exceeding 2000 mm, but this is reduced to 400 – 800 mm on the Central Tibetan Plateau and is even lower on the northwestern and northeastern parts of the Tibetan Plateau (< 400 mm) (Fick and Hijmans, 2017).

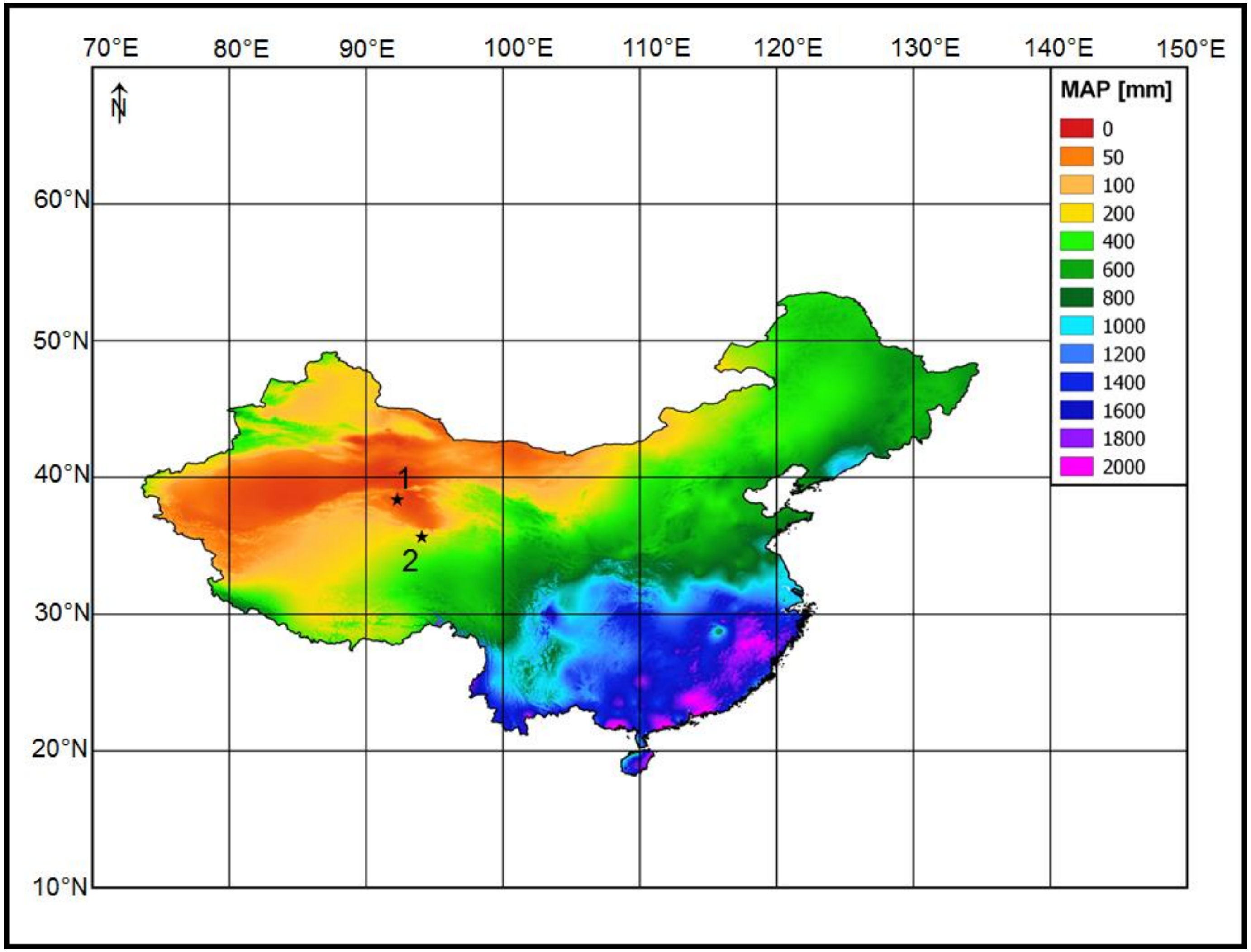

Fig. 2 - 3: MAP in China based on data from WorldClim (Fick and Hijmans, 2017; Hijmans et al., 2005). The map has been drawn using QGIS 2.18.4 (QGIS Development Team, 2016). Study sites in this thesis are indicated by 1 (SG-1b core) and 2 (Kunlun Pass Basin).

2.1.2 Climate

2.1.2.1 Moisture sources in NW China

The moisture source for the regions of northwestern China is based on the penetration of the different atmospheric circulation systems (ISM, EASM, westerlies) into the Asian interior (Fig. 2 – 1b). Since the ISM, EASM and the westerlies reach the western parts of China, the dominant moisture source varies from region to region depending on topographical features and the strength of the particular atmospheric circulation.

The biggest contributors to precipitation in East Asia are the EASM and ISM, which are subsystems of the Asian Monsoon System (Wang et al., 2005). In general, a monsoon is a wind system that shows a seasonal reversal of surface wind direction (Ramage, 1972). The reversal of wind direction is driven by the contrast of the land and ocean warming in summer and winter leading to opposing atmospheric circulations (e.g. Wang et al., 2003). During boreal summer, the Northern Hemisphere receives more solar radiation leading to warming of landmasses and oceans. Since oceans are warming and cooling much slower than land masses, a thermal contrast between the Eurasian continent and the surrounding Indian Ocean, South Chinese Sea and Pacific Ocean is created, in which the Eurasian continent is becoming significantly warmer compared to the oceans (Roxy et al., 2015; Sun and Ding, 2011). As a result, the dominant wind is directed towards the Eurasian continent during the boreal summer months. During boreal winter, the thermal contrast is the opposite, which leads to the wind being directed from the Eurasian continent to the oceans in the south and east (Sun and Ding, 2011).

Wang and Lin (2002) used rainfall characteristics and the 850 hPa level to determine monsoonal domains of the ISM (west of 100 – 105°E) and the EASM (east of 100 – 105°E) over East and Central Asia, which has also been suggested by further studies (Wang et al., 2003; Wang et al., 2005). However, there is still ongoing debate about the north and northwestward penetration of the summer monsoons (Maussion et al., 2014) and some studies suggest that the EASM could also penetrate west of 100°E into the Qaidam Basin (Xu et al., 2011; Zhou et al., 2007). Thus, the atmospheric circulation over the northeastern Tibetan Plateau remains complex (Maussion et al., 2014). Mean summer wind fields (Fig.

2 – 4) at the 1000 hPa level show that westerlies, ISM and EASM converge over the eastern part of the Tibetan Plateau (e.g. Wang et al., 2010).

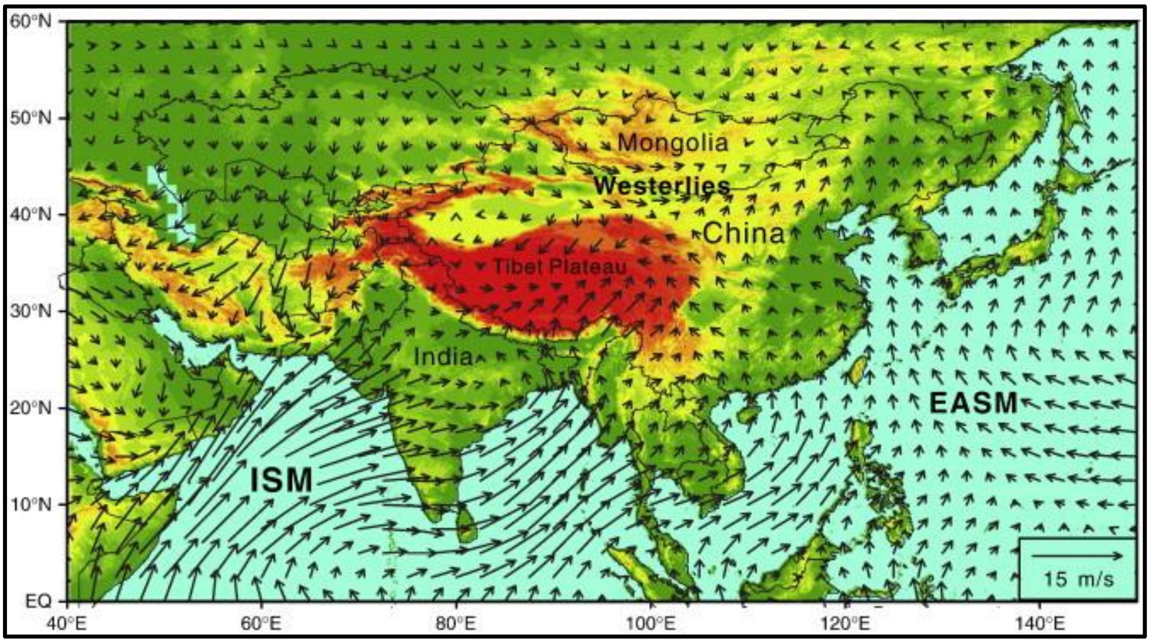

Fig. 2- 4: Mean summer (June, July, August) wind fields in East Asia (1000 hPa) from Jan. 1948 to Dec. 2008 (Wang et al., 2010).

To distinguish between monsoonal and westerly moisture sources, Tian et al. (2001) suggested that the direct ISM precipitation is limited to the Tanggula Mountains (~ 34°N) because δ^{18}O and δD values of water resources did not show the typical depletion that is characteristic for summer monsoon precipitation north of the mountain range. To further identify precipitation sources in NW China via their isotopic signal, Tian et al. (2007) collected water samples from various site locations. The study shows that Yushu (33°01’N, 97°01’E) is still under the influence of ISM precipitation, although the δ^{18}O values are heavier than those of Lhasa (29°43’N, 91°02’E), which can be attributed either to prolonged transport of moisture over land mass, recycling of water (condensation and re-evaporation) or a second moisture source. In contrast to Lhasa and Yushu, the rainfall signal in the Tian Mountains (43°46’N, 87°37’E) and Altay Mountains (47°44’N, 88°05’E) is different. The δ^{18}O values are high in summer and low in winter, which is opposite to the monsoon signal. Henceforth, these regions are most likely influenced by moisture from the Atlantic Ocean or polar ocean regions transported by the Westerly jetstream (Tian et al., 2007). The westerlies become the pre-dominant source of moisture, the further north and westward study sites are located on the central and northern Tibetan Plateau (e.g. Aichner et al., 2015;

Bershaw et al., 2012; Caves et al., 2015; Chen et al., 2010a; Tian et al., 2007). A boundary representing the maximum extent of predominantly monsoonal moisture source can be drawn that is crossing the Tibetan Plateau at around 33 – 35°N and extending northwards east of 100°E up to 45°N at 125°E (Caves et al., 2015; Chen et al., 2010a).

2.1.2.2 Indian Summer Monsoon

The Indian Monsoon System results from thermal differences between the land masses in the Northern Hemisphere and the Indian Ocean to the south (Wu, 2017). During boreal summer, the Eurasian continent is becoming significantly warmer compared to the Indian Ocean (Webster et al., 1998; Wu, 2017; Zhao and Zhou, 2009), which results in massive rainfalls between June and September (Fick and Hijmans, 2017) caused by the ISM. The high Himalayan and Tibetan Plateau prohibit a penetration of moisture to the study areas of this thesis (Caves et al., 2015; Tian et al., 2007) and thus, the ISM is not regarded further.

2.1.2.3 East Asian Monsoon

The EAM consists of the EASM during boreal summer and EAWM during boreal winter. The EASM differs from the ISM in various aspects: The land ocean distribution, which results in the thermal contrast necessary for the formation of the EASM, is zonal (east – west) compared to the meridional (north – south) setup for the ISM (Ha et al., 2012; Wu, 2017). During boreal summer, the Eurasian landmass including the Tibetan Plateau heats up much faster than the oceans (Pacific Ocean and South Chinese Sea in this case) creating a low-pressure cell over East China (Asian Continental Low) and a high pressure cell over the western Pacific called the Western North Pacific Subtropical High or Bonin High (He et al., 2015). However, there is also a north-south contrast between the warming North Pacific and the cooling Australia forcing the formation of the Australian High that leads to strong cross-equatorial low-level winds, which transport vapour into the western North Pacific and the South Chinese Sea (Xue et al., 2004). During May and June, the Western North Pacific Subtropical High extends to the east and increases in strength (Wu and Wang, 2001) leading to first peaks in precipitation over the Philippines and the South Chinese Sea. Summer precipitation on the Asian mainland is dependent on the location of the

Westerly jetstream. During boreal winter, the Westerly jetstream is located south of the Tibetan Plateau (Nagashima et al., 2011). During spring and especially summer, this wind band moves north of the Tibetan Plateau and continues to migrate northward (Schiemann et al., 2009). The northward migration of the Westerly jetstream is forcing a northward movement of the Mei-yu weather front, which is responsible for the heavy rainfalls on the Chinese mainland between June and September (Fu and Qian, 2011).

Contrary to the EASM, the EAWM is driven by the thermal contrast between the faster cooling Asian mainland (Siberian High) and the still warmer Pacific Ocean during boreal winter. The EAWM is directed south and eastwards providing cold and dry air (Wen et al., 2000).

2.1.2.4 Monsoonal variability

In his review, Wang et al. (2005) presented a collection of data from numerous marine sites that provide information about the variability of the Asian Monsoon system. Among the short-term variations are the El Niño Southern Oscillation (ENSO) with periods between 3 and 8 yr (Klein et al., 1997), various solar cycles with periodicities of 60 yr, 84-102 yr, 210 yr, 510-560 yr, 700 yr and 900 yr (Agnihotri et al., 2002; Klein et al., 1997; Sarkar et al., 2000; Yu et al., 2004). Furthermore, Dansgaard-Oeschger cycles have been identified in marine sediments with their dominant 1470 yr cycle (Colin et al., 1998; Jian et al., 2000). Among earth orbital parameters, precession (19-24 kyr) cycles (e.g. Almogi-Labina et al., 2000; Budziak et al., 2000; Clemens et al., 1996; Clemens and Prell, 1991; Colin et al., 1998; Prell and Kutzbach, 1992), obliquity (41 kyr) cycles (e.g. Almogi-Labina et al., 2000; Budziak et al., 2000) and eccentricity (95/124 kyr and 413 kyr) cycles (e.g. Almogi-Labina et al., 2000; Budziak et al., 2000; Clemens et al., 1996; Clemens and Prell, 1991; Prell and Kutzbach, 1992) were identified. In addition, cycles with 11.5 kyr (Beaufort et al., 2003), 30 kyr (e.g. Budziak et al., 2000; Clemens and Prell, 1991; Prell and Kutzbach, 1992) and 66 kyr (Budziak et al., 2000; Clemens and Prell, 1991) were found in the geological record. Tectonic events such as continental plate drift or orogeny have a big impact on climate systems (such as monsoonal climate) but they only occur on timescales between 10^7 and 10^8 years (An et al., 2001; Kutzbach et al., 1989; Molnar et al., 1993). While the strength of Asian Summer Monsoons increases during interglacial periods, the intensity of the Asian Winter Monsoons increases during glacial periods (Ding et al., 1995; Tian et al., 2004).

2.1.2.5 Mid-latitudinal Westerly jetstream

The mid-latitude Westerly jetstream results from the difference in solar heating between the mid-latitudinal and subpolar regions that create a thermal and air pressure contrast (Zhang et al., 2016). Consequently, winds are directed towards the subpolar regions. However, due to the Coriolis force, these winds are being redirected eastwards in the Northern Hemisphere. The strength of the Westerly jetstream is determined based on the difference of the zonal mean winds between 35° and 55°N (Zhang et al., 2016), which can be further simplified to a pressure gradient force, the geopotential height and finally air temperature (Rossby, 1939; Zhang et al., 2016). Due to the dependence of the air temperatures on the solar insolation at different latitudes, the strength of the Westerly jetstream varies with the orbital configuration. The latitude of the prevailing westerlies shifts poleward during times of increased solar insolation in the Northern Hemisphere and equatorward during times of decreased solar insolation (Ineson et al., 2011). The moisture source that is provided by westerly winds to NW China derives from the North Atlantic, Mediterranean Sea, Black Sea and Caspian Sea (Jin et al., 2012).

2.1.3 Vegetation

The diverse climate in China is determined by the varying altitude, precipitation and temperature. The Köppen-Geiger climate classification (Fig. 2 – 5) shows that the south and southeast of China is dominated by subtropical climate influenced by the summer monsoon. The southernmost parts belong to the tropical monsoon climate and wet savanna, respectively. The monsoon system is also the driving force for the climate in NE China. Due to lower temperatures, NE China is dominated by humid continental and subarctic climates. The large distance to the monsoon source regions led to the establishment of dry climates in northern and northwestern China (especially cold semi-arid and cold desert climates). Most of the Tibetan Plateau is covered by alpine tundra as a result of the higher altitude.

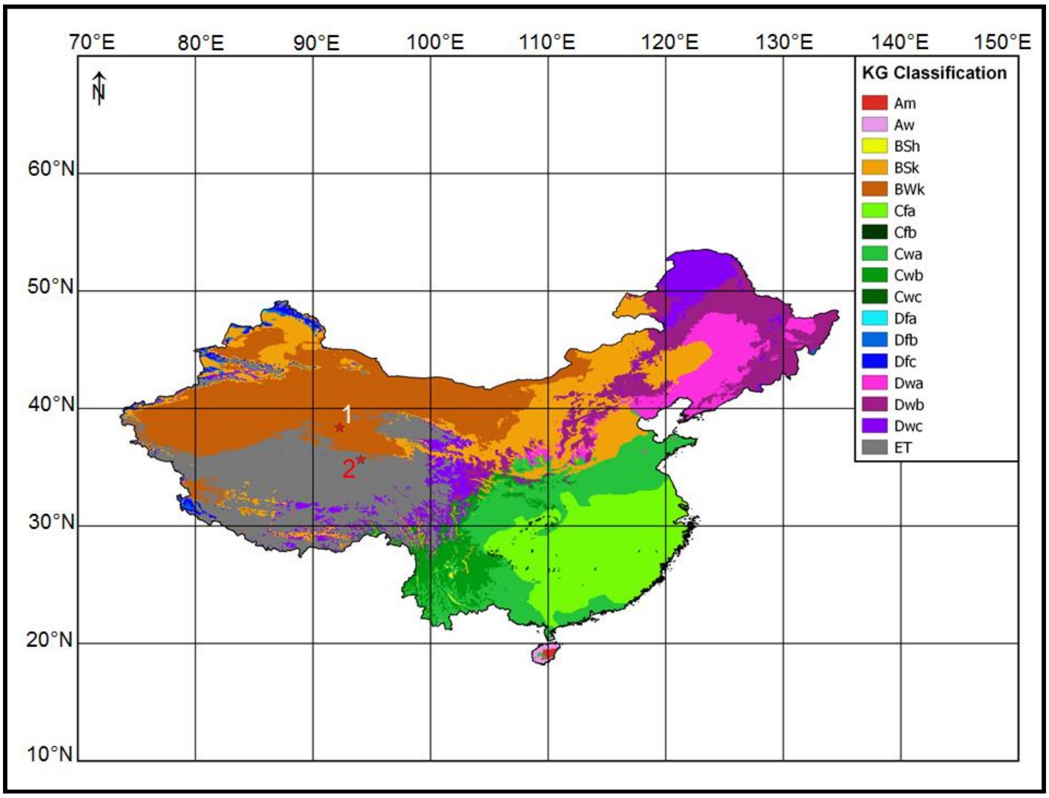

Fig. 2 - 5: Köppen-Geiger climate classification of China based on Kottek et al. (2006) with high-resolution downscaling from Rubel et al (2017). The map has been drawn using QGIS 2.18.4 (QGIS Development Team, 2016). Study sites in this thesis are indicated by 1 (SG-1b core) and 2 (Kunlun Pass Basin).

The biome classification (Fig. 2 – 6) from Ni et al. (2000) based on the Vegetation Atlas of China (Hou, 1982, 2001) provides an overview of the vegetation types in China: Eastern and southeastern parts of China are dominated by temperate deciduous forests in more northern locations and temperate broadleaved evergreen forests in more southern locations, while tropical rain forest and tropical seasonal forest dominate the southernmost parts of China. The temperate deciduous forest are mainly composed of *Pinus*, *Quercus*, *Cotinus*, *Pistacia*, *Vitex*, *Dalbergia* and *Exochorda*, whereas the temperate broadleaved evergreen forest show high abundances in *Pinus*, *Cunninghamia*, *Cupressus*, *Cyclobalanopsis*, *Platycarya*, *Castanopsis*, *Fagus*, evergreen *Quercus*, *Phyllostachys*, *Rhododendron*, *Vaccinium* and *Zanthoxylum*. The tropical seasonal forest is dominated by *Gironniera*, *Burretiodendra*, *Kleinhovia* and *Antiaris*. The tropical rain forest consists of tropical mangroves as well as *Vatica*, *Dipterocarpus*, *Pometia*, *Myristica*, *Melastoma*, *Aporosa*, *Castanopsis*, *Schima*, Lauraceae, *Ficus*, *Alchornea* and *Boehmeria*.

In contrast, NE China is characterised by colder temperatures, and hence, boreal deciduous forest/woodland, coniferous forest/woodland and temperate boreal mixed forest are prevailing. The temperate boreal mixed forests, which are close to the coastline, are dominated by *Pinus*, *Acer*, *Tilia*, *Fraxinus*, *Ulmus*, *Betula*, *Corylus*, *Ostryopsis* and *Spiraea*. These temperate boreal mixed forests are replaced by boreal deciduous forest/woodland in locations where continental climate is enhanced. They mainly consist of *Larix*, *Betula* and *Populus*. Within these boreal deciduous forests, patches of boreal coniferous forests/woodlands are occurring that are composed of *Picea*, *Abies* and *Pinus*.

In northern China, temperate deciduous forests are replaced by moist savannas as well as tall and short grassland within a short distance reflecting the strongly reduced precipitation coming from the EASM. The tall grassland is characterised by temperate and meadow steppes, and mainly consists of varying Poaceae (e.g. *Stipa*, *Leymus*, *Filifolium*). Short grassland includes steppes and temperate semi-deserts with *Artemisia*, *Ajania*, *Caragana*, *Stipa* and *Festuca*.

West of 105 to 110°E, grasslands transition into xerophytic shrublands and deserts. Xerophytic shrublands are characterised by *Tamarix*, *Sympegma*, *Anabasis*, *Reaumuria*, *Artemisia*, *Kalidium*, *Ephedra*, *Zygophyllum*, *Nitraria*, *Caragana*, *Calligonum* and *Haloxylon*. Deserts include rocky hills, mobile sand dunes and salt crusts, and can be found especially in the centre of large basins with low precipitation and high evaporation. On the Tibetan Plateau, alpine tundra is the dominating vegetation type. It can be characterised by montane scrub (*Salix*, *Vaccinium*, *Dasiphora*), alpine scrubs (*Arenaria*, Androsace), alpine semi-deserts (*Caragana*, *Ceratoides*, *Ajania*), alpine steppes (*Festuca*, *Stipa*) or, subalpine meadow/swamp (*Kobresia*).

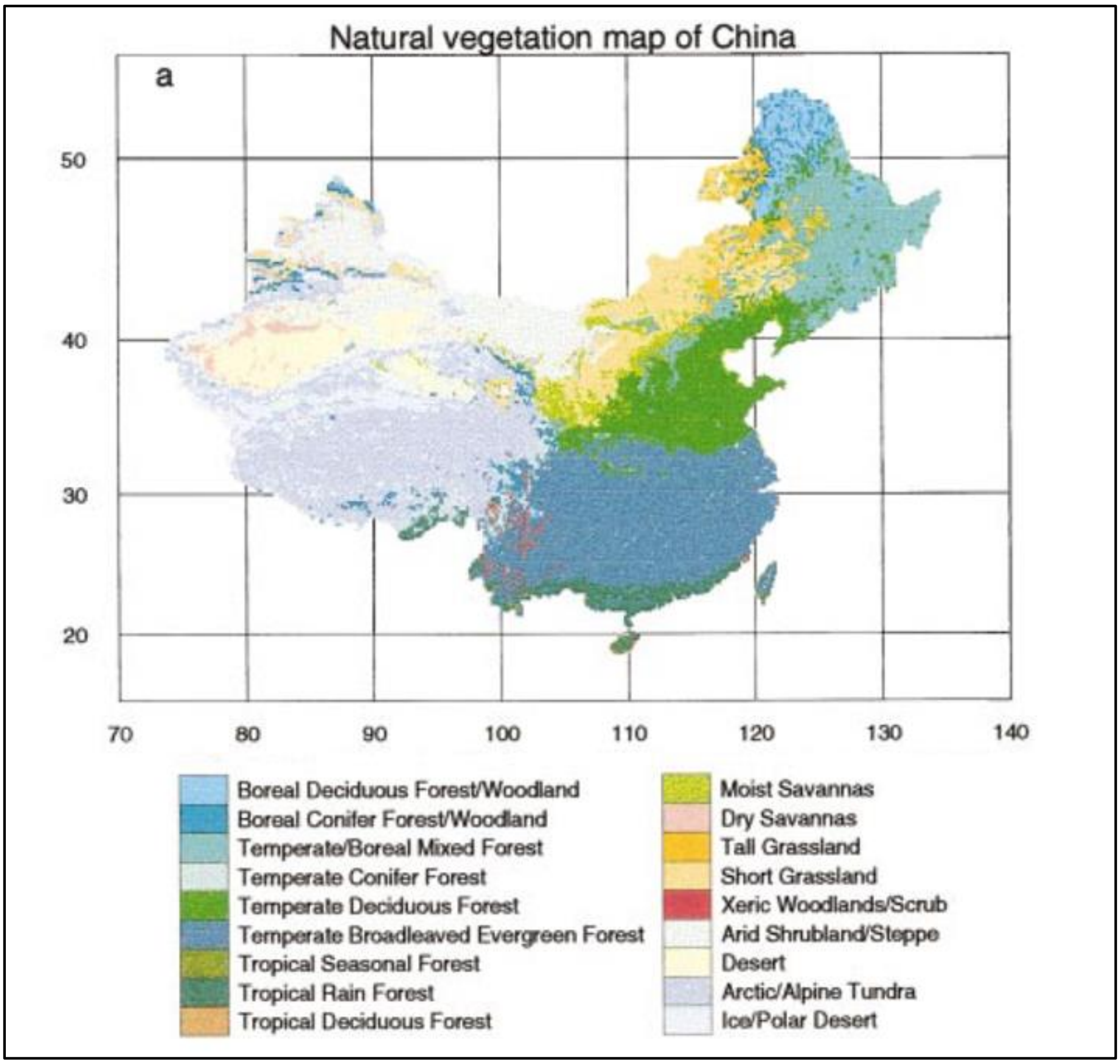

Fig. 2 - 6: Natural vegetation map of China categorised into 18 Biome3 groups based on vegetation type units from the Vegetation Atlas of China (Hou et al., 1982, 2001; Ni et al., 2000).

2.2 Drivers for Neogene climate change in NW China

2.2.1 Evolution of the Tibetan Plateau

The Asian Monsoon System underwent significant changes throughout the Cenozoic (Tada et al., 2016). Especially the uplift of the Himalayan and Tibetan Plateau, which resulted from the collision of the Indian and Eurasian continental plates, had a lasting effect on the monsoon. The high altitude of the Tibetan Plateau intensifies the land-ocean heat contrast (Wang and Chen, 2014; Webster et al., 1998; Zhao and Zhou, 2009) that is the driving force for the monsoon. Moreover, the height of the Tibetan Plateau determines how much precipitation can reach NW China directly from the monsoon system. Based on palaeomagnetic data, the convergence of the Indian plate towards Eurasia slowed down significantly at ca. 57 Ma (Aitchison et al., 2007; Klootwijk et al., 1992). Even though the exact date of collision is still a subject of controversy (e.g. Aitchison et al., 2007), most authors place the onset of the continent-continent collision between the Indian and Eurasian plate around the transition from the Paleocene to Eocene (e.g. DeCelles et al., 2014; Hu et al., 2016b; Wu et al., 2014b; Yang et al., 2015).

Sediment data and oxygen isotopes of pedogenic carbonates from various site locations at the SE margin of the Tibetan Plateau suggest that a first rapid exhumation phase occurred between 50 and 40 Ma (Amidon and Hynek, 2010; Clark et al., 2010; Clift et al., 2002; Hoke et al., 2014; Tapponnier et al., 2001). This is in accordance with deposited conglomerates at Hoh Xil (central Tibetan Plateau), which were transported from the Qiantang and Lhasa blocks in the central south Tibetan Plateau (Tapponnier et al., 2001; Wang et al., 2008a).

A second phase of intensified uplift in the Tibetan Plateau was identified between 25 and 20 Ma in the northern and central part of the Tibetan Plateau (Lease et al., 2011; Xiao et al., 2012) as well as in the Qilian Mountains (George et al., 2001; Wang et al., 2008a) using thermochronometry and sediment erosion rates. Gebelin et al. (2013) suggest that parts of the Himalaya already reached their modern altitude.

A third major phase of tectonic uplift in the Tibetan Plateau occurred in the time interval from 15 to 10 Ma in the NE part, which is indicated by an increase in grain size and erosion rates as well as a change in provenance (Tian et al., 2015; Yuan et al., 2013). Several regions in the NE Tibetan Plateau display tectonic uplift: Jishi Shan ~ 13 Ma (Lease et al., 2011), Qilian Shan ~ 10 Ma (Zheng et al., 2010), Liupan Shan ~ 8 Ma (Zheng et al., 2006).

Although all these palaeoaltimetry estimates suggest that the regions of the Tibetan Plateau underwent tectonic uplift at different times, there are still two contradicting views on the uplift history of the Tibetan Plateau: a) the Tibetan Plateau already reached modern elevation in the Late Oligocene or the Middle Miocene (e.g. DeCelles et al., 2007) and b) strong uplift (and therefore modern day elevation) did not occur until the Late Miocene (e.g. An et al., 2001; Cui et al., 1998; Wang et al., 2006b; Zheng et al., 2000).

In addition, palaeoaltimetry estimates of the same study site can vary enormously depending on the method (e.g. stable oxygen isotope, mammal composition, palynology, magnetostratigraphy) that was used (Deng and Ding, 2015). For instance, the Kunlun Pass Basin (NE Tibetan Plateau) shows how different approaches can lead to significantly different palaeoaltimetry estimates. The modern altitude of the Kunlun Pass Basin is 4600 – 5300 m. Palaeoaltimetry estimates of the Late Pliocene suggest that it has been at an elevation of 2000 m +/- 1600 m based on stable isotopes (Wang et al., 2008b), between 3200 and 4200 m based on the identification of the fish species *Gymnocypris eckloni* and *G. przewalskii* (Wang and Chang, 2010), and between 1000 and 1500 m based on studies of fossil ostracods and pollen (Wu et al., 2001).

2.2.2 Atmospheric carbon dioxide concentrations during the Pliocene

Climate changes are often associated with carbon dioxide levels in the atmosphere. Carbon dioxide is a greenhouse gas that among others (water vapour, methane, ozone, nitrous oxide etc.) absorbs outgoing radiation, that was reflected from the Earth’s surface, thereby heating up the atmosphere and surface of the Earth (e.g. Khalil, 1999). The amount of carbon dioxide in the atmosphere is not constant but rather fluctuating over geological timescales (e.g. Pagani, 2002).

Based on the alkenone proxy, Pagani et al. (2010) shows that the atmospheric carbon dioxide concentrations were ranging between 360 and 410 ppmv across several study sites in the Atlantic and Pacific Ocean during the Early Pliocene. Since 4.5 Ma the carbon dioxide concentrations were declining constantly to about 340 – 380 ppmv during the mPWP. Martinez-Boti et al. (2015) showed that atmospheric carbon dioxide concentrations (reconstruction based on $\delta^{11}B$) were ranging between ~ 200 and ~ 450 ppmv during the Late Pliocene (3.3 – 2.6 Ma) with high values during the mPWP. Seki et al. (2010) compared both methods at ODP site 999 in the Caribbean Sea stating that both records show elevated carbon dioxide concentrations (300 – 400 ppmv) between 3.2 and 2.8 Ma. There are some similarities between the different palaeorecords, but the carbon dioxide concentration range is still very large. Attempts to model the carbon dioxide concentrations reveal that they are also not in accordance and differ up to 150-200 ppmv (Stap et al., 2016; van de Wal et al., 2011). Elaborating on this further, Badger et al. (2019) proposed that alkenone isotopes do not always record atmospheric carbon dioxide concentrations very well, specifically those from Plio-Pleistocene times.

Atmospheric carbon dioxide concentrations do not only indicate warmer and colder periods, but when they fell below a certain threshold value (280 ppm), it is suggested that the NHG became inevitable through orbital forcing (DeConto et al., 2008). Compared to the pre-industrial level of atmospheric carbon dioxide concentrations (280 ppmv), all previous studies (Martinez-Boti et al., 2015; Pagani et al., 2010; Seki et al., 2010) suggest higher values during the mPWP.

2.2.3 Glaciation and astronomical forcings

Multiple marine geological proxies were established in the past, in order to determine warming/cooling trends of deep-ocean waters and the extent of high-latitudinal glaciation. During the Cenozoic, the benthic $\delta^{18}O$ foraminifera record shows a general increasing trend from low values in the Paleocene and Eocene (~ 0 – 1.6 ‰) to the high values during the Pliocene and Pleistocene (~ 2.8 – 4.4 ‰) (Zachos et al., 2001). This long-term trend of the benthic $\delta^{18}O$ signal shows stronger fluctuations on shorter time scales. Between 5.3 and 4.0 Ma, benthic $\delta^{18}O$ values range from 2.7 – 3.3 ‰ indicating warm deep-ocean temperatures / reduced glaciation (Lisiecki and Raymo, 2005). After 4.0 Ma, benthic $\delta^{18}O$ values increase steadily, but they were fluctuating between 2.9 and 3.8‰ during the remainder of the Pliocene. The values were slightly higher in the time interval from 3.6 to 3.0 Ma, ranging from ~ 2.7 to 3.6 ‰ (Zachos et al., 2001) respectively ~ 2.9 to 3.7 ‰ (Lisiecki and Raymo, 2005). During the mPWP, the benthic $\delta^{18}O$ values are < 3.3 ‰ except for a short interval between 3.150 and 3.125 Ma, which is in accordance with lower atmospheric carbon dioxide concentrations.

During the Early Pliocene (4.5 – 3.0 Ma), the extent of the WAIS (Naish et al., 2009) and the Greenland ice sheet (Hill et al., 2010) were reduced (McKay et al., 2012). The extent of the WAIS underwent changes forced by obliquity cycles during this time (Naish et al., 2009). Based on IRD offshore Wilkes Island, Patterson et al. (2014) showed that fluctuations of the EAIS were also dominated by obliquity cycles between 4.3 and 3.5 Ma. However, the period between 3.3 and 2.2 Ma was dominated by eccentricity and precession cycles. In the transition phase between 3.5 and 3.3 Ma, the long-time eccentricity (400 ka cycles) shows a minimum (Zachos et al., 2001) which produces conditions suitable for extended cold summers and a minima in seasonality, leading to Antarctic Ice Sheet growth (Patterson et al., 2014). Global cooling and expansion of Antarctic sea-ice after 3.5 Ma caused a northward migration of Southern Ocean fronts (McKay et al., 2012; Patterson et al., 2014).

The glaciation of the Northern Hemisphere began around 3.5 Ma ago (Gao et al., 2012), which is much later than the Antarctic glaciation. Along with decreasing atmospheric carbon dioxide concentrations, the closure of the CAS played an important role in the initiation of NHG. According to early theories, the CAS was closing gradually since the Late Miocene (Collins et al., 1996) until 2.7 Ma, when land mammal fauna could exchange between the northern and southern parts of Central America (Marshall et al., 1982). In addition, Haug and Tiedemann (1998) argue that from 4.6 Ma on the CAS was too shallow to allow deep-water circulation, resulting in the rearrangements of the global thermohaline circulation, which led to warm and salt-rich surface waters being directed to the North Atlantic. However, more recently (Montes et al., 2015) argued that the CAS was potentially already closed during the Middle Miocene. The moisture transport to the northern high latitudes resulted in the precipitation of snow once the carbon dioxide reduction induced cooling of the high latitudes reached a threshold (DeConto et al., 2008). Jansen et al. (2000) reconstructed IRD in the North Atlantic at ODP Site 907 stating that a first major input of IRD occurred around 3.3 Ma coinciding with the cold phase of MIS M2 (Lisiecki and Raymo, 2005). During the mPWP, IRD remained at a low level with a slight increase between 3.15 and 3.1 Ma (Jansen et al., 2000). After 3.05 Ma, IRD was continuously found in large amounts at ODP Site 907, which outlines the intensification of the NHG during the Late Pliocene and Plio-Pleistocene transition (Jansen et al., 2000).

Martinez-Boti et al. (2015) suggest that global mean annual surface air temperatures were about 2 – 3°C higher during the mPWP compared to the pre-industrial. This is in good agreement with previous studies (Haywood et al., 2009; Haywood and Valdes, 2004; Haywood et al., 2000; Lunt et al., 2010). Due to polar amplification effects, warming in the high latitudes strongly exceeded those in the low latitudes, which led to a reduction of the equator-pole temperature contrast (Ballantyne et al., 2010).

2.3 Palaeoenvironmental history of NW China during the Neogene

2.3.1 Global vegetation and climate during the Pliocene

The global distribution of vegetation was significantly different during the Pliocene compared to modern-day. Salzmann et al. (2008, 2011, 2013) reconstructed the global biomes during the Piacenzian using a combination of palaeobotanical data and model simulations, which suggest that climatic conditions were globally warmer and wetter. In particular, there was a northward expansion of the evergreen taiga in the high latitudes of the Northern Hemisphere along with a northward shift of temperate forests and grasslands, an expansion of warm-temperate forests in central Europe and a replacement of deserts by tropical savannas in Africa and Australia (Salzmann et al., 2008). The following sections will provide an overview about global vegetation changes during the Pliocene for the high-, mid- and low-latitudes, followed by a more detailed description of Neogene vegetation and climate change of China.

2.3.1.1 Pliocene vegetation in the high latitudes: expansion of boreal forests at the expense of tundra

Although Pliocene high-resolution pollen records are scarce for the high latitudes (Miller et al., 2010), studies have shown that tundra vegetation in the high latitudes and polar regions were significantly smaller than they are today (e.g. Andreev et al., 2014). The landscape in the Russian Arctic underwent frequent changes of vegetation between 3.5 and 2.75 Ma with coniferous forests dominated by *Larix*, *Abies* and *Picea* alternating with tundra type vegetation, which mainly consisted of Poaceae, Cyperaceae, *Artemisia*, Caryophyllaceae and *Selaginella* (Andreev et al., 2014). After 2.75 Ma, coniferous forests decreased significantly coinciding with the onset of the NHG. Boreal forests were also found in Canada as far north as Bylot Island (Csank et al., 2013) and Ellesmere Island (Ballantyne et al., 2010; Ballantyne et al., 2006) during the Pliocene. The latter study area was covered by a boreal forest dominated by *Betula*, *Larix*, *Picea*, *Thuja* and *Alnus* illustrating the polar amplification effect of global warming, during which the temperature increase in the high latitudes is significantly stronger than that of the mid- or low latitudes. Temperature estimates suggests that Arctic temperatures were up to 19°C higher (Ballantyne et al., 2010). In Norway, warmer conditions led to a northward expansion of warm-temperate taxa by several degrees (Willard, 1994). However, this expansion was not stable throughout the Pliocene as has been demonstrated by a high-resolution pollen record from Panitz et al. (2016). The cool-temperate forests were rather alternating with boreal forests, suggesting warmer and colder intervals during the Late Pliocene. In Antarctica, fossil plant remains of *Nothofagus* indicate a possible tundra landscape cover (Francis and Hill, 1996) and therefore, significant retreat of ice sheets during the Pliocene, but the discussion about the age of the Sirius Group Formation is still ongoing (e.g. Retallack et al., 2001).

2.3.1.2 Pliocene vegetation in the mid-latitudes: northward expansion of warm-temperate forests

The Pliocene vegetation in the mid-latitudes indicate an increase in temperature and precipitation compared to present-day (Hansen et al., 2001; Suc et al., 1995). In Europe, the composition of forests was distributed differently from the modern setting. Instead of the modern boreal coniferous forests, temperate forests (including tropical, subtropical and warm-temperate taxa such as *Engelhardtia*, *Pterocarya*, *Carpinus, Fagus, Quercus* and *Carya*) covered central and northern Europe (Mai, 1995; Rousseau et al., 1992). In southern and western Europe, warm-temperate forests were dominating until global cooling caused a transition towards temperate deciduous forests (Mai, 1995). The southern Mediterranean vegetation record shows that the typical modern open xeric vegetation and climate seasonality were already established during the Pliocene (Suc et al., 1995). This might be the result of increased temperatures during the Pliocene leading to a higher evaporation, which could outpace increases in precipitation.

2.3.1.3 Pliocene vegetation in the low latitudes: Expansion of savannas and shrublands at the expense of deserts

The tropical rainforest zone did not deviate much from its modern size (Hansen et al., 2001; Kershaw and Sluiter, 1982; Salzmann et al., 2011). However, in Africa, subtropical woodlands, savannas and shrublands expanded much further northwards at the expense of deserts, which implies higher precipitations in today’s semi-arid and arid areas (Jolly-Saad and Bonnefille, 2012; Leroy and Dupont, 1994; Leroy and Dupont, 1997). Leroy and Dupont (1997) point out that the northward shift of savannas and shrublands was controlled by orbital forcing (especially changes in obliquity). Stepwise increase of the Sahara desert began in the Late Pliocene around 3.5 Ma ago, before the major expansion took place at the Plio-Pleistocene transition (Leroy and Dupont, 1997).

In Ethiopia, fossil wood samples of *Albizia* were found at much lower elevation (600 m) than present-day (1200 – 2000 m) suggesting the expansion of forests into lowlands due to higher precipitation (Jolly-Saad and Bonnefille, 2012). Contrary, the modern vegetation is dominated by bushland and steppes, as a result of prevailing semi-arid and arid climate. A similar expansion of woodland/forests was also observed in Tanzania (Andrews and Bamford, 2008; Bonnefille, 2010).

In North America, warm-temperate taxa (including *Pterocarya*) were present in evergreen coniferous forests covering coastal areas in northern Florida (Hansen et al., 2001). However, the thermophilic taxa were not abundance and occasionally became absent in the record leading to temperature estimates that are similar or slightly warmer than modern-day (Hansen et al., 2001; Salzmann et al., 2011).

2.3.2 Neogene vegetation development in China – state of the art

The modern landscape of large parts in northern and western China is covered by deserts, semi-deserts and steppes, whereas eastern China is covered by savannas, woodlands and forests. Guo et al. (2002) proposed that the extensive semi-arid and arid areas in northern and western China might be the result of a long-term aridification process that started as early as 22 Ma.

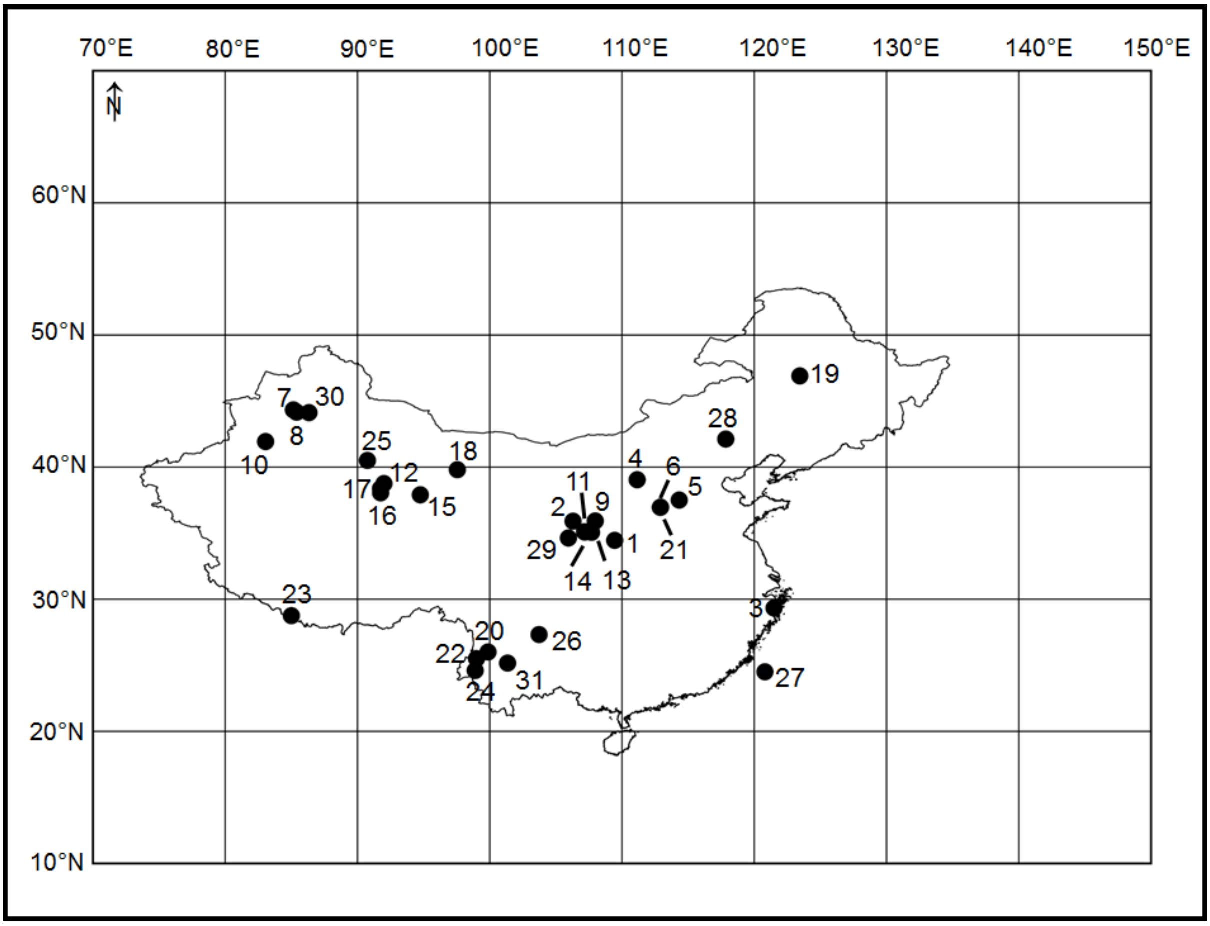

Fig. 2 - 7: Palaeobotanical records in China covering the Miocene and Pliocene vegetation (details see Tab. 2 – 1)

2.3.2.1 Miocene vegetation

The Miocene in eastern China (Fig. 2 – 8) was characterised by extensive woodland and forests vegetation composed of *Ulmus*, *Quercus*, *Carya*, *Alnus* and *Juglans* (Jiang and Ding, 2009). Pollen analysis from the Songliao Basin (Nr.19, Tab.2 – 1) indicate the Early and Middle Miocene was dominated by deciduous broadleaved forests with minor elements of coniferous forests and evergreen broadleaved forests (*Carya*, *Juglans*, *Ulmus*, *Celtis*, *Carpinus*, *Betula*, *Quercus*, *Fagus*, *Pinus*) (Wan et al., 2014). The vegetation changed during the Late Miocene to broadleaved mixed forests with lower abundances of subtropical taxa and an increase in herbaceous taxa such as *Artemisia*, *Nitraria*, Chenopodiaceae and *Ephedra*. The increase in xerophytic shrubs indicates that cooling and drying took place in the study area (Wan et al., 2014).

Tab. 2 - 1: Palaeobotanical study sites covering Miocene and Pliocene vegetation in China. Time span of the studies are shown as indicated by the authors. In cases where no absolute ages were given, respective Miocene (Mio) and Pliocene (Plio) age interpretations of geological formations made by the authors were stated.

Site	Author	Year	Latitude	Longitude	Age [Ma]
1	Han et al.	1997	34°28'N	109°40'E	3.08 - 1.9
2	Jiang et al.	2008	35°55'N	106°20'E	20 - 0
3	Li et al.	2010	29°20'N	121°31'E	Late Plio
4	Li et al.	2011	39°01'01"N	111°09'32"E	5.8 - 2.8
5	Li et al.	2004	37°30'N	114°20'E	5.5 - 2.5
6	Liu et al.	2002	36°55'N	112°50'E	3.1 - 2.1
7	Sun et al.	2007	44°20'N	85°10'E	8.7 - 2.58
8	Tang et al.	2011	44°10.4'N	85°27.4'E	28 - 4.2
9	Wang et al.	2006	35°53'N	107°58'E	6.2 - 2.4
10	Zhang et al.	2011	41°55.097'N	83°03.28'E	13.3 - 2.6
11	Ma et al.	2005	35°7'N	107°12'E	8.1 - 2.6
12	Wang et al.	1999	38°45'N	92°E	65 - 2.5
13	Wu et al.	2001	35°04'N	107°43'E	6.5 - 3.4
14	Wu et al.	2007	35°7'N	107°12'E	3 - 0
15	Wu et al.	2011	37°50'N	94°45'E	5.3 - 1.83
16	Miao et al.	2011/2013	38°03'N	91°45'E	18 - 5
17	Cai et al.	2012	38°22'47.8"N	91°44'53.43"E	3.1 - 0
18	Ma et al.	2005	39°47'N	97°32'E	13 - 2.21
19	Wan et al.	2014	46°50'N	123°25'E	Mio + Plio
20	Kuo et al.	2006	26°00.02'N	99°49.06'E	Pliocene
21	Qin et al.	2011	36°58'N	112°51'E	2.77 - 2.52
22	Sun et al.	2011	25°30'N	99°E	Mio + Plio
23	Xu et al.	2012	28°45'N	85°E	10.8 - 1.7
24	Xu et al.	2004	24°41'N	98°50'E	Plio
25	Hao et al.	2012	40°30'N	90°45'E	7 - 0
26	Chang et al.	2015	27°19'41.8"N	103°44'13.7E	6.73 - 6.03
27	Hao et al.	2017	24°30'N	120°49'E	14.5 - 5.5
28	Li et al.	2009	42°07'34"N	117°50'27"E	Early Mio

29	Liu et al.	2016	34°38'N	105°55'E	11.4 - 6.4
30	Sun et al.	2008	44°07'N	86°20'E	26.5 - 2.6
31	Xu et al.	2008	25°10'N	101°22'E	Late Mio

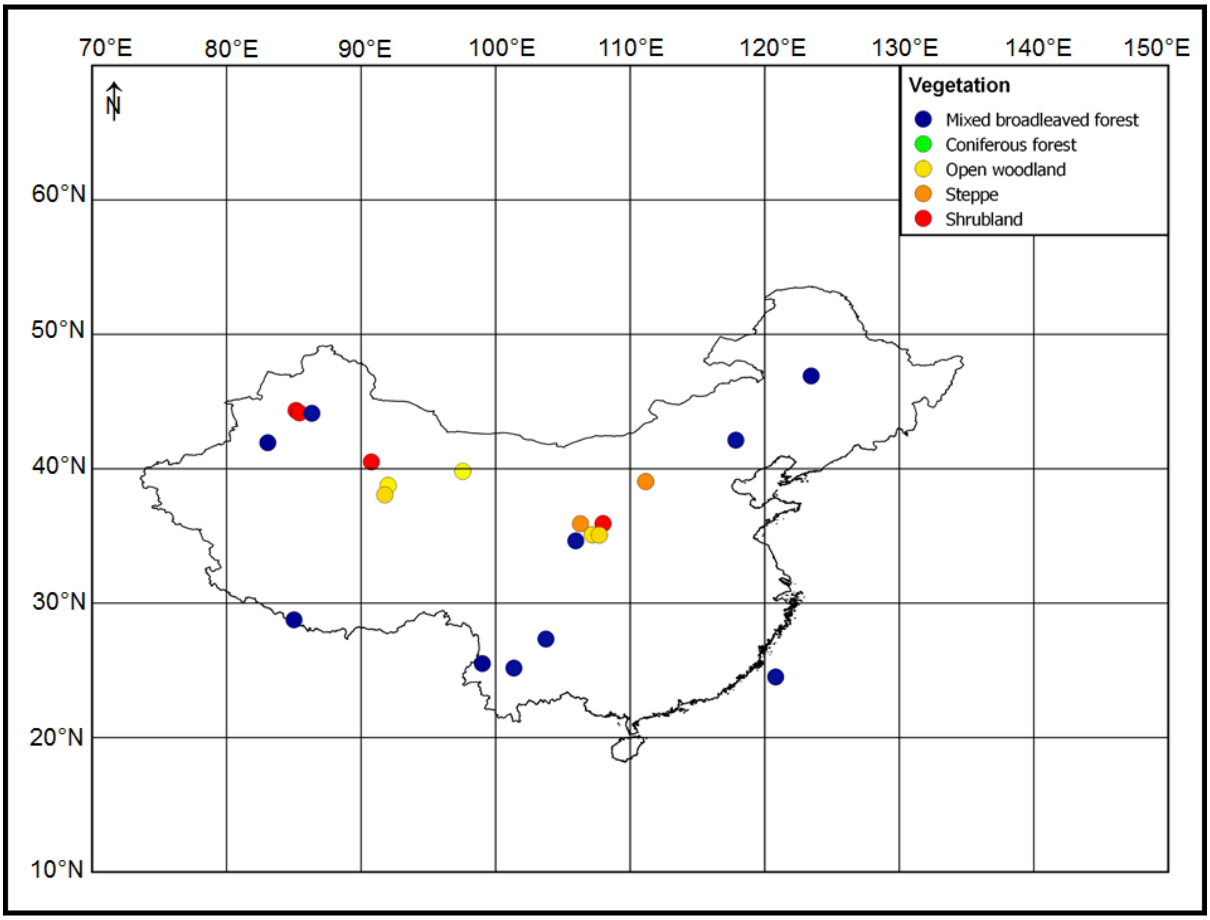

Fig. 2 - 8: Overview of Miocene vegetation in China shows that mixed broadleaved forests were widely distributed not only in the southern, southeastern and eastern parts as it is nowadays (see also Fig. 2 – 6) but also in the northwestern parts of China. Open woodlands occurred in northern China, whereas steppes and xerophytic shrublands were greatly reduced and only present in some site locations. Site locations are given in Tab. 2 – 1 and Fig. 2 – 7, respectively.

In Yunnan (south China), the composition of forests changed during the Late Miocene from broadleaved deciduous forests (*Quercus*, *Corylus*, *Alnus*) with some evergreen elements (*Quercus*, *Carya*, *Carpinus*, *Liquidambar*, *Platycarya*) to mixed coniferous and broadleaved forests and subseqeuntly coniferous forests, which suggests cooling of the area (Chang et al., 2015; Xu et al., 2008). The Late Miocene in Yunnan also features swampy elements, which indicates that the precipitation was high (Chang et al., 2015).

In the Miocene, mixed coniferous (*Pinus*, *Tsuga*, *Abies*, *Picea*, *Larix*) and broadleaved (*Alnus*, *Betula*, *Corylus*) forests with subtropical taxa/elements

(*Carya*, *Juglans*, *Pterocarya*, *Tilia*, *Ginkgo*) were not only present in southern and eastern China but also in northern China (Li et al., 2009). This implies that the precipitation and temperatures were much higher in northern China (Nr.28, Tab.2 – 1) during the Miocene leading to an expansion of subtropical conditions from the south.

The Miocene vegetation in western China was characterised by less dense and more open vegetation compared to other parts of China. The vegetation was dominated by open woodland, steppes and shrublands, in which trees were growing in small localised patches that experienced higher precipitation (Jiang and Ding, 2009). In the Longzhong Basin (Nr.29, Tab.2 – 1), a mid and late Miocene pollen record (11.4 – 6.4 Ma) reveals that mixed deciduous forests (*Pinus*, Cupressaceae, *Ulmus*, *Quercus*) grew in the basin and surrounding hills, while coniferous forests (*Abies*, *Picea* and *Cedrus*) covered the uplands (Liu et al., 2016). Temperate forests were replaced by warm-temperate open woodlands and steppes (increase in Poaceae, *Artemisia*, Chenopodiaceae) in two aridification steps at 10.1 and 7.4 Ma (Liu et al., 2016).

In the Qaidam Basin (Nr.12/16, Tab.2 – 1), the vegetation history of the Miocene suggests that continuous aridification took place, possibly linked to uplift of the Tibetan Plateau (Wang et al., 1999). During Early and Middle Miocene, coniferous forests prevailed (*Pinus*, *Cedrus*, *Picea*, *Podocarpus*, *Tsuga*) with only few broadleaved trees (*Ulmus*, *Quercus*, *Betula*). Subtropical trees, such as *Juglans*, *Carya*, *Castanea*, were present at low levels. Steppe and semi-desert shrubland taxa (*Artemisia*, Chenopodiaceae, *Ephedra*, *Nitraria*) contributed up to 20% of the total pollen count (Miao et al., 2011). From 14 Ma onwards, coniferous forests decreased continuously, whereas steppes and semi-deserts expanded until 5 Ma (Miao et al., 2011).

During the Early Miocene, the Tian Mountains (Nr.30, Tab.2 – 1) in NW China were mostly covered with coniferous forests (*Pinus*, *Picea*, *Abies*) and some deciduous trees (*Betula*, *Tilia*, *Juglans*, *Quercus*, *Carpinus*, *Carya*) (Sun and Zhang, 2008). Between 18 and 15 Ma, broadleaved forests increased at the expense of coniferous forests, which indicates a warm climate during the mid-Miocene Climatic Optimum. After 15 Ma, broadleaved forests declined again and the forest composition was almost exclusively made of coniferous trees (Sun and Zhang, 2008). From 6 to 2.6 Ma, herbaceous taxa (*Artemisia*, Chenopodiaceae) increased sharply, which reflects strong aridification during the Late Miocene and Pliocene (Sun and Zhang, 2008).

2.3.2.2 Pliocene vegetation

In contrast to the Miocene, the Pliocene vegetation in China (Fig. 2 – 9) is characterised by a replacement of mixed broadleaved and coniferous forests with open woodlands, steppes and shrublands, which indicates that aridification took place in many regions in China, especially the northwestern parts.

Tropical and subtropical evergreen broadleaved trees covered the coastal areas of eastern and southern China (Nr.3, Tab. 2 – 1), which indicates still warm and wet conditions during the Pliocene (Li et al., 2010). In SW China, mixed evergreen coniferous and broadleaved forests were present (*Quercus*, *Alnus*, *Acer* and *Pinus*), which suggests warmer conditions during the Pliocene compared to modern-day (Kou et al., 2006; Sun and Wang, 2005). Kou et al. (2006) argue that the temperature difference of up to 5°C between the Pliocene and modern-day palynoflora might be due to altitudinal changes, implying that significant tectonic uplift of the eastern Tibetan Plateau took place after the Pliocene. In contrast, Sun and Wang (2005) attribute the temperature differences to the generally warmer Pliocene and only minor uplift in the Eryuan area.

In northern and northeastern China (Nr.6, Tab. 2 – 1), the vegetation was dominated by humid broadleaved deciduous forests during the Early Pliocene, which also contained subtropical trees (*Carya*, *Podocarpus*, *Liquidambar*), and open woodlands during the Late Pliocene, while nowadays grasslands and few open woodlands characterise the vegetation in northern China (Liu et al., 2002a; Sun and Wang, 2005). The retreat of subtropical elements to the south during the Pliocene indicates decreasing temperatures and precipitation in northern China, which resulted in the expansion grasslands and xerophytic shrublands.

The Pliocene of NW China was characterised by an expansion of semi-deserts (Ephedraceae, *Artemisia*, Chenopodiaceae, *Nitraria*) replacing the open woodlands and steppes. Xerophytic shrublands are prevailing until today or have been been fully transformed into deserts absent of any vegetation (Ma et al., 2005b; Miao et al., 2013; Sun and Wang, 2005; Wang et al., 1999). On the northern Tian Mountains, the Early Pliocene vegetation was characterised by xerophytic shrublands (*Artemisia*, Chenopodiaceae) with rare occurrences of arboreal pollen suggesting very dry climate (Tang et al., 2011).

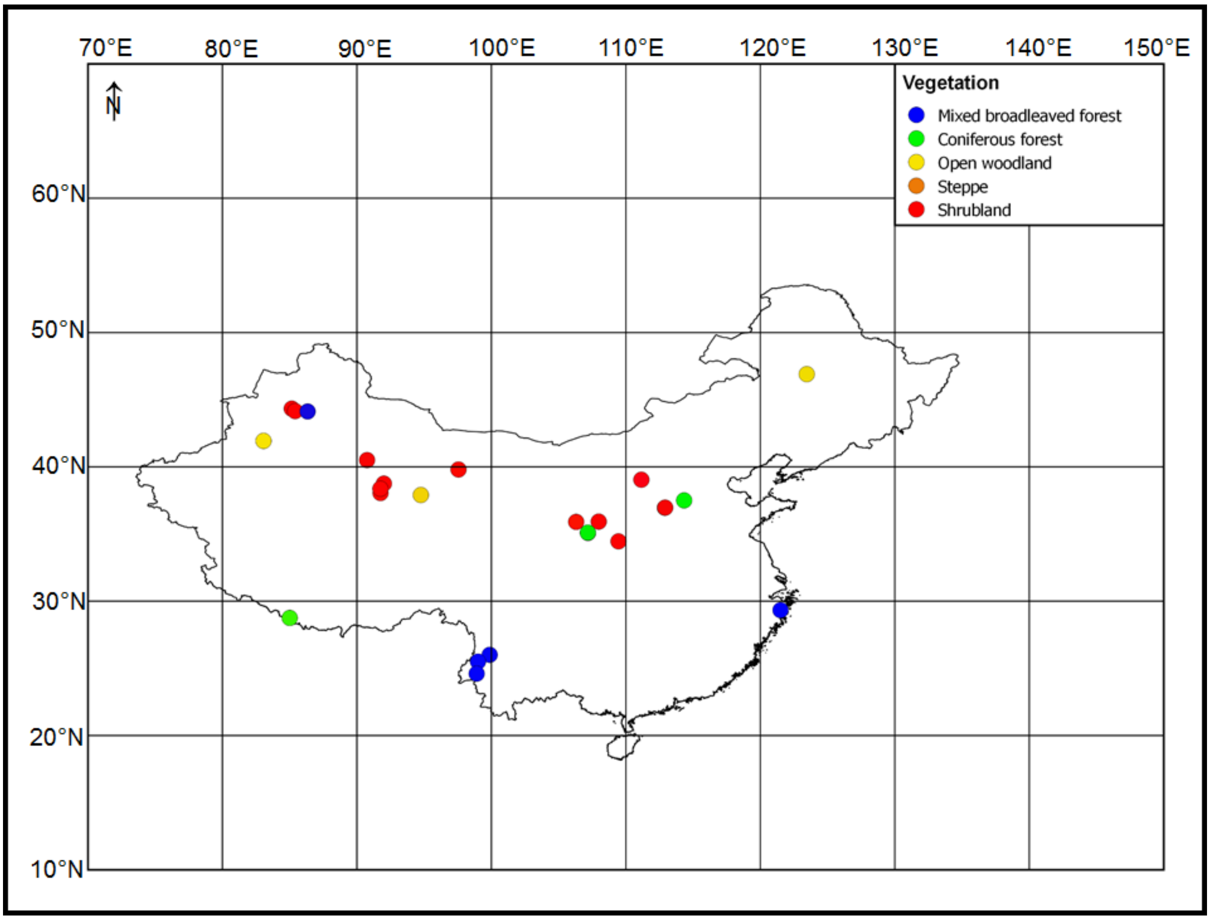

Fig. 2 - 9: Overview of Pliocene vegetation in China shows that mixed broadleaved forests retreated to southeastern locations whereas coniferous forests, steppes and xerophytic shrublands expanded in northern and western parts. Site locations are given in Tab. 2 – 1 and Fig. 2 – 7, respectively.

In the NW Qaidam Basin, pollen records from Miao et al. (2011) and Cai et al. (2012) show that the Miocene steppes and shrublands, which contained significant amounts of coniferous trees were transforming into xerophytic shrublands during the Pliocene (Fig. 2 – 10). These vegetation changes point to a reduction of precipitation in the study area. Since the pollen records from Cai et al. (2012) and Miao et al. (2011) have an age gap between 5.0 and 3.1 Ma, it can only be speculated, if the Pliocene aridification was a continuous process similar to the suggestion of Miao et al. (2013), or if the aridification between 5.0 and 3.1 Ma occurred sharply. In the central Qaidam Basin (Yahu Section), a pollen record from Wu et al. (2011) suggests that two aridification steps took place at 3.6 and 2.6 Ma, transforming open woodland vegetation into shrublands with locally growing trees (Fig. 2 – 11). Between 5.3 and 3.6 Ma, highly fluctuating

(0 – 80%) coniferous trees dominated the vegetation. After 3.6 Ma, the xerophytic shrubs *Artemisia* and Chenopodiaceae become more prominent, which led to frequent changes in the abundance of coniferous trees and xerophytic shrubs in the time interval from 3.6 to 2.6 Ma. Following 2.6 Ma, xerophytic shrubs continue to increase while coniferous trees decline to their lowest abundances. Cooling and drying is also characterised by the absence of *Pterocarya* after 2.6 Ma (Wu et al., 2011). Coniferous trees still frequently occurred in the pollen record from the Yahu Section until 1.8 Ma (Fig. 2 - 11; Wu et al., 2011), whereas they were present only in low abundances in the NW Qaidam Basin after 3.1 Ma (Fig. 2 - 10; Cai et al., 2012; Miao et al., 2011; Miao et al., 2013), suggesting that the central Qaidam Basin was considerably wetter in the Late Pliocene.

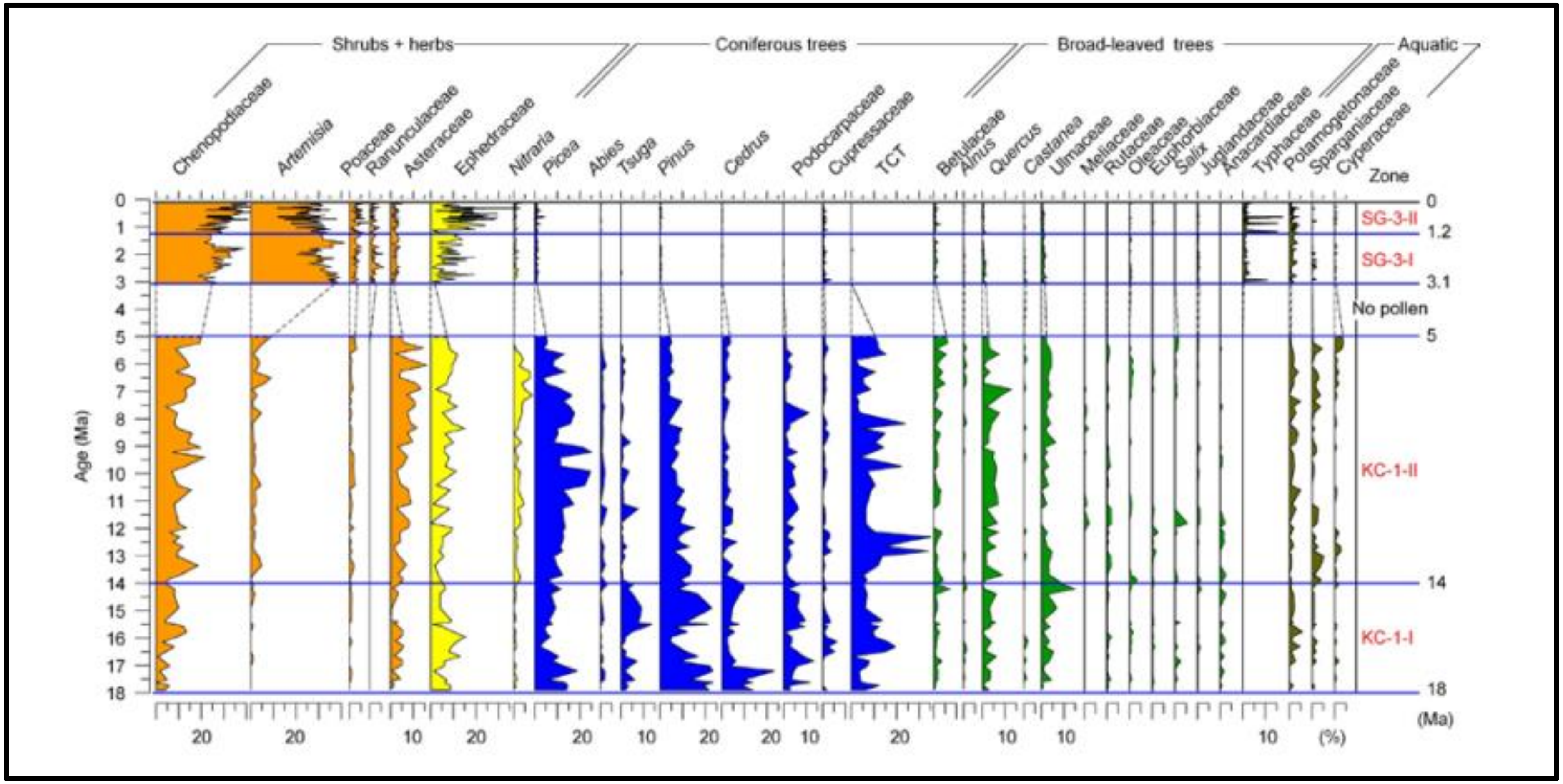

Fig. 2 - 10: Combined pollen diagram (Miao et al., 2013) of the NW Qaidam Basin based on data from Cai et al. (2012) and Miao et al. (2011). Although no pollen data exists between 5 and 3.1 Ma, strong aridification can be assumed as Chenopodiaceae and especially *Artemisia* increase, whereas coniferous and broadleaved trees decrease during this period.

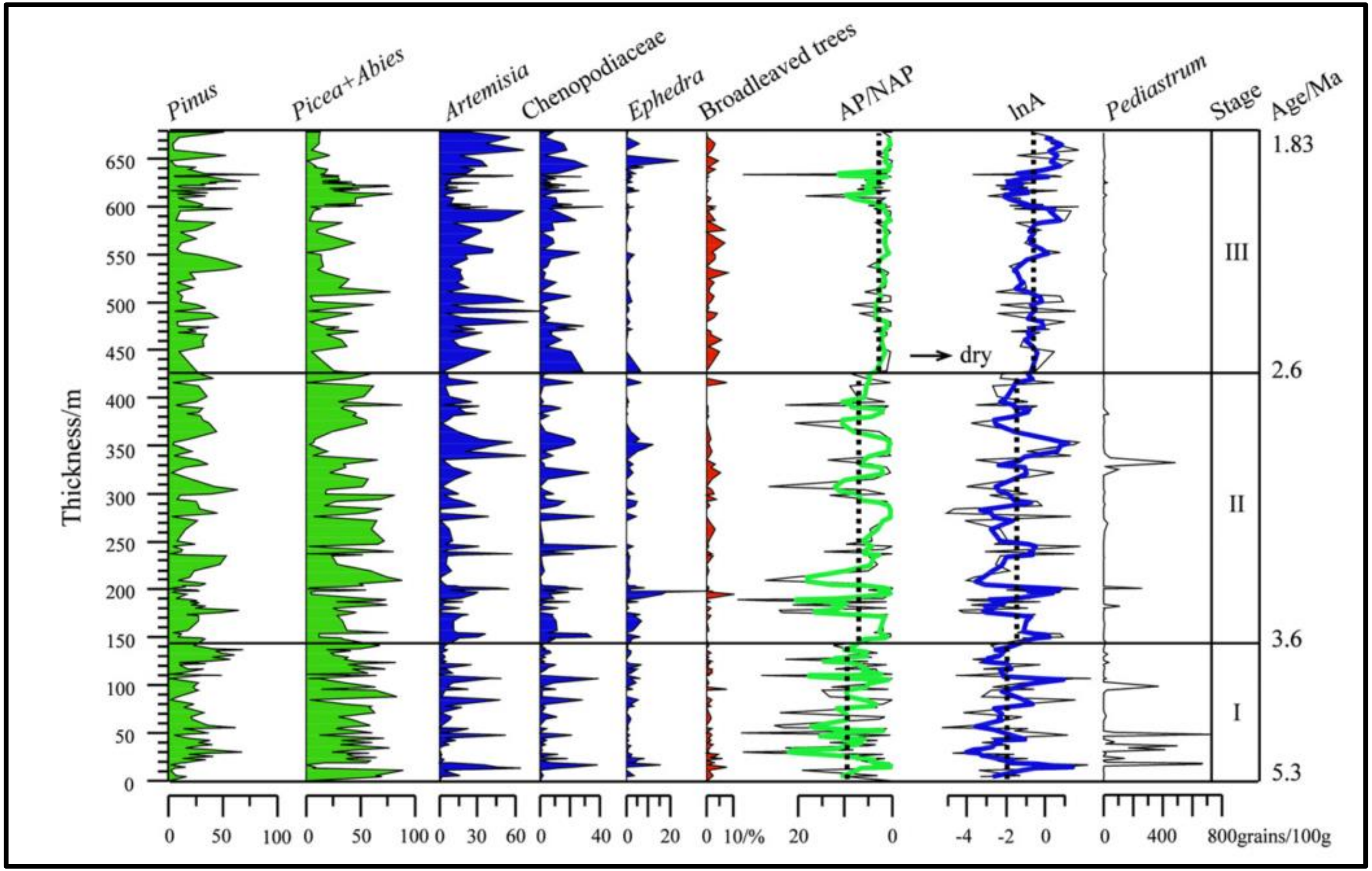

Fig. 2 - 11: Pollen diagram of the Yahu Section, central Qaidam Basin (Wu et al., 2011).

The Pliocene vegetation on the northern CLP was characterised by gradual changes from open woodlands with *Pinus*, *Betula*, *Ulmus* and *Quercus* to steppes and shrublands that feature only small amounts of trees (Fig. 2 – 12), possibly growing in localised patches (Li et al., 2011). Between 3.5 and 3.1 Ma, the xerophytic shrublands were strongly dominated by *Artemisia* (Li et al., 2011) leading to highest *Artemisia*/Chenopodiaceae (A/C) ratios in the record, which could be an indication of wetter conditions (El-Moslimany, 1990; Zhao et al., 2012). However, the reduction of tree percentages suggests rather cooling and drying on the CLP during this time interval (Li et al., 2011). The low resolution pollen records from the Yushe and Taigu Basins on the eastern part of the CLP suggest that between 4 and 2.5 Ma coniferous forests (*Pinus*, *Picea*, *Abies*) dominated, which were subsequently replaced by *Artemisia* shrublands after 2.5 Ma (Li et al., 2004). Additionally, a pollen record from Ma et al. (2005a) indicates that between 3.71 and 2.58 Ma coniferous forests were present in the western CLP (Chaona), replacing steppes and open woodlands (*Artemisia*, Poaceae, Chenopodiaceae, *Pinus* and *Picea*) (Fig.2 – 13). These coniferous forest consisted almost solely of *Juniperus*, whereas other coniferous trees such as *Pinus*, *Picea* and *Tsuga* declined sharply at the beginning of this interval (Ma et al., 2005a). Therefore, the vegetation history on the CLP seemingly included the expansion of coniferous forests in the western part (Ma et al., 2005a), while coniferous forests retreated from the northern parts.

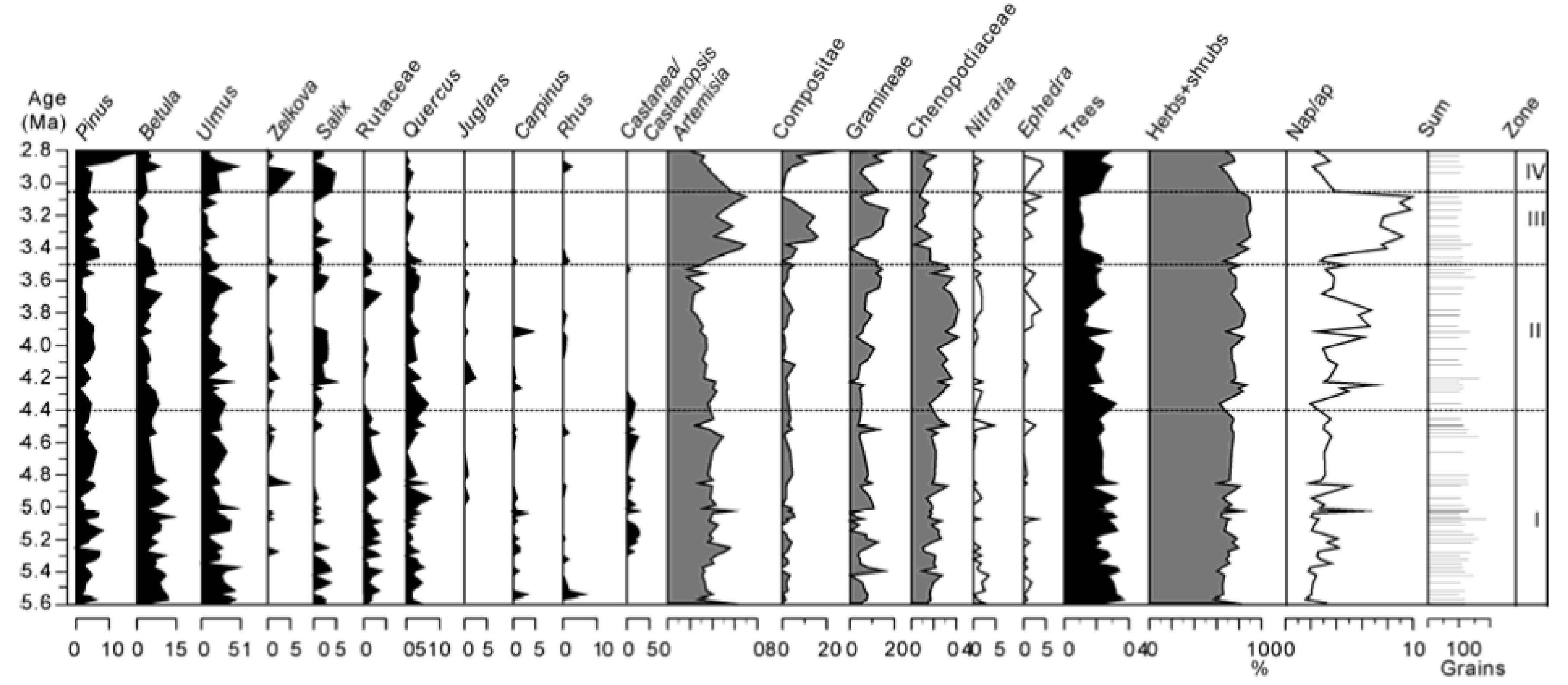

Fig. 2 - 12: Pollen diagram from Baode, northern CLP (Li et al., 2011). The pollen diagram shows that Baode was mainly dominated by steppes with transitions to open woodlands and shrublands.

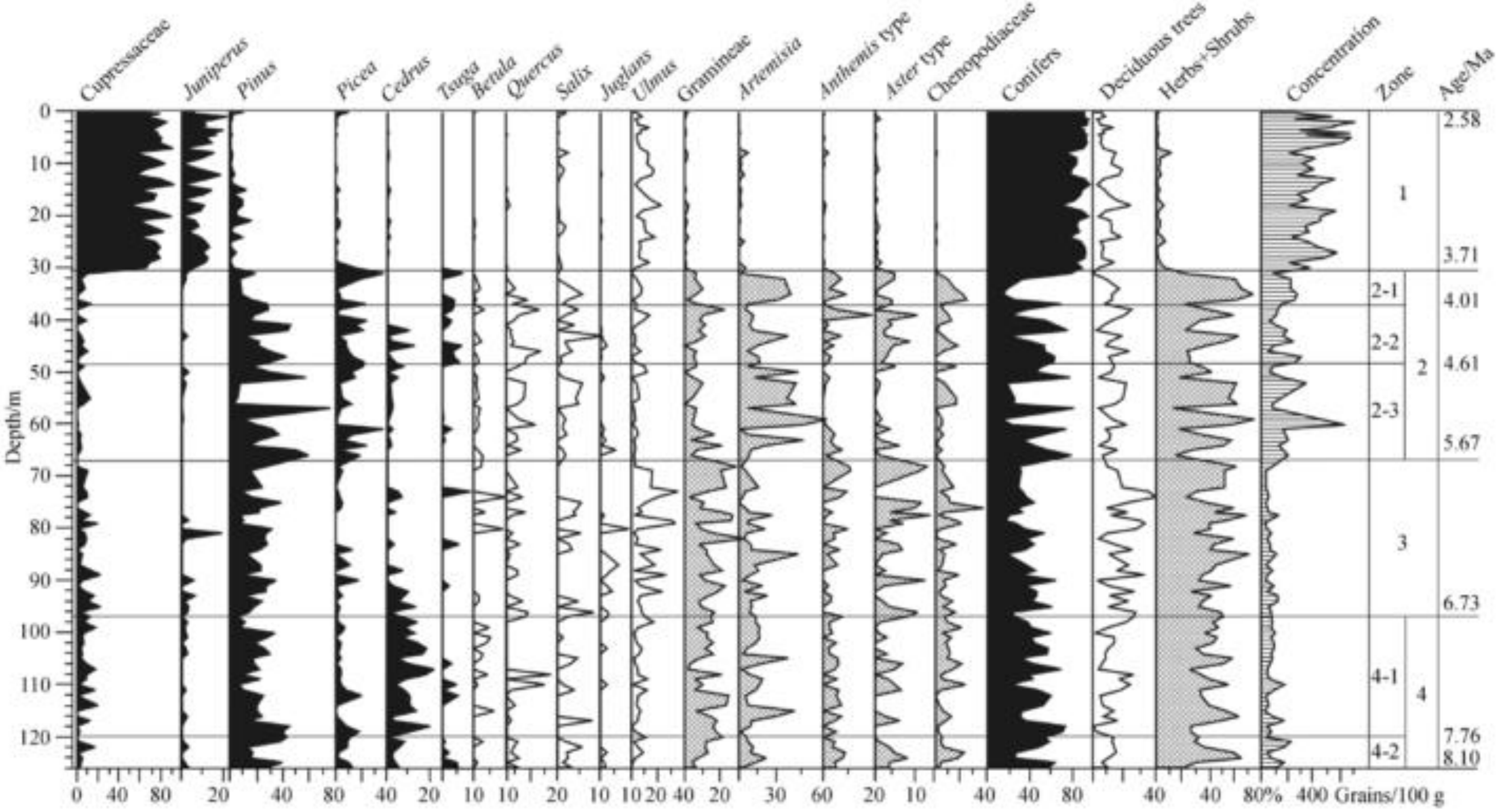

Fig. 2 - 13: Pollen diagram of the Chaona Section on the western CLP from Ma et al. (2005a). The strong increase of Cupressaceae around 3.71 Ma ago is in sharp contrast to the pollen diagram from Baode (Fig. 2 – 12) and suggests that coniferous forests existed on the CLP during the mPWP.

Chapter 3: Study sites and methodology

3.1 Study sites

3.1.1 NW Qaidam Basin: SG-1b core

The Qaidam Basin (ca 120,000 km²) is located in western China on the NE Tibetan Plateau. It is surrounded by three mountain ranges, the Altun Mountains to the north, the Qilian Mountains to the east and the Kunlun Mountains to the south and west. Following the collision of the Indian and Eurasian plate around 60 to 55 Ma and the subsequent indenting (e.g. DeCelles et al., 2014; Huang et al., 2010; Sun et al., 2012), strong extensional and contractional forces shaped the Asian interior. During a second phase of strong exhumation, the central and northern Tibetan Plateau (including Qilian Mountains) were uplifted between 25 and 20 Ma. Since then, the Qaidam Basin experienced extensive deformations as a direct cause of the Altun and Kunlun fault (Liu et al., 2009; Wang et al., 2007; Xia et al., 2001; Yin et al., 2007; Yin et al., 2002; Zhang et al., 2014; Zhou et al., 2006). From the Oligocene until today, the Qaidam Basin is still actively shortening in the NE-SW direction. This led to uplift of the surrounding mountains as well as the anticlines between the Northern Qaidam Thrust System and the Southern Qaidam Thrust System, which follow a NW-SE direction (Fang et al., 2006; Wang et al., 2007). As a result, the interior of the Qaidam Basin (~2800 m) and the surrounding mountain ranges (4000 – 5000 m) do not only show a strong altidutinal gradient, but also the establishment of the Qaidam Basin as an intramontane basin led to significant accumulation of more than 10 km Cenozoic sediments (e.g. Herb et al., 2013; Yin et al., 2007). The Cenozoic lithostratigraphy (Yin et al 2007) is divided into seven formations: Lulehe Formation covers the Paleocene and Eocene, Xia Ganchaigou Formation covers Oligocene, Shang Ganchaigou Formation covers the Early Miocene, Xia Youshashan Formation covers the Middle Miocene, Shizigou Formation covers the Pliocene and the Qigequan Formation covers the Early Pleistocene (Herb et al., 2015; Yin et al., 2007; Zhang et al., 2014). The Shizigou Formation is the only formation covering the Pliocene, and hence, of importance for this study. It consists mainly of conglomerates and sandstones that are intercalated with mudstones and siltstones (Fang et al., 2007; Herb et al., 2015). The location of the Qaidam Basin at the monsoonal limit leads to a precipitation gradient between higher MAP in the south-east and lower MAP in the north-west (Wang et al., 2014). Based on 8 meteorological stations, Wang et al. (2014) found that MAT and MAP were rising in the Qaidam Basin between 1961 and 2010. The NW part of the Qaidam Basin, where the SG-1b core (N 38.352628, E 92.273533; 2711 m a.s.l) is located (Fig. 3 – 1), only receives MAP of 28 mm, while its MAT is about 3 °C (see Fig. 2 – 1, 2 – 2 and 2 – 3). Locations at higher altitude receive slightly higher MAP but have generally lower temperatures. Since the potential evaporation rate of up to 3250 mm (Herb et al., 2013; Yang et al., 1995) exceeds the actual precipitation more than tenfold, the Qaidam Basin is a hyper-arid basin with only “few shallow perennial or ephemeral lakes” (Yang et al., 1995).

3.1.2 Kunlun Pass Basin

The Kunlun Pass Basin (~ N 35.64, E 94.063964; 4781 m a.s.l.) is located in the East Kunlun Mountains to the west of the Qaidam Basin (Fig. 2 – 1). The Kunlun Pass Basin (modern elevation: 4700 – 5300 m) is surrounded by the Budongquang Fault (south) and Kunlun Pass Fault (north) (Song et al., 2005a). The basin has been characterised as a pull-apart basin of Pliocene and Pleistocene age (Song et al., 2005a and Chinese References therein). The Kunlun Mountains (including the Kunlun Pass Basin) were formed due to the indention of the Indian into the Eurasian plate. The uplift history of the Kunlun Pass Basin area is not fully established yet and several different theories exist how high the area had been uplifted by Late Pliocene (see Chapter 5). The sediments in the Kunlun Pass Basin are of Pliocene and Quaternary origin (Song et al., 2005a) and grouped into the Kunlun Formation (3.58 – 2.69 Ma), Qiangtang Formation (2.58 – 0.78 Ma) and Wangkun Formation (0.78 – 0.5 Ma). These late Cenozoic sediments are unconformably underlain by Triassic bedrock (Song et al., 2005a). The Kunlun Formation contains conglomerates, the Qiangtang Formation contains siltstones and mudstones from lacustrine and alluvial fan delta deposits and the Wangkun Formation contains glacially formed tills with mixed breccia and poorly sorted gravel (Cui et al., 1998; Song et al., 2005a; Wang et al., 2008b). The modern climate in the Kunlun Pass Basin area is characterised by very low temperatures (MAT ~ - 6.1 °C) and precipitation (MAP ~ 225 mm)

(Fick and Hijmans, 2017), however, temperature and precipitation varies significantly from site to site depending on the actual elevation. According to Tu (1964) and Wu et al. (2001), the snowline in the Kunlun Mountains is around 5100 m on the north slope and 5300 m on the south slope, and while much of the high Kunlun Pass Mountain and Basin area are in the permafrost zone, the lower parts are not. Samples for this research project were provided by Dr. Feng Cheng and Prof. Dr. Carmala N. Garzione (University of Rochester, New York, USA).

3.2 Age models

3.2.1 SG-1b core

As part of a joint Sino-German project, the 723 m long SG-1b core was drilled in the Jianshan anticline in western Qaidam Basin (Zhang et al., 2014). The purpose of this project is to study the long-term tectonic and climate evolution at this transitional zone between the wetter monsoon regions to the southeast and drier Asian interior to the northwest (Zhang et al., 2014). The age model of the core was constructed using magnetostratigraphy (Zhang et al., 2014). The identified 18 normal and 19 reversed polarity zones were assigned to the magnetic chrons C1r to 3Br and matching of observed polarity with the geomagnetic polarity timescale (GPTS) resulted in a SG-1b core time interval spanning from 7.3 to 1.6 Ma (Zhang et al., 2014). In Tab. 3 – 1, a brief overview of the published ages, depths, and sedimentation rates, which cover the interval of interest in this study, are given (see age-depth plot in Fig. 3 – 1). All samples have been taken from the core with regard to the drilling depth, for which a correction to real depth was necessary. The recovery rate of the SG-1b core was 93% on average except for the uppermost 60 m where the recovery rate fell to 80% (Zhang et al., 2014). This is due to the fact that core losses have to be accounted for. The relationship between drilling depth and real depth is shown in Equation 3 – 1 (Drilling Depth: 129.26 – 184.03 m) and Equation 3 – 2 (Drilling Depth: 184.03 – 256.87 m). The real depths were converted into ages based on the sedimentation rate (Tab. 3 – 1). Individual depths and ages of each sample is given in the Appendix (Tab. A – 1).

$$Real\ Depth\ [m] = 150.19m + (Drilling\ Depth - 129.26m)x\ \frac{49.93}{54.77} \qquad Eq. 3-1$$

$$Real\ Depth\ [m] = 200.12m + (Drilling\ Depth - 184.03m)x\ \frac{70.88}{72.84} \qquad Eq.3-2$$

Tab. 3 - 1: Depth – Age relationship and respective sedimentation rates of the SG-1b core between 3.596 and 2.581 Ma.

Real Depth - top (m)	**Real Depth – bottom (m)**	**Age – top (Ma)**	**Age – bottom (Ma)**	**Sedimentation rate (cm/ka)**
84.54	160.52	2.581	3.032	16.85
160.52	175.77	3.032	3.116	18.15
175.77	182.17	3.116	3.207	7.03
182.17	203.40	3.207	3.330	17.26
203.40	237.66	3.330	3.596	12.88

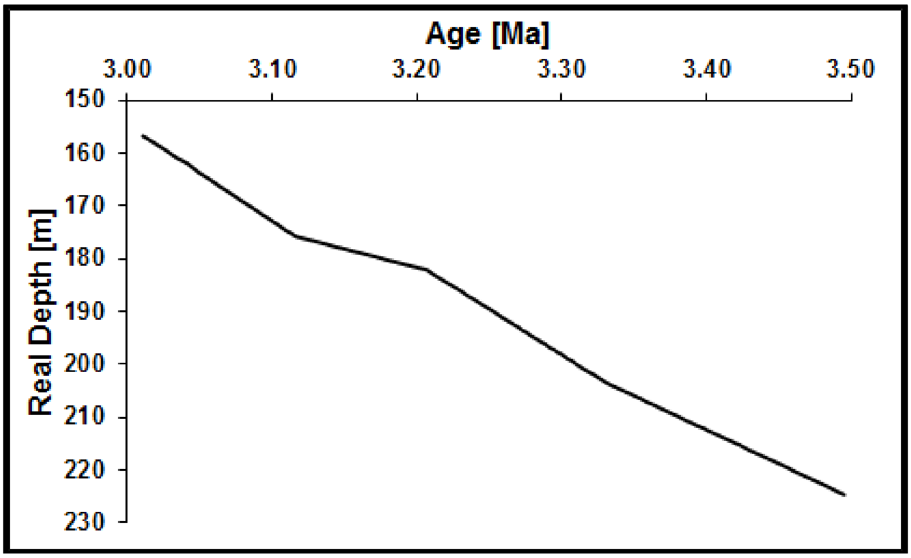

Fig. 3 - 1: Relationship between age and real depth in the SG-1b time interval from 3.5 to 3.0 Ma.

3.2.2 Kunlun Pass Basin

The age model for the Kunlun Pass Basin samples was developed by project partners, Dr. Feng Cheng and Prof. Dr. Carmala N. Garzione (University of Rochester, New York, United States). The age model is based on a combination of lithostratigraphy and orbital tuning of isotope data from the outcrop samples. First of all, the lithology of the samples was compared to the record of Song et al. (2005a), which have conducted research in the same area. After aligning the sedimentological features (Fig. 3 – 2), ages were assigned based on the magnetostratigraphic work of Song et al. (2005a). Subsequently, isotope data of the samples were compared and adjusted to the numerical solutions of orbital parameters from Laskar et al. (2004) (Fig. 3 – 3). The resulting ages for samples are given in Tab. A – 2 (Appendix).

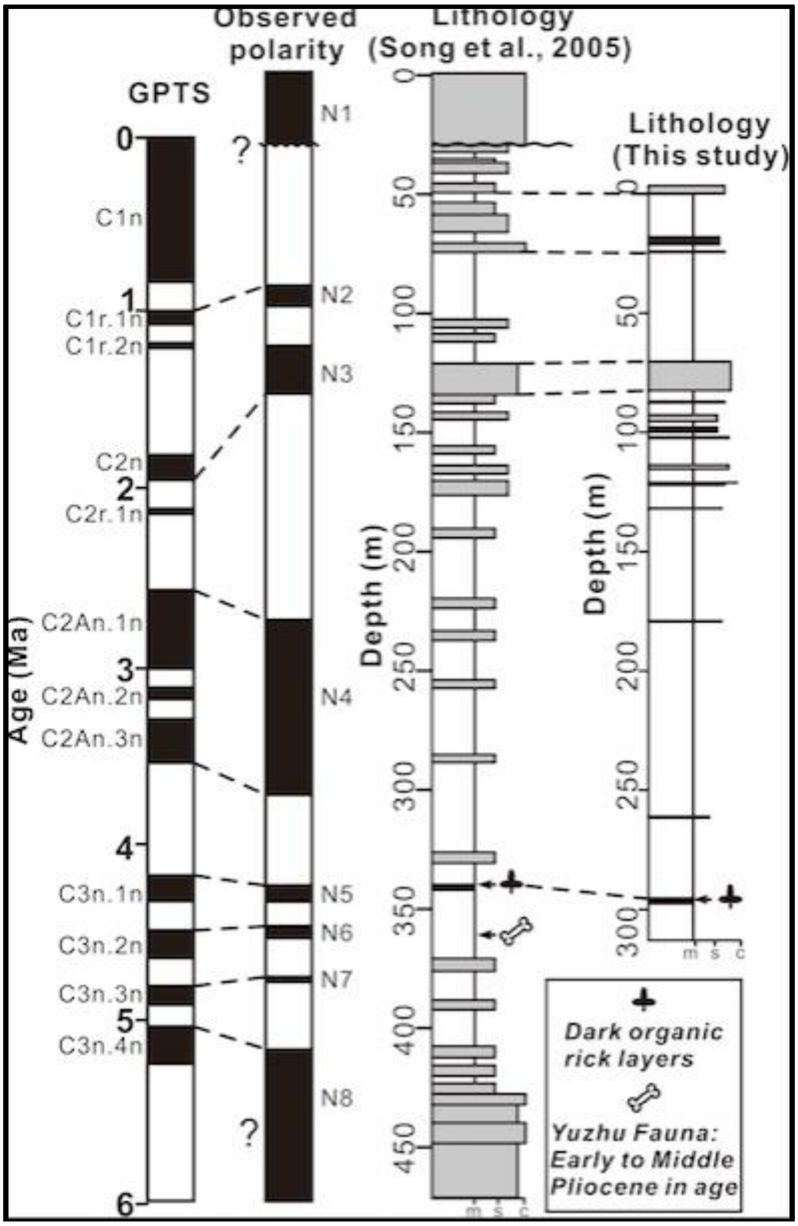

Fig. 3 - 2: Comparison of sedimentological features from the Kunlun Pass Basin section (this study) with the record published by Song et al. (2005a). Development of age-model done by Feng Cheng (in prep.).

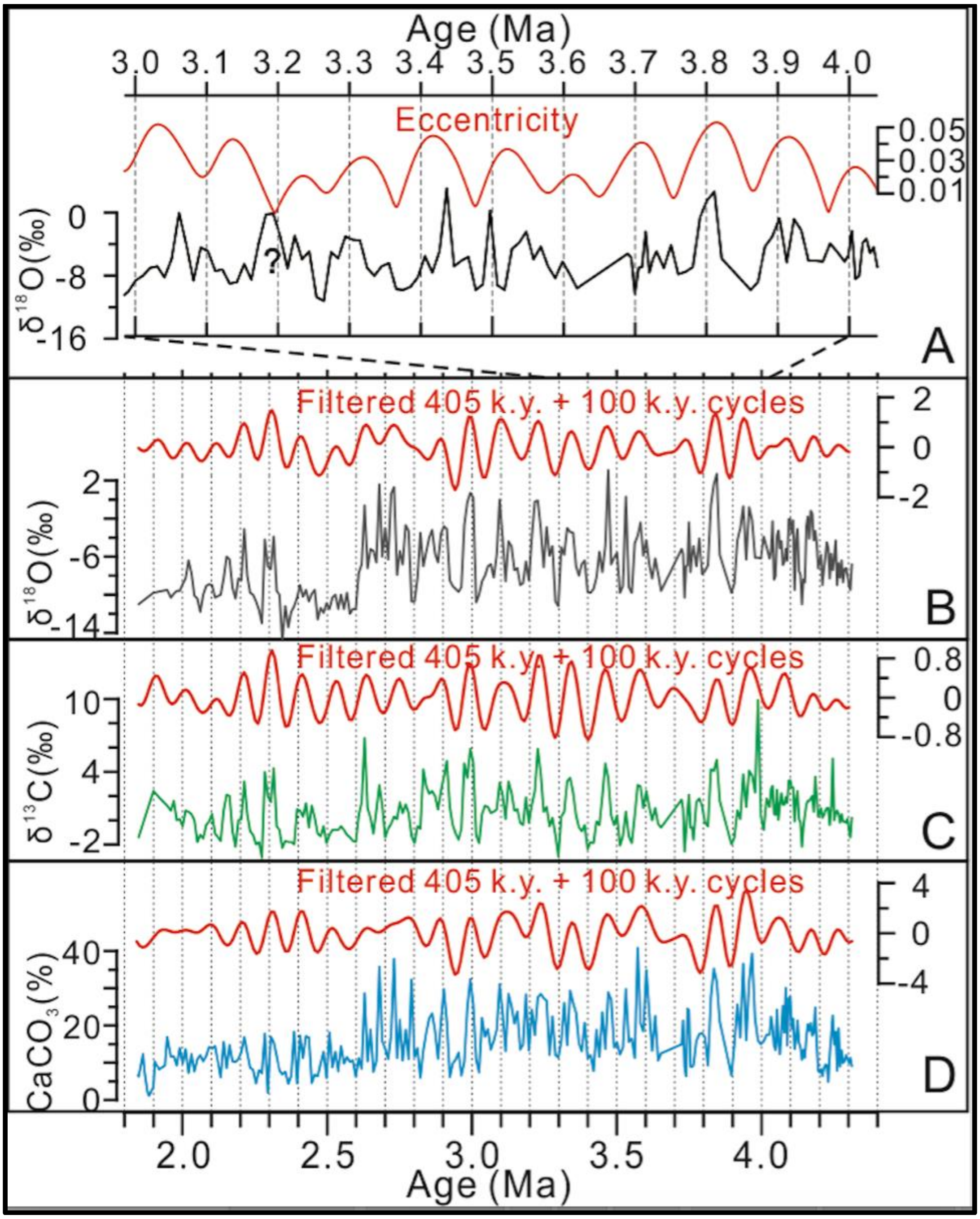

Fig. 3 - 3: Comparison of the isotope records from the Kunlun Pass Basin site with numerical calculation of orbital parameters from Laskar et al. (2004). Development of age-model done by Feng Cheng (in prep.).

3.3 Methodology

3.3.1 X-ray fluorescence core scanning

3.3.1.1 Laboratory setup

The X-ray fluorescence core scanning of the SG-1b core was done by Dr. Andreas Koutsodendris at the University of Heidelberg, Germany, using an Avaatech® Itrax Core Scanner. The data was acquired every 10 mm with a generator setting of 10 kV for the light elements and 30 kV for the heavy elements. The sampling time varied between 12 and 31 s. Elements detected during the 10 kV scan include Mg, Al, Si, P, S, Cl, Ar, K, Ca, Ti, V, Cr, Mn, Fe, Co, Ni, Cu, and Ba. Elements detected during the 30 kV scan include K, Ca, Sc, Ti, V, Cr, Mn, Fe, Co, Ni, Cu, Zn, Ga, As, Br, Rb, Sr, Y, Zr, Mo, and Pb.

3.3.1.2 Data processing

Following the data acquisation, depth profiles for major elements were established, in order to identify errors during measurement (e.g. due to surface roughness, cracks, end of cores). Therefore, negative values in any of the following elements: Mg, Al, Si, S, Cl, K, Ca, Ti, Mn, Fe, Sc, Br, Rb, Sr, Y, Zr and Mo were deleted. This resulted in the removal of 66 data points. As a next step, unusually low peaks (only few data points excursion) in major elements (Si, Ca, Fe) that were not part of a significant trend have been examined carefully. In case of a concurrent high Cl peak (part of operating scanner source) with no obvious change in lithology (core scanning images), these data points were removed. This led to a further reduction of data points by a total of 260. Additionally, 12 data points were deleted between 205.43 and 205.56 m due to very unusual XRF composition leading to a total of 338 data points that were removed. To account for lower or higher throughput / scanning time, the elemental counts were normalised by the total counts of the respective data point.

3.3.1.3 Principle Component Analysis

Principle Component Analysis (PCA) of the XRF data was done in R (R Development Core Team, 2008) for the whole record. Prior to PCA, the XRF data was log normalised in R. The PCA of the XRF was run in centered and scaled mode. Centered means that all variables (elements) were centered at 0, while the scale mode transforms the variables (elements) to have a standardised 1 unit variance.

3.3.1.4 XRF facies analysis

After data screening, cluster analysis of the XRF data was conducted using the program R (R Development Core Team, 2008) (see full R code in Appendix) to distinguish different sedimentation periods of the palaeolake. R packages used for this purpose include *magrittr*, *factoextra* and *dplyr (Kassambara and Mundt, 2017; Milton and Wickham, 2016; Wickham et al., 2019)*. Cluster analysis was performed using Euclidean distance and Ward's D2 method (Ward, 1963). After initial observation of the cluster diagram, a decision was made into how many clusters the data set should be divided (six, see Fig. 4 – 7). After assigning cluster numbers to each data point, mean values for each element were calculated for each individual cluster as well as for the whole record, in order to calculate the enrichment/depletion ε of each element in each cluster compared to the whole record (Equation 3 – 3).

$$\varepsilon = \frac{Element_{Cluster} - Element_{Whole\ Core}}{Element_{Whole\ Core}}\ x\ 100 \qquad Eq.3-3$$

3.3.2 C/N elemental analysis

3.3.2.1 Setup of Element Analyser

C/N Analysis was performed on all SG-1b samples (see Tab. A – 1) using the FLASH 2000 Elemental Analyzer^{TM} from Thermo Fisher Scientific Inc^{TM}. The analysis was conducted using Helium as the carrier gas with a constant flow rate of 140 ml / min. In order to combust the samples, O_2 flow (140 ml / min) was initiated for 5 s after a sample has been dropped into the autosampler. The measured signal was sent to the Eager Xperience^{TM} software.

3.3.2.2 Pre-treatment of samples

Prior to instrumental analysis, the samples were pretreated in the following way: All samples were dried in a heating cabinet at 40 – 50°C, homogenised using a mortar and stored. Ca. 40 mg of samples were weighted in a silver cup and placed onto a sample holder. In order to remove inorganic carbonates, the samples were acidified in the silver cups with increasing concentrations of hydrochlorine (added dropwise): 1%, 2%, 2.5%, 4%, 5%, 6.5% and 8%. After each addition of acid, the samples were dried (40 – 50°C) and the reactive behaviour of the samples was evaluated to assess a possible increase in acid concentration. After the formation of carbon dioxide gas stopped, the samples were treated with two final rounds of acid to rule out the presence of any remaining carbonates in the samples. Finally, the samples were dried on the heating plate (80 – 100°C) for 2 hours until desiccation. The silver cups were put into larger tin capsules so that the combustion of the silver cups was enhanced. A typical analysis run comprised the following sequence: 4 bypasses, 2 blanks, 2 – 3 standards, unknown samples with control standards every 10 samples. The 4 bypasses consist of standard material and were run in order to have the Elemental Analyzer running smoothly, burn any possible contaminations (e.g. in the crucible) and check for possible errors (i.e. high nitrogen peaks due to air coming into the system). The 2 blanks were run, in order to identify possible contaminations. The standards were used to establish a calibration curve for carbon and nitrogen (see further below) and therefore, enable quantification of the unknown samples. Fig. 3 – 4 shows the different chromatograms for bypasses (a), blanks (b), standards (c) and unknown samples (d).

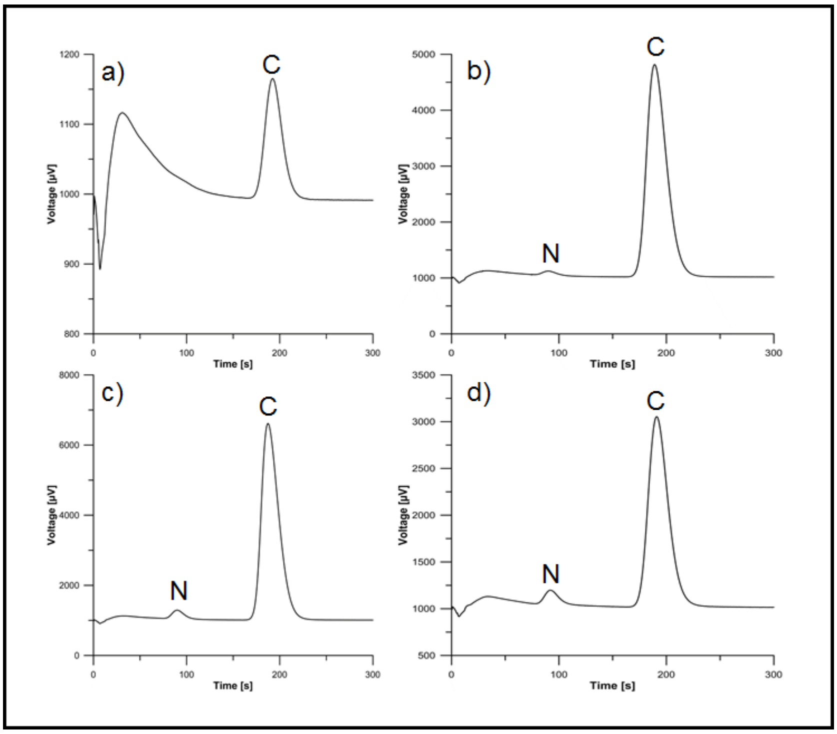

Fig. 3 - 4: Typical Chromatograms of blanks (a), bypass material (b), soil standards (c), and unknown sample material (d). Not that the scale for the y-axis changes from type to type. Carbon and nitrogen peak areas are indicated by C and N.

3.3.2.3 Development of calibration curves for carbon and nitrogen

Because the SG-1b core sample material was characterised by low carbon and especially nitrogen concentrations, the standard K-factor calibration was not an option to use for our measurements as it heavily relies on a single measurement. Calibration curves for the Element Analyser were developed for carbon (Fig. 3 – 5) and nitrogen (Fig. 3 – 6) to overcome this problem. Since the development of calibration curves is not an essential part of this thesis, the procedure can be found in the Appendix. During each analysis multiple soil standard measurements were conducted to act as a reference material: carbon (2.29 ± 0.07 %) and nitrogen (0.21 ± 0.01 %).

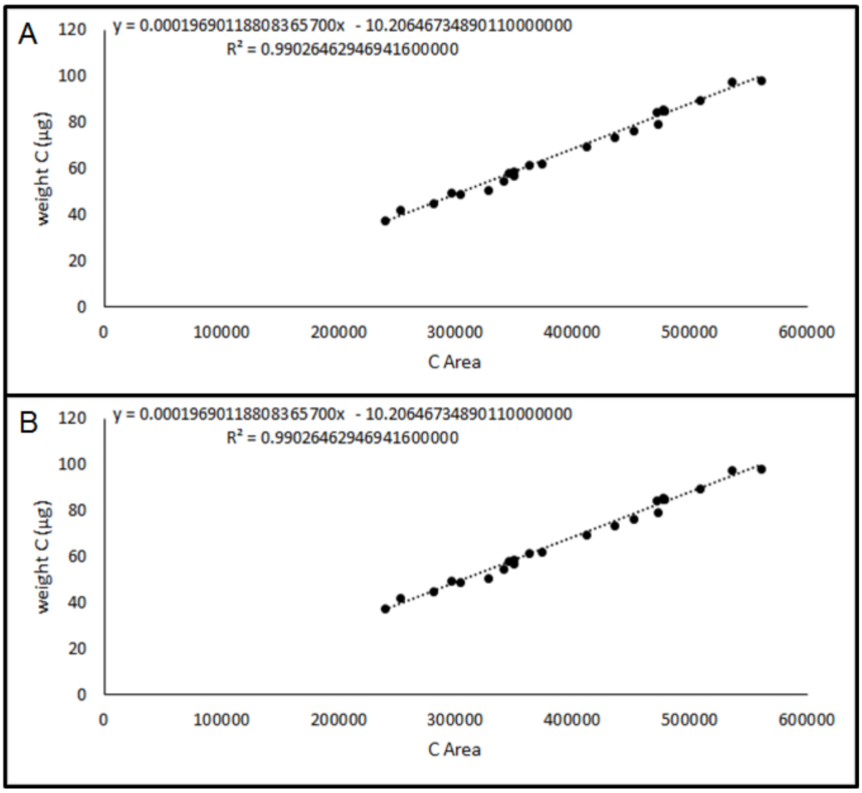

Fig. 3 - 5: Calibration curves for low (A; Area: < 600000) and high (B; Area: > 600000) carbon areas.

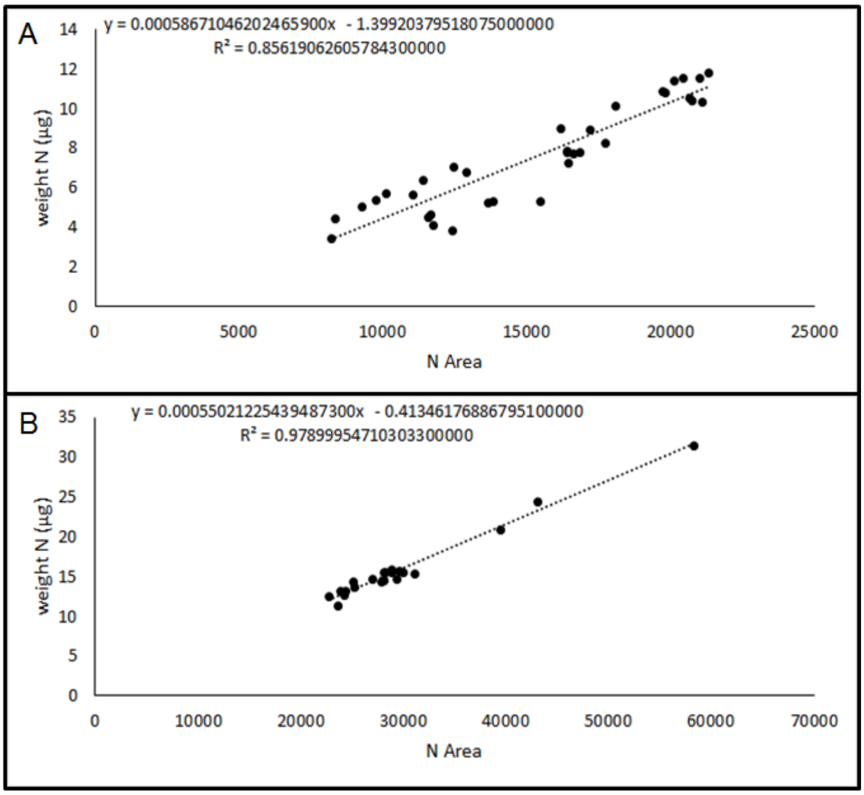

Fig. 3 - 6: Calibration curves for low (A; Area: < 22000) and high (B; Area: > 22000) nitrogen areas.

3.3.3 Pollen Analysis

3.3.3.1 Laboratory methods

Lab processing for pollen analysis was conducted in the same way for the SG-1b core and the Kunlun Pass Basin samples, however, the sediment weight used differs between those two study sites (SG-1b core: ca. 4 – 5 g; Kunlun Pass Basin: ca. 15 – 20 g). Pollen samples were processed according to a modified method of Berglund (1986), which includes the removal of carbonates by addition of hydrochloric acid (10%), sieving (125 µm), removal of silica compounds by hydrofluouric acid (48%) treatment and removal of fluorosilicates by two hot hydrochloric acid (10%) washes. Afterwards the samples were sieved (10 µm) again to remove clayey and other small particles. After processing was completed, the residues were mounted in silicon oil. Counting was performed at 400x magnification, and a minimum of 300 grains per sample were counted where possible. Two tablets of *Lycopodium* spores (Batch-Nr. 3862) (Stockmarr, 1971) were added to calculate pollen concentrations. In total, 108 samples (average resolution 4.48 ka) from the SG-1b core (see Tab. A – 1) and 154 samples (average resolution 22.48 ka) from the Kunlun Pass Basin (see Tab. A – 2) were counted.

3.3.3.2 Identification of pollen and spore grains

In order to identify the various pollen types, the following sources/literature were used: Northumbria pollen reference collection, Li et al. (2014), Kou et al. (2006) Beug (2004) and Demske et al. (2013). An overview about the most important taxa is given in Fig. 4 – 9. The pollen diagrams were produced using the program Tilia (Grimm, 1991). Pollen assemblage zones were established according to the cluster analysis of CONISS (Grimm, 1987).

3.3.3.3 Principle Component Analysis

PCA was conducted, in order to identify possible forcing mechanisms (i.e. climate) for the pollen record. In contrast to the XRF PCA, the pollen percentages were square-root transformed. PCA was conducted in R (R Development Core Team, 2008) (see R Code attached in Appendix).

3.3.3.4 Spectral Analysis

For the SG-1b record, spectral analysis has been conducted on the A/C ratio. Prior to the analysis, the data has been linearly interpolated to equal spacing intervals of 1 ka using the program PAST3 (Hammer et al., 2001). Spectral analysis was done using continuous wavelet transforms (Torrence and Compo, 1998).

For the Kunlun Pass Basin record, spectral analysis was conducted for the sum of broadleaved and coniferous trees, the A/C ratio, and palaeoclimate estimates (MAP and MAT). Prior to the analysis, the data was linearly interpolated to equal spacing intervals of 1 ka using the program PAST3 (Hammer et al., 2001). Spectral analysis was done using the Lomb Periodogram (Zechmeister and Kürster, 2009) because the continuous wavelet transform did not show clear results due to the lower resolution of the Kunlun Pass Basin record.

3.3.4 Reconstruction of pollen source areas in the Qaidam Basin

Broadleaved and coniferous forests

The following section will outline potential pollen source areas for the NW Qaidam Basin and Kunlun Pass Basin based on the modern pollen, vegetation and biome distribution in China, and especially on the Tibetan Plateau (Ni, 2001; Ni and Herzschuh, 2011).

On the Tibetan Plateau cold-temperate mixed forests are characterised by taxa that include *Betula*, *Corylus*, *Quercus*, *Tsuga*, *Pinus*, Asteraceae, Ericaceae and Poaceae. Furthermore, temperate deciduous forests in China include *Betula*, *Corylus*, *Quercus*, *Tsuga*, *Salix*, *Ulmus*, *Tilia*, *Alnus*, *Carpinus* with some warm-temperate elements such as *Castanea*, *Juglans*, *Pterocarya* or *Fagus*. Cour et al. (1999) found *Quercus*, *Alnus*, *Cedrus*, *Podocarpus*, *Castanea* and Moraceae pollen grains in Northern China where they are not growing today and explain the occurence of this taxa with long-distance transport from warm and humid areas south of the Himalayas. Even *Juniperus*, which occurs in semi-arid areas in the western Tibetan Plateau, supposedely originated from areas > 800km away (Cour et al., 1999). Coniferous trees, such as *Abies*, *Pinus*, *Picea*, *Juniperus* can be found in evergreen montane forests, cool-temperate coniferous forests or temperate coniferous forests (Ni, 2001; Ni and Herzschuh, 2011).

Based on the modern distribution, this study will distinguish between pollen derived from two types of forests. First of all, *Betula*, *Corylus*, *Quercus*, *Alnus*, *Salix*, *Elaeagnus*, *Ulmus*, *Juniperus* and *Pinus* were derived from cool- or cold-temperate mixed coniferous and broadleaved forests located on mountains and mountain slopes. Occurrences of *Juglans*/*Pterocarya*, *Fagus*, *Fraxinus*, *Tilia* or *Carya* are warm-temperate or subtropical broadleaved tree and could have either been derived from very warm and humid sites in the study areas or transported over a long distance. The coniferous tree pollen *Pinus*, *Picea* and *Abies* are sourced from cold-temperate coniferous forests or montane forests and were possibly growing at higher altitude in mountainous areas compared to the cool- or cold-temperate mixed coniferous and broadleaved forests.

Xerophytic shrublands

In a study about Hurleg Lake, SE Qaidam Basin, Zhao et al. (2007) described a vegetation transect: The lakeshore is characterised as marsh dominated by Poaceae (*Phragmites c*.), Plantaginaceae and Cyperaceae. Further away from the lake, *Nitraria* and Poaceae dominated the vegetation. With an increasing distance from the lake various types of Chenopodiaceae and *Artemisia* occur, whereas higher south-facing mountain slopes are covered by *Artemisia* and *Ephedra*. The highest elevations on the Qilian Mountains are dominated by *Juniperus*.

In a different study, Zhao and Herzschuh (2009) characterised vegetation types for most the central and southern parts of the Qaidam Basin and including the areas surrounding Qinghai Lake. They distinguished four different vegetation types: desert, steppe desert, steppe and alpine meadow. The desert vegetation in the Qaidam Basin is dominated by Chenopodiaceae, *Ephedra*, *Nitraria*, Asteraceae and *Artemisia* and is typically found at lower elevation (< 3200 m) with MAP < 200 mm. Steppe desert vegetation is dominated by *Artemisia*, Poaceae and Chenopodiaceae with minor occurrences of *Ephedra*, *Nitraria*, Brassicaceae and Asteraceae. These sites are located at a slightly higher elevation and thus, also higher annual precipitation (200 – 300 mm). Steppe vegetation mainly consists of Poaceae and *Artemisia* with some Cyperaceae and

Fabaceae. Steppe vegetation is restricted to lower mountain slope (3400 – 3600 m) sites which receive 300 – 400 mm of annual precipitation. Alpine meadow sites (> 3600 m, MAP > 400 mm) are dominated by Cyperaceae and Poaceae with further occurrences of Asteraceae, *Rhododendron* (Ericaceae), Gentianacaeae, Fabaceae, Saxifragaceae and *Polygonum*.

Taking the above into account, in this thesis Chenopodiaceae, *Ephedra*, *Nitraria*, *Artemisia*, Asteraceae, Caryophyllaceae, and *Tamarix* are representing temperate semi-desert vegetation in the Qaidam Basin or alpine semi-desert vegetation in the Kunlun Pass Basin area. The distinction between temperate and a semi-desert vegetation of the Kunlun Pass Basin will be made in detail in Chapter 5.3.1.

Poaceae and Cyperaceae

Poaceae and Cyperaceae can have two contrasting sources of origin. Zhao et al. (2007) addressed high Poaceae contents (25%) at Hurleg Lake, Qaidam Basin, to abundant *Phragmites* in the lakeshore marsh. Furthermore, at Lake Sugan (Qaidam Basin), an analysis of modern pollen distribution showed that Poaceae and Cyperaceae were more abundant at shallower lake depths due to close proximity of Poaceae and Cyperaceae containing marsh around the lake (Zhang et al., 2010). Therefore, Poaceae and Cyperaceae can be interpreted as lakeshore vegetation and their increase suggests a reduced lake size. On the other hand, Poaceae and Cyperaceae are two major components of temperate grasslands and meadow vegetation on the Tibetan Plateau (Zhao and Herzschuh, 2009). According to the analysis of Tibetan Plateau vegetation from Ni and Herzschuh (2011), low- and high shrub, graminoid and forb tundra vegetation include *Salix*, Rosaceae, Ericaceae, Fabaceae, *Juniperus*, *Artemisia*, Poaceae, Cyperaceae, Asteraceae, *Typha* and Caryophyllaceae.

Since these two pollen source areas (lakeshore vs steppe/meadows) imply different climate conditions, the interpretation of Poaceae and Cyperaceae will be made individually in the SG-1b chapter (Chapter 4) and Kunlun Pass Basin chapter (Chapter 5).

3.3.5 Quantitative and semi-quantiative climate reconstructions

In order to establish quantitative climate estimates based on the pollen signal, three different methods were used: Coexistence Approach, A/C ratio and pollen-climate transfer function.

3.3.5.1 Coexistence Approach

The Coexistence Approach (Mosbrugger and Utescher, 1997; Utescher et al., 2014), is based on the presence and absence of taxa/families in a record. Furthermore, the Coexistence Approach assumes that the climatic conditions between the modern taxa and their Pliocene nearest living relatives has not changed significantly. Since different taxa grow under different climate conditions, the climatic range, in which all taxa can exist, will be narrowed down making the Coexistence Approach a viable option to establish palaeoclimate estimates (see Fig. 3 – 7).

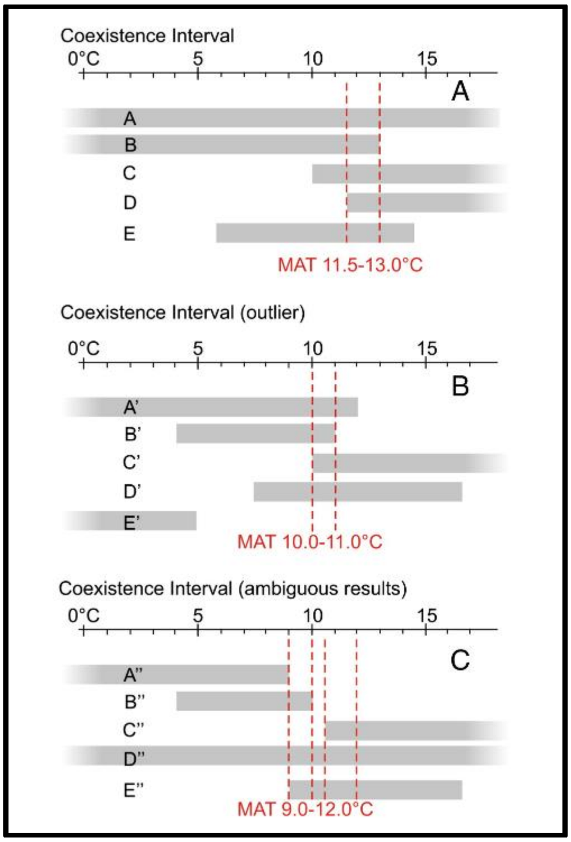

Fig. 3 - 7: Examples of the Coexistence Approach applied to three case studies taken from Utescher et al. (2014). Case study A shows a common interval for MAT for all taxa A to E. In case study B, one outlier (E) is present in the sample that can not be put into the common climatic range of the other four taxa. This might be due to transport of taxa from a different vegetation zone into the study area or change of climatic ranges through time. In case study C, the results of the Coexistence Approach are ambiguous and interpretation of MAT should be done cautiously.

The Coexistence Approach was originally designed to reconstruct palaeoclimate ranges of Tertiary European forests (Mosbrugger and Utescher, 1997). However, in settings with prevailing cold climates, long-distance transport of taxa, strong altitudinal gradients or a low variability of taxa, the results of the Coexistence Approach become less reliable (e.g. Grimm and Denk, 2012; Mosbrugger and Utescher, 1997; Zhang et al., 2015).

The data to conduct the Coexistence Approach in this study is based on the NECLIME Palaeoflora database (Mosbrugger and Utescher, 1997; Utescher et al., 2014; Utescher and Mosbrugger, 2015). Below, the relevant taxa for this study are given with their related climatic ranges (Tab. 3 – 2 and 3 – 3).

Tab. 3 - 2: Nearest living relative species (NLRS) and the related climatic ranges based on the NECLIME Palaeoflora database (Mosbrugger and Utescher, 1997; Utescher et al., 2014; Utescher and Mosbrugger, 2015). MAT = mean annual temperature, CMT = coldest month temperature, WMT = warmest month temperature.

NLRS	**MAT$_{min}$**	**MAT$_{max}$**	**CMT$_{min}$**	**CMT$_{max}$**	**WMT$_{min}$**	**WMT$_{max}$**	**MAP$_{min}$**
Abies sp	-6.7	27.4	-26	25.6	7.1	29.5	373
Alnus sp	-13.3	27.4	-40.9	25.6	12	38.6	41
Betula sp	-15	25.8	-41	21.1	1.3	28.7	110
Carpinus sp	0	25.8	-22.7	21.1	16.8	28.7	164
Carya sp	4.4	26.6	-11.5	22.2	19.3	30.6	373
Castanea sp	8.7	24.2	-3.9	16.7	21.6	29.4	473
Cedrus sp	11.6	18.4	-0.3	12.5	19.4	31.8	164
Celtis sp	2.5	25.8	-17.7	23	18.7	28.8	116
Chenopodiaceae	-11	27.7	-29.5	23.6	12	36.1	193
Corylus sp	-4.9	24	-32.4	16.7	12.9	29.4	389
Cupressaceae	-15.6	24.9	-48.9	22.2	12	29	155
Elaeagnus sp	-0.4	27.7	-24.2	27	18.2	28.5	84
Ephedra sp	3.1	28.8	-12	25	16.4	32.9	33
Fagus sp	4.4	23.1	-11.5	17	17.3	28.5	376
Fraxinus sp	0	24	-25.8	16.7	14.9	33.9	148
Geranium sp	-7.7	18.5	-22.7	13.8	9.8	23.1	224
Hippophae sp	1.6	17.4	-11.1	8.3	13.4	27	552
Humulus sp	-0.4	17.5	-21.7	7.7	14	27.9	451
Hyoscyamus n.	3.1	16.8	-16.2	9	15	25	615
Ilex sp	-0.4	27.7	-12.9	27	10.4	33.6	641
Juglandaceae	0	27.5	-22.7	25	13.7	31.2	210
Nitraria sp	-10	25.9	-43.2	20.3	18.8	29.7	24
Picea sp	-8.9	21.7	-28.6	15.6	7.3	31.6	142
Pinus sp	-9.2	25.5	-36.8	21.4	7.1	32.9	180
Pterocarya sp	3.9	24.2	-12.8	17	15.3	31.6	246
Quercus sp	-1.4	27	-25.1	25.9	8.4	28.3	201
Salix sp	-17	27.7	-50.1	26.5	7.6	32.9	122
Sciadopityaceae	3.7	14	-8.4	3.7	15.8	24.3	1300
Sparganium sp	-14	24.2	-36.2	17.8	10.2	28.9	122
Sphagnaceae	-6.7	24.2	-24.4	17.8	13.8	28.9	373
Tamarix sp	9.6	24.8	1.3	15.6	16	33.1	37
Tsuga sp	-1.8	21.9	-15.6	15.6	11	29.5	285
Typha angust.	4.6	19.2	-7.9	13.8	14.8	29.7	160
Typha doming.	8.2	25.7	-5.6	23.9	20.3	27.9	373
Ulmus sp	-4.9	26.6	-25.8	26.1	16	29.4	201

Tab. 3 - 3: Nearest living relative species (NLRS) and the related climatic ranges based on the NECLIME Palaeoflora database (Mosbrugger and Utescher, 1997; Utescher et al., 2014; Utescher and Mosbrugger, 2015). MAP= mean annual precipitation, MPwet = mean precipitation during wettest month, MPdry = mean precipitation during driest month, MPwarm = mean precipitation during warmest month.

NLRS	**MAP$_{max}$**	**MP$_{wetmin}$**	**MP$_{wetmax}$**	**MP$_{drymin}$**	**MP$_{drymax}$**	**MP$_{warmmin}$**	**MP$_{warmmax}$**
Abies sp	2648	57	369	0	135	0	344
Alnus sp	2559	8	353	0	135	8	207
Betula sp	2559	23	353	0	135	2	312
Carpinus sp	2648	20	350	2	55	2	344
Carya sp	1724	68	434	8	93	45	258
Castanea sp	1857	70	424	3	88	3	239
Cedrus sp	1577	43	434	0	41	0	175
Celtis sp	2730	25	597	0	88	2	533
Chenopodiaceae	1958	46	358	0	83	0	224
Corylus sp	1682	45	343	3	73	3	239
Cupressaceae	1958	33	303	0	83	0	258
Elaeagnus sp	3151	28	389	2	165	13	221
Ephedra sp	932	5	178	0	45	2	61
Fagus sp	2648	46	448	5	94	5	431
Fraxinus sp	1844	28	358	2	95	0	239
Geranium sp	1958	46	236	0	83	1	141
Hippophae sp	1151	64	149	5	57	20	89
Humulus sp	1146	68	139	9	64	24	95
Hyoscyamus n.	1958	72	236	13	83	19	136
Ilex sp	3151	98	389	2	165	4	431
Juglandaceae	2617	44	582	1	114	2	189
Nitraria sp	705	8	177	0	35	0	177
Picea sp	6000	36	700	2	400	2	400
Pinus sp	1741	28	293	0	94	0	304
Pterocarya sp	2648	46	424	1	64	2	424
Quercus sp	3905	33	610	0	180	5	180
Salix sp	2399	22	448	0	108	0	252
Sciadopityaceae	2648	130	369	25	75	115	344
Sparganium sp	2453	24	605	0	108	0	343
Sphagnaceae	2453	57	605	0	43	0	343
Tamarix sp	1150	8	131	0	61	0	90
Tsuga sp	2648	48	350	0	108	0	344
Typha angust.	1179	20	157	0	46	1	83
Typha doming.	1534	78	241	8	63	10	177
Ulmus sp	3285	33	569	0	75	0	239

3.3.5.2 Artemisia/Chenopodiaceae ratio for semi-quantitative precipitation estimates

The A/C ratio has been used as an indicator to identify wetter and drier periods in semi-arid and arid areas since *Artemisia* is growing favourably during wetter intervals, whereas Chenopodiaceae grows stronger during drier intervals (El-Moslimany, 1990). Zhao et al. (2012) analysed the relationships between the A/C ratio and climate parameters in modern surface pollen assemblages in China reaching the conclusion that MAP is the most important influence on the ratio assuming *Artemisia* and Chenopodiaceae make up more than 45-50% of the total pollen assemblage. A/C ratios of <1 were mostly related to MAPs of less than 200 mm, A/C ratios between 1 and 2 were found in areas receiving between 200 and 350 mm rainfall a year and A/C ratios > 2 (up to 5) were mostly related to MAPs of 350 to 450 mm. In this study, the semi-quantitative classification from Zhao et al. (2012) will be applied to determine changes in precipitation in the NW Qaidam Basin. Furthermore, the A/C ratio itself will be used as a signal to characterise changes in precipitation when comparing with other regional and global datasets.

3.3.5.3 Development of pollen – climate transfer function

Pollen – climate transfer functions are based on the relationship between modern pollen rain and the corresponding climate (Birks, 1995; Birks et al., 2010). In sophistically large datasets, a clear climatic range for each taxa/family can be observed with an optimal zone where the pollen rain is strongest (Fig. 3 – 8). This does not necessarily mean that the taxa/family are actually growing within these climate ranges, but that the pollen rain of these taxa/families is strongest within these climate ranges. Thus, long-distance transport of pollen does not negatively impact the results.

By combining all input taxa/families with their individual climate ranges, transfer functions establish a mathematical connection between the pollen assemblages and the climate variable through calculating optimal parameters for each taxa/family. For example, the highest pollen percentages of *Betula* occur at MAP between 500 and 1000 mm, whereas the highest pollen percentages of Amaranthaceae occur below 500 mm in the dataset of Zheng et al. (2014) (Fig.

3 – 8). Therefore, the climate parameter for MAP should be smaller for Amaranthaceae than *Betula*.

The example from Zheng et al. (2014) covers a very large area with very large climate ranges (Fig. 3 – 8). Since pollen – climate transfer functions aim to reduce the root mean square error of prediction (RMSEP) for every part of a climate range, having a larger climate range means that the RMSEP is larger compared to modern pollen dataset with a smaller climate range. This research project focusses on the vegetation and climate evolution in NW China, where the climate is much drier compared to the southeastern Chinese regions (Fig. 2 – 3), and therefore, it is not necessary to distinguish between semi-desert and tropical vegetation. The modern pollen dataset used in this study include pollen assemblages from a total of 926 sample sites ranging from 74.5 to 104.17 °E and 30.0 to 45.0 °N and has been provided by Prof. Dr. Jian Ni (Zhejiang Normal University, China) based on the work of Ni et al. (2014) and Chen et al. (2010b).

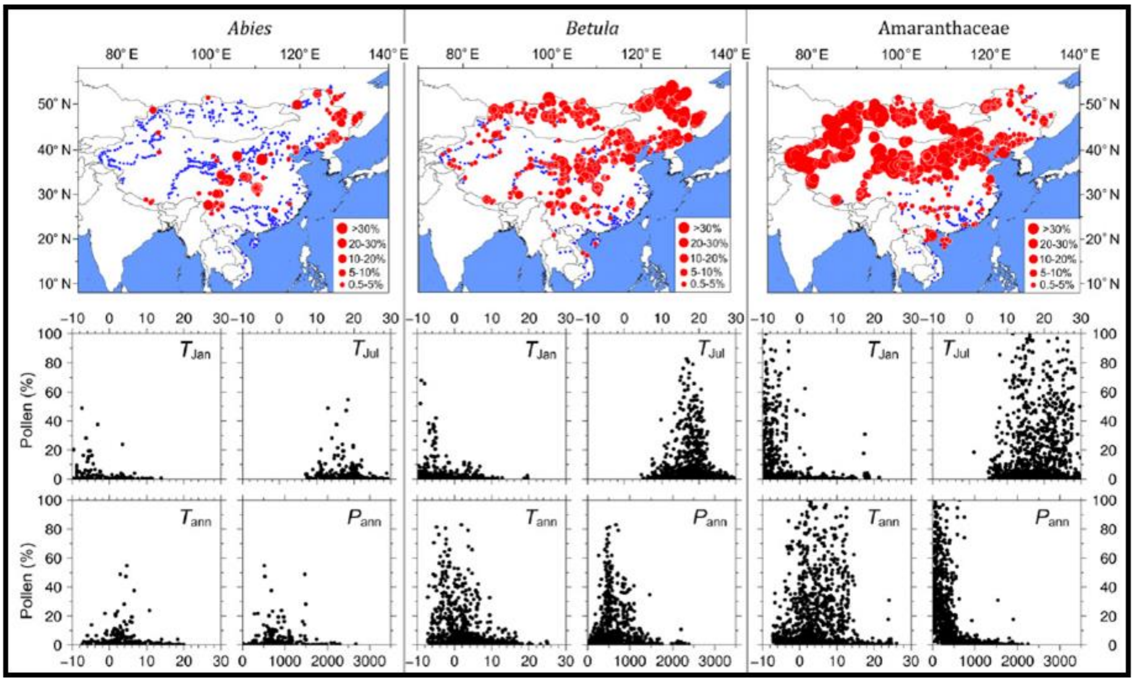

Fig. 3 - 8: Distribution of *Abies*, *Betula* and Amaranthaceae in East Asia and their corresponding climate relationship (TJan = temperature of the coldest month, TJul = temperature of the warmest month, Tann = mean annual temperature, Pann = mean annual precipitation) (Zheng et al., 2014).

All samples sites, which matched the climate ranges shown in Tab. 3 – 4, were included in the development of the six transfer functions. This selection was done in order to have a broad range of climate values, which are centered around the modern climate conditions of the SG-1b coring site and the Kunlun Pass Basin.

Tab. 3 - 4: Climate ranges for the development of pollen – climate transfer functions in this study based on the modern pollen dataset from Prof. Dr. Jian Ni (Chen et al., 2010b; Ni et al., 2014). Actual climate conditions from the SG-1b coring location and Kunlun Pass Basin are shown in column 3 and 4 and are based on data from WorldClim (Fick and Hijmans, 2017; Hijmans et al., 2005).

Climate Parameter	Minimum	Maximum	SG-1b core	Kunlun Pass Basin
MAT	-10.5°C	+8.0°C	+3.0°C	-6.1°C
MST	+0.4°C	+21.4°C	+15.2°C	+4.3°C
MWT	-23.1°C	-0.6°C	-10.2°C	-16.8°C
MAP	30 mm	600 mm	28 mm	225 mm
MSP	12 mm	471 mm	22 mm	150 mm
MWP	0 mm	30 mm	0 mm	4 mm

The modern pollen dataset contains different sample types (lake, soil, moss polster, dust). Because all of these sample types have a different pollen source area and preservation (Jacobson and Bradshaw, 1981; Wilmshurst and McGlone, 2005; Zhao et al., 2009), this could potentially be a factor why the palaeoclimate estimates could deviate from expectations based on the palaeovegetation history.

Using procedures outlined in the works of Wen et al. (2013), Cao et al. (2013) and Cao et al. (2014), the development of the transfer functions will be described here onwards. Fig. 3 – 9 shows a summary of the screening and homogenisations prior to the calculation of the transfer functions. Initially, all taxa/families containing only “0” values were removed. Subsequently, taxa/families were merged together following the homogenisation done by Cao et al. (2013). In this thesis, more taxa/families were merged together compared to Cao et al. (2013). A complete overview of the initial taxa and families together with their final nomenclature is shown in the Appendix (Tab. A – 3). Afterwards, taxa were removed, which either occurred in less than 9 samples (~1%) of the total dataset, and/or did not have a single sample with more than 5% of that pollen assemblage. This follows roughly the approach of Cao et al. (2014) and Prentice (1980) and is aimed to improve the signal to noise ratio. Additionally, *Plantago* was removed from the dataset, since it is often connected to anthropogenic influence (Behre, 1981).

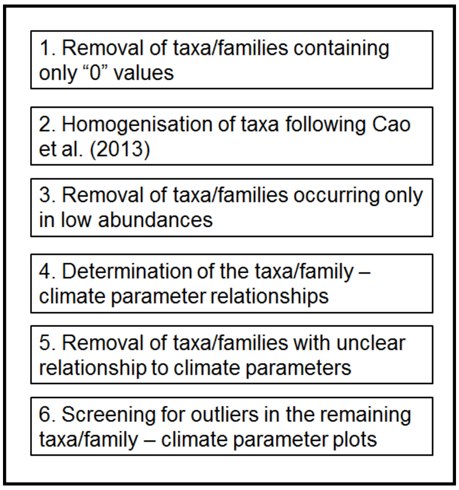

Fig. 3 - 9: Schematic order of pre-screening and homogenization steps undertaken to prepare a reliable modern pollen database subset from the original database (Chen et al., 2010b; Ni et al., 2014).

After plotting each taxa against each climate parameter, the distribution of the taxa was visually determined. Since the robustness of transfer functions rely on good monotonically increasing/decreasing patterns or unimodal distributions of the underlying taxa (optima of taxa growth along climatic range), those taxa that did not confidently showed either of these two patterns were removed for the specific climate parameter transfer function. This could have been either due to an unclear pattern resulting from too few data points (Fig. 3 – 10) or data points showing unclear relationship (Fig. 3 – 11). Additionally, each diagram (taxa – climate parameter) was screened for outliers to the taxa’s pattern. In case an outlier had been identified (Fig. 3 – 12), the whole sample was removed from the specific dataset. Thus, six unique initial datasets (MAT, MST, MWT, MAP, MSP, MWP) emerged out of the initial sample screening. After pre-screening of the datasets was completed, the initial transfer functions were calculated using the package *rioja* (Juggins, 2009) in R (R Development Core Team, 2008). The complete sequence of R Code used is given in the Appendix.

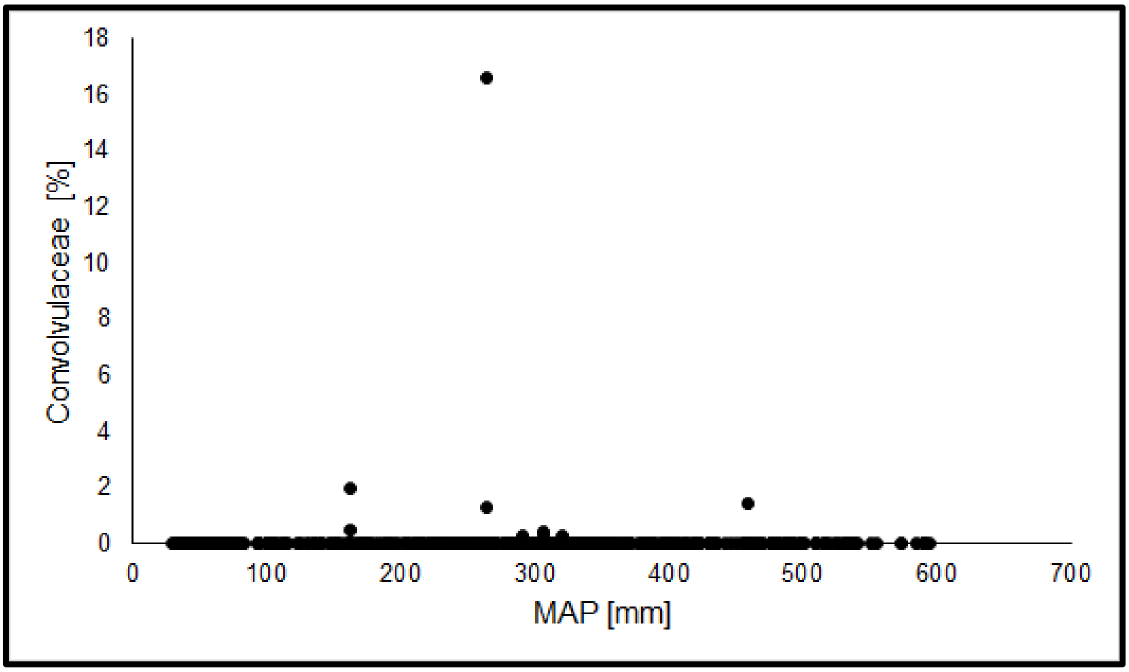

Fig. 3 - 10: Example of a removed taxa due to too few data points

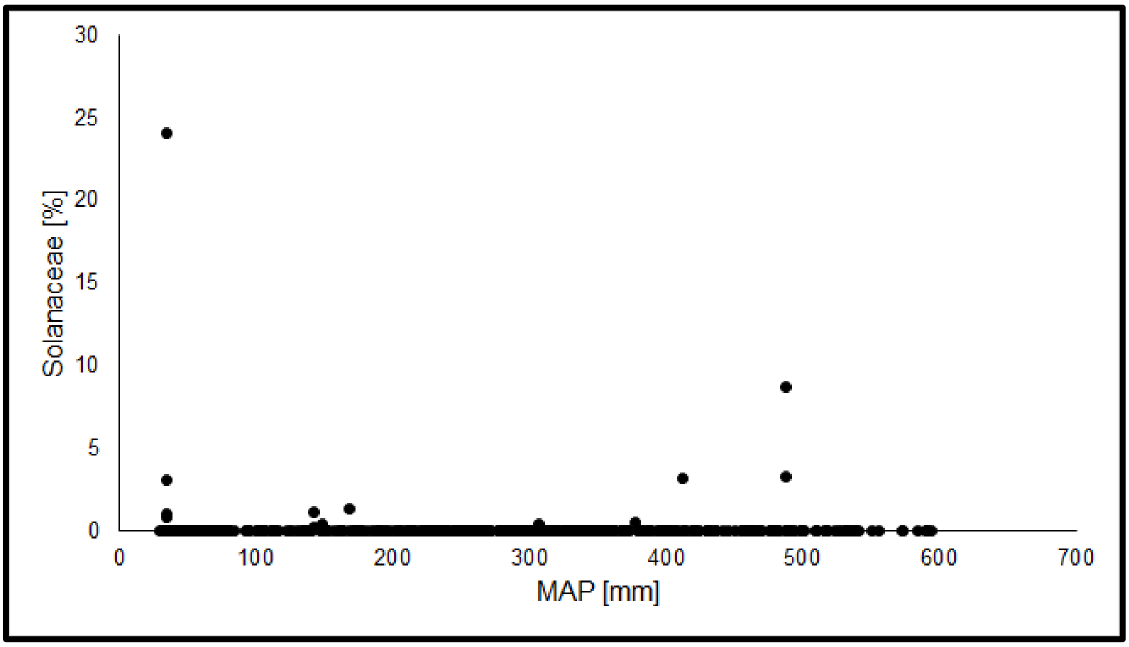

Fig. 3 - 11: Example of a removed taxa due to an unclear relationship between the taxa and the climate parameter.

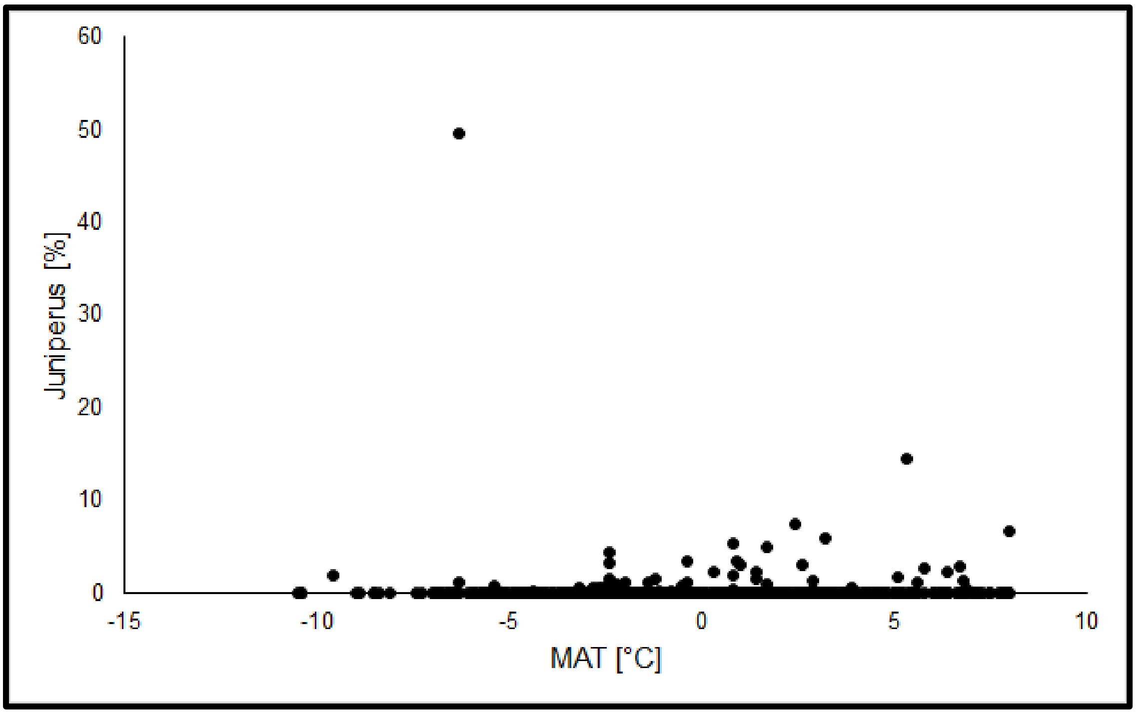

Fig. 3 - 12: Example of an outlier (~ 50% *Juniperus* around -7 °C), which has been removed during the prescreening of the modern pollen dataset.

For the calculation of the transfer functions, weighted average partial least squares (WA-PLS) was chosen as a regression technique, since it provides substantial improvements over simple weighted average techniques with regard to large noisy datasets, large climatic ranges and edge effects (Seppä et al., 2004; ter Braak et al., 1993). Two sets of transfer functions were established for each climate parameter: In one analysis the pollen percentages was used, whereas in the second analysis the square-rooted pollen percentages were used. Cao et al. (2014) only used square-root transformed pollen percentages, whereas Wen et al. (2013) used the real pollen percentage data. In this study, both approaches are considered and their outcome will be compared with each other in terms of the resulting correlation coefficient (r^2), RMSEP and the average/maximum bias.

After the initial transfer functions were calculated, a second phase of screening data points was done. This is following Wen et al. (2013) approach, in which residuals, that are larger than the RMSEP, have been classified as outlying samples. This procedure was done for both sets of transfer functions (pollen percentage and square-root transformed pollen percentages) that were calculated for the six climate parameters. Since the calculation of the transfer functions resulted in two unique outcomes for pollen percentages and the square-root transformation of the pollen percentages, also unique datasets were established after the second screening step. This is due to sample sites, which might have produced a residual larger than RMSEP in one transfer function set, whereas it hasn't in the other.

The second (and final) transfer functions were calculated in the same manner as the initial ones with the revised dataset of modern pollen sample sites. In order to assess the accuracy of the developed transfer functions, cross-validation has been done using the leave-one-out method (Vehtari et al., 2017). In Tab. 3 – 5, Tab. 3 – 6, Tab. 3 – 7 and Tab. 3 – 8 the statistics of the various transfer function calculations are shown for the initial and final analysis, respectively. The RMSEP for the final transfer functions were retrieved from the cross-validation run.

Tab. 3 - 5: Relevant statistics for the initial transfer functions (real pollen percentage) showing the correlation coefficient (r^2), root mean square error of prediction (RMSEP), average bias, maximum bias and number of components (comp).

	MAT	**MST**	**MWT**	**MAP**	**MSP**	**MWP**
r^2	0.30	0.37	0.29	0.64	0.71	0.25
RMSEP	3.08	3.18	3.30	81.85	57.72	4.81
Av Bias	0.00	0.00	0.00	0.00	0.00	0.00
Max Bias	10.06	9.53	9.97	176.92	77.31	21.72
Comp	5	4	3	4	4	4
Nr of sites	802	819	891	762	897	916

Tab. 3 - 6: Relevant statistics for the initial transfer functions (square-root transformed pollen percentage) showing the correlation coefficient (r^2), root mean square error of prediction (RMSEP), average bias, maximum bias and number of components (comp).

	MAT	**MST**	**MWT**	**MAP**	**MSP**	**MWP**
r^2	0.38	0.42	0.38	0.66	0.74	0.37
RMSEP	2.90	3.04	3.10	78.91	54.97	4.43
Av Bias	0.05	0.03	0.08	1.00	0.57	0.0006
Max Bias	9.48	8.85	10.03	181.96	59.70	23.57
Comp	5	5	4	5	4	4
Nr of sites	802	819	891	762	897	916

Tab. 3 - 7: Relevant statistics for the final transfer functions (real pollen percentage) showing the correlation coefficient (r^2), root mean square error of prediction (RMSEP), average bias, maximum bias and number of components (comp).

	MAT	**MST**	**MWT**	**MAP**	**MSP**	**MWP**
r^2	0.72	0.72	0.69	0.87	0.90	0.65
RMSEP	1.54	1.60	1.68	42.21	30.63	2.43
Av Bias	0.00	0.02	-0.02	0.08	-0.04	0.02
Max Bias	1.88	2.35	2.37	40.84	23.38	2.60
Comp	4	4	5	5	4	6
Nr of sites	551	590	617	541	591	667

Tab. 3 - 8: Relevant statistics for the final transfer functions (square-root pollen percentage) showing the correlation coefficient (r^2), root mean square error of prediction (RMSEP), average bias, maximum bias and number of components (comp).

	MAT	**MST**	**MWT**	**MAP**	**MSP**	**MWP**
r^2	0.72	0.72	0.69	0.87	0.90	0.65
RMSEP	1.54	1.60	1.68	42.21	30.63	2.43
Av Bias	0.00	0.02	-0.02	0.08	-0.04	0.02
Max Bias	1.88	2.35	2.37	40.84	23.38	2.60
Comp	4	4	5	5	4	6
Nr of sites	564	600	649	539	610	668

The comparison of the statistics for real pollen percentage and square-root pollen percentage runs show that the square-root pollen percentage ones performed better, and thus, the coefficients gained from the final transfer function run was used in this study (Tab. 3 – 9).

Tab. 3 - 9: Coefficients for specific taxa and climate parameter from final transfer function using square-root transformed pollen percentages. “n.i.“ indicates that this taxa was not part of the specific pollen-climate transfer function because its relationship to the climate parameter was not clear or sample sites too few.

Taxa/Family	**MAP**	**MAT**	**MSP**	**MST**	**MWP**	**MWT**
Abies	1474.59	12.41	932.08	4.89	56.49	14.71
Alnus	n.i.	12.06	709.58	10.53	28.03	8.61
Apiaceae	192.11	-14.93	326.06	2.77	-0.92	-23.27
Artemisia	296.51	-0.47	107.69	11.02	7.78	-12.57
Asteraceae	350.55	0.77	177.81	10.12	6.81	-10.66
Betula	468.99	11.19	577.46	17.23	17.06	2.55
Brassicaceae	543.16	-13.00	136.42	2.78	6.08	-29.13
Calligonum	-418.93	38.91	-75.91	59.69	-50.22	13.73
Caryophyllaceae	366.73	-17.89	211.62	-6.78	-0.94	-27.76
Chenopodiaceae	-11.33	3.35	-24.94	15.97	6.73	-10.61
Corylus	922.93	24.49	843.56	26.77	80.66	23.05
Crassulaceae	84.76	-26.23	134.05	-9.45	-19.21	-46.31
Cupressaceae	876.02	9.53	456.64	10.50	13.07	2.05
Cyperaceae	489.60	-5.82	343.45	4.49	11.34	-15.76
Elaeagnus	n.i.	n.i.	853.30	n.i.	-40.31	4.16
Ephedra	12.20	-12.08	46.39	3.47	-0.67	-25.95
Ericaceae	368.77	-11.85	389.86	-3.76	10.81	-19.96
Fabaceae (undiff)	495.18	2.51	260.57	13.32	7.28	-9.36
Fagaceae	n.i.	n.i.	n.i.	n.i.	-30.10	3.30
Hippophae	154.60	5.72	313.97	15.64	-34.44	2.30
Juniperus	-319.21	16.90	854.12	2.16	15.14	2.40
Lamiaceae	557.30	-3.65	211.89	4.05	0.19	-18.07
Liliaceae	87.16	17.31	43.15	16.84	-2.48	-12.07
Nitrariaceae	-11.23	20.54	-32.23	32.71	-2.62	5.41
Picea	447.07	0.39	240.82	14.28	12.23	-14.42
Pinus	297.04	6.12	401.14	14.65	5.97	1.18
Poaceae	142.68	-0.82	117.65	6.95	4.12	-9.31
Polygonaceae	503.73	-2.69	251.50	3.04	-0.22	-10.94
Populus	-772.26	n.i.	-469.07	n.i.	n.i.	-28.05
Primulaceae	390.46	9.80	232.78	7.87	-1.77	-7.26
Quercus (undiff)	347.04	-2.49	317.56	8.95	-5.54	-4.12
Ranunculus	404.51	2.20	364.13	8.15	0.68	-7.93
Rhamnaceae	726.22	36.16	74.95	51.53	-21.17	10.48
Rosaceae	743.08	0.39	448.27	10.88	8.64	-9.70
Salix	451.44	9.48	332.64	13.59	59.20	-7.53
Saxifragaceae	1390.01	3.05	895.24	5.84	33.94	-2.46
Scrophulariaceae	131.55	-3.01	395.36	1.56	0.19	-7.01
Tamaricaceae	92.32	13.39	27.28	18.94	21.40	-13.55
Thalictrum	514.37	-11.66	306.21	-3.82	14.22	-22.71
Tsuga	n.i.	n.i.	n.i.	24.49	n.i.	n.i.
Ulmus	-23.65	95.02	-331.85	n.i.	n.i.	1.17
Zygophyllaceae	n.i.	28.44	-419.74	n.i.	-7.11	3.39

Chapter 4: Palaeovegetation and palaeoclimate variability in the Qaidam Basin between 3.5 and 3.0 Ma

4.1 Introduction

The Pliocene was the last geological epoch that is characterised by higher than pre-industrial atmospheric carbon dioxide concentrations and global temperatures that exceeded the modern average by 2 – 3 °C (Haywood and Valdes, 2004). Thus, a further understanding of the Pliocene in general and the mPWP in specific (Haywood et al., 2013) is of great importance to increase the understanding of future global warming scenarios and improve data-model comparisons.

During the Pliocene, the distribution of landmasses was similar to the modern distribution although it has to be stated that the closure of the CAS and the ITF were not completed but were rather gradually evolving towards the modern setting (Haug and Tiedemann, 1998; Karas et al., 2009). These developments played a critical role in the reorganisation and strengthening of the global thermohaline circulation (THC) by restricting the fresh water surface flow from the equatorial Pacific to the Caribbean Sea (Schneider and Schmittner, 2006). The initiated/enhanced formation the North Atlantic Deep Water (NADW) in the Labrador Sea subsequently led to a strengthened Atlantic Meridional Overturning Circulation (AMOC), increased northward transport of moisture and possibly the onset of the NHG (Haug and Tiedemann, 1998). In the EEP, the closure of the CAS caused the establishment of a strong upwelling zone as well as the initiation of a thermal gradient along the equatorial Pacific and shallowing of the EEP thermocline (Dekens et al., 2007; Lawrence et al., 2006; Steph et al., 2010). The latter could have been a direct consequence of global changes in thermocline depths caused by a stronger AMOC influencing deep ocean current flow in the Pacific (Steph et al., 2010; Timmermann et al., 2005). Nowadays, a strong thermal gradient characterises the equatorial Pacific, whereas weak thermal gradients (so called El Niño events) only occurs every 2 – 8 years when the EEP experiences a warming of sea-surface temperatures (SST) (Moy et al., 2002). Since the modern thermal gradient across the Pacific was only established gradually during the Pliocene, several studies have discussed the possibility of a permanent El Niño like state in the Pacific Ocean during the Early Pliocene (Fedorov et al., 2006; Haywood et al., 2007; Ravelo et al., 2004; Steph et al., 2010; Wara et al., 2005).

Differences between present-day and the Pliocene exist in the scale of high-altitude ice sheets. During the Late Pliocene, intervals of increased IRD suggest that glaciers were growing in the Northern Hemisphere during significant cooling events (such as M2; 3.3 Ma), however, the build-up of the widespread permanent ice sheets did not take place until the Plio-Pleistocene transition (Jansen et al., 2000; Kleiven et al., 2002). In the Southern Hemisphere, strong cyclic reductions in marine-based parts of the WAIS and EAIS were recognised during the early to mid-Pliocene (until 3.5 – 3.3 Ma), which might have been caused by migration of warmer ocean temperatures into higher latitudes due to orbital forcings (Naish et al., 2009; Patterson et al., 2014). After 3.5 – 3.3 Ma, the southern high latitudes underwent stronger cooling leading to a stabilisation of the EAIS margin (Patterson et al., 2014).

The benthic oxygen isotope records from Zachos et al. (2001) and Lisiecki and Raymo (2005) show that ocean temperatures declined gradually during the Pliocene. Due to less extensive ice sheets, sea level may have been ~ 20 – 25 ± 10 m higher during the mid-Pliocene (e.g. Dowsett et al., 1999; Miller et al., 2012). The warmer Pliocene world was characterised by ~ 3 °C higher global surface air temperatures (Haywood and Valdes, 2004; Lunt et al., 2010) compared to present-day and carbon dioxide concentrations of 330 – 400 ppm (Pagani et al., 2010; Seki et al., 2010) which were considerably higher than pre-industrial values (280 ppm). Due to polar amplification, high-latitude study sites show significantly higher than averaged global temperatures with up to 8 – 19 °C higher temperatures in Canada and Norway (Ballantyne et al., 2010; Ballantyne et al., 2006; Panitz et al., 2016). Associated with higher temperatures was a northward migration of vegetation zones compared to modern-day (Salzmann et al., 2008). Recent high-resolution palynology studies from Siberia and Norway (Andreev et al., 2014; Panitz et al., 2016) furthermore suggest, that the mPWP was characterised by strong climate variability (caused by orbital forcings) in contrast to earlier views that proposed a more stable warm period (Willard, 1994).

In East Asia, a strengthened EASM and EAWM has been proposed between 3.6 and 2.6 Ma by An et al. (2001) based on the evaluation of sediment proxies on the CLP, such as magnetic susceptibility, Rb/Sr ratios, grain size analysis and Al fluxes. In the NW Qaidam Basin, palynology studies from Miao et al. (2011), Miao et al. (2013) and Cai et al. (2012) show that there is a continuous long-term aridification trend starting in the early Miocene until today. However, crucially, between 5 and 3.1 Ma a gap exists during which it is unclear whether the aridification trend has been gradual or stepwise. Although Miao et al. (2011) was able to link pollen assemblage based trends in precipitation and temperature in the NW Qaidam Basin to global benthic oxygen isotopes, the source of moisture (EASM) could not be resolved robustly since cooling occurred in all moisture source areas. Other pollen records from the Qaidam Basin do either not have the necessary resolution to address questions of climate variabilities or only have a limited age-model making a high-resolution assessment of vegetation changes difficult (Wang et al., 1999; Wu et al., 2011).

In this study, a new high-resolution multi-proxy record from the NW Qaidam Basin is presented that covers the time interval from 3.5 to 3.0 Ma. A combination of lithological, XRF and pollen data is used to assess the palaeolake development of the SG-1b core as well as the palaeovegetation and palaeoclimate history and variability of the NW Qaidam Basin during and before the mPWP. Pollen-based proxies and transfer functions will highlight the EASM as the main source of precipitation in the NW Qaidam Basin while also indicating that a teleconnection exists between moisture in the Qaidam Basin and warming in the EEP.

4.2 Results

4.2.1 Lithology of SG-1b core

The 723 m long SG-1b core consists of fine-grained mudstones, siltstones, sandstones, halites, gypsum crystals and gypsum beds (Zhang et al, 2012). Zhang et al (2012) divide the sedimentary sequence further into three broad intervals: a) between 0 and 90 m the main sedimentation features are mudstones which can contain gypsum crystals, with some gypsum and marl layers, b) between 90 and 232 m the sediment is dominated by variations of grey mudstones with some siltstones and clay-silt layers and c) between 232 and 723 m the sediments are made up of grey mudstones containing calcic concretions, and calcareous layers.

This study is focused on the sedimentation history of the SG-1b core for the interval between 135.88 and 209.48 m. The sediment description is based on high-resolution core scanning images with some help of XRF core scanning data for interpretation of evaporite layers. Fig. 4 – 1 gives an overview of sediments occurring in the core interval. Most of the core material consists of mudstones in varying colours (green, light brown, dark brown) with some carbonate/sulfate rich mudstones, which have a lighter colour. Sandy mud- and sandstones occur in the upper part of the core interval. Gypsum crystals occur frequently in varying sizes, whereas carbonate/sulfate layers are only few in number. Halite occurs as very thin layers, together with other evaporite crystals or interspersed with/in mudstones. In addition to the sediment description, a detailed analysis of the sediment texture was conducted (Fig. 4 – 2). Features include parallel lamination, cross lamination, which also includes disturbances and wavy laminations, turbidites and textureless beds with no or only weak visible lamination.

Fig.4 – 3 shows the lithological record of the SG-1b core interval. To see more details of this interval, the record has been split into eigth sections. For each of the core sections, the core scanning image, the assigned core lithology and the assigned core texture is shown.

In the upper part of the record (until ~ 175 m), brownish to dark brownish mudstones dominate the lithology. Three larger sandy mud- or sandstone layers have been identified in the uppermost interval (until 152.50 m), however, another small layer of sandy mud- or sandstones is re-occurring at a core depth ~ 165 m. Carbonate/sulfate rich mudstones layers are occurring only in small numbers. Gypsum crystals are present in the upper part, bound to sandy or carbonate/sulfate rich mudstone layers.

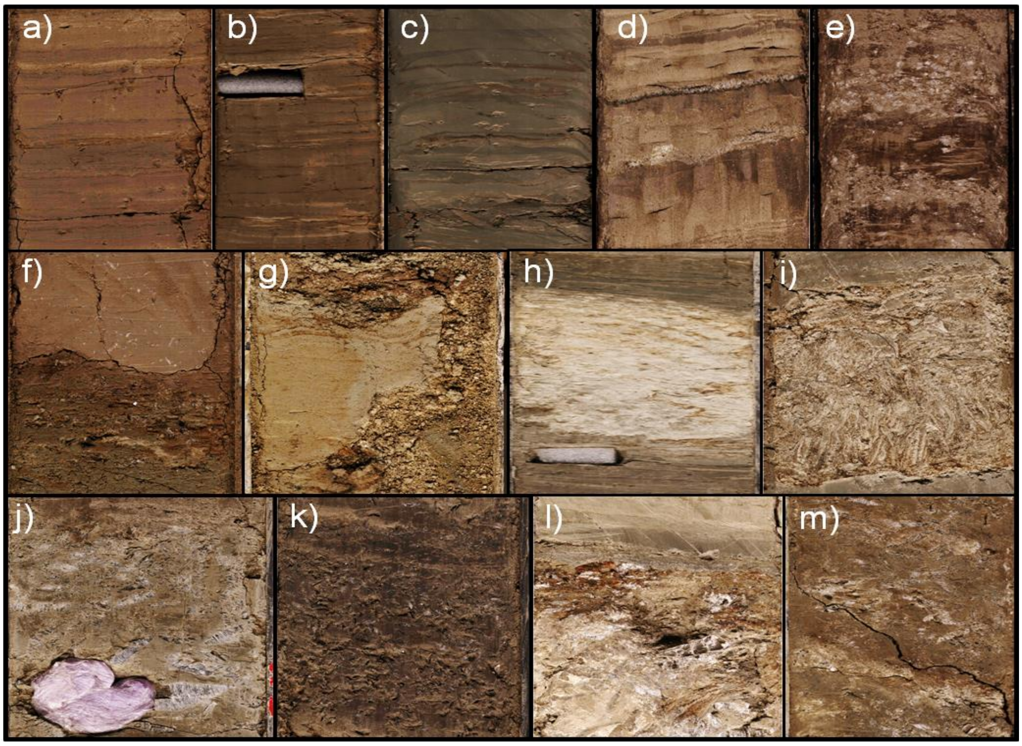

Fig. 4 - 1: Overview of lithological units in SG-1b core between 135.88 and 209.48 m: a-c) mudstones, d) mudstones with halite vein, e) mudstones interspersed with halite, f) transition from mudstone-bearing gypsum (top) to sandy mudstone-bearing gypsum (bottom), g) sandstones, h-i) carbonates/sulfates, j-k) gypsum crystals embedded in sediments, l) sequence of mudstones (top) into crystalline halite and gypsum/carbonates/sulfates (bottom), m) halite and gypsum crystals in mudstone layer.

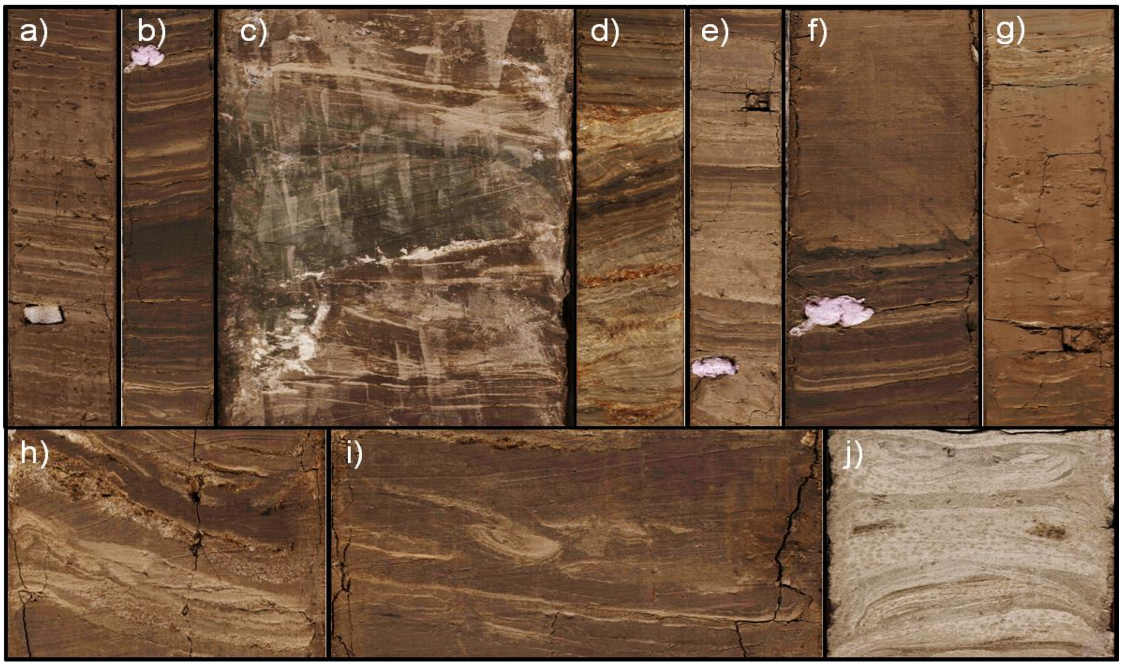

Fig. 4 - 2: Overview of textural features in SG-1b core sediments between 135.88 and 209.48 m. a) parallel lamination, b-d) cross-lamination e) 3 Turbidite sequences f) no/weak lamination (top), g) no/weak lamination (middle), h-j) wavy laminations/disturbed sediments.

In the lower part of the record (below 175 m), mudstones are less dominant and more greenish in colour. Frequent layers of carbonates/sulfates and a significantly higher number of carbonate/sulfate rich mudstone layers are characterising this lower part. Additionally, halite layers and halite containing mudstone layers occur throughout this interval. Gypsum crystals are embedded frequently in the record, especially in the lower most sections. Generally, cross laminations and textureless sediments are dominating the lower part of the record, whereas parallel lamination becomes dominant in the upper part of the record.

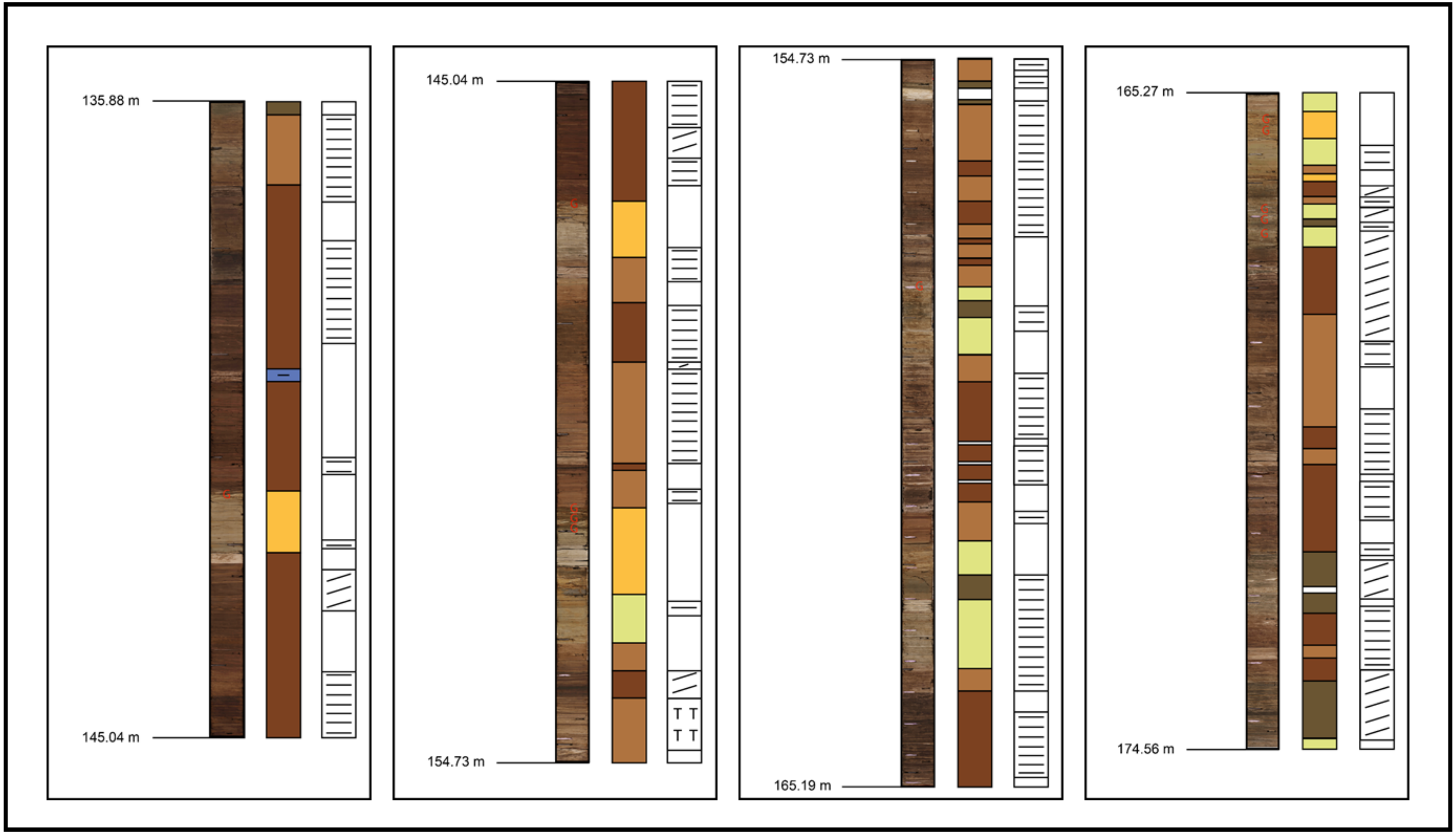

Fig. 4 - 3: Sedimentation record of SG-1b core between 135.88 and 209.48 m shown in eight different sections for larger resolution. The figure shows the core scan (CS), assigned core lithology (CL) and core texture (CT).

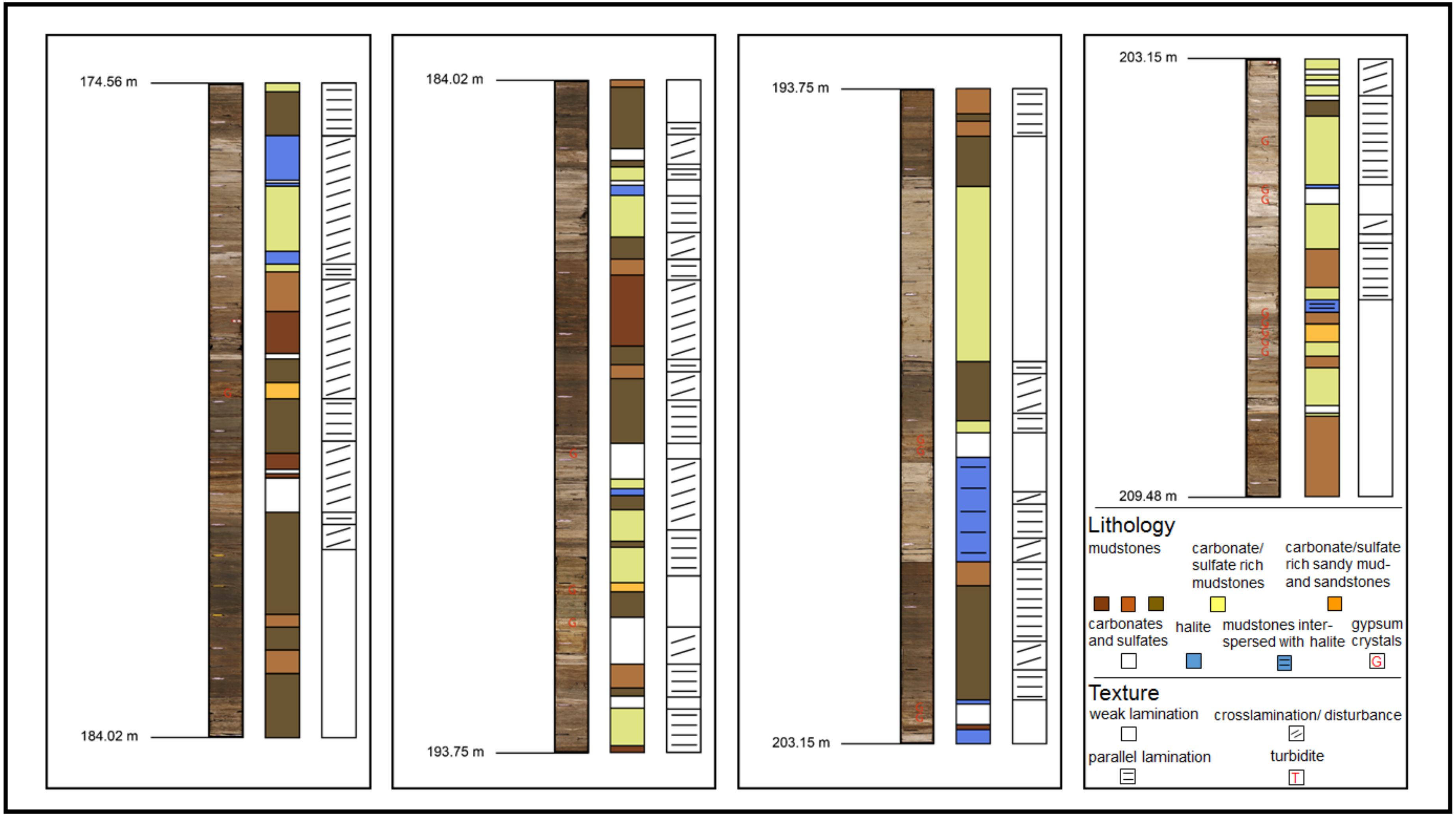
174.56 m
184.02 m
184.02 m
193.75 m
193.75 m
203.15 m
203.15 m
209.48 m
G
Lithology
mudstones
carbonate/ sulfate rich mudstones
carbonate/sulfate rich sandy mud- and sandstones
carbonates and sulfates
halite
mudstones inter- spersed with halite
gypsum crystals
Texture
weak lamination
crosslamination/ disturbance
parallel lamination
turbidite
T

Fig.4 - 3: (cont.)

4.2.2 X-ray fluorescence analysis

The depth profile of the XRF core scanning data are shown in Fig. 4 – 4. Elements with consistently negative or very low values were removed. The units for each element are total counts. Based on the depth profiles of the elements, the figure was split into two figures. In Fig. 4 – 4 the elements Al, Si, K, Ti, Fe, Rb, Y, Zr, Mn and Mg are shown. The main characteristic is that the depth profiles for all of these elements is similar, so elements belonging to the Fig. 4 – 4 are referred to as group 1 elements. Fig. 4 – 5 includes all other elements– Ca, Sr, Sc, S and Cl – and Ti as a reference for the group 1 elements. Ca, Sr, Sc, and S seem to be anti-correlated to group 1 elements whereas Cl seem to be different from these four elements as well. In order to assess similarities and discrepanices between all these elements further, correlation coefficients have been calculated (Tab. 4 – 1) and Principle Component Analysis has been conducted (Fig. 4 – 6).

The correlation matrix (Tab. 4 – 1) shows a positive correlation for group 1 elements which is specifically strong between Al, Si, K, Ti and Fe. Rb, Y, Zr and Mn also show a considerable but less strong positive relationship. Mg has the lowest positive correlation coefficients with all other group 1 elements but seem to have a strong correlation with Mn. Although it seemed that Ca, Sr, Sc and S are anti-correlated to the group 1 elements, the correlation coefficients provide a different, more diversified view. Ca is strongly positive correlated with Sc and moderately correlated with Sr. In general, S is not positively correlated or anti-correlated with any of the other elements. Ca shows anti-correlations with Cl, Rb, Y and Zr, whereas Sr only has anti-correlations with Rb and Y. Sc is anti-correlated to many other group 1 elements, namely Ti, Mn, Fe, Rb, Y and Zr. Cl does not show positive relationships with any of the other elements, and is anti-correlated to Al, Si, K, Ca, Ti, Mn and Fe.

The PCA (Fig. 4 – 6) of the log-normalised XRF data reflects the observations of the depth profiles and correlation matrix. Group 1 elements are closely aligned together with very strong negative values of PCA Axis 1. However, some variability exists within this group as Al, Si, K and Fe have positive values in PCA Axis 2, whereas Rb, Y and Zr have negative values in PCA Axis 2.

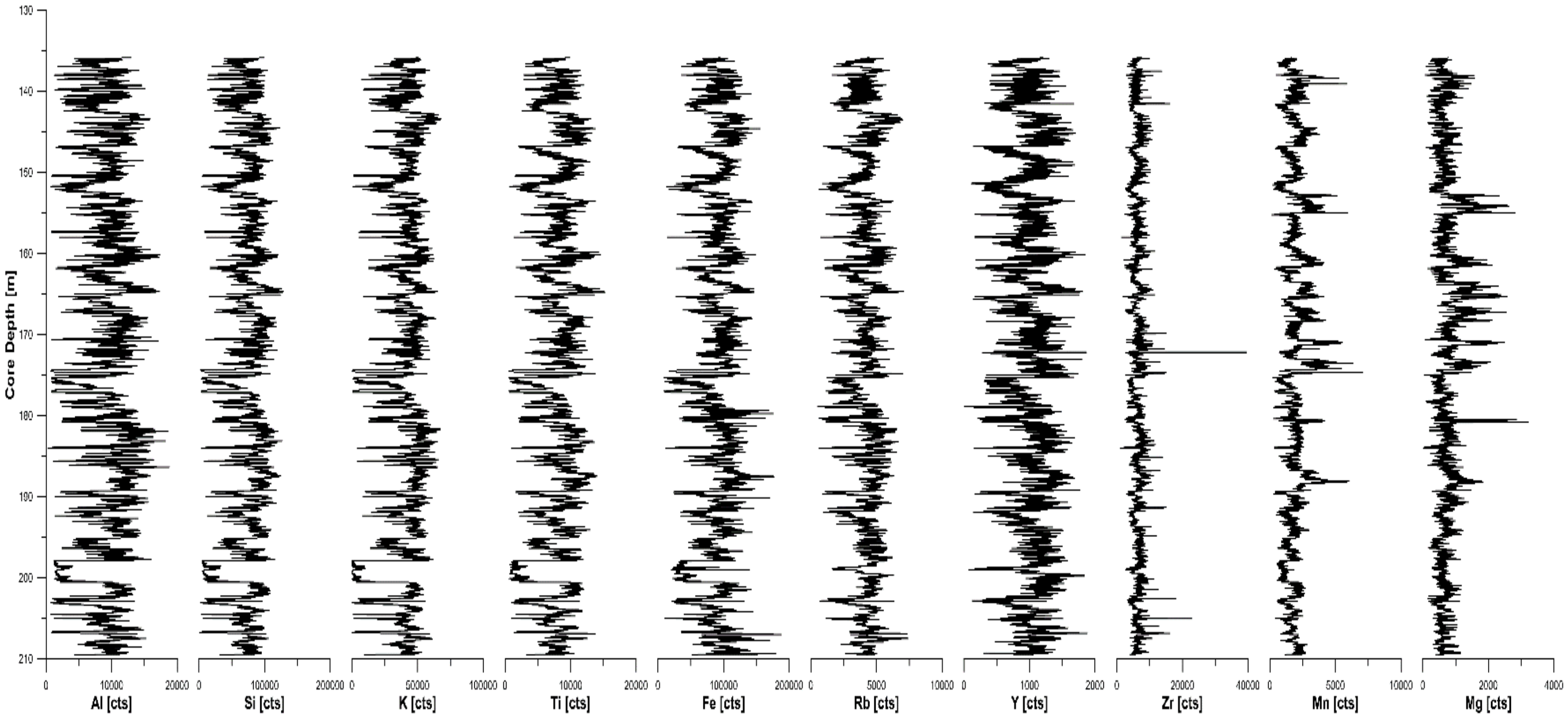

Fig. 4 - 4: Element depth profile from the XRF core scanner. Elements are shown as counts. Elements with a similar depth profile include Al, Si, K, Ti, Fe, Rb, Y, Zr, Mn and Mg, and will be from here on referred as group 1 elements.

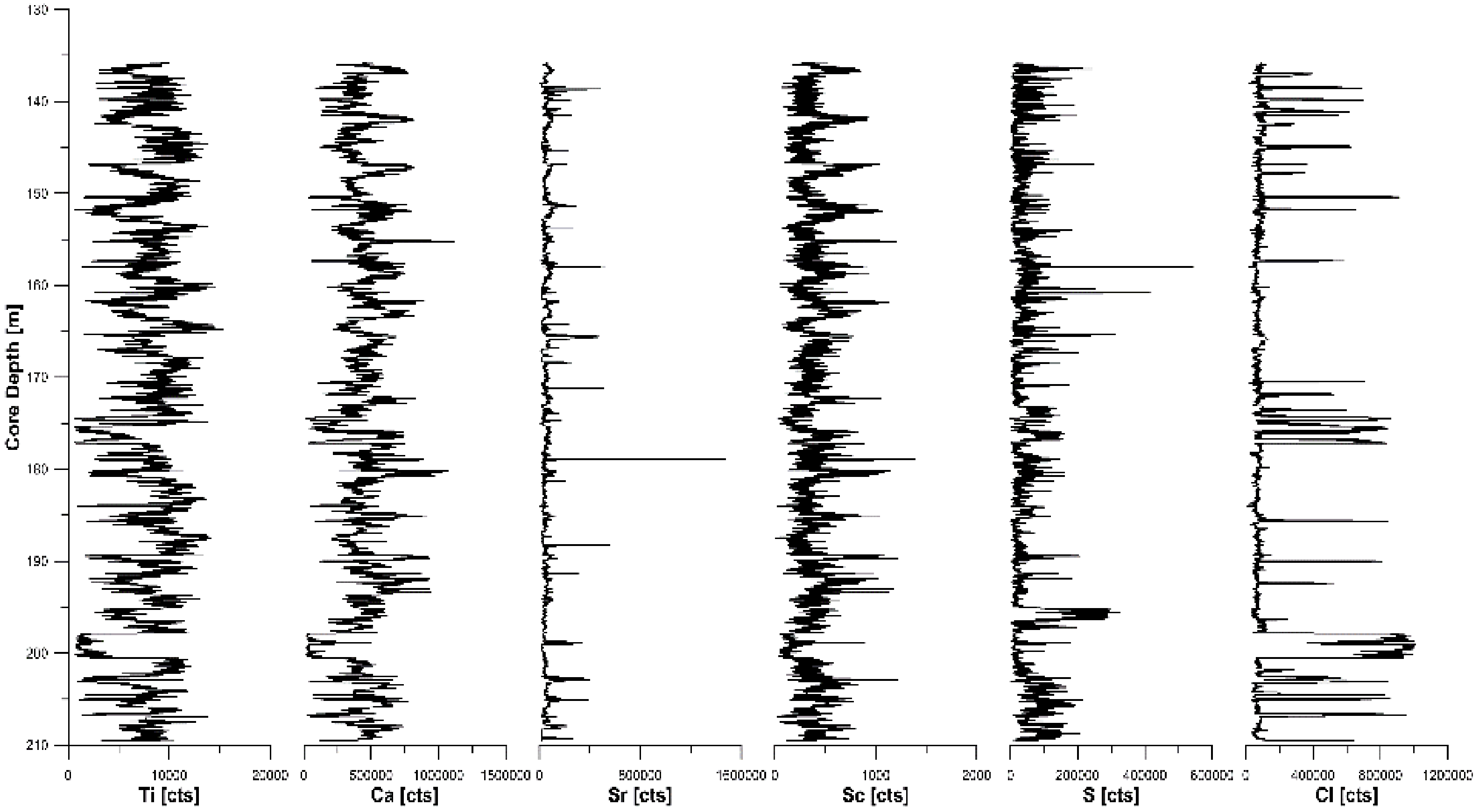

Fig. 4 - 5: Element depth profile from XRF core scanner. The elements Ca, Sr, Sc, S and Cl are shown as their counts in this separate figure because they do not follow the group 1 elements depth profile (Ti as a reference).

Tab. 4 - 1: Correlation matrix of selected elements detected by XRF (negative correlation in red).

	Mg	**Al**	**Si**	**S**	**Cl**	**K**	**Ca**	**Ti**	**Mn**	**Fe**	**Sc**	**Rb**	**Sr**	**Y**	**Zr**
Mg	1.00	0.36	0.37	-0.16	-0.17	0.29	-0.04	0.35	0.76	0.37	-0.16	0.21	-0.13	0.22	0.10
Al		1.00	0.98	-0.25	-0.61	0.96	0.07	0.91	0.47	0.85	-0.23	0.68	-0.23	0.56	0.42
Si			1.00	-0.25	-0.67	0.95	0.10	0.94	0.51	0.87	-0.21	0.63	-0.21	0.56	0.45
S				1.00	-0.13	-0.22	0.27	-0.27	-0.15	-0.20	0.24	-0.20	0.16	-0.20	-0.11
Cl					1.00	-0.74	-0.59	-0.58	-0.31	-0.53	-0.28	-0.06	-0.02	-0.00	-0.02
K						1.00	0.18	0.90	0.47	0.85	-0.16	0.63	-0.22	0.48	0.33
Ca							1.00	-0.13	-0.16	-0.14	0.84	-0.50	0.32	-0.53	-0.38
Ti								1.00	0.59	0.92	-0.40	0.73	-0.28	0.69	0.57
Mn									1.00	0.60	-0.34	0.41	-0.27	0.44	0.26
Fe										1.00	-0.41	0.73	-0.29	0.64	0.47
Sc											1.00	-0.67	0.46	-0.68	-0.46
Rb												1.00	-0.44	0.85	0.60
Sr													1.00	-0.50	-0.16
Y														1.00	0.71
Zr															1.00

Mn and Mg should be treated with caution since their close position to Rb, Y and Zr implies similar processes driving all these elements but the correlation coefficients indicate otherwise. There is actually no correlation between Mg and Rb, Y and Zr, and only a moderate correlation from Mn with Rb and Y. In contrast to group 1 elements, Sr, Sc and S have positive values in PCA Axis 1 and a somewhat close alignment to each other. Furthermore, Cl also has a strong positive value in PCA Axis 1, though it is on the opposite end of PCA Axis 2. Sr, Sc and S are grouped together (group 2), whereas Cl is assigned as the sole member of group 3. Ca is located in-between group 1 and group 2 elements with a very high positive PCA Axis 2 value. Therefore, it might be that Ca belongs to both groups. PCA Axis 1 and PCA Axis 2 explain 52.09 % and 24.73 % of the variance in elemental counts, respectively. In order to track intervals with similar XRF data composition throughout the record, cluster analysis of the XRF data has been performed. In Fig. 4 – 7, the resulting dendrogram of the cluster analysis is shown. Based on the general shape of the dendrogram six different facies that characterise changes in the sedimentation history of the SG-1b core have been identified. Enrichment of the elements have been calculated (Eq. 3 – 3) for each cluster normalised to whole core values (Tab. 4 – 2). Cluster 1 is characterised by higher counts of Al, Si, K, Ti, Fe, Rb, Y, Zr, Mg, Mn and Ca while Cl, Sc, Sr and S were depleted with respect to the whole record.

Cluster 2 is characterised by enrichment of K, Ca, Sc, Sr and S while the amounts of all other elements were depleted. Cluster 3 is characterised by enrichment of Ca, Sc, Sr and S while all other elements have been depleted. Although cluster 3 seems to be similar to cluster 2 in terms of which elements are enriched/depleted with K being the only element changing from being enriched to depleted, the absolute numbers indicate some larger changes. Group 1 elements seem to be depleted much more than in cluster 2 whereas group 2 elements and Ca are enriched much more than in cluster 2. Cluster 4 is characterised by a strong enrichment of Cl, whereas all other elements are depleted. Cluster 5 is similar to cluster 1 but the enrichments of group 1 elements (and depletion of group 2 elements) is much stronger. In contrast to cluster 1, Ca is only slightly depleted in cluster 5. Cluster 6 is characterised by enrichment in group 1 elements, but in contrast to clusters 1 and 5 enrichments for most elements is lower, however, Mn and Mg are being strongly enriched. Ca and Sc are also slightly enriched, whereas Sr and S are less depleted than in clusters 1 and 5.

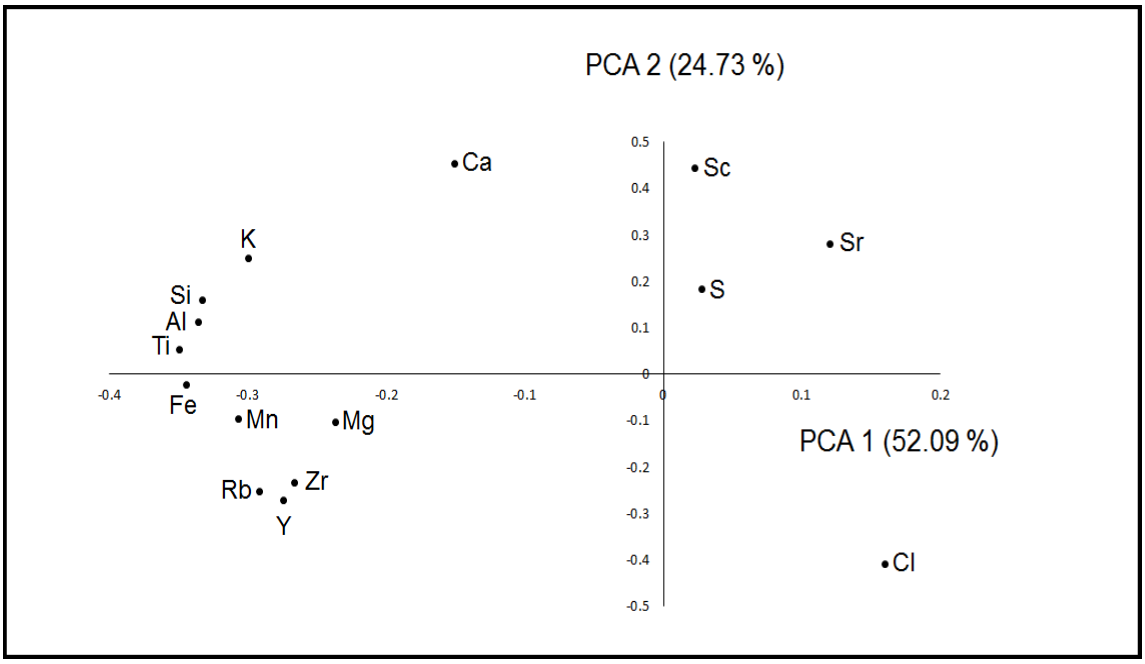

Fig. 4 - 6: PCA of SG-1b XRF data. Prior to PCA, the XRF data was screened for negative values in its main elements and unusual Cl values (see explanation XRF Raw Data and Screening). The XRF data was log-normalised, centered and scaled using the program R (R Development Core Team, 2008). The PCA shows a clear separation of between elements representing silici-clastic sedimentation (Al, Si, K, Ti, Fe, Rb, Y, Zr, Mn, Mg) and those elements which occur predominantly during deposition of evaporites (S, Sc, Sr). The position of Ca in-between these two groups probably indicates that it is occurring during both, deposition of silici-clastic material and evaporites. Cl does occur during evaporite precipitation, is however, separate from S, Sc, and Sr.

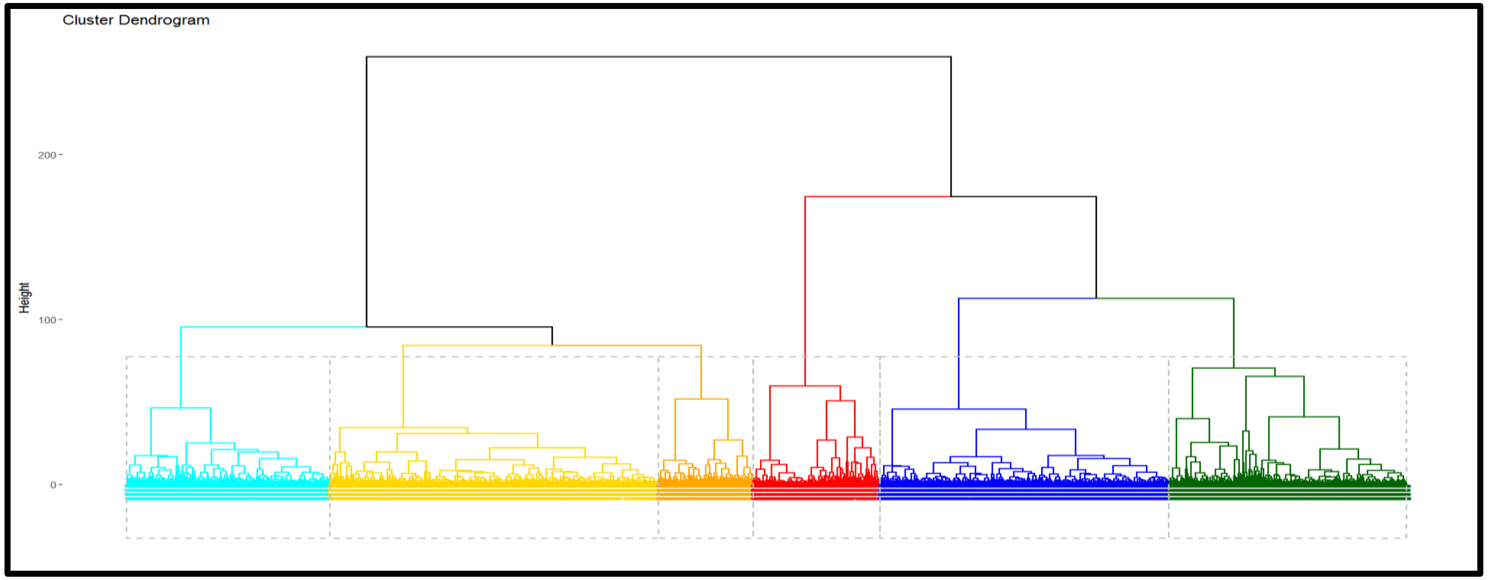

Fig. 4 - 7: Dendrogram of cluster analysis from selected elements measured by XRF core scanning. Whole sample set was screened and normalised prior to cluster analysis (see explanatory text). Cluster analysis itself was done using Euclidean distance and Ward.D2 method (Ward, 1963).

Tab. 4 - 2: Enrichment (black) / depletion (red) of the elements in each cluster normalised to whole record

Cluster	Mg	Al	Si	S	Cl	K	Ca	Ti	Mn	Fe	Sc	Rb	Sr	Y	Zr
1	5.03	24.40	23.88	-12.54	-35.52	22.58	0.19	24.02	11.10	19.32	-10.16	15.60	-4.99	15.70	13.10
2	-17.49	-1.10	-1.56	2.48	-44.11	1.44	15.19	-8.62	-14.01	-6.75	11.72	-9.32	0.02	-12.46	-12.19
3	-37.89	-43.52	-41.13	70.03	-44.98	-37.81	23.50	-47.88	-47.25	-40.93	40.84	-43.52	55.12	-47.27	-33.35
4	-38.07	-71.31	-71.79	-31.22	348.88	-75.01	-65.65	-60.12	-41.15	-47.21	-41.60	-18.09	-15.10	-13.20	-10.94
5	26.55	53.72	51.58	-43.58	-31.12	47.68	-11.40	60.37	39.30	47.59	-22.07	47.31	-28.30	50.86	41.72
6	125.02	8.21	10.73	-3.78	-32.33	10.45	7.01	14.05	93.52	17.34	0.67	5.98	-39.65	10.38	0.34

4.2.3 Carbon/nitrogen ratio

The C/N data of the SG-1b core is shown in Fig. 4 – 8. The samples used to obtain the C/N data are the same used for pollen analysis. In general, the C/N values vary between 4.7 and 14.6. Throughout the record, multiple intervals of sustained higher and lower C/N values can be observed from the three-point average. Variability in the C/N ratios might indicate changes in palaeoproductivity or palaeolake size because the C/N ratio of organic matter derived from lacustrine (< 10) and terrestrial sources (> 10) differs from each other (Hedges et al., 1986; Hedges et al., 1997). A detailed interpretation of the C/N proxy for the SG-1b core is given in the discussion section of this chapter (4.3.1.2).

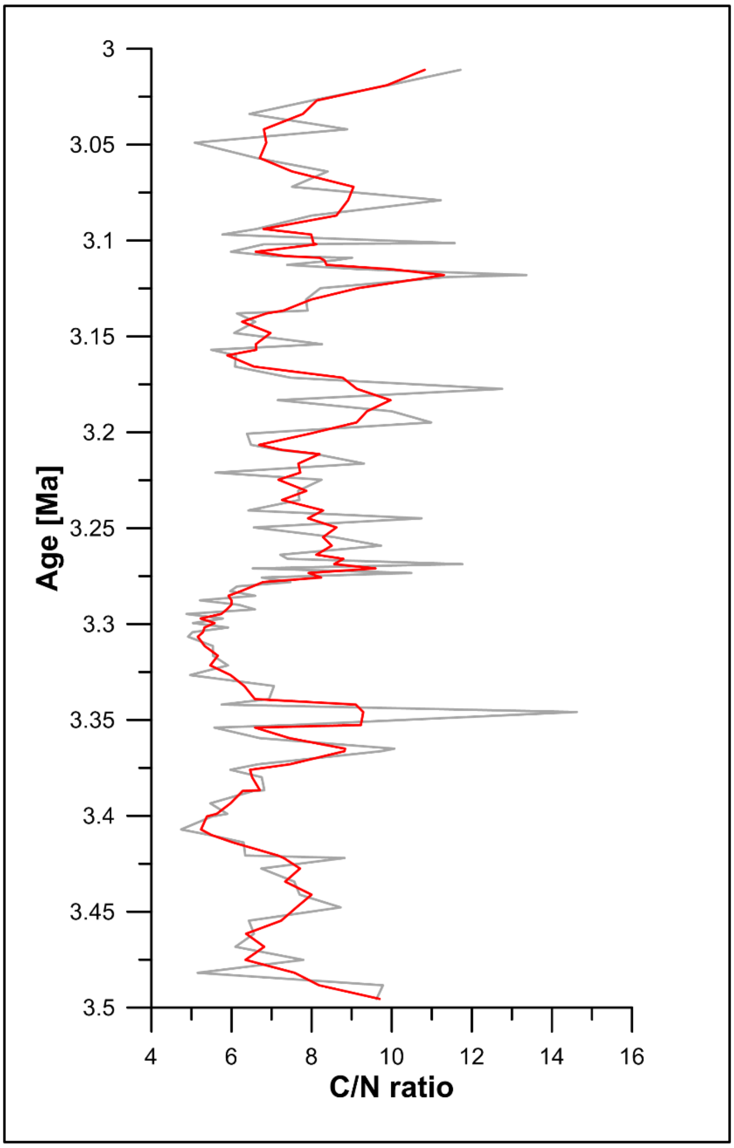

Fig. 4 - 8: Depth profile of C/N data for the SG-1b core between 3.5 and 3.0 Ma. Original data (grey), 3pt averages (red).

4.2.4 Palynology results

108 samples have been counted in the interval between 156.79 and 224.71 m, which relates to an age range of 3.495 to 3.011 Ma. An overview of the most important taxa is given in Fig. 4 – 9. Due to low pollen sum (< 50), one sample was excluded from the pollen diagram. The pollen and spore concentrations range between 400 and 5000 grains/g sediment (dry) for most of the samples. However, between 3.17 and 3.15 Ma remarkably higher pollen and spore concentration were calculated, exceeding 4000 grains/g sediment (dry) up to a maximum of ~ 17000 grains/g sediment (dry). Based on CONISS (Grimm, 1987), the pollen assemblages from the SG-1b record (Fig. 4 – 10 and Fig. 4 – 11) can be divided into 3 main and 14 sub zones. The pollen assemblage of the SG-1b core is dominated by xerophytic shrub taxa, such as Chenopodiaceae, *Artemisia*, *Ephedra spp.* and *Nitraria*. Poaceae and Cyperaceae show higher percentages in the lowermost and uppermost pollen assemblage zones. Coniferous and broadleaved trees only show minor amounts except for the interval between 3.17 and 3.15 Ma during which coniferous trees sharply increase. A more detailed description of the pollen assemblage zones (PAZ) is given below:

The PAZ 1-A (3.495 – 3.412 Ma) is characterised by high amounts of xerophytic taxa, especially *Artemisia* (18.96 – 42.05%) and Chenopodiaceae (28.03 – 51.37%). *Ephedra spp.* (2.12 – 18.24%) is also abundant. The grasses Poaceae (5.93 – 18.83%) and Cyperaceae (0.61 – 7.69%) occur in high percentages. Other herbaceous taxa that are present in low amounts this pollen zone are Asteraceae (0 – 4.40%), *Nitraria* (0 – 1.96%) and Caryophyllaceae (0 – 4.28%). Coniferous trees, which are dominated by *Pinus*, add up to 1.54 – 9.80%. Further tree pollen (*Betula*, *Alnus*) are very low.

The PAZ 1-B (3.412 – 3.382 Ma) is marked by a significant decrease in *Ephedra spp.* (0.54 – 6.21%) and an increase in Poaceae (10.46 – 33.10%) and Cyperaceae (2.05 – 11.97%). *Artemisia* (7.75 – 29.24%) and Chenopodiaceae (24.65 – 41.20%) remain at high levels. Other herbaceous taxa that are present in low abundances are Asteraceae (0 – 3.05%), *Nitraria* (0 – 2.13%) and Caryophyllaceae (1.17 – 4.58%). Coniferous show almost no change whereas broadleaved trees increase to 3.32 – 13.40%.

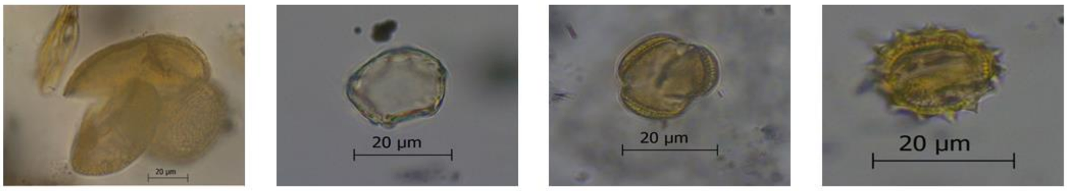

Abies *Alnus* *Artemisia* Asteraceae - Tubiliflorae

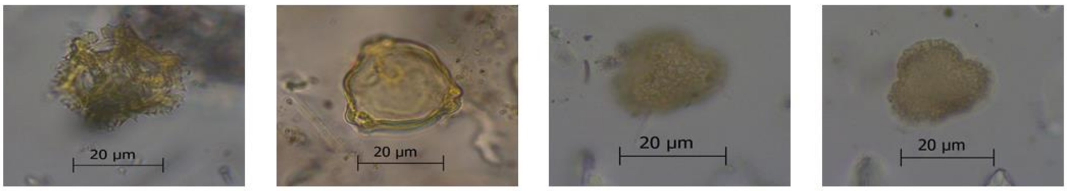

Asteraceae - Liguliflorae *Betula* Brassicaceae Brassicaceae

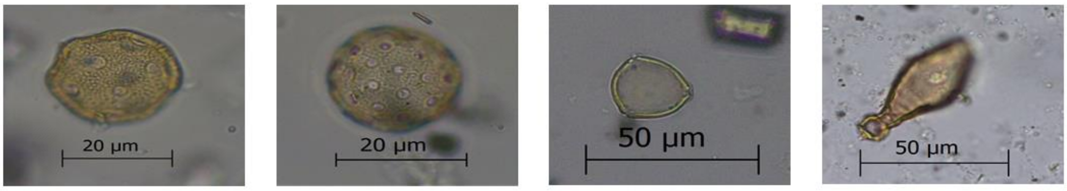

Caryophyllaceae Chenopodiaceae *Corylus* Cupressaceae c.f

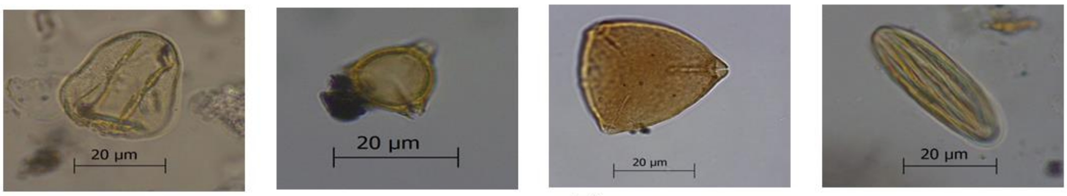

Cyperaceae *Elaeagnus* *Elaeagnus* *Ephedra* – fragilis type

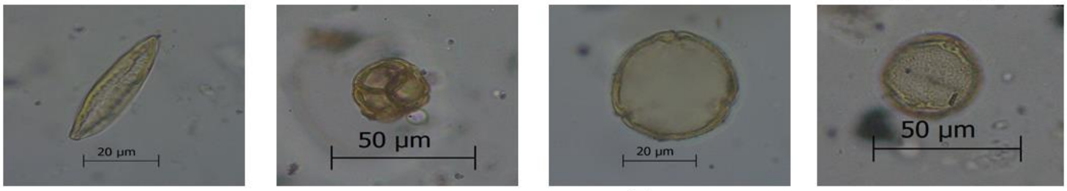

Ephedra - distachya type Ericaceae *Fagus* *Fagus*

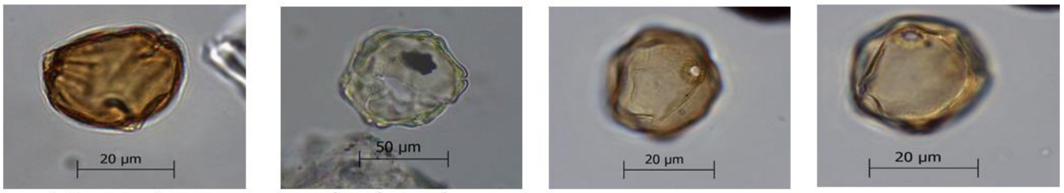

Hippophäe *Juglans/ Pterocarya* *Juglans/ Pterocarya* *Juglans/ Pterocarya*

Fig. 4 - 9: Selection of pollen taxa found in samples from Qaidam Basin and Kunlun Pass Basin.

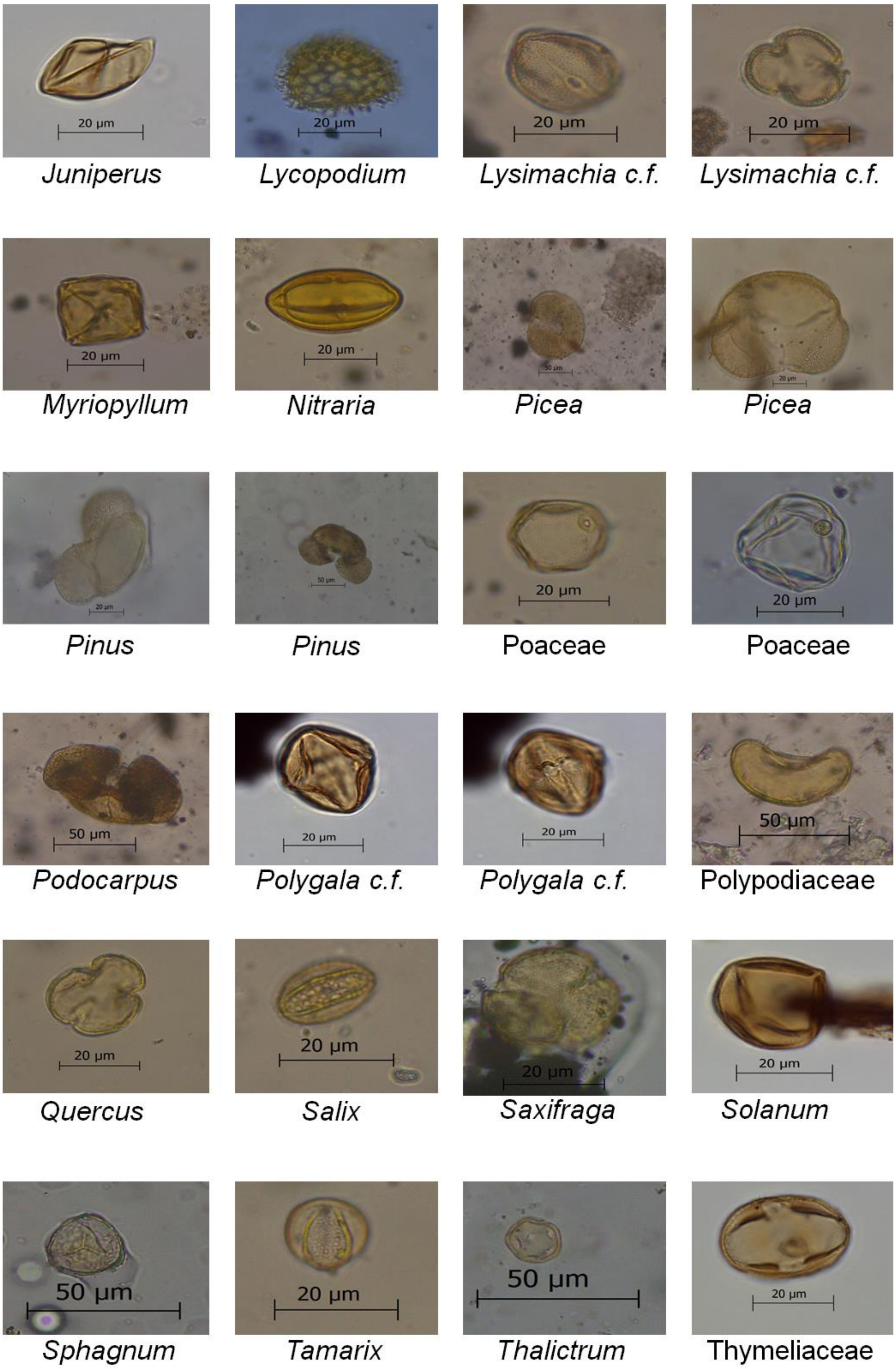

Juniperus *Lycopodium* *Lysimachia c.f.* *Lysimachia c.f.*

Myriopyllum *Nitraria* *Picea* *Picea*

Pinus *Pinus* Poaceae Poaceae

Podocarpus *Polygala c.f.* *Polygala c.f.* Polypodiaceae

Quercus *Salix* *Saxifraga* *Solanum*

Sphagnum *Tamarix* *Thalictrum* Thymeliaceae

Fig. 4 – 9: (cont.)

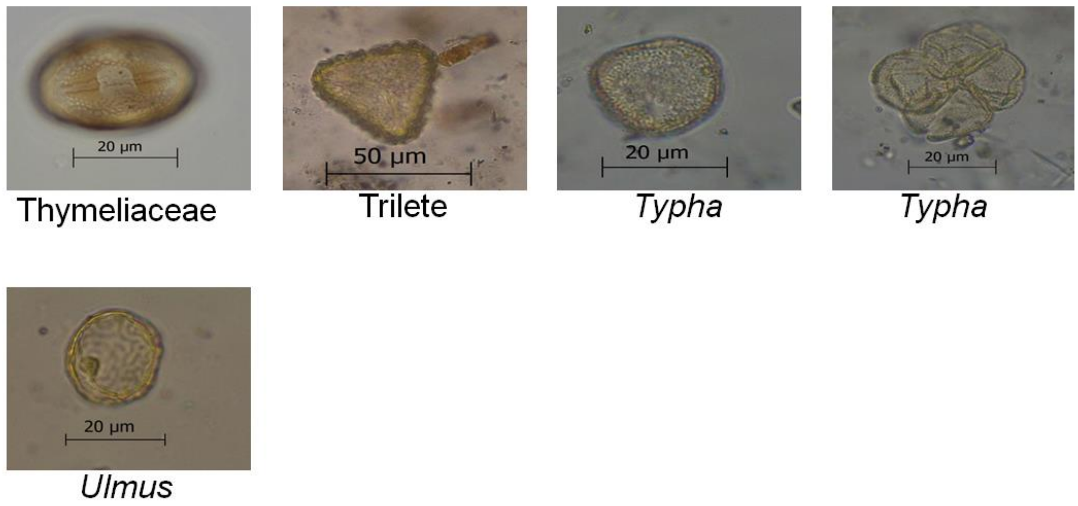

Thymeliaceae Trilete *Typha* *Typha*

Ulmus

Fig. 4 – 9: (cont.)

In PAZ 1-C (3.382 – 3.340 Ma) Poaceae (5.74 – 15.22%) and Cyperaceae (2.27 – 6.32%) decrease to levels similar of PAZ 1-A. Chenopodiaceae (22.68 – 50.12%) and *Ephedra spp.* (1.71 – 13.46%) increase whereas *Artemisia* (9.71 – 43.17%) shows a decreasing trend towards the top. Percentages of Asteraceae (0 – 4.83%), *Nitraria* (0.25 – 2.62%) and Caryophyllaceae (0.50 – 7.14%) are low. Coniferous trees increase slightly to 1.37 – 10.10% whereas broadleaved trees decline to 3.66 – 8.73%.

The PAZ 2-A (3.340 – 3.305 Ma) is characterised by a sharp decrease in Poaceae (1.02 – 3.62%) and Cyperaceae (0 – 0.57%) and a smaller decrease in Chenopodiaceae (21.01 – 40.68%). *Artemisia* (23.54 – 40.25%) shows significantly higher percentages, especially at the beginning of this zone. *Ephedra spp.* (5.11 – 16.79%) and *Nitraria* (1.55– 10.31%) also increase strongly in the bottom part. Asteraceae (2.49 – 5.28%), Caryophyllaceae (0.85 – 3.05%), coniferous trees (2.80 – 9.66%) and broadleaved trees (3.13 – 7.46%) remain unchanged. Most notably is that *Juglans*/*Pterocarya* starts to appear regularly in low abundances.

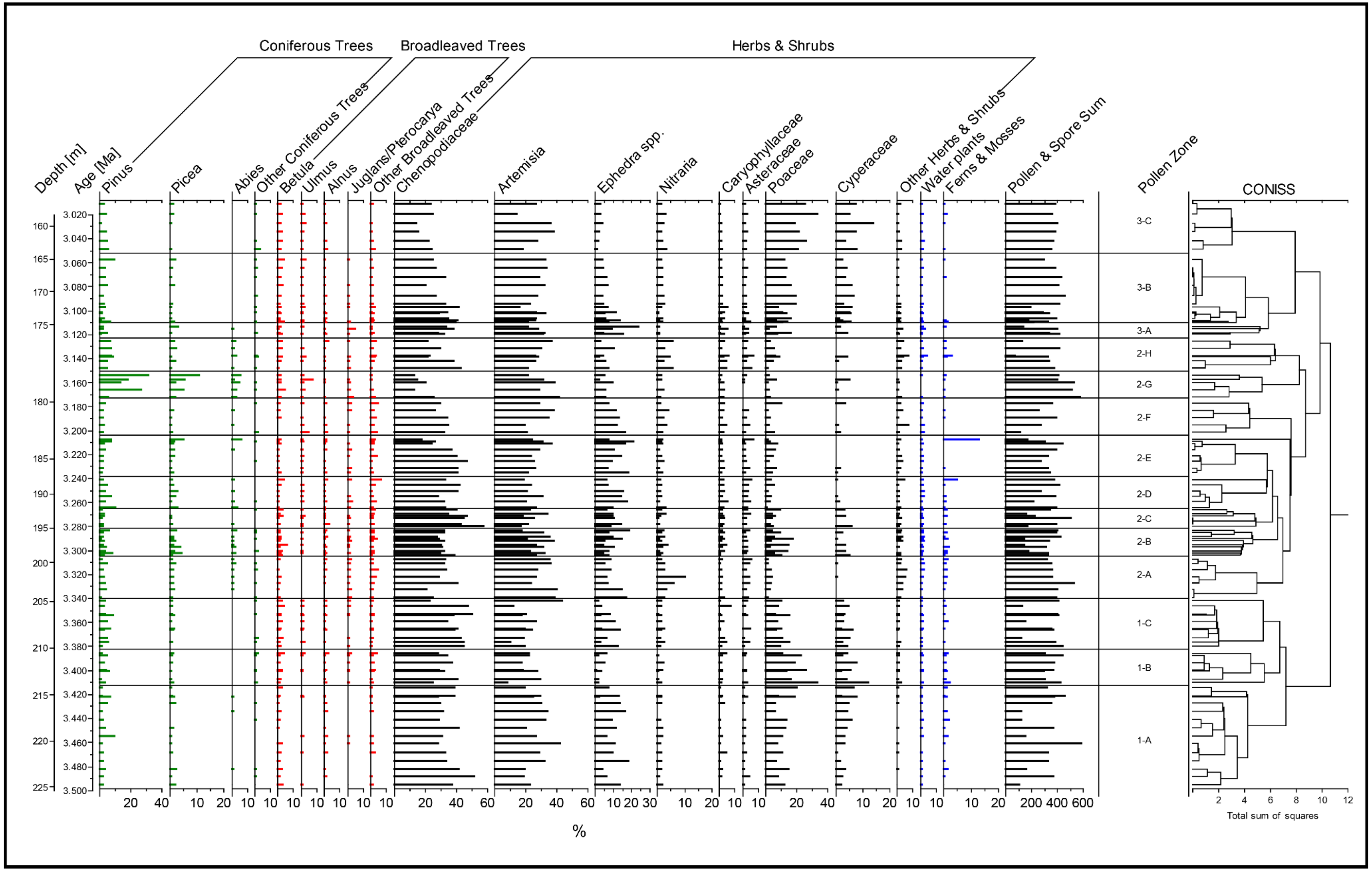

Fig. 4 - 10: Percentage pollen and spore diagram of SG-1b core between 3.5 and 3.0 Ma (main taxa).

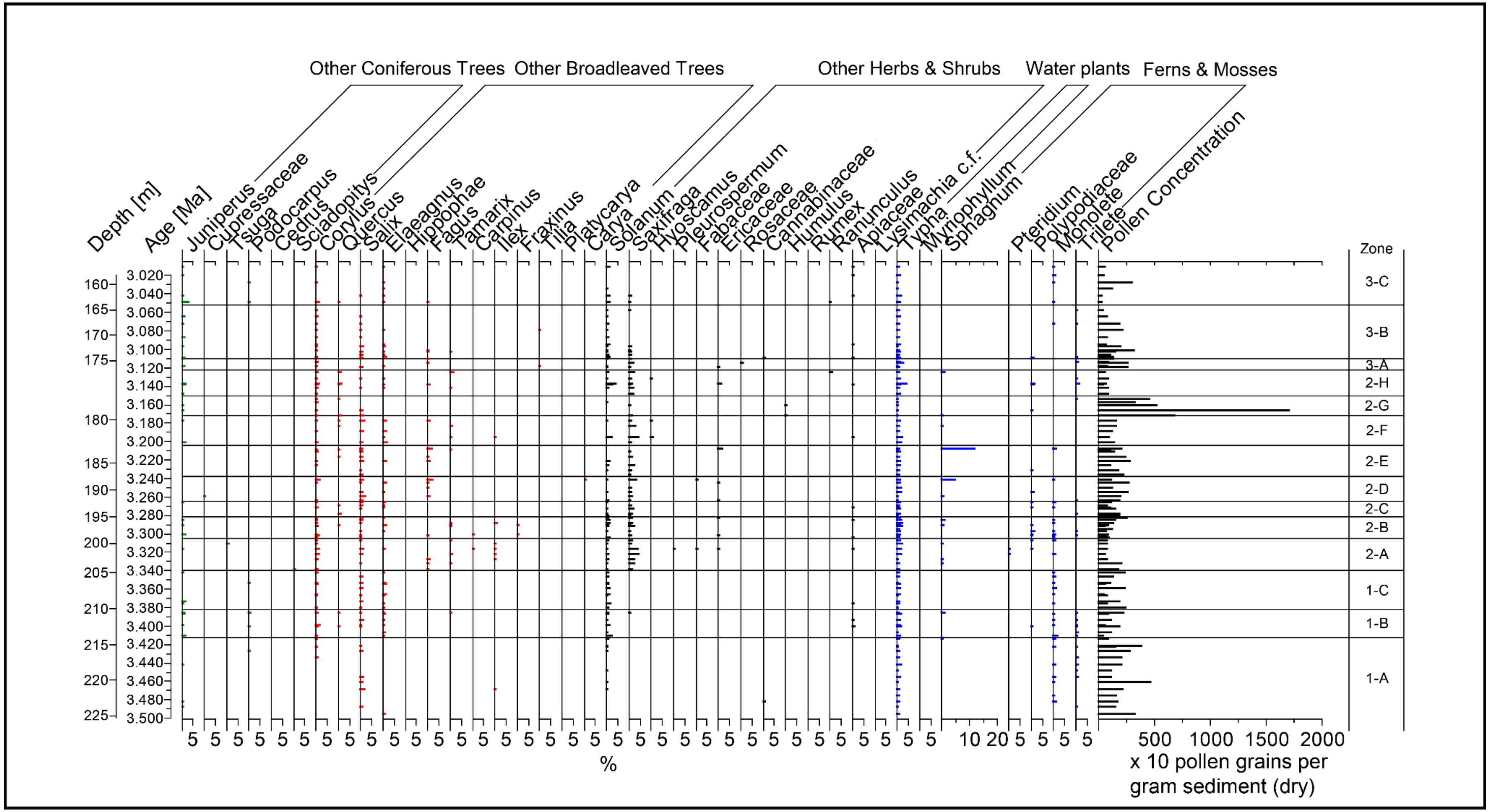

Fig. 4 - 11: Percentage pollen and spore diagram of SG-1b core between 3.5 and 3.0 Ma (all other taxa).

In PAZ 2-B (3.305 – 3.281 Ma), Poaceae (2.88 – 17.27%) and Cyperaceae (0 – 5.26%) are increasing at the expense of *Artemisia* (17.46– 38.25%). Chenopodiaceae (27.59 – 39.01%) and *Ephedra spp.* increase (4.23 – 18.70%) whereas Asteraceae (0 – 4.24%), *Nitraria* (0 – 3.52%) and Caryophyllaceae (0.31 – 4.23%) remain unchanged. Coniferous trees vary between 2.84 – 14.51%. Broadleaved trees remain unchanged (3.41 – 7.75%).

In PAZ 2-C (3.281 – 3.265 Ma), Poaceae (2.56 – 9.36%) and *Artemisia* (16.87–33.95%) decline significantly while Cyperaceae (0 – 6.02%) remains at the same level. Chenopodiaceae (35.19 – 57.83%) is increasing strongly. *Ephedra spp.* remains at a high level (5.85 – 14.10%). Asteraceae (0 – 4.94%), *Nitraria* (0 – 3.09%) and Caryophyllaceae (1.75 – 2.98%) remain unchanged. Coniferous trees (1.81 – 3.33%) are decreasing sharply and also broadleaved trees (0.60 – 7.08%) show lower values.

In PAZ 2-D (3.265 – 3.238 Ma), *Artemisia* (18.83 – 30.37%) continues to decrease whereas Chenopodiaceae (28.27 – 41.93%) shows similar values compared to pollen assemblage zone 2-B. Poaceae (0.77 – 5.54%) and Cyperaceae (0 – 1.38%) drop to a low level. *Ephedra spp.* (5.84 – 17.51%) increases significantly at the onset of this interval but gradually decrease thereafter. *Nitraria* (0.46 – 3.06%), Asteraceae (2.81 – 5.57%) and Caryophyllaceae (1.57 – 5.07%) remain unchanged. Coniferous trees (4.77 – 16.07%) and broadleaved trees (3.31 – 14.32%) expand significantly. The top of this interval features the occurrence of *Sphagnum* in a single sample (4.51%).

Artemisia (21.05 – 36.47%) gradually increased in PAZ 2-E (3.238 – 3.204 Ma) contrary to Chenopodiaceae (17.79 – 47.06%) which showed highest values at the onset of this interval, and then constantly declines. *Ephedra* spp. (6.38 – 21.19%) increases until the top, however, around 3.207 Ma and therefore shortly after the peak value, *Ephedra spp.* decreased abruptly to the lowest value. *Nitraria* (0.51 – 2.21%), Asteraceae (0.99 – 6.75%), Poaceae (1.23 – 7.11%), Cyperaceae (0 – 1.52%) and Caryophyllaceae (1.21 – 3.04%) do not change significantly. The coniferous trees range between 2.94 – 18.40%. Their highest value is coinciding with a peak in *Sphagnum* (11.66%) at 3.207 Ma and the lowest value of *Ephedra* spp. The broadleaved trees, on the other hand, decrease to values between 2.21 and 6.13%.

The PAZ 2-F (3.204 – 3.172 Ma) is characterised by high amounts of xerophytic taxa, especially *Artemisia* (19.05 – 37.80%) and Chenopodiaceae (26.38 – 34.80%). Whereas *Artemisia* is increasing gradually after an initial drop, Chenopodiaceae values increase until ~ 3.190 Ma and decrease thereafter. *Ephedra spp.* (7.26 – 16.07%) constantly declines. Other herbaceous taxa that are present in low percentages include Asteraceae (0.28 – 4.40%), *Nitraria* (1.12 – 3.94%) Poaceae (1.18 – 9.78%), Cyperaceae (0 – 3.63 %) and Caryophyllaceae (1.78 – 4.76%). Coniferous trees decrease to a low level (2.80 – 4.72%), whereas broadleaved trees are increasing (3.15 – 10.71%).

The PAZ 2-G (3.172 – 3.150 Ma) is characterised by a sharp increase in coniferous trees (10.03 – 48.28%). Broadleaved trees percentages, on the other hand, remain constant (3.94 – 11.11%). In contrast to Chenopodiaceae, which decreases remarkably (12.92 – 20.15%), *Artemisia* (21.43 – 41.18%) remains at a high level. As a result, the highest A/C ratios are observed during this time period for the whole pollen record. *Ephedra spp.* (2.02 – 9.70%), *Nitraria* (0 – 2.15%), Asteraceae (0.20 – 1.97%), Poaceae (1.14 – 6.82%), Cyperaceae (0 – 5.30%) and Caryophyllaceae (0.25 – 2.94%) show low values.

The PAZ 2-H (3.150 – 3.123 Ma) is marked by a return to high values of Chenopodiaceae (21.36 – 43.01%), which gradually decrease though until the top. In contrast to Chenopodiaceae, *Artemisia* (21.24 – 36.80%) shows the opposite trend and increases from the beginning until the end of this interval. The coniferous trees decline sharply to 6.45 – 11.43%, broadleaved trees only slightly (2.69 – 9.29%). *Ephedra spp.* (2.17 – 9.90%) remains unchanged. *Nitraria* (0 – 5.65%), Asteraceae (1.93 – 7.14%), Poaceae (1.08 – 8.67%) and Caryophyllaceae (0.97 – 5.71%) increase slightly whereas Cyperaceae (0 – 4.33%) remains at a low level.

In PAZ 3-A (3.123 – 3.110 Ma) *Artemisia* (21.37 – 31.95%) and Chenopodiaceae (28.11 – 38.40%) show once again opposite trends with Chenopodiaceae increasing towards the top of this zone. *Ephedra spp.* is abundant (4.44 – 23.66%). Poaceae (2.00 – 15.68%) shows a marked increase. Asteraceae (0.76 – 3.25%), Cyperaceae (0.24 – 4.44%) and Caryophyllaceae (0.59 – 4.99%) do not change significantly, however, *Nitraria* (0 – 0.76%) drops to very low levels. Coniferous (0.73 – 6.21%) and broadleaved trees (3.55 – 6.23%) occur at a low level.

The PAZ 3-B (3.110 – 3.052 Ma) is characterised by strong increase in Poaceae (6.40 – 19.51%) and Cyperaceae (1.28 – 6.65%). *Artemisia* (15.71 – 33.16%) does not change significantly, however, Chenopodiaceae (20.20 – 41.36%) and *Ephedra spp.* (1.53 – 13.37%) decrease gradually. Asteraceae (0.67 – 5.12%) and Caryophyllaceae (0.31 – 5.24%) decrease abruptly to low abundances, whereas *Nitraria* (0 – 2.42%) remains at a low level. Coniferous trees (0.58 – 11.78%) increase slightly as well as *Betula* and *Ulmus*. In contrast, *Juglans*/*Pterocarya* becomes almost absent. Broadleaved trees remain relatively unchanged (3.14 – 8.08%).

In PAZ 3-C (3.052 – 3.011 Ma) Poaceae (18.75 – 33.05%) and Cyperaceae (3.78 – 13.75%) increase further at the expense of *Artemisia* (14.01 – 38.22%), Chenopodiaceae (14.00 – 24.65%) and *Ephedra spp.* (0.85 – 3.75%). *Nitraria* (1.57 – 3.41%), Asteraceae (1.31 – 3.14%) and Caryophyllaceae (0.52 – 1.99%) remain at low values. Coniferous trees (1.25 – 9.38%) decrease slightly. Broadleaved trees remain at their previous level (3.66 – 7.10%).

4.3 Discussion

4.3.1 Palaeolake evolution

4.3.1.1 Sedimentation history

The type and amount of sediments deposited in lakes depends on a multitude of factors, which can be broken down into two large groups: climate and tectonics (Carroll and Bohacs, 1999; Olsen, 1990). Since the Qaidam Basin is an intramontane basin, surrounded by high mountain ranges to the north (Altun Mountains), south/west (Kunlun Mountains) and south/east (Qilian Mountains), both, climate and tectonics are major controlling factors for the deposition of sediments in the SG-1b palaeolake. Climate, i.e. precipitation and temperature, affects the sedimentation process foremost by influencing the lake size through its direct control of the water budget (precipitation + runoff vs evapotranspiration) (Lenters et al., 2005) and the weathering process of rocks leading to either predominantly physically or chemically altered rocks (Lamy et al., 1999; Riebe et al., 2004; Wan et al., 2012; Yang et al., 2004). Climate also has an indirect effect through the development of a vegetation cover, which can limit erosion and transportation of sediments to the lake, and therefore, can lead to lower sedimentation rates (Lancaster and Baas, 1998; Loch, 2000). Tectonics, on the other hand, influences sedimentation processes mainly in two ways: First, uplift of mountainous areas can have an effect on precipitation and runoff (interplay with climate) into the lake area through blocking or diverging the moisture transport (Blisniuk et al., 2005; Hoorn et al., 1995; Liu et al., 2014; Sun et al., 2008). Second, the uplift of areas increases topographical contrast between the lows in the basin and the highs in the mountains, leading to higher erosion rates and thereby, higher sedimentation rates and a coarsening of deposited rocks in the lake (Liu et al., 1996; Sun et al., 2005).

The sediments in the SG-1b core represent different depositional environments. Mudstones are known to be deposited by falling out of suspension (Mángano et al., 1994; Zhang et al., 1998) since their grain size is very small (clay). In order to form mudstones, it is necessary that no coarse material reaches the deposition site (actual SG-1b coring site). Therefore, the hydraulic energy must be rather low (Håkanson and Jansson, 1983; Hilton et al., 1986; Sly, 1978). This is well represented in lakes that are large and at least semi-deep to deep.

Furthermore, the colour of mudstones provides information about the oxidation state of the bottom water, since darker colours represent higher total organic carbon (TOC) and more reducing environments (Piovano et al., 2002; Stockhecke et al., 2014), whereas lighter colours represent environments of higher oxidation at the deposition site. In this study, the greenish, light brownish and dark brownish mudstones are interpreted as sediment deposition in a semi-deep to deep lake which is characterised by variable oxygen depletion in the bottom water (Potter et al., 2005).

Laminated sediments are interpreted to represent a higher lake depth compared to sediments, which either lack lamination or show cross lamination / wavy lamination features. The reason behind this interpretation is the assumption that massive non-laminated sediments require a high sedimentation energy, such as flooding (Potter et al., 2005) or alternatively, lamination of sediments can be prevented by high bottom water oxygen levels that allow bioturbation to occur (Potter et al., 2005). This requires a good ventilation of the lake bottom water, which can vary substantially though from year to year and does not necessarily reach the water-sediment interface (Olsen, 1990; Shimaraev et al., 1993; Weiss et al., 1991). Therefore, laminated sediments are assumed to occur only during times of increased lake depth and lake size. Cross lamination and wavy lamination features occur when sediments are above the wave base which indicates deposition in a relatively shallower lake environment (Adams, 2007; Lu et al., 2015).

The carbonate/sulfate rich mudstones are interpreted separately from the other mudstones since they are not consisting only of the clastic sediment component but they also contain a substantial chemical component. The higher carbonate/sulfate content can be explained either by the occurrence of calcareous organisms (such as gastropods, ostracods, bivalves), deposition of detrital carbonates/sulfates through fluviatile erosion and sedimentation (Pueyo et al., 2011) or authigenic carbonate/sulfate precipitation during intervals of higher lake salinity (Last and Schweyen, 1983; Piovano et al., 2002; Teller and Last, 1990). No calcareous (or silica) organisms were found in the sediments, and thus, this possibility is dismissed. The SG-1b palaeolake area is characterised by a long-term aridification trend which resulted in the formation of evaporite crystals (this study) and layers that became more and more frequent at the top of the SG-1b core (strong increase of aragonite and halite after 3.3 Ma) until the palaeolake desiccated ~ 1.6 Ma ago (Fang et al., 2016; Zhang et al., 2014). Therefore, authigenic carbonate/sulfate precipitation during intervals of high lake salinity is the preferred interpretation for the higher carbonate/sulfate content in the mudstones. This study concludes that the palaeolake size and depth were reduced in order to increase the salinity during the deposition of these carbonate/sulfate rich sediments as has been seen in modern lakes during times where evapotranspiration is much larger than precipitation, runoff and groundwater supply to the lake (Piovano et al., 2002) .

The carbonate/sulfate rich sandy mud– and sandstones are light coloured detrital sediments similar to the carbonate/sulfate rich mudstones. However, in opposition to their pure mudstone equivalents, they are coarser grained and do not show lamination textures. Since the grain size in these sediments is higher compared to the mudstones, the hydrodynamic energy must be high enough (Hilton et al., 1986; Sly, 1978) to support the continued transport of sand sized grains to the coring position (Fig.4 – 12). This can be achieved by either an increase in wind speed (e.g. storm events) or gravitational movements (Dearing, 1997; Håkanson and Jansson, 1983; Nelson, 1982; Sun et al., 2002), or by a depositional environment that is located closer to the edge of the lake (Olsen, 1985). Accompanied are these sandy mud- and sandstones by the occurrence of gypsum crystals, which were found in all four occurring layers of this sediment type. Thus, the depositional environment is also characterised by supersaturation of sulfate minerals (Last and Schweyen, 1983), which leads to the conclusion that this lithofacies represents shallow lake water conditions during which the coring site location was closer to the edge of the lake.

In contrast to the predominantly clastic sediments above, there are two groups of sediments that belong to the evaporite facies (Carroll and Bohacs, 1999). The carbonate/sulfate layers in the record display early stages of evaporation cycles in lakes that are characterised by strong water budget deficit at shallow lake levels (Last and Schweyen, 1983). These endogenic carbonate and sulfate formations (including the precipitation of gypsum crystals) represent hypersaline conditions of the remaining shallow lake. Halite and halite-containing mudstones represent an even more extreme shallowing of the palaeolake, since the precipitation of halite from a water body happens only at very high salinities (Tab. 4 – 3) (Schreiber and Tabakh, 2000).

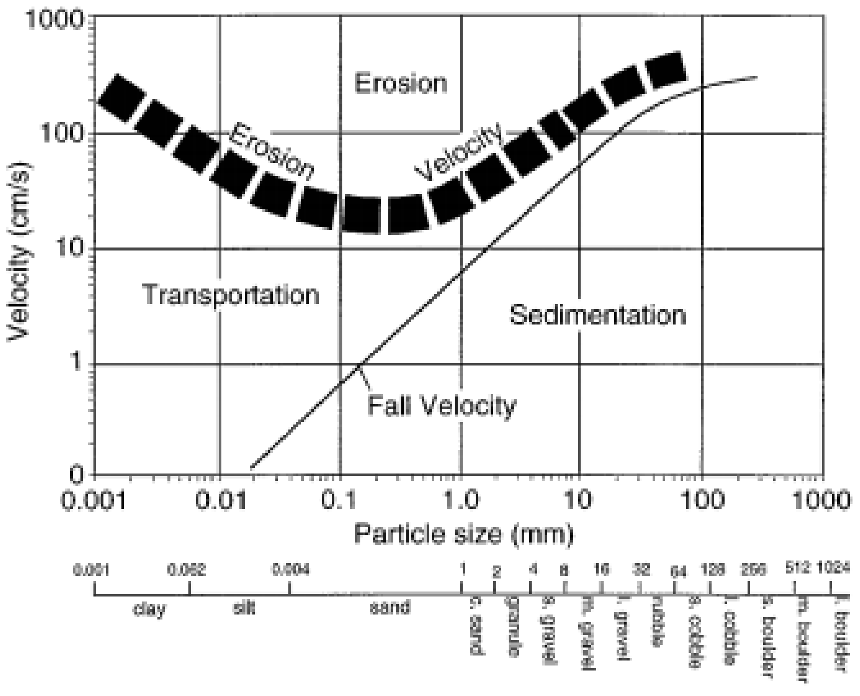

Fig. 4 - 12: Hjulström Diagram illustrating the relationship between the velocity (energy) in a transport system with grain size of a particle (taken from Crowe and Sharp Jr., 1997). The diagram shows that a higher transport energy is necessary to keep sand particles in motion compared to clay particles, which form mudstones.

The interpretation of the SG-1b lithofacies is in good agreement with the reconstruction of the nearby SG-1 palaeolake from Wang et al. (2012). Wang et al. (2012) concluded that the SG-1 palaeolake (2.8 – 0.1 Ma) shallowed from a semi-deep fresh to semi-deep brackish lake (40-120 m deep), that was characterised by dark laminated mudstones, to a playa saline lake and mudflats (< 0.5 m deep), that were characterised by thick halite beds, halite and gypsum crystals and massive brownish-yellowish silt- and mudstones. In contrast to the SG-1 palaeolake, sediment deposition of the SG-1b core interval (3.5 – 3.0 Ma) was not characterised by metre-thick halite beds or sediments that were accumulated during desiccation periods of the palaeolake. Therefore, this study concludes that the SG-1b palaeolake was at least a few meter deep during the driest periods. In this study, variation of the lake depths/size (deep/shallow and large/small) is assessed by comparing the predominant lithofacies. The dark-coloured mudstones represent time intervals of increased lake size and lake depth, whereas the carbonate/sulfate rich mudstones, sandy mud- and sandstones and evaporite layers represent time intervals of decreased lake size and lake depths.

Tab. 4 - 3: Observed salnities for precipitation of salts across Mediterranean sites, taken from (Schreiber and Tabakh, 2000). Note that the “Organic Matter” sediment feature includes predominantly carbonates with organic matter and/or finely laminated gypsum.

Sediment feature	**Salinity (g/l)**
Carbonates	36 – 80
Organic Matter (predominantly carbonates)	80 – 140
Gypsum	140 – 300/325
Halite	300/325 - 350

Based on the changes in lithofacies, the SG-1b core interval has been divided into five units (Fig.4 – 13): In Unit I (3.495 to 3.345 Ma), the palaeolake can be characterised as highly fluctuating between shallow and semi-deep lake conditions. Mudstones are the major sediment being deposited, even though they are rich in carbonate/sulfates indicating a high level of precipitation from the water body. Furthermore, this unit is characterised by numerous evaporite (halite, carbonates, sulfates) or evaporite-containing layers (halite interspersed with mudstones) and gypsum crystals are frequently embedded in the sediment matrix. These salt layers were formed during dry conditions in a shallow lake. However, since also mudstones occur in thick layers, the palaeolake must have undergone drastic fluctuations in lake level.

In Unit II a (3.345 to 3.294 Ma), the palaeolake was consistently deeper compared to Unit I, as indicated by the mudstone sequence. Only a small evaporite layer occurs in the middle of this unit, whereas gypsum crystals are completely absent. The limited deposition of evaporites indicates wet conditions and a semi-deep lake. Since most mudstones show cross lamination, the palaeolake can be described as semi-deep above the wave base.

In Unit II b (3.294 to 3.265 Ma), the palaolake returned to the frequent changes in lake size from Unit I as is displayed by the changes from mudstones to evaporite layers. Although this unit is not as thick as Unit I, similar palaeoconditions can be assumed because of the similarity of sediment deposition.

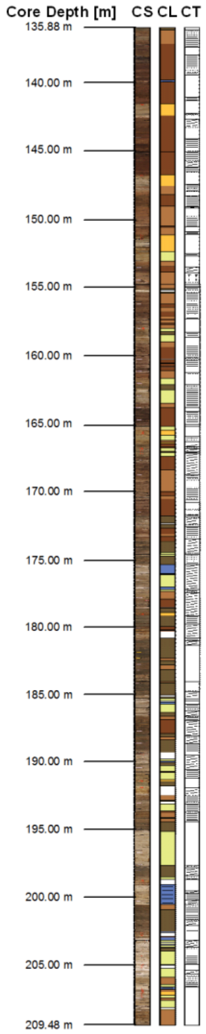

Unit	Description	Palaeolimnological interpretation
3.008 Ma **Unit III** 3.101 Ma	• Mudstones dominating lithology • Three large intervals of sandstones/sandy mudstones occur within this unit • Gypsum crystals present (associated with the occurrence of the coarser grained material) • Mudstones mainly dominated by parallel lamination • Occurrences of turbidites, crosslaminated sediments and structureless sediments (mostly related to coarser sediments)	• Base of Unit characterised by gradual shallowing trend • Deposition of mudstones during semi-deep lake conditions • Three thick sandstone/sandy mudstone layers indicate evens of strong lake shrinkage / increased hydrodynamic conditions • After onset of sandy layers, palaeolake conditions were shallow allowing gypsum crystals to grow within these thick sand layers
Unit II c 3.265 Ma	• Silica rich mdstones dominating throughout the unit (carbonate/sulfate rich mudstones occur in three smaller intervals) • Gypsum crystals present in the middle part of the unit and in one layer closer to the top of the unit • Thick carbonate/sulfate layer close to the top of the unit • Texture of the sediments is mainly dominated by parallel lamination (some wavy or cross laminated sediments present)	• Palaeolake was deep and large as suggested by the almost exclusively silica rich mudstones • During the three small intervals of carbonate/sulfate rich mudstones the palaeolake was slightly shallower and can be described as semi-deep
Unit II b 3.294 Ma	• Mudstones alternating with evaporites • Re-occurrence of thick evaporite layers (similar to Unit I) • Gypsum crystals present in the lower part of the unit • Sediments are dominated by crosslamination	• Frequent changes in palaeolake size and depth occur as characterised by changes of mudstone to evaporite deposition • Palaeolake conditions similar to Unit I
Unit II a 3.345 Ma	• Silica rich mudstones dominating lithology • Evaporites and carbonate/sulfate rich mudstones almost absent • No gypsum crystals present in sediments • Crosslaminated and structureless sediments alternate with parallel laminated sediments	• Palaeolake consistently deeper and larger compared to Unit I because of strong dominance from mudstones • Absence of gypsum and only 1 small evaporite layer suggest wet conditions
Unit I 3.497 Ma	• Mudstones alternating with evaporites (halite, gypsum, carbonates) • Mudstones dominated by carbonate/sulfate rich fraction • Gypsum crystals occur frequently sediment matrix • Crosslamination and structureless sediments dominate over parallel lamination	• highly fluctuating palaeolake size and depth characterised by alternating sedimentation of mudstones and evaporite layers • salt layers are formed during dry conditions in a shallow lake • (mainly carbonate/sulfate rich) mudstones occur point to semi-deep conditions

Lithology

mudstones	carbonate/ sulfate-rich mudstones	carbonate/ sulfate-rich sandy mud- and sandstones	carbonates and sulfates	halite	mudstones interspersed with halites	gypsum crystals
🟫 🟫 🟫	🟨	🟧	☐	🟦	☰	G

Texture

no/weak lamination, thick bed	parallel lamination	crosslamination, wavy lamination, disturbance	turbidite
☐	☰	▨	T

Fig. 4 - 13: Lithological overview and palaeolimnological interpretation of the SG-1b core. Core Scan (CS), Core Lithology (CL) and Core Texture (CT) are used to characterise the sediments and establish lithological units (I: 3.497 – 3.345 Ma, II a: 3.345 – 3.294 Ma, II b: 3.294 – 3.265 Ma, II c: 3.265 – 3.101 Ma, III: 3.101 – 3.008 Ma). A summary of the palaeolimnological implications is given in the figure, for more detailed information see text.

In Unit II c (3.265 to 3.101 Ma), the palaeolake can be described as semi-deep and large. The sediments are almost exclusively silica-rich mudstones. The texture shows a transition from pre-dominantly cross laminated mudstones in the lower part of the unit to almost parallel laminated mudstones and partly carbonate/sulfate rich mudstones in the upper part of the unit. Cross- or wavy laminations represent phases during which the palaeolake was above the wave base whereas the parallel laminated mudstones represent phases during which deposition took place below the wave base. Gypsum crystals are present in two intervals in this unit. Whereas the upper occurrence is confined to a single small layer, the lower occurrence (165.00 – 167.00 m) is much thicker. Most likely is that during the formation of these gypsum crystals the palaeolake reached its lowest lake level for this unit.

In Unit III (3.101 to 3.008 Ma), the palaeolake is characterised by parallel laminated mudstones for most of the interval, however, three thick sandy mudstone/sandstone layers interrupt these sediments. Sandy mud- and sandstones did previously only occur in three very small layers in the SG-1b record. Gypsum crystals accompany these sandy layers. These layers represent time intervals of strong shallowing and lake-size reduction. In addition, the base of this unit also shows a gradual shallowing trend from parallel laminated mudstones to a sequence of turbidites, which was followed by cross laminated mudstones and carbonate/sulfate rich mudstones before transitioning into the first thick sandy layer. The sediments in this unit suggest that the palaeolake was fluctuating between semi-deep and large and shallow and small conditions.

Lu et al. (2015) argue that an observed increase in mean grain size associated with a weakened sorting of grain sizes and a change in the growth strata dip angle shows that the Jianshan Anticline was uplifted strongly between 3.6 Ma until 3.3 Ma (Fig. 4 – 14). As a consequence, the depositional environment changed from a deep to semi-deep lake to a shallow lake environment (Lu et al., 2015). The high frequency of evaporite layers occurring in Unit I confirms the interpretation of a shallow lake environment from Lu et al. (2015). Lu et al. (2015) do not discuss a return to deeper palaeolake conditions after 3.3 Ma (probably due to their long-term scope of palaeolake changes) but rather argue that the palaeolake continued to be characterised as a shallow lake. However, the mean grain size and sorting proxy in the study from Lu et al. (2015) show that the palaeolake deepened between 3.330 and 3.116 Ma. This study suggests that sustained deepening of the palaeolake took place after 3.265 Ma (Unit II c). After 3.116 Ma (~ Unit III), both mean grain size and MSD increase until ~ 3.030 – 3.000 Ma during which the three thick sandy layers that include gypsum crystals indicate lake shrinking and shallowing. Thus, the lithofacies analysis in this study seems to be in good agreement with the proxy data from Lu et al. (2015).

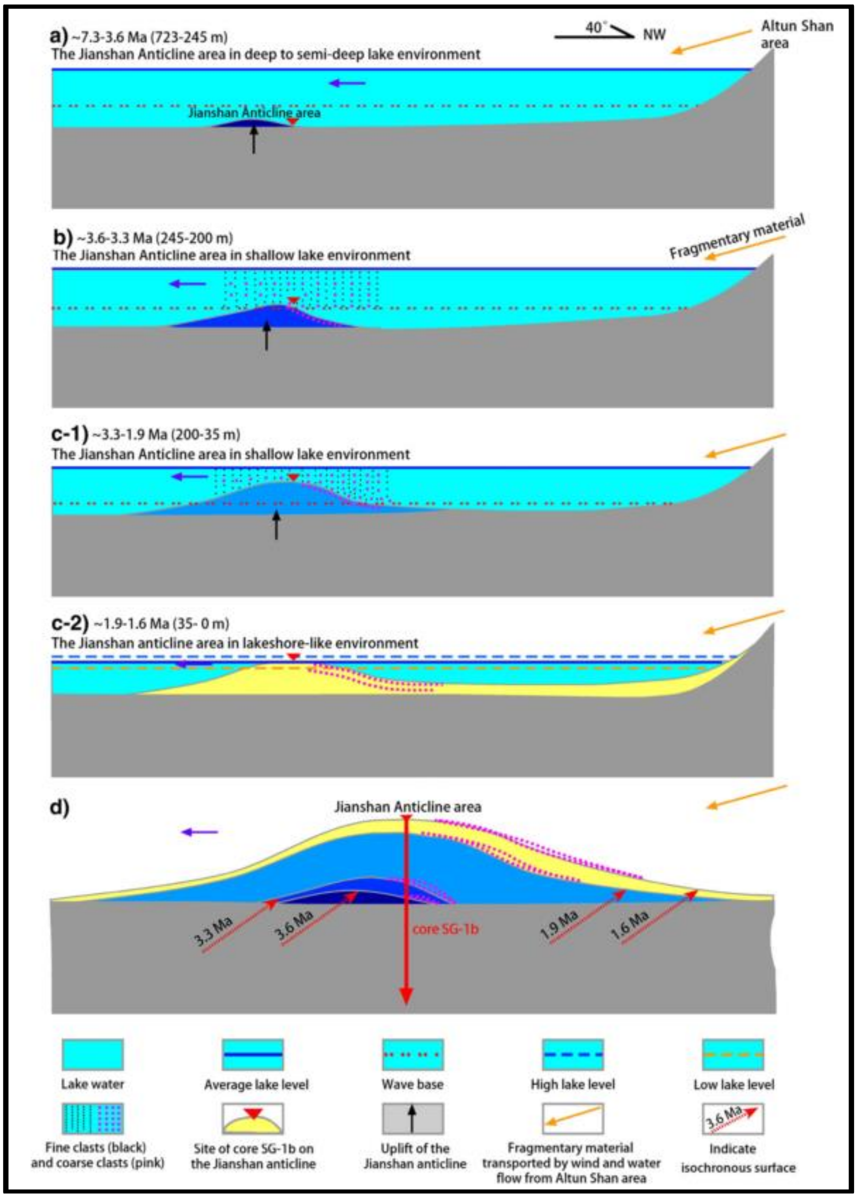

Fig. 4 - 14: Development of the Jianshan Anticline based on the evaluation of growth strata dip angles, mean grain size and sorting (Lu et al., 2015).

Based on the magnetostratigraphy from Zhang et al. (2014), the sedimentation rates for the interval of the SG-1b core are:
3.032 – 2.581 Ma: 16.85 cm / ka
3.116 – 3.032 Ma: 18.15 cm / ka
3.207 – 3.116 Ma: 7.03 cm / ka
3.330 – 3.207 Ma: 17.26 cm / ka
3.596 – 3.330 Ma: 12.88 cm / ka

Three groups can be distinguished: high sedimentation rates (3.032 – 2.581 Ma, 3.116 – 3.032 Ma, 3.330 – 3.207 Ma), medium sedimentation rates (3.596 – 3.330 Ma) and low sedimentation rates (3.207 – 3.116 Ma). In addition to Lu et al. (2015), Zhang et al. (2014) concluded that three phases of tectonic uplift took place in the SG-1b core at > 7.3 – 6.03 Ma, 5.24 – 4.18 Ma and 3.60 – 2.58 Ma based on high sedimentation rates (Fig. 4 – 15). Both studies suggest a phase of tectonic uplift starting at 3.6 Ma, which Zhang et al. (2014) connects with sedimentation of conglomerates in the eastern Qaidam Basin (Zhang, 2006) and around the Tibetan Plateau (Song et al., 2005a), and changes of growth strata in the eastern Qaidam Basin (Fang et al., 2007) that shall indicate a change in depocenter in the Qaidam Basin. Although Lu et al. (2015) mentioned the possibility of climatic changes responsible for the palaeolake variability leading to a drop in lake level and lake size around 3.6 to 3.3 Ma, this possibility was not explored further and only tectonic uplift was considered as a major driving force. The lithofacies analysis in this study shows, that after 3.3 Ma (especially after 3.265 Ma, Unit II c) a return to finely laminated mudstones occurred, which indicates deeper lake level sediment deposition compared to the frequently occurring evaporites in Unit I. It is apparent that the lowest sedimentation rate in the time interval from 3.5 to 3.0 Ma comprises most of the Unit II c, which is almost exclusively made up of mudstones. Blais and Kalff (1995) and Håkanson (1982) argue that the lake morphometry, especially slope gradient, lake area and lake depth, have a great influence on the deep water sediment deposition through re-distribution processes such as turbidite currents. Since the interpretation of the lithofacies suggested that the palaeolake was deepest and widest, a larger distance to the lake edge could have led to a reduced sedimentation rate (Xu et al., 2010a). Furthermore, the lower authigenic carbonate/sulfate precipitation from the water column in Unit II c could have had an influence on the sedimentation rate, since different sediment fluxes (e.g. detrital, authigenic inorganic carbonates, biogenic carbonates, biogenic silica) have varying magnitudes of sediment accumulation in different sinks (Honjo, 1982; McManus et al., 1998; Mingram et al., 2004; Xu et al., 2010a).

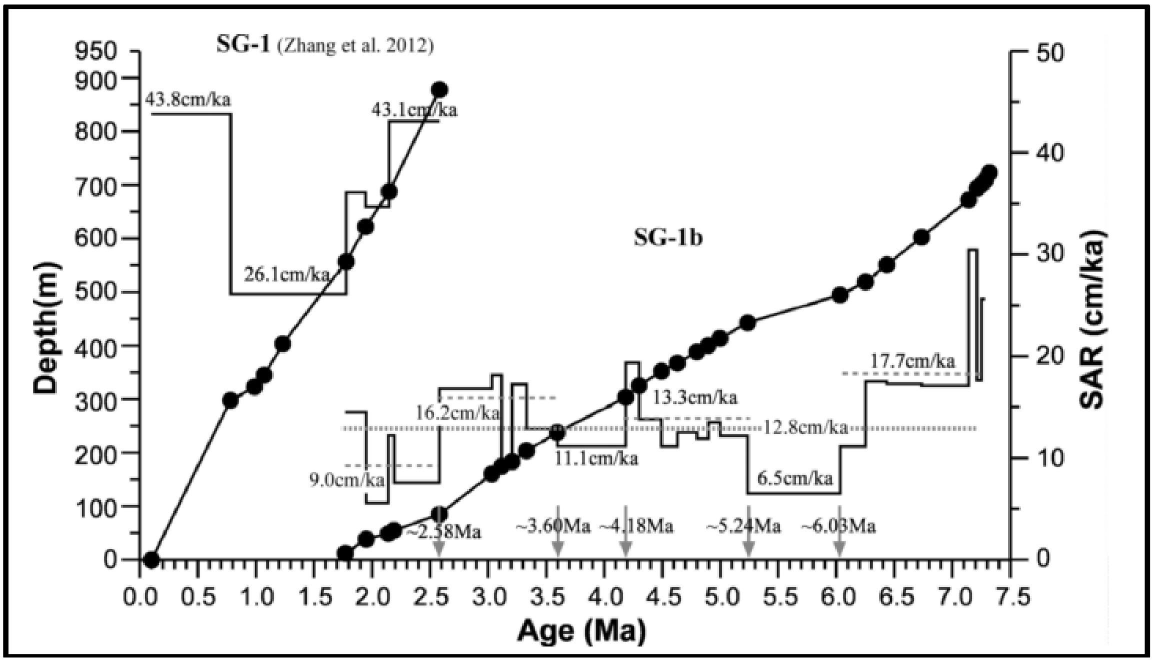

Fig. 4 - 15: Sedimentation rates from the SG-1 core (Zhang et al., 2012a) and the SG-1b core (Zhang et al., 2014), taken from Zhang et al. (2014). Zhang et al. (2014) identified three intervals of possibly tectonic uplift of the Jianshan Anticline (>7.3 – 6.03 Ma, 5.24 – 4.18 Ma, 3.60 – 2.58 Ma.

4.3.1.2 Geochemical analyses

Origin of elements

Based on the correlation matrix and PCA of the XRF core scanning data, the elements of the first elemental group (Al, Si, K, Ti, Fe, Rb, Y, Zr, Mn, Mg) are interpreted as detrital input / terrigenous origin. Generally, Si can record multiple signals: As part of all silicate minerals, Si can be a typical proxy for detrital input, however, Si is also a constituent part of shells from certain biogen sources, such as diatoms, which can lead to unit/facies dependent explanations of the controlling mechanism for Si in the sediment record (Johnson et al., 2011; Kylander et al., 2011). Thus, precaution must be taken when interpreting the Si signal in lakes. However, in the Late Pliocene section of the SG-1b core, Si and the other detrital elements show very similar trends and ratios throughout the whole record (Si/Ti ratio), indicating either constant input of Si from a biogenic source or a neglectable role/influence of biogenic Si. Since bioproductivity often varies through time (Johnson et al., 2011), it seems unlikely that biogenic input is constant in this record over such a long time. Thus, no biogenic Si is occurring in this part of the SG-1b core. In contrast to Si, Al, Zr, Rb and Ti are conservative, lithogenic element with no connection to biogen sources or diagenetic alteration effects (Boës et al., 2011). In this study, Ti has been selected to represent detrital input.

Contrary to group 1 elements, Sr, Sc, and S have high loadings on PCA Axis 1. Although Sr and especially Sc are elements that are mostly associated with terrigenous sediments (Moreno et al., 2010; Shotyk et al., 2001), in this record a different underlying forcing is responsible for the distribution of these elements. Ca, Sr and S are strongly related to the crystallisation of carbonates and sulfates from an oversatured water body (Cohen, 2003) leading to the frequently occurring gypsum crystals, carbonates and sulfate beds and carbonate rich mudstones (Kylander et al., 2011). According to X-ray diffraction analysis of carbonate minerals in the SG-1b core (Fang et al., 2016), abundant phases besides calcite are aragonite, dolomite and ankerite. Furthermore, gypsum is present in the core, especially between 7.3 and 6.6 Ma, 3.3 and 2.9 Ma, and close to the top of the SG-1b core (1.6 Ma). The Sr-modification of gypsum, celesite, is also present in the core. Carbonates and sulfate precipitations from the lake are important indicators of oversaturated waters that can represent lower lake levels. Oversaturation necessary to produce aragonite and gypsum are roughly 2x and 5x salinity of modern sea water, respectively (Fang et al., 2016; Warren, 1989). Aragonite has been used in modern study sites to reconstruct low lake/sea levels (Bookman et al., 2004; Garber and Friedman, 1983; Machlus et al., 2000). The carbonate analysis of the SG-1b core (Fang et al., 2016) show that round 3.3 Ma, calcite significantly decreases whereas aragonite increases. This is especially apparent in the aragonite peaks that are very high (Fang et al., 2016), which could indicate strong fluctuations in lake level between 3.3 and 1.6 Ma. Sr is incorporated preferentially into aragonite over calcite due to the different crystal lattice and the Sr atomic radius (Füllenbach et al., 2015). Consequently, the Sr/Ca will be used here in this study to identify periods with increased salinity that will be interpreted as low lake levels. Previous studies already showed that Sr/Ca ratios in carbonates show a strong positive correlation to salinity (Chang et al., 2004; Dissard et al., 2010). In contrast to Sr, Sc and S, Ca cannot be clearly allocated to group 2 elements. Ca is an element that can be attributed to multiple different sources of sediment deposition, primarily as carbonates. According to Kelts and Hsü (1978) and Dean and Fouch (1983), Ca can enter the sediment matrix either as allochtonously delivered element from clastic input, authigenic carbonate formation due to exceeding of solubility, biogenic carbonate formation (shells/skeletons of lacustrine organisms) or diagenetic/ post-depositional changes resulting in the formation of Ca-carbonates. Therefore, this study proposes that Ca in the SG-1b core is not solely driven by evaporite formation, i.e. carbonate and sulfate precipitation during dry periods, but is also deposited along with detrital elements during times, which are characterised by high detrital input, possibly as weathered carbonates from the lake surroundings in the catchment area (Fang et al., 2016). Cl also has high positive loadings on PCA Axis 1 (but negative loadings on PCA Axis 2). Cl is representing halite formation which occurs when salinity reaches ~ 12x modern seawater values (Fang et al., 2016). Consequently, the Cl/Ti ratio is used to distinguish between halite-bearing and halite-absent sediment deposition, which is providing further support for high salinity, low lake level periods of the palaeolake (along with the Sr/Ca ratio). Thus, PCA Axis 1 is interpreted as increased deposition of evaporites.

To interpret PCA Axis 2, a more detailed look into group 1 elements is essential. The detrital elements plot in mainly two groups. Al, Si, Ti and K are very closely aligned to each other, which suggests that they occur together in dominant mineral phases. Al and Si are the two main constituents of aluminosilicates which make up most of the clay minerals, such as kaolinite ($Al_2Si_2O_5(OH)_4$), illite ($(K, H_3O)(Al, Mg, Fe)_2(Si, Al)_4O_{10}$), chlorite ($(Mg, Fe)_3(Si, Al)_4O_{10}$) or smectite ($(Na, Ca)_{0.33}(Al, Mg)_2(Si_4O_{10})(OH)_2 \times n\ H_2O$). Clay mineral assemblage analysis using XRD (Fang et al., 2016) showed that illite (20 – 70%) is most dominant clay mineral in the SG-1b core followed by chlorite (4 – 20%), smectite (0 – 10%) and kaolinite (4 – 8%). When comparing the general chemical composition of the clay minerals, it becomes apparent that Al, Si, K, Fe and Mg can be explained by the dominant clay mineral illite. This leaves Ti, Mn, Rb, Y and Zr. All of these elements could also be included in the illite structure by substituting other elements

(Schimpf et al., 2011). Ti, Mn, Rb and Y are often related to small grain sizes, whereas Zr is often found in coarser silt and sand grain sizes (Jin et al., 2006; Liu et al., 2002b; McLennan et al., 1993). Since K can also be present in smaller grain sizes (Cuven et al., 2010), it is difficult to explain PCA Axis 2 with a grain size gradient. However, Rb, Y and Zr are also known to be immobile lithogenic elements that can resist higher levels of weathering (Schimpf et al., 2011). There against, alkali elements, such as Na, K or Ca are mobilised easier through water interactions (Chang et al., 2013; Chen et al., 1999; Jin et al., 2006). Additionally, carbonates are also more easily weathered under intense chemical weathering. Therefore, in this study, PCA Axis 2 is interpreted to represent chemical weathering intensity. When alloachtonous carbonates are present, Ca, Fe, Mg and Mn can also be explained by secondary alteration of these carbonates in the lake, e.g. through hydrothermal fluids. Ankerite ($Ca(Fe, Mg, Mn)(CO_3)_2)$) and dolomite ($(Ca, Mg)(CO_3)_2$) have been reported to be present in the whole SG-1b core (Fang et al., 2016). This would explain why Mn and Mg are so similar in our record. Mg can form carbonates under reducing conditions as has been shown in shallow-lake hypersaline and anoxic lagoon sediments in Brazil (Vasconcelos & McKenzie, 1997). Mn can also form carbonates under reducing conditions, however, requires a high pH value (Glasby & Schulz, 1999; Rincon-Tomas et al, 2016). This does not affect our interpretation of PCA Axis 2 though.

The position of Sc in the PCA diagram suggests that Sc is associated with evaporite minerals. As a conservative lithogenic element (Shotyk et al., 2001; Weiss et al., 1999) Sc behaves even more resistant to weathering than Al (Dias & Prudencio, 2007). However, not only does Sc not show any correlations with other typical lithogenic elements or group 1 elements in general, but it is also correlated to Ca. Douglas et al. (2015) found a strong relationship between Sc and Ca in Proterozoic stromatolites when biologically mediated calcite precipitation in shallow water took place. The authors found no explanation for the Ca-Sc relationship though.

It seems likely that a different process other than simple detrital input controlled the Sc deposition in the sediment record. Holmes & Zoller (1996) reported that Sc alongside with Al and other trace elements is part of Asian dust storms over the North Pacific with highest concentrations between December and May. Furthermore, Sc is being used to distinguish dust source areas in China (Xiao et al, 1997; Wang et al, 2009; Ferrat et al, 2012), making it an important constituent of eolian transport. Since the dust transport in China is directly linked to the EAWM (An et al, 1990), Sc is interpreted as a proxy for dust transport/aridity in the SG-1b record. Because no concentration measurements have been concluded (especially rare earth elements), provenance analysis can not be conducted. The Qaidam Basin itself though is regarded as a source area for dust transport to the CLP (Zhang et al, 2003; Pullen et al, 2011), and therefore, it seems likely that the Qaidam Basin itself could be the source area for dust transport recorded in the SG-1b core. To support this theory, the Sc/Ti record will also be compared to Zr/Rb record which is being used as an indicator for the strength of the EAWM on the CLP (Chen et al., 2006; Liu et al., 2002b). To assess potential differences in grain size, in this study the Zr/Ti ratio is used as a proxy as Zr is occurring in coarse grained sediments, whereas Ti rather substitutes for other elements in clay minerals, and thus higher Zr/Ti ratios should belong to periods of coarser sediment deposition in the SG-1b core.

Interpretation of XRF Facies Analysis

In Tab.4 – 4, a summary is shown for each XRF facies determined by the cluster analysis. ln (Si/Al) has been chosen over ln (Si/Ti) to determine if possible biogenic silica is present in order to rule out grain size effects. The results show that the ln (Si/Al) ratio does not change with the XRF facies, and therefore, the presence of biogenic silica has been ruled out.

In XRF facies 4, halite deposition is the dominant process, whereas in XRF facies 3 the combination of high carbonates and high ln (Sr/Ca) indicates that precipitation of carbonates (especially aragonite) and sulfates (gypsum, celesite) dominated this facies. In contrast, XRF facies 1, 2, 5 and 6 are characterised by lower than average salinities. According to our grain size proxy (ln (Zr/Ti)), the coarsest sediments were deposited in XRF facies 3 and 4. The two winter monsoon proxies show that XRF facies 3 and 4 (and possibly XRF facies 2) were dominated by higher sediment input from eolian sources whereas XRF facies 1, 5 and 6 received less sediment input via eolian transport.

Tab. 4 - 4: Enrichment/depletion of proxy indicators for each cluster. The black numbers indicate higher values of the proxy indicators (enrichment) and the red numbers indicate lower values of the proxy indicators (depletion), respectively. A good agreement of proxy indicator shows that the clusters 3 and 4 are characterised by higher salinity, grain size and possibly stronger winter monsoon, which suggest a drier environment compared to clusters 1, 2, 5 and 6 resulting in lower lake size and depth. Contrary, the clusters 1, 2, 5 and 6 are characterised by wetter environmental conditions (lower lake salinity, smaller grain size, weaker winter monsoon).

Proxy	Bio-Silica	Salinity	Salinity	Grain Size	Winter Monsoon	Winter Monsoon
Cluster	ln (Si/Al)	ln (Sr/Ca)	ln (Cl/Ti)	ln (Zr/Ti)	ln (Sc/Ti)	ln (Zr/Rb)
1	-0.20	-2.55	-24.01	-34.74	-10.25	-5.47
2	-0.23	-6.80	-18.05	-15.04	6.39	-8.06
3	2.00	10.97	1.99	92.63	31.60	41.38
4	-0.81	43.53	88.86	302.72	12.12	20.91
5	-0.68	-10.18	-31.02	-46.57	-22.94	-9.66
6	1.11	-27.55	-19.16	-48.24	-3.97	-13.65

The analysis of these proxies show a good agreement that the XRF facies 3 and 4 were dominated by sediments indicative of higher salinity, higher grain size and pronounced increase in winter monsoon strength. This can be explained by a lower lake level during colder and drier periods. A reduction of precipitation at the SG-1b site led to a reduction of fluviatile transported terrigenous material into the palaeolake which shifted the balance between precipitation and runoff on the one side and evaporation of the palaeolake on the other side towards periods of higher evaporation. During the course of these dry periods, carbonate, sulfate and halite compounds precipitated from the oversatured palaeolake due to a decrease in lake size. Besides, a decrease in lake size can also explain grain size coarsening. Since the distance between the actual coring site (close to former palaeolake center) and the palaeo shoreline became smaller, the deposition of coarser grained material further into the lake centre was easier. The winter monsoon proxies show that eolian transported sediments during colder periods were highest in XRF facies 3 and 4 which further supports that precipitation and lake size were smallest in these facies. Therefore, the palaeolake is characterised by lowest lake levels (size) in XRF facies 3 and 4 and highest lake levels with high detrital input from fluviatile sources in XRF facies 1, 5 and 6. XRF facies 2 seems to be an intermediate state, which is characterised by higher carbonate deposition which features lower ln (Sr/Ca) and ln (Zr/Ti) values. So, it remains unknown whether sediment deposition was dominated by detrital input or evaporation.

In Fig. 4 – 16, the record of the XRF facies analysis is shown. The record can be divided into several parts:

Between 3.496 and 3.442 Ma, the SG-1b palaolake was characterised by elevated levels of salinity which resulted in the formation of evaporites in shallow waters. The high grain size during this interval suggests that the coring site was located closer to the edge of the palaeolake. The winter monsoon proxies suggests that this time interval featured cold and arid winds. Between 3.442 and 3.429 Ma, the palaeolake underwent a short transgressive period which is characterised by higher input of terrigeneous sediment, a lower salinity, a smaller mean grain size and a weakened winter monsoon. The grain size measurements in the SG-1b core from Lu et al. (2015) show that after 3.43 – 3.42 Ma the grain size increased steeply until ~ 3.3 Ma.

Following 3.429 Ma (until 3.360 Ma), the XRF facies record is characterised by strong increase of the salinity and grain size proxy which indicates that the palaeolake was very shallow and small. The lithology record of Unit I supports this view since mudstones transitioned to halite and halite-bearing mudstones at the onset of this time interval which were subsequently replaced by carbonates and sulfates and carbonate/sulfate rich mudstones. In the grain size study of the SG-1b record from Lu et al. (2015), the increase in grain size and weakened sorting of particles peak at around 3.3 Ma. In contrast, this study shows that the very dry period leading to palaeolake shallowing and shrinkage was completed by 3.360 Ma. From 3.360 until 3.295 Ma, the XRF facies analysis suggest a return to deep or semi-deep lake conditions since the salinity, grain size and winter monsoon proxies decrease in this interval. In comparison to the sedimentation history, a change in units occurs at 3.345 Ma, when Unit II a replaces Unit I. Unit II is mainly characterised by the dominance of mudstones which led to strong reduction in evaporite layers (and almost absence of gyspum crystals). This is consistent with the suggested wetter environment from the XRF facies analysis. In Fang et al. (2016), strongly fluctuating calcite concentrations were noticed just before 3.3 Ma, however no change in aragonite or gypsum has been noticed. The latter two reflect shallow lake conditions better since calcite content can also be of detrital origin (Fang et al., 2016). Therefore, the reconstructed larger palaeolake depth is confirmed by the mineral composition of the SG-1b core (Fang et al., 2016). From 3.295 to 3.260 Ma, a return to high salinities in the palaeolake characterises lake shallowing at the SG-1b coring site. Furthermore, increased aridity can be inferred from the increase in the grain size proxy indicating a lake size reduction. According to Fang et al. (2016) analysis of mineral compositions, a remarkable change occurs around 3.3 Ma. Before 3.3 Ma, calcite showed large fluctuations between low and high values whereas aragonite was rather low and muted (Fang et al., 2016). After 3.3 Ma, calcite drops to low values and does not show large variations anymore, whereas aragonite started to fluctuate strongly after ca 3.15 Ma (Fang et al., 2016). Since aragonite is a good proxy for salinities/palaeolake depth, repeating fluctuations between deep and shallow palaeolake conditions can be interpreted. Concomittantly with the change in carbonate composition at 3.3 Ma is the occurrence of gypsum for a short interval which suggests that the brine was saline enough for the formation of sulfates (Fang et al., 2016). This is in good agreement with the results of the XRF facies analysis and the sedimentation history. From 3.260 to 3.195 Ma, the XRF facies analysis point to wetter conditions since the salinity, grain size and winter monsoon proxy decline. In comparison to the sedimentation history, at 3.265 Ma Unit II c commences, which is characterised by the long-term dominance of mudstone deposition at the SG-1b coring site that indicate a change from shallow water sedimentation to semi-deep water sedimentation. The change from a dry environment with a shallow lake to a wet environment with a semi-deep lake can also be seen in the continued drop in mean grain size values from Lu et al. (2015) and the end of gypsum precipitation from Fang et al. (2016). After 3.195 Ma, changes in the palaeolake level and size based on the XRF facies analysis become more frequent.

Higher fluctuations of aragonite between 3.2 and 3.1 Ma (Fang et al., 2016) suggest repeated strong trans- and regressions of the lake. Between 3.195 and 3.173 Ma, high salinities, grain size and winter monsoon proxies indicate pronounced shallowing and lake size reduction. The mean grain size increases slightly according to Lu et al. (2015) but is still substantially lower than around 3.3 Ma. From 3.173 to 3.142 Ma, the palaeolake was characterised by wet conditions as the salinity proxy suggests a freshening at the SG-1b coring site. The grain size and winter monsoon proxies also show rather low values implying a relatively larger lake during this time interval. After 3.142 Ma until 3.112 Ma, palaeolake shallowing and shrinkage occurred, which is characterised by the rise in salinities, grain size and winter monsoon proxy. During this time interval, carbonates were deposited indicating a decrease in lake depth. This is in good agreement with the mineral composition record of the SG-1b core from Fang et al. (2016), which show that aragonite starts to fluctuate significantly just before 3.1 Ma. Since aragonite characterises higher salinities (= lower lake levels) compared to calcite (Fang et al., 2016), sustained lower lake levels after the onset of the large aragonite variability could be deduced. Increased aridification around 3.1 Ma has also been suggested by Heermance et al. (2013) in the northern central Qaidam Basin by a change in carbonate $\delta^{18}O$ values in palaeosol samples and the subsequent deposition of thick saline layers. The dominant sedimentation of mudstones in Unit II c suggests semi-deep palaeolake conditions through most of this time interval, however, the XRF facies analysis indicates that fluctuations in the palaeolake level occurred much more frequently. After 3.112 wetter intervals (3.112 – 3.095 Ma, 3.084 – 3.070 Ma, 3.062 – 3.043, 3.033 – 3.014 Ma) with a larger lake size and lake depth alternate with drier intervals (3.095 – 3.084 Ma, 3.070 – 3.062 Ma, 3.043 – 3.033 Ma, 3.014 – 3.006 Ma). The drier intervals are characterised by higher salinites, larger grain size and stronger winter monsoon proxies.

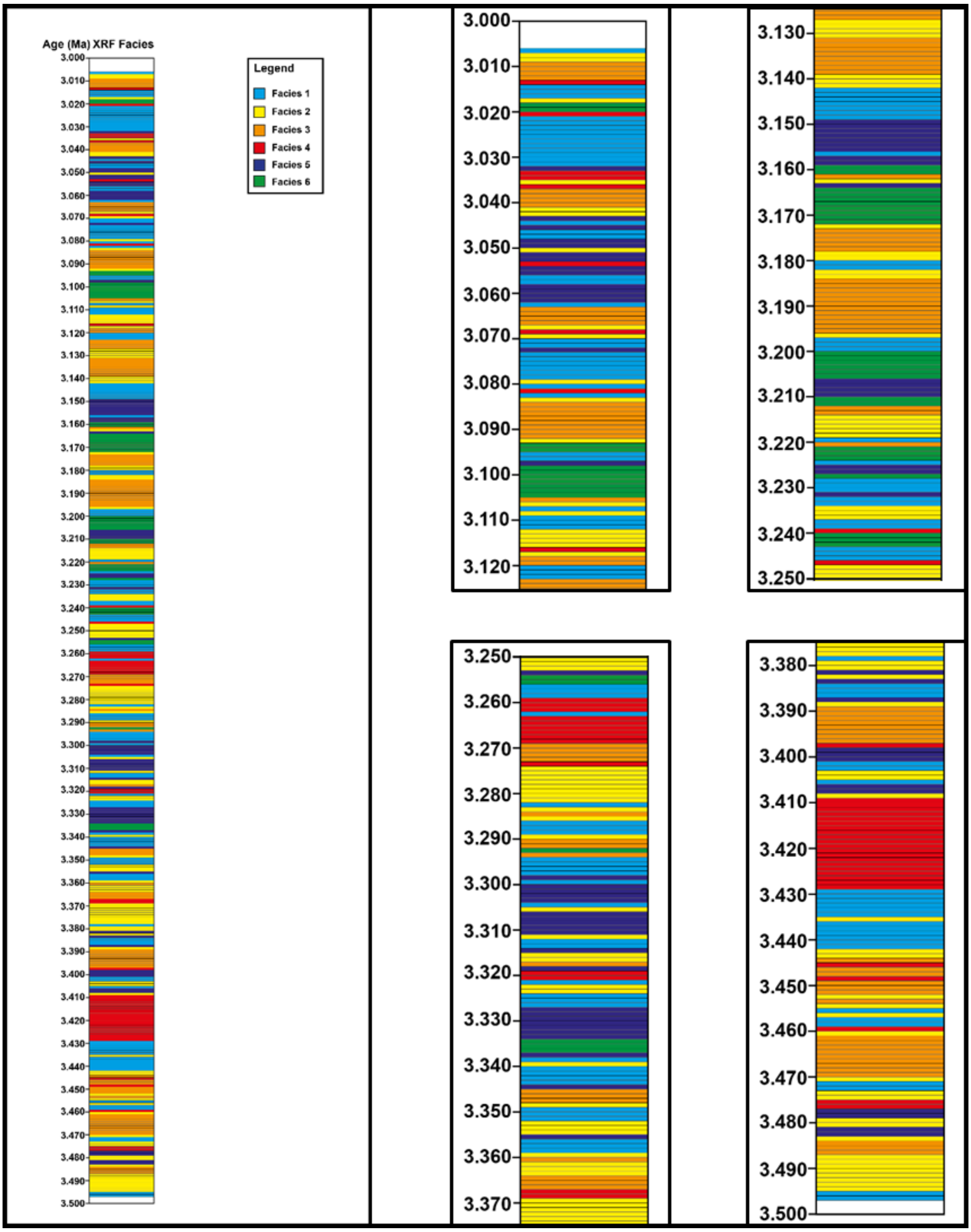

Fig. 4 - 16: Facies analysis of SG-1b core based on the results from the cluster analysis of XRF core scanning data. Assignment of a certain facies was made based on the majority facies comprising the time slice interval. Detailed characterisation of each different facies (1-6) is given in the text. Facies 3 and 4 represent higher evaporative precipitation (halite, carbonate, sulfate) whereas facies 1, 5 and 6 are dominated by detrital input. Facies 2 shows mixed signals.

The sediment sequence from laminated mudstones towards turbidites, carbonate/sulfate rich mudstones and the sandy carbonates/sulfates reflects the drying that commences after 3.101 Ma. Three of the dry intervals after 3.112 Ma are associated with the sandy intervals in which gypsum is present which confirms the results of the XRF facies analysis. The grain size record from Lu et al. (2015) shows an increase of grain sizes from 3.116 Ma to 3.074 Ma and after ~ 3.020 Ma, whereas the grain sizes decrease slightly from 3.074 to ~ 3.020 Ma. Associated with the strong fluctuations in aragonite content after 3.1 Ma are also strong occurrences of gypsum in the mineral composition record until 2.9 Ma (Fang et al., 2016). Therefore, the results of this study are in a very good agreement with the mineral composition and grain size record from Fang et al. (2016) and Lu et al. (2015), respectively, and indicate that frequent and strong reductions in palaeolake size and depth occurred after 3.101 Ma.

Palaeoproductivity

Fig. 4 – 17 shows the C/N record of the SG-1b core together with the Ti record derived from the XRF core scanning. The dominant organic matter source is interpreted using knowledge about the ranges of terrestrial and aquatic plants. The C/N ratios of vascular plants are higher than 20 and can reach up to 500, which is mainly due to the occurrence and high abundance of cellulose and lignin in terrestrial plants (Hedges et al., 1986; Hedges et al., 1997). Aquatic plankton, on the other hand, only has C/N ratios of roughly 3 – 9 (bacteria ca 4, fungi ca 10) because they contain considerably higher proportions in amino acids (Brodie et al., 2011; Hedges et al., 1986; Hedges et al., 1997; Meyers, 1994; Meyers and Ishiwatari, 1995). Therefore, the C/N record of the SG-1b core indicates that mainly aquatic organic matter was deposited in the palaeolake since the C/N ratio rarely exceeds a ratio of 10. The C/N ratios in lake do not reflect organic matter derived from either terrestrial or aquatic source, but rather a mixture of both. The proportions of organic matter sources can vary from lake to lake, e.g. Lake Alexandria, Australia, is composed of 90-95% organic matter derived from aquatic sources whereas the remaining 5-10% are derived from fluviatile input of terrestrial organic matter (Herczeg et al., 2001). In this project, carbon isotopes were not determined, and thus, no end-member modelling was done. However, since C/N values of lake sediments are representing a mixed aquatic – terrestrial signal, any shift towards lower or higher values will be interpreted as relative

changes in the organic matter source. Therefore, a decrease in C/N values represents higher proportions of aquatic organic matter whereas higher C/N values are representative of increased proportion of terrestrial organic matter. Diagenetic processes preferentially forces breakdown of N-containing compounds, such as amino acids, and therefore, the geological C/N signal can deviate from the freshly deposited C/N signal (Meyers, 1994; Meyers and Ishiwatari, 1995; Prahl et al., 1994). Although this means, that the absolute C/N ratio will be shifted towards higher C/N ratios post sedimentation (Meyers and Ishiwatari, 1995), this effect will be negelected here in this study since only relative changes in the C/N ratio of the total organic matter are of interest.

Vogel et al. (2010) and Kaushal and Binford (1999) examined the spatial distribution of C/N ratios in modern lakes, which show that C/N values are highest at areas of river inlets to a lake whereas lower C/N values were recognised at sites with a larger distance to the rivers/shoreline. Falling C/N gradients were also noticed at transects from rivers to outer estuaries which raised the question whether high C/N values can be used to characterise the strength of river discharges (Lamb et al., 2006 and references therein). At Lake Ohrid (North Macedonia/Albania), deposition of organic matter with high C/N values closer to the lake center was accompanied by an increase in coarse silt grain size which led to the conclusion of higher transport energy caused by river inflow at that area (Vogel et al., 2010).

Xu et al. (2006) showed that in Lake Qinghai C/N values are increasing with precipitation. However, the Laguna Potrok Aike (Argentina) record from Haberzettl et al. (2005) shows that C/N values increased during dry periods, which were characterised by low Ti values (XRF core scanning). Thus, increased precipitation can lead to both, higher and lower C/N values. To find out control mechanisms of the C/N signal in this study, the Ti signal from the XRF core scanning has been plotted as a 100 point average against the C/N ratios (Fig 4 - 17). A clear anti-correlation can be seen between these two curves with the exception of two intervals (3.46 – 3.42 Ma and 3.33 – 3.28 Ma). Ti has been interpreted as a group 1 element characterising changes in detrital input and Ti has also been used in past studies as a proxy for increased runoff (Haberzettl et al., 2005; Haug et al., 2003; Hendy et al., 2015; Metcalfe et al., 2010). The good correlation between higher runoff and increased proportion of aquatic biomass in the organic matter in this study is similar to the study of Haberzettl et al. (2005) which concluded that the C/N ratio can be used as a proxy for palaeoshore proximity. The reason why higher runoff led to decreased and not increased C/N values as in the nearby Lake Qinghai (Xu et al., 2006) is difficult to answer. The major difference between Lake Qinghai (Xu et al., 2006) and this study as well as Laguna Potrok Aike (Haberzettl et al., 2005) are the climatic conditions and vegetation densities. Lake Qinghai has a significantly lower evaporation to precipitation (and runoff) ratio (Li et al., 2007; Shen et al., 2005) in contrast to Laguna Potrok Aike (Endlicher, 1993; Haberzettl et al., 2005; Soriano et al., 1983) and the modern Qaidam Basin (and therefore potentially the SG-1b palaeolake) (Herb et al., 2013; Yang et al., 1995). Lake Qinghai is surrounded by alpine meadows, whereas this study shows that the SG-1b palaeolake was surrounded by sparse temperate semi-desert vegetation.

This suggests that in dry environments the positive effects of runoff on total aquatic phytoplankton production in a lake – transport of organic and inorganic nitrogen to the lake (Donald et al., 2011; Levine and Whalen, 2001; Prairie et al., 1989), a large surface area (Fee et al., 1992; Guildford et al., 1994; Staehr et al., 2012), less saline lake conditions beneficial for nitrogen fixing cyanobacteria (Marcarelli et al., 2006) – outpace the increased influx of terrestrial organic matter. Since increased runoff has a positive effect on the lake size and based on the relatively good analogy of study sites between Laguna Potrok Aike (Haberzettl et al., 2005) and the SG-1b palaeolake, the C/N ratios will be used as an indicator for palaeolake size variability. Based on the C/N ratio, large lake sizes in the SG-1b occurred around 3.470 Ma, 3.400 Ma, 3.300 Ma, 3.150 Ma, 3.100 Ma and 3.050 Ma. Especially the period between 3.340 to 3.280 Ma seem to have been characterised by a large lake system, since C/N values are consistently at a very low level. Times at which the palaeolake was rather small occurred around 3.495 Ma, 3.425 Ma, 3.350 Ma, 3.270 Ma, 3.185 Ma, 3.120 Ma, 3.08 Ma and 3.010 Ma.

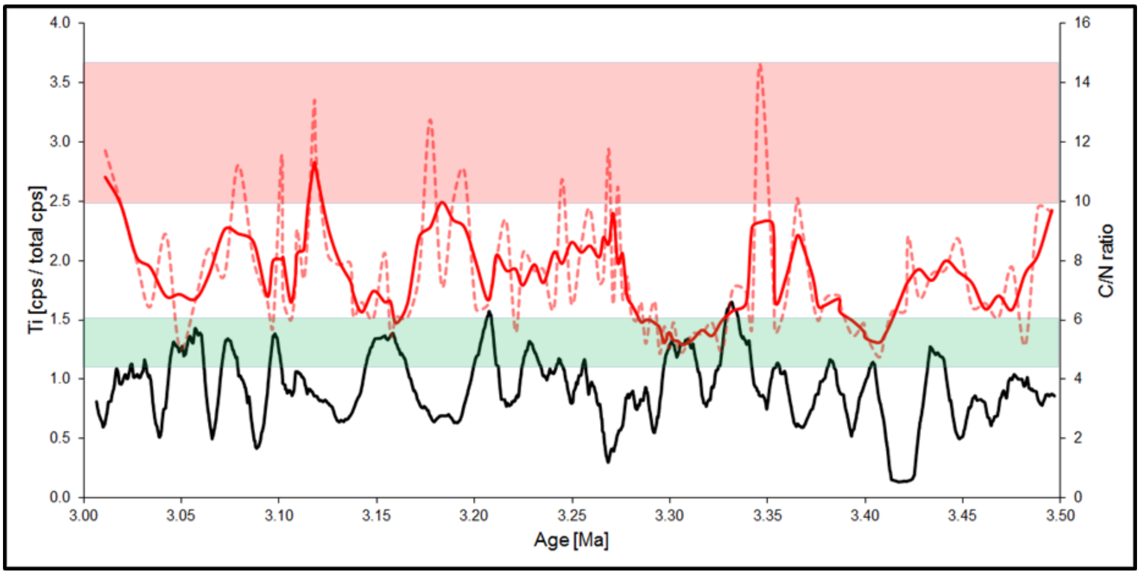

Fig. 4 - 17: Comparison of C/N data (dashed red: original data; solid red: 3pts average) with Ti record (black line: 100 pts average) from XRF analysis showing that the productivity in palaeolake at SG-1b coring location was mainly controlled by runoff/precipitation. A lower band (green) and an upper band (red) indicate repeatedely extreme values in the C/N ratio suggesting maxima and minima in palaeolake size.

4.3.1.3 Synthesis of palaeolake size development

As previously mentioned, proxies were established that are able to characterise varability in palaeolake size. In addition to the XRF facies cluster analysis and C/N ratios, tree pollen data from the pollen analysis will be used to identify changes in lake size. Changes in the lithology are not included in the assessment of palaeolake size changes, since they would not show strong deviations from the XRF facies analysis.

C/N analysis in conjunction with the runoff signal (Ti from XRF core scanning) revealed that the C/N ratio of organic matter in the palaeolake was controlled by precipitation. Because precipitation affects the water budget of the lake and thereby lake size, a relationship between C/N values and lake size can be drawn. Therefore, C/N ratios are indicators of palaeolake size, with higher C/N values representing shorter distances of the SG-1b coring site to the palaeo shoreline, and lower C/N values representing larger distances from the SG-1b coring site to the palaeo shoreline.

Noting that every lake is unique in regard to the proportion of organic matter derived from terrestrial sources and aquatic sources, there is no general rule, which C/N ratio could be applied to distinguish between phases of smaller and larger lake size. Furthermore, the C/N signal in lakes cannot always be applied as a proxy for palaeolake shore proximity (Xu et al., 2006). Fig. 4 – 17 shows the C/N profile of the SG-1b core with a lower band (green) and an upper band (red). These bands show the C/N ranges in which many samples were found that are characteristic for the largest (between 4 and 6) and the smallest lake size (between 10 an 15). A C/N ratio of 8 is average value between the upper limit of the lower band (6) and the lower limit of the upper band (10) and has been chosen as a threshold value to distinguish between a larger lake (< 8) and a smaller lake size (> 8). This threshold value is close to the average C/N value for all samples (7.45) which supports the assumption that the palaeolake transitioned between larger and smaller lake sizes around this level.

The third parameter that is being used to determine lake size changes is the total percentage of tree pollen because the lake size has a considerable effect on the pollen influx. Whereas a small lake size represents pre-dominantly local pollen assemblages (Jacobson and Bradshaw, 1981), a higher lake size enlargens the effective pollen source area and regional/extraregional pollen occurs in higher frequencies. Generally speaking, the likelihood of pollen grains reaching a lake increases with higher pollen production rate and decreases with distance from the lake (Sugita, 1994). Studies about the dispersal of pollen and modelling approaches from Prentice (1988) and Sugita (1994) led to the establishment of the Prentice-Sugita model which calculated the effective pollen source area surrounding lakes that lie in forested areas. According to Sugita (1994), the effective distance within the pollen assemblage of a water body can be explained depending on the size of the water body: A forest hollow with a radius of 2 m can be explained by vegetation within a 50 to 100 m radius, a small lake with a radius of 50 m can be explained by the surrounding vegetation in 300 to 400 m distance and the pollen assemblage in a medium sized lake (250 m radius) can be explained by vegetation from within a 600 to 800 m radius (Sugita, 1994). According to this model, 30 – 45% of the total pollen are coming from within these distances which is enough to reflect the local vegetation composition in the simulated landscape. However, the model requires regions of similar vegetation type and spatial pattern. In contrast, Bradshaw and Webb (1985) and Prentice et al. (1987) defined optimal pollen source areas for varying tree taxa in the tens of km for medium sized lakes to account for 70% of the total pollen count. Although these absolute numbers are very different, which is also caused by different approaches (model vs real data mapping of vegetation), these studies show that the effective pollen source area for lake systems depends on the lake size. The palaeolake of the SG-1b core is located in the Qaidam Basin, which is characterised as an intramontane basin with sparse vegetation. The recorded openess of the Late Pliocene vegetation in this study requires larger pollen source areas compared to Sugita (1994). A reasonable assumption is that pollen grains from within the basin and the surrounding mountains add to the pollen assemblage detected in the SG-1b record. Modern pollen spectra analysis in the Qaidam Basin from Zhao and Herzschuh (2009) revealed that tree pollen content is usually below 5% and mainly from *Pinus*, *Picea*, *Betula*, *Ulmus* and *Juniperus*. The authors relate the tree pollen found in their modern samples to source areas in the high mountains surrounding the Qaidam Basin.

Given the fact that tree pollen in the Pliocene were also originating from surrounding mountainous area (a complete vegetation reconstruction is given in 4.3.2.1), there are generally two mechanisms that could increase the total tree content in the palaeolake. If climate amelioration (especially precipitation) in the source area leads to an expansion of forests or forest patches it is possible that they were expanding towards the basin center and therefore growing at lower elevation sites. Thus, the trees would be growing closer to the palaeolake resulting in an increase in tree taxa detected in the pollen record. The second option is that the palaeolake size increased and, therefore an expansion of the pollen source area occurred covering more sites at which trees were growing. Since their high dispersal, trees (especially coniferous trees) are overrepresented in many basin sites (Cour et al., 1999; Herzschuh, 2007) leading to an increase in total tree pollen content. Since increased precipitation in the mountainous areas most likely causes increased runoff and thereby an increase in palaeolake size, both mechanisms are probably occurring at the same time leading to stronger increase of tree taxa. Thus, the total tree content will be used as a third parameter in order to distinguish between small and large lake sizes.

Zhao and Herzschuh (2009) reported that usually arboreal content was below 5%. In this study, the arboreal content is consistently larger. Especially from 3.5 to 3.3 Ma, the pattern of the trees does not show clear separations between phases of higher and phases of lower arboreal content, but instead appears like background noise. In order to avoid interpreting a higher level of noise as a larger lake size because of the increased arboreal content, the treshold to make a distinction between a small and a large lake size has been set to 15%.

In Fig. 4 – 18, the resulting lake size history of the SG-1b palaeolake is shown. In order to decide whether the palaeolake size was small or large, at least 2 out of the 3 parameter had to show the same signal. For example, between 3.485 and 3.450 Ma, the arboreal content and the XRF facies suggest a small lake size, whereas the C/N ratios point to a larger lake size. Due to the fact that 2 out of the 3 parameter suggest a small lake size, the resulting palaeolake size has been interpreted to be small.

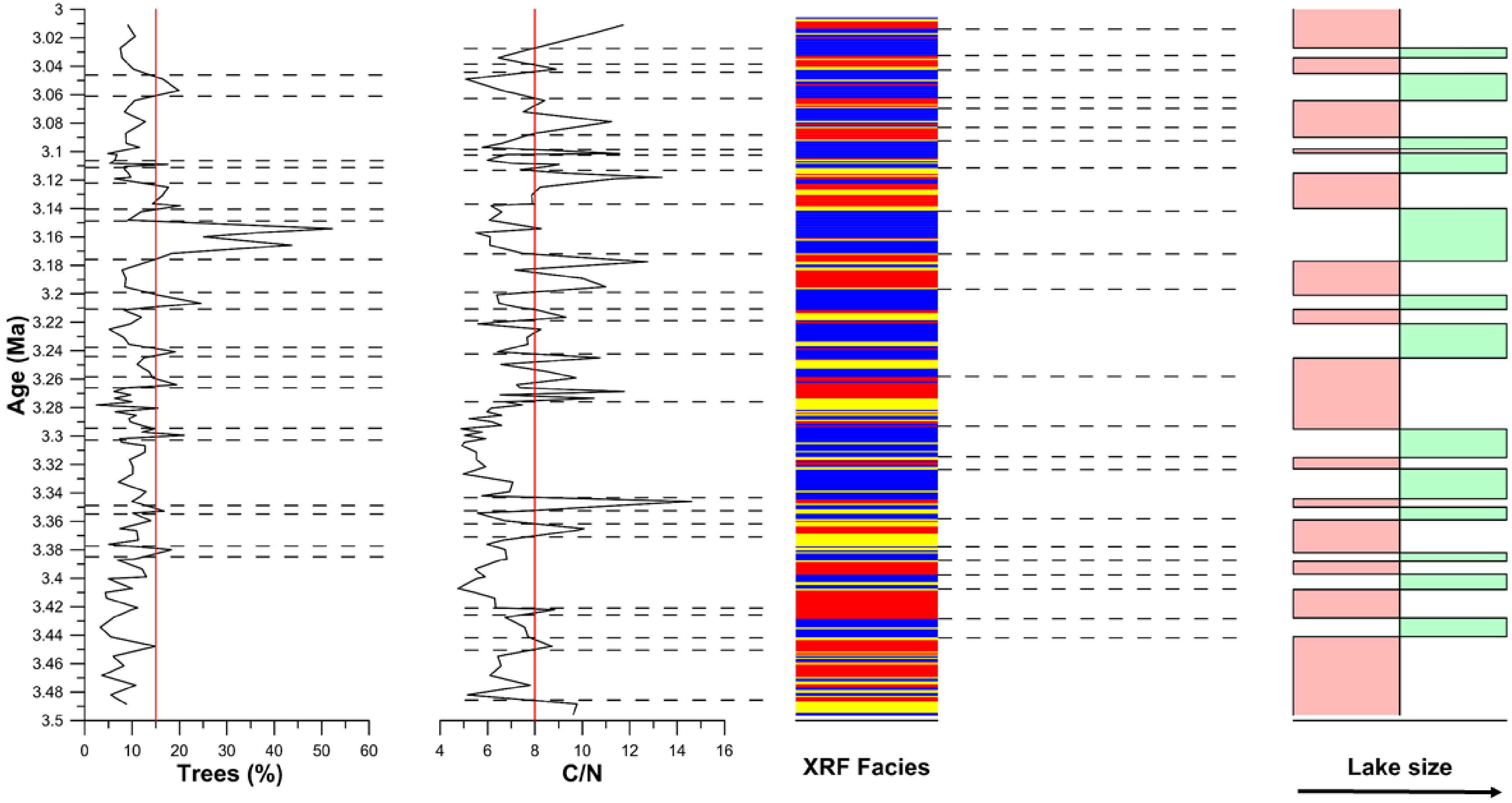

Fig. 4 - 18: Synthesis of palaeolake size evolution of the SG-1b core from 3.5 to 3.0 Ma based on sum of tree%, C/N ratios and XRF facies.

The palaeolake size history can be divided into 9 intervals of alternating small or large lake size:

1. 3.496 – 3.350 Ma: small
2. 3.350 – 3.290 Ma: large
3. 3.290 – 3.240 Ma: small
4. 3.240 – 3.200 Ma: large
5. 3.200 – 3.175 Ma: small
6. 3.175 – 3.137 Ma: large
7. 3.137 – 3.118 Ma: small
8. 3.118 – 3.090 Ma: large
9. 3.090 – 3.006 Ma: small

In Fig. 4 – 19, the multi-proxy reconstructed palaeolake size estimations are compared to the five units from the sedimentation history. For simplification reasons, each lithological unit was interpreted either as a small or large palaeolake size based on the dominant sedimentation feature. The variability in the sedimentation history has been described in detail in the lithology section of this chapter. In general, a good agreement can be seen from the comparison of the lithology based palaeolake size estimations and the multi-proxy reconstruction. However, between ~ 3.265 and ~ 3.101 Ma the multi-proxy reconstruction showed that a larger variability of the SG-1b core existed which has not been seen in the lithological record.

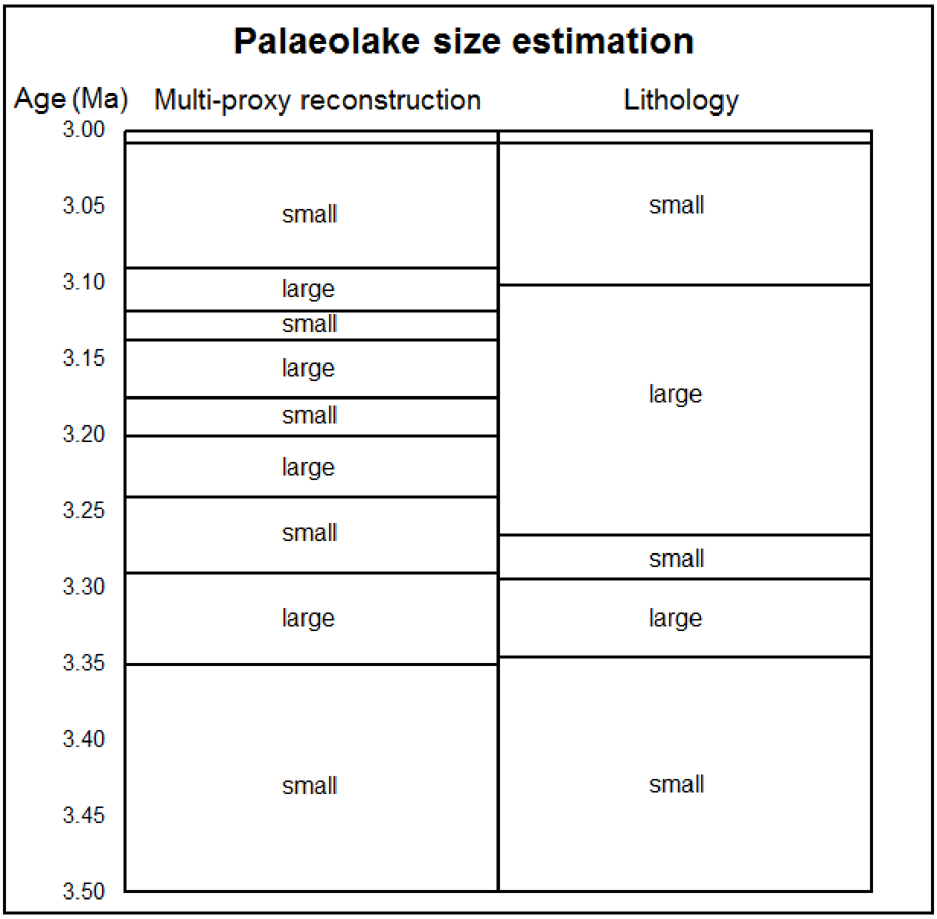

Fig. 4 - 19: Comparison of palaeolake size estimations based on the multi-proxy reconstruction described in the Synthesis of the Palaeolake Size sub-chapter and the estimation based on the different lithological units from the sedimentation history. To simplify, only one status (small / large) has been assigned for each lithological unit, although larger variability has been described in the lithology section.

4.3.2 Palaeovegetation

4.3.2.1 Interpretation of pollen source areas – differentiating the pollen signal

As discussed in the previous section, the palaeolake size has a profound influence on the potential pollen source area (Prentice, 1988; Sugita, 1994). Since the lithology and multi-proxy reconstruction of the palaeolake size (Fig.4 – 18 and 4 – 19) demonstrate that the SG-1b palaeolake underwent strong lake size changes between 3.5 and 3.0 Ma, this variability will be taken into account when interpreting the pollen signal. In Chapter 3.3.4, a characterisation of potential pollen source areas in the Qaidam Basin has been conducted based on modern pollen, vegetation and biome distributions in China, and especially on the

Tibetan Plateau from Ni (2001), Ni and Herzschuh (2011), Cour et al. (1999) and Zhao and Herzschuh (2009).

Mountainous broadleaved and coniferous forest vegetation

In the SG-1b core, two different types of forests can be distinguished based on the tree pollen. Cool- or cold-temperate mixed coniferous and broadleaved forests are composed of *Betula*, *Corylus*, *Quercus*, *Alnus*, *Salix*, *Elaeagnus*, *Ulmus*, *Juniperus* and *Pinus* with warm-temperate or subtropical elements from *Juglans*/*Pterocarya*, *Fagus*, *Fraxinus*, *Tilia* and *Carya*. In Chapter 3.3.4 it was pointed out that long-distance transport of pollen from warm and humid regions to NW China occurs (Cour et al., 1999) which could suggest that also some of the warm-temperate taxa in the SG-1b record were not derived from within the Qaidam Basin.

Pinus, *Picea* and *Abies* represent cold-temperate coniferous forests or montane forests, which were possibly growing at a higher altitude in mountainous areas compared to the cool- or cold-temperate mixed coniferous and broadleaved forests. According to the spatial analysis of *Abies* and *Picea* distribution on the Tibetan Plateau from Lu et al. (2008), abundant *Abies* and *Picea* pollen (> 20 %) are confined to 3000 – 5000 m in the southern part (21 – 32°N), 3000 – 4000 m on the central part (32 - 37°N) and 2000 – 3000 m on the northern part (43 – 49°N). These study areas are in good agreement with the actual presence of coniferous forests comprising *Abies* and *Picea*. Lu et al. (2008) suggest that the appearance of *Abies* and *Picea* pollen (< 10%) in study areas where they are not growing (MAP < 100 mm) is related to very low local pollen production. Between 3.17 and 3.15 Ma, the coniferous tree pollen are significantly elevated compared to any other time interval in the pollen record. Simultaneous to the increase in coniferous tree pollen is a strong increase in pollen concentrations which suggests that Lu et al. (2008) assumption of appearance of *Abies* and *Picea* at sites of low pollen production does not hold up during this time interval. It is possible that coniferous forests were expanding from mountainous areas to the mountain slope and thereby closer to the SG-1b palaeolake.

Regional semi-desert vegetation

Included in the xerophytic shrubs are Chenopodiaceae, *Artemsia*, *Ephedra*, *Nitraria*, Caryophyllaceae and Asteraceae. Xerophytic shrubs are derived from the Qaidam Basin itself where they grow at lower elevations (< 3200 m) and drier conditions in the region around the palaeolake (Zhao and Herzschuh, 2009; Zhao et al., 2007). The xerophytic shrubs represent temperate semi-desert vegetation.

Lakeshore vegetation

In the SG-1b core, the Poaceae and Cyperaceae signal is dominantly derived from grasses growing at the vicinity of the palaeolake. Fig.4 – 20 shows the depth profile of Poaceae and Cyperaceae against the lithology of the SG-1b core. As has been demonstrated previously in the sedimentation history (4.3.1.1), the lowermost parts of the SG-1b core show alternating mudstone and salt sedimentations (Unit I), which then changes into mudstone dominated sedimentation (Unit II a-c) and a phase of mudstone dominated sediments that are intercalated by three thick sandstone layers and associated gypsum crystals (Unit III). Poaceae and Cyperaceae are highest during the deposition of salt precipitates in the bottom part of the core and in the top part when the sandstone layers occur. The link between high grass contents and relatively smaller lake size indicates that Poaceae and Cyperaceae are dominantly derived from the immediate surrounding of the palaeolake. When the lake size decreases, also the pollen source area decreases which effectively increases the amount of locally-derived pollen. In addition to Poaceae and Cyperaceae, *Typha* also belongs to the lakeshore vegetation.

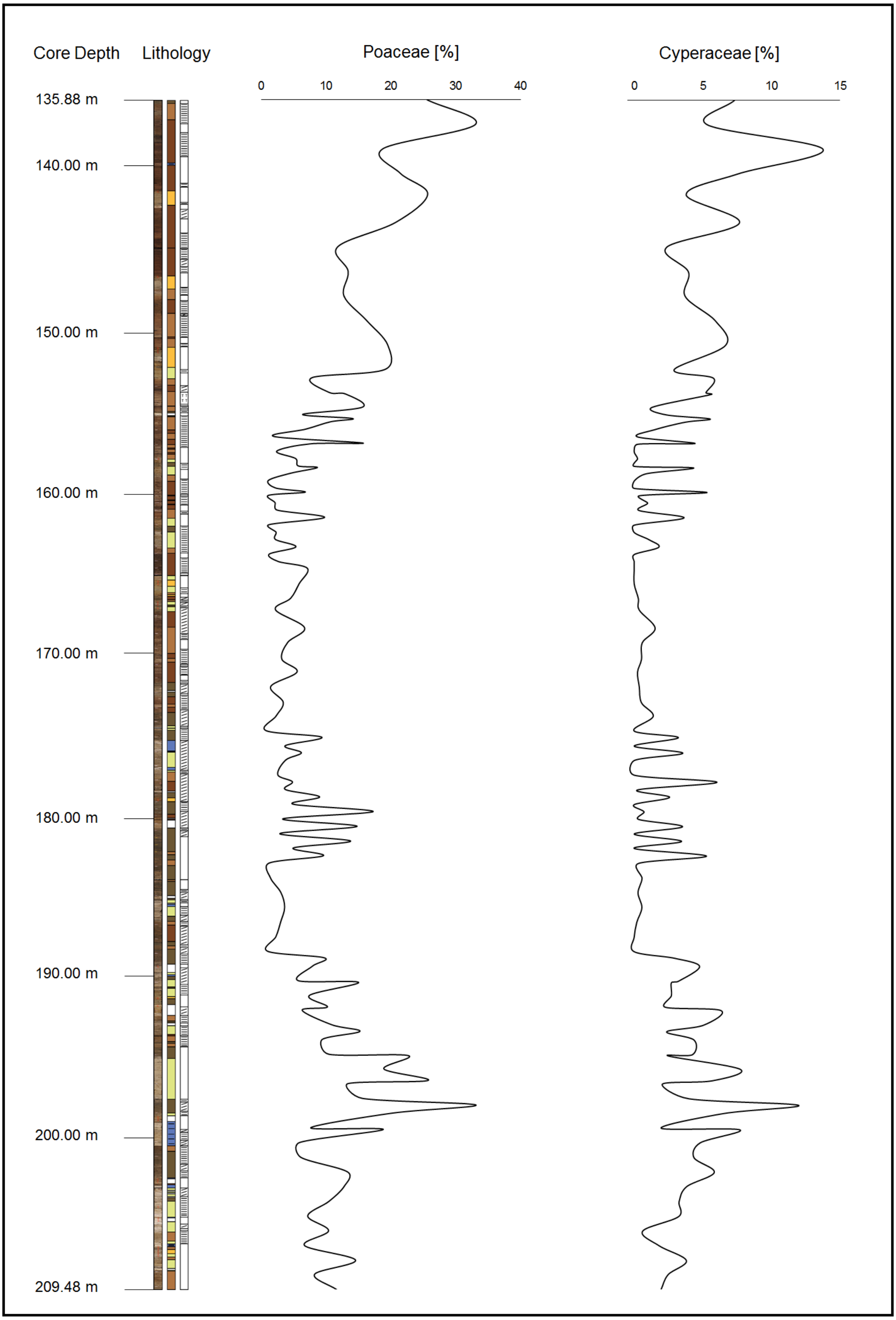

Fig. 4 - 20: Depth profile of Poaceae and Cyperaceae against lithology of the SG-1b core.

Tab. 4 – 5 shows a summary of major pollen taxa found in the SG-1b record and their respective source area and reconstructed biome.

Tab. 4 - 5: Potential source area for various pollen types for the SG-1b core.

Location	**Biome**	**Taxa**
Lake		*Myriophyllum*
Local - lake shore		Poaceae, Cyperaceae, *Typha*
Regional – intrabasin, dry	Temperate semi-desert	Chenopodiaceae, *Ephedra*, *Nitraria*, *Artemisia*, Asteraceae, Caryophyllaceae, Poaceae, *Tamarix*
Regional – mountain slope and mountain	Temperate to alpine semi-desert and alpine tundra	*Artemisia*, Caryophyllaceae, *Saxifraga*, Asteraceae, Ericaceae, Apiaceae, Chenopodiaceae
Regional – mountain slope	Cool- or cold temperate mixed coniferous and broadleaved forests	*Elaeagnus*, *Betula*, *Corylus*, *Alnus*, *Ulmus*, *Salix*, *Juniperus*, *Pinus*, *Quercus*, *Juglans/Pterocarya*, *Fagus*, *Fraxinus*, *Tilia*
Regional – mountain	Cold-temperate or montane forests	*Abies*, *Picea*, *Pinus*

PCA

In Fig. 4 – 21, the PCA diagram of major pollen taxa is shown from the SG-1b core. Based on the PCA diagram different groups can be distinguished:coniferous trees, broadleaved trees, lakeshore grasses and xerophyic shrubs and herbs. Although a coniferous tree, *Juniperus* plots within the group of broadleaved trees, and thus, might have a different pollen source area than the other coniferous trees. The PCA diagram shows a clear separation of Poaceae and Cyperaceae (palaeolake shore vegetation) from all remaining pollen, which come from regional or long-distance source areas. Hence, PCA Axis 1 (33.49 % of variance) indicates changes in palaeolake size. When comparing the remaining pollen taxa a clear distinction can be made between xerophytic shrubs and coniferous trees (excluding *Juniperus*).

Within the group of the xerophytic shrubs, the PCA suggests that different environmental conditions exist between Chenopodiaceae and *Ephedra* spp. on the one hand, and *Artemisia*, Asteraceae, *Nitraria* and Caryophyllaceae on the other hand. Modern pollen assemblages from lakes in the Qaidam Basin show that percentages of Chenopodiaceae and *Ephedra* spp. pollen are higher in very dry areas, whereas *Artemisia* pollen are found in wetter regions. The ratio between *Artemisia* and Chenopodiaceae (A/C) is often used as a moisture or precipitation indicator in semi-arid and arid areas since Artemisia grows favourably under wetter conditions compared to Chenopodiaceae (El-Moslimany, 1990; Zhao et al., 2012). *Artemisia* and Chenopodiaceae are the dominant xerophytic shrub taxa in the pollen record with a combined percentage of generally more than 45 % of the total pollen sum (32.39 – 74.70%). Based on the climate relationship between these two taxa (Zhao et al., 2012), and their significance in this pollen record, PCA Axis 2 (17.06 %) can be interpreted as changes in precipitation with lower PCA Axis 2 values representing drier conditions. The xerophytic shrubs have been split into two groups: xerophytic shrubs I and xerophytic shrubs II and other herbs. Xerophytic shrubs I grow under drier conditions compared to the xerophytic shrubs II. Besides *Artemisia*, also Asteraceae, Caryophyllaceae and *Nitraria* belong to this group. *Nitraria* generally grows at high water tables in semi-deserts (Cour et al., 1999; Zhao et al., 2007), whereas Asteraceae occurs on a large climatic range on the Tibetan Plateau, from semi-deserts to alpine meadow vegetation (Yu et al., 2001; Zhao and Herzschuh, 2009). Caryophyllaceae often occurs in alpine meadows, steps and shrublands together with *Saxifraga* and Asteraceae (Yu et al., 2001). The broadleaved trees have similar PCA Axis 2 values compared to the xerophytic shrubs II and other herbs group. The lowest PCA Axis 2 values belong to the coniferous trees (excl *Juniperus*). The strong contrast between the xerophytic shrubs I and xerophytic shrubs II/other herbs, broadleaved trees and especially coniferous trees supports the assumption that the PCA Axis 2 represents changes in precipitation.

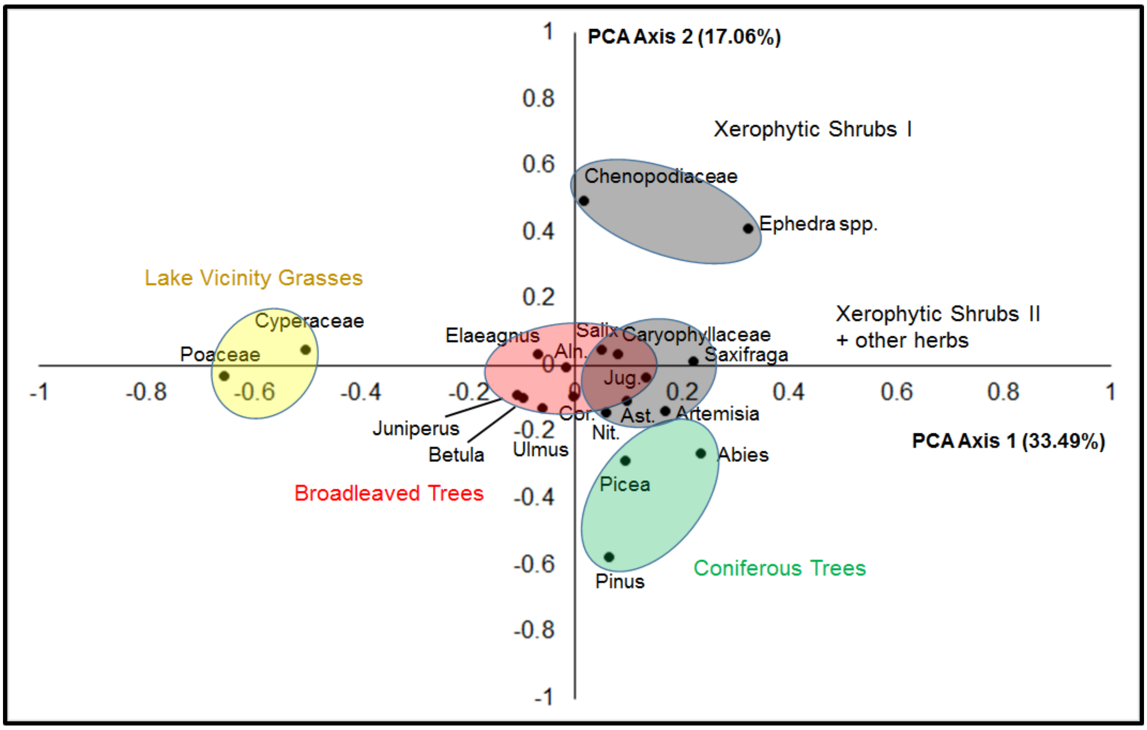

Fig. 4 - 21: PCA of major pollen taxa/families. Aln = *Alnus*, Cor = *Corylus*, Jug = *Juglans/Pterocarya*, Ast = Asteraceae, Nit = *Nitraria*. A distinction between coniferous trees (without *Juniperus*), broadleaved trees (including *Juniperus*), grasses growing at the lakeshore and xerophyic shrubs and herbs can be interpreted from the PCA diagram. PCA Axis 1 explains 33.49% of the total variance and could be the distinction between small (low PCA Axis 1 value) and large lake size (high PCA Axis 1 value). PCA Axis 2 explains 17.06% of the total variance and shows a trend from high values with xerophytic shrubs with taxa surviving driest conditions to xerophytic shrubs and herbs that thrive under wetter conditions (along with broadleaved trees) to coniferous trees with lowest PCA Axis 2 values. This suggests that precipitation is controlling PCA Axis 2.

4.3.2.2 Vegetation history

In Fig. 4 – 22, a conceptual sketch is shown, how the vegetation and palaeolake could have developed from 3.495 to 3.011 Ma. The sketches have in common, that the immediate lakeshore will be covered by *Typha*, Poaceae and Cyperaceae, while the regional vegetation of the NW Qaidam Basin surrounding the palaeolake was covered by xerophytic shrubs in the low lands. At higher elevation, the mountain slopes were still covered by xerophytic shrubs but changes in the compositions are likely due to different climate conditions (colder, wetter). Moreover, broadleaved trees occurred in remote areas on the mountain slopes, which were climatically favourable for their growth. Broadleaved trees are interpreted to have been growing on the mountain slope and not mountain ranges, because they require higher temperatures than coniferous trees.

Coniferous forests were probably growing at the top of the mountains, where precipitation was higher but temperatures lower. The highly arid conditions in the Qaidam Basin and in the surrounding mountains nowadays show that the vegetation was very open at higher elevations. In the following, I will explore further the five major stages of the SG-1b vegetation history.

Vegetation between 3.495 and 3.340 Ma

Between 3.495 and 3.340 Ma the pollen record was strongly dominated by locally produced lakeshore vegetation (Fig. 4 – 23) which supports the results from the sedimentation history and XRF facies analysis that the palaeolake has been rather small and shallow during this interval. The xerophytic shrublands were dominated by Chenopodiaceae, *Artemisia* and *Ephedra. Artemisia* shrubs peaked around 3.46 Ma, after which a they declined gradually leading to a decreasing trend in the A/C values until 3.340 Ma. The decreasing trend of A/C ratios point to an aridification trend of the NW Qaidam Basin, which is accompanied by sparse distribution of forest patches. Climate deterioration peaked around 3.420 – 3.400 Ma after when the lakeshore vegetation was less abundant in the pollen record and forests expanded. The A/C curve indicates a continuation of dry conditions until 3.340 Ma though. A cold and dry interval has also been recorded at three high resolution study sites in the higher latitudes (Andreev et al., 2014; Demske et al., 2002; Panitz et al., 2016).

At Lake El'gygytgyn (NE Siberia), the cool and dry period (from 3.481 Ma) was characterised by a decline in thermophilic taxa and increase in herbs leading to an increased openess of the coniferous forest dominated landscape (Andreev et al., 2014). Interestingly, this cooler and drier interval was interrupted by a warmer period from 3.419 to 3.387 Ma, during which *Picea* and *Abies* replaced herbs such as Poaceae and Cyperaceae (Andreev et al., 2014). At Lake Baikal, moist forests were transitioning into dry forests and open steppes after 3.5 Ma indicated by a decline in *Tsuga* and increase in Ericaceae and *Betula* (Demske et al., 2002).

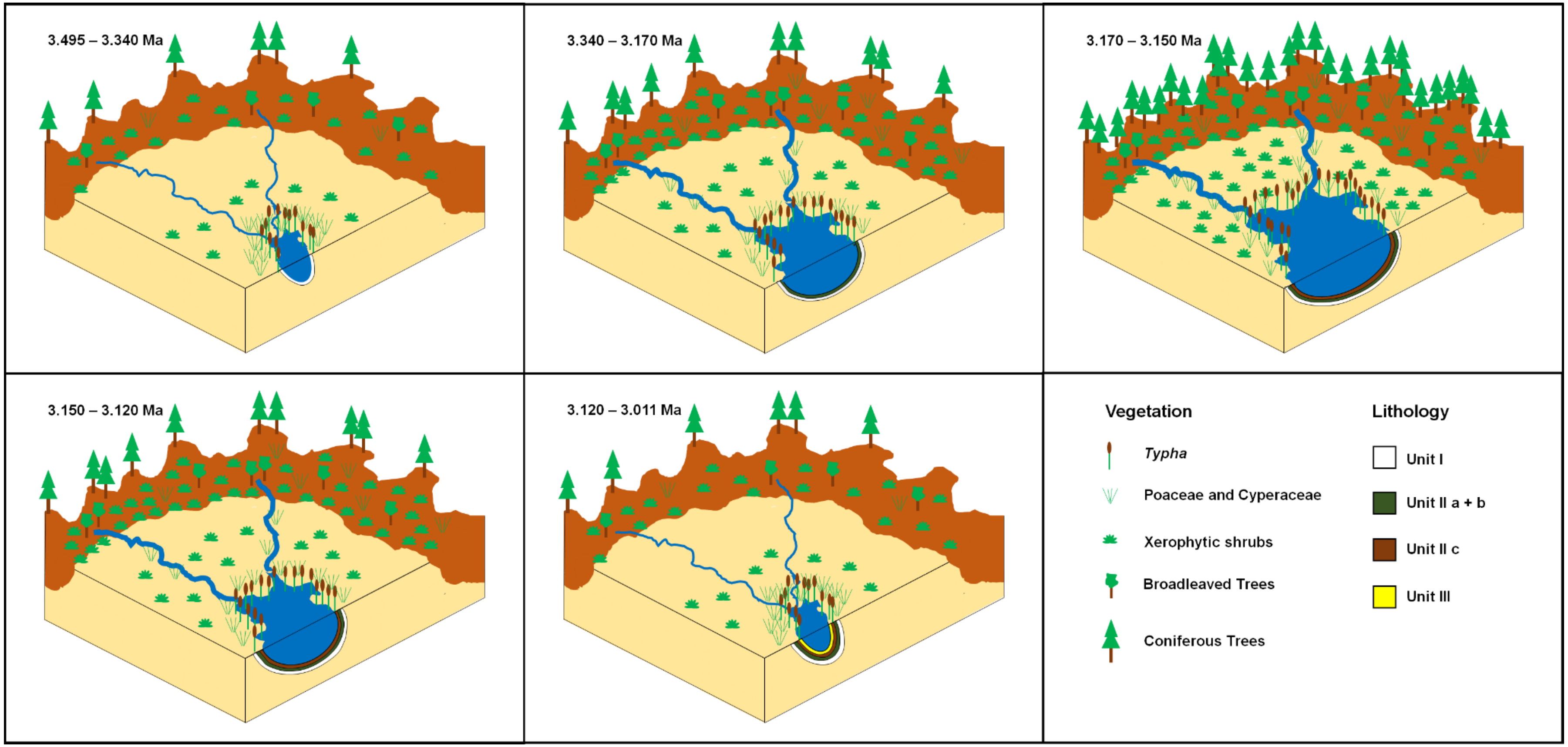

Fig. 4 - 22: Suggested vegetation development around the SG-1b palaeolake. Sediment deposition is shown in a simplified version according to the sedimentation history of the SG-1b core (see Chapter 4.3.1.1).

Furthermore, the occurrence of patches of permafrost at high elevation sites surrounding Lake Baikal at ~ 3.39 Ma is discussed by the author because of high amounts of *Selaginella selaginoides (Demske et al., 2002).* In Norway (ODP Site 642B), an opening of cool – temperate coniferous forests has been observed after 3.47 until 3.35 Ma, which culminated around 3.42 Ma when occurrences of Asteraceae (Liguliflorae) peaked (Panitz et al., 2016). Subsequent gradual decrease of Asteraceae until 3.35 Ma indicates increasing wetter conditions (Panitz et al., 2016). Despite the observed warming at Lake El'gygytgyn (Andreev et al., 2014), the pollen records at Lake Baikal (Demske et al., 2002) and at ODP Site 642B (Panitz et al., 2016) suggest that the coldest conditions occur between 3.42 and 3.39 Ma. Furthermore, cold and dry conditions were also inferred at 3.4 Ma from DSDP Holes 440B and 438A (east of Japan) when warm-temperate trees (*Cryptomeria*, *Fagus*) were replaced with boreal trees (*Pinus*, *Picea*) (Heusser and Morley, 1996). Thus, the observed cooling and drying in the high-latitude study sites are in good agreement with the drying of the NW Qaidam Basin in this study which culminated in the strong advancements of lakeshore vegetation in shallow waters towards the SG-1b coring site.

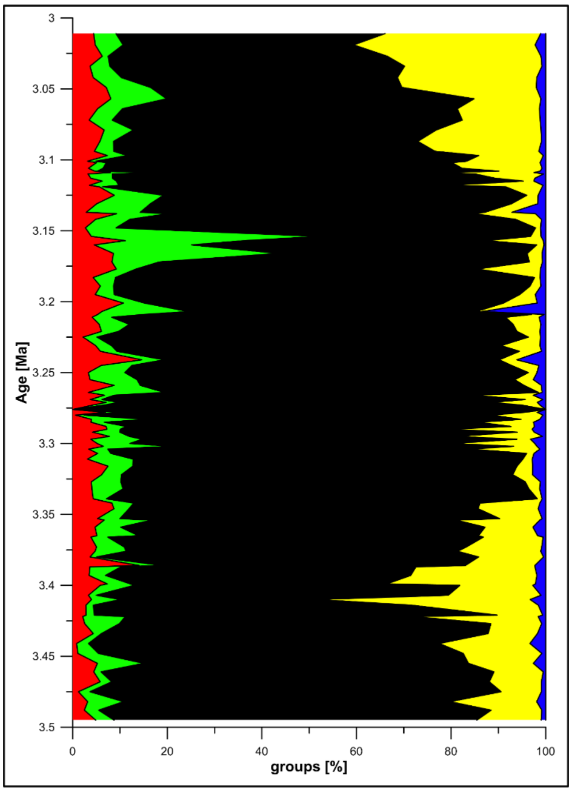

Fig. 4 - 23: Proportion of broadleaved tree pollen (red), coniferous tree pollen (green), herb & shrub pollen (black), grass pollen (yellow) and water plant, ferns & mosses pollen and spores (blue) of the SG-1b core.

Vegetation between 3.340 and 3.170 Ma

After 3.340 Ma, the Chenopodiaceae dominated shrublands were replaced by Chenopodiaceae-*Artemisia* shrublands. The sharp change around 3.340 Ma is also characterised by the strongest increase of *Nitraria* shrubs in the record which indicates that high water tables were present (Cour et al., 1999; Zhao et al., 2007). Together with higher A/C values the presence of *Nitraria* up to 10% suggests that the NW Qaidam Basin became significantly wetter. On the mountain ranges, the *Pinus* dominated coniferous forests transitioned into *Pinus*-*Picea* forests, in which also *Abies* started to grow consistently. The strong reduction of lakeshore pollen, which indicates an increase in palaeolake size, supports the reconstruction of wetter conditions. Transgressive conditions are also deduced from the sedimentation history which showed that mudstones replaced alternating mudstone/evaporite deposition. A short return towards drier conditions occurred from 3.305 to 3.265 Ma and can be characterised in two phases: Initially (3.305 – 3.280 Ma), lakeshore vegetation advanced towards the palaeolake center, while A/C values suggests that no change occurred in the xerophytic shrublands. The return of higher Poaceae and Cyperaceae values matches the timing of the MIS M2 event, during which a strong cooling in the Northern Hemisphere took place (Andreev et al., 2014; Jansen et al., 2000; Kleiven et al., 2002; Lisiecki and Raymo, 2005), however, the drying in the SG-1b palaeolake was not as strong compared to the 3.420 – 3.400 Ma event. The second phase of the dry interval was characterised by a reduction in lakeshore vegetation but significantly lower A/C values. Increased aridification at the SG-1b site has also been recorded in the sedimentation history, which showed that evaporite lithofacies were deposited between 3.295 and 3.265 Ma. Following 3.265 Ma, the NW Qaidam Basin was characterised by wet conditions expressed by an increase in A/C values and increased trees on the mountain slopes and ranges. At 3.241 Ma and 3.207 Ma, two peaks in *Sphagnum* have been detected. *Sphagnum* moss is a major constituent of peatlands, however it is difficult to explain where they are coming from since the region was semi-arid throughout the entire Late Pliocene. Liu et al. (2018) also found Holocene and pre-Holocene peatlands in the Mu Us Desert in Northern China and they relate the occurrences of peatland to an increased EASM strength. Modern-day occurrences of *Sphagnum* can be found in NE China, where climate conditions are typically cold and wet (MAT) (Liu et al., 2019), in central China, where climate conditions are warm and wet (MAT 19°C; MAP 1700 mm) (Huang et al., 2012) and on the Tibetan Plateau, where climate conditions are cold and wet (Zhang et al., 2012b). The second *Sphagnum* peak at 3.207 Ma is coinciding with increased coniferous tree pollen so it is possible that they are derived from an alpine location with higher moisture where coniferous trees were growing.

Further cooling and drying has been observed in Norway and Lake El'gygytgyn before the onset of the MIS M2 event between 3.340 and 3.290 Ma. Whereas in Norway, coniferous trees decrease and warm-temperate taxa became absent (Panitz et al., 2016), the vegetation around Lake El'gygytgyn was also characterised by a decrease in coniferous trees that culminated in the development of treeless tundra between 3.310 and 3.283 Ma (Andreev et al., 2014). At Lake Baikal, cold and dry conditions persisted until 3.3 Ma, however, just before the MIS M2 event slight increases in *Cedrus*, *Ulmus*/*Zelkova* and *Corylus*/*Myrica* (Demske et al., 2002) might indicate a short interval of slightly warmer conditions. At Lake El'gygytgyn, remigration of *Larix*, *Picea* and *Pinus* forests after 3.283 Ma suggests warmer and wetter conditions which persisted until ~ 3.087 Ma with short interruptions of drier intervals (Andreev et al., 2014). Cool temperate deciduous and mixed forests reached northern Norway again after 3.29 Ma which indicates warmer conditions following the MIS M2 event (Panitz et al., 2016). This was especially apparent from 3.29 to 3.26 Ma, whereas after 3.26 until ~ 3.16 Ma the vegetation was characterised by more open conditions (Panitz et al., 2016). At Lake Baikal, Demske et al. (2002) suggest that climate conditions became wetter after 3.3 Ma until 3.15 Ma due to the spread of mixed coniferous forests. However, between 3.28 and 3.26 Ma (and again between 3.20 and 3.18 Ma) cooling and drying took place as suggested by an increase in Ericaceae, *Betula*, Lycopodiaceae and *Selaginella selaginoides* (Demske et al., 2002). This is in very good agreement with the observed drying at the SG-1b palaeolake when A/C values decreased and evaporites were deposited.

Vegetation between 3.170 and 3.150 Ma

Between 3.17 and 3.15 Ma a strong expansion of coniferous forests on the mountain ranges and possibly down to the mountain slope took place in the NW

Qaidam Basin. The advance of coniferous forests was accompanied with a transition in the semi-desert basin vegetation from Chenopodiaceae dominated xerophytic shrublands towards *Artemisia* dominated shrublands.

The resulting A/C values are one of the highest in the whole record and thus reflect wet conditions. Despite the wetter conditions and increase in coniferous forests, the broadleaved forests are not showing a strong increase which might be an indicator that temperatures were not significantly higher during this period. Despite the general good agreement between this record and the other three high resolution records (Andreev et al., 2014; Demske et al., 2002; Panitz et al., 2016) in the high latitudes of the Northern Hemisphere, no strong increase in precipitation or temperature has been recognised between 3.17 and 3.15 Ma. Lake El'gygytgyn (Andreev et al., 2014) and Lake Baikal (Demske et al., 2002) continued be characterised by wet and warm taxa comparatively to their respective records. In Norway, a cooling after 3.16 Ma can be seen, which is characterised by a decline in *Pinus* and increase of *Sphagnum* (Panitz et al., 2016).

Vegetation between 3.150 and 3.120 Ma

The time interval from 3.15 to 3.12 Ma was characterised by a re-advance of xerophytic shrublands, which were initially dominated by Chenopodiaceae shrubs. Coniferous forests retreated uphill to the mountain ranges during this drier period. A/C values dropped significantly at the onset of this period but gradually recovered towards higher values. The sharpness of this change suggest a very strong drying event. In the sedimentation history, carbonates were deposited around this time, which indicates that a sudden drop in lake level occurred at the beginning of this interval. In northern Norway a cooling trend can be observed from 3.16 Ma as previously mentioned (Panitz et al., 2016). At Lake Baikal, a severly dry and cold period has been recorded from 3.15 to 2.89 Ma, during which especially *Picea* and *Tsuga* declined (Demske et al., 2002). Open steppe and tundra vegetation characterised by higher abundances of Cyperaceae, *Artemisia*, Asteraceae and Pteridophyta (Demske et al., 2002).

Vegetation between 3.120 and 3.011 Ma

Further drying at the SG-1b palaeolake occurred after 3.120 Ma. The *Artemisia* shrublands were transitioning into Chenopodiaceae – *Ephedra* shrublands and Chenopodiaceae – *Artemisia* shrublands after 3.100 Ma. Concomitantly, the pollen record became more and more dominated by lakeshore vegetation as Poaceae and Cyperaceae increased stepwise around 3.120, 3.090 and 3.050 Ma. The forests on the mountain slopes and ranges were thinning as a result of continued aridification in the region. Comparatively warm and wet conditions were still recognised at Lake El'gygytgyn until ~ 3.080 Ma, after which herb pollen and dwarf *Betula* increase leading to an opening of the *Pinus*, *Picea* and *Larix* forests (Andreev et al., 2014). Additionally, Andreev et al. (2014) reports that possibly snow algae cysts (*Locus nivalis*) were found in the palynomorph record, which could be an indication of prolonged snow and ice cover, and thereby cooling, of NE Siberia at that time.

Vegetation history of SG-1b core compared to vegetation developments in China

In contrast to these three high resolution studies (Andreev et al., 2014; Demske et al., 2002; Panitz et al., 2016), a comparison of this pollen record to other palynological studies from the Pliocene of China is restricted to broader trends due to either a lack of resolution (or age model) (Li et al., 2011; Ma et al., 2005a; Wang et al., 1999; Wu et al., 2011) or gaps in the pollen record (Miao et al., 2013). In the NW Qaidam Basin, pollen records from Miao et al. (2011) and Cai et al. (2012) show that the earliest Pliocene (5.3 – 5.0 Ma) was characterised by considerably higher tree pollen and lower herbs and shrubs. Furthermore, the composition of the xerophytic shrublands was dominated by Chenopodiaceae in the Early Pliocene, whereas the xerophytic shrublands were dominated by *Artemisia* in the Late Pliocene. Miao et al. (2013) indicated that continuous aridification led to the change from Early to Late Pliocene. However, this study shows that such a continuous drying trend did not occur between 3.5 and 3.0 Ma. Instead, broadleaved and coniferous trees are variable throughout the interval and are highest between 3.34 and 3.12 Ma where climate conditions have been significantly wetter. Additionally, the strong gradual increase of *Artemisia* as suggested by Miao et al. (2013) has not been recognised in this study. Abundances of *Artemisia* were already high in the lowest part of this record. Thus, the change in *Artemisia* could have occurred either gradually or abruptly between 3.5 and 5.0 Ma. In the central Qaidam Basin, a pollen record from the Yahu Section (Wu et al., 2011) indicates that changes in the vegetation (shifts between woodland and steppe vegetation) took place with high variability rather than gradually, however, due to a lack of age control a direct comparison between the Yahu Section record and this study is not possible.

On the CLP, the pollen records indicate partly contradicting results. According to Li et al. (2011), a transition from open woodlands to steppes and shrublands characterises cooling and drying between 3.5 and 3.05 Ma before “forest steppes” re-advanced on the northern CLP after 3.05 Ma. In contrast, the pollen record from Ma et al. (2005a) indicates that between 3.71 and 2.58 Ma *Juniperus* forests were replacing steppes and open woodlands suggesting that the climate became warmer and wetter. The low resolution pollen record from the Yushe and Taigu Basins on the eastern part of the CLP also suggest that coniferous forests (*Pinus*, *Picea*, *Abies*) dominated between 4 and 2.5 Ma and that cooling and drying only occurred after 2.5 Ma when *Artemisia* shrublands expanded (Li et al., 2004).

Interplay of moisture availability and palaeolake size in the NW Qaidam Basin and driving forces for moisture availability

The link between the C/N ratios as an expression of palaeolake size, and potential runoff was demonstrated in Chapter 4.3.1.2. A/C has been used as an indicator for moisture availability in semi-arid and arid areas (El-Moslimany, 1990; Zhao et al., 2012; Zhao et al., 2008), and as such a positive relationship of moisture availability and increased palaeolake size through increased runoff could be expected. Fig. 4 – 24 shows a comparison between the A/C ratio, the C/N ratio and the grain size proxy (ln Zr/Ti). The figure can be separated into four sections. In the first section (3.5 – 3.36 Ma), higher A/C values do not show a good correlation with lower C/N ratios indicative of a larger lake size. Instead, the two ratios are partly anti-correlated within this interval. In the second section (3.36 – 3.15 Ma), trends towards higher A/C ratios are correlated well with lower C/N ratios which suggests that a higher moisture availability was in phase with a larger lake size. In the third section (3.15 – 3.04 Ma), the moisture availability (A/C) is again anti-correlated with the palaeolake size (C/N). In the uppermost part (section 4; 3.04 – 3.011 Ma), moisture availability and palaeolake size as indicated by the C/N ratio suggest collinearity again.

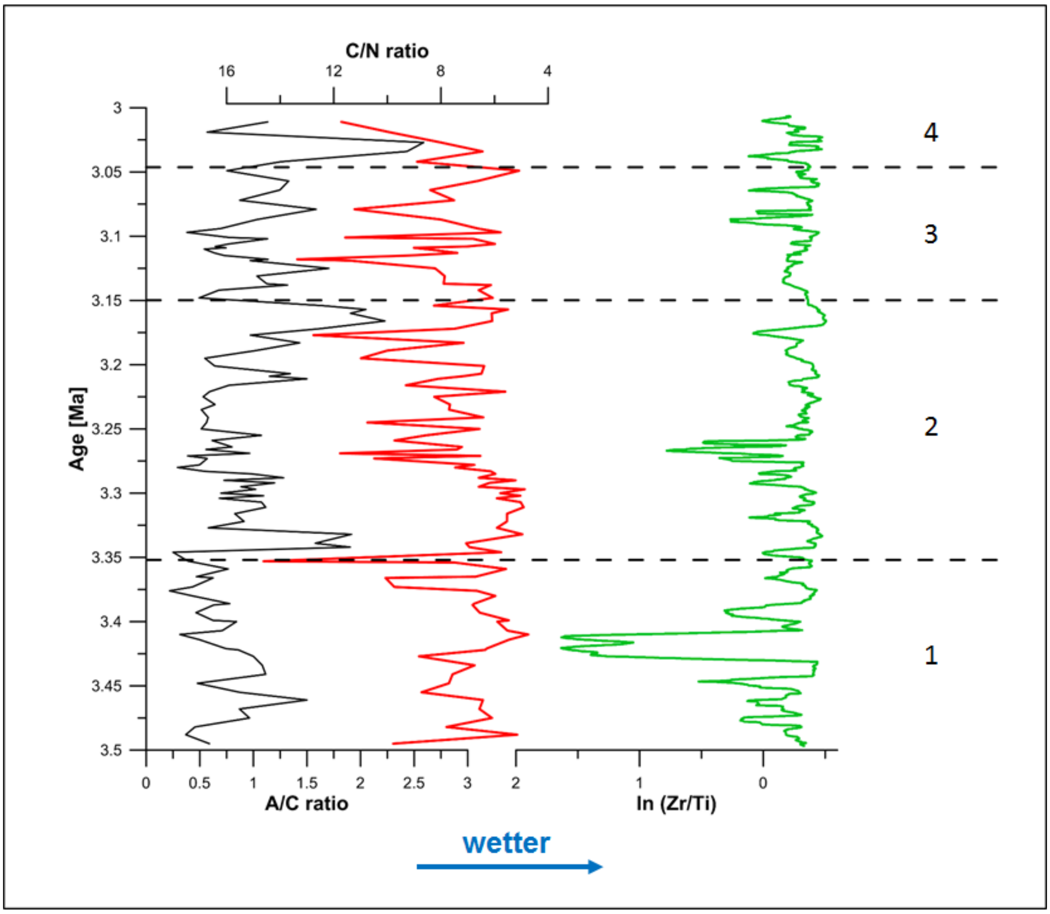

Fig. 4 - 24: Comparison of the A/C ratio (moisture availability) with the C/N ratio (low values are indicative of a higher palaeolake size) and grain size proxy (low values indicating a higher palaeolake size).

Fig. 4 – 25 shows the comparison of the A/C ratio against the 65°N summer insolation and the obliquity solution from (Laskar et al., 2004). In section 1 and 3, the moisture availability is highest at times of low Northern Hemisphere summer insolation, whereas in sections 2 and 4 the moisture availability increases during times of higher Northern Hemisphere summer insolation. Fig. 4 – 26 shows the continuous wavelet transform of the A/C ratio for the whole core interval and sections 1 – 3 using the program PAST (Hammer et al., 2001). For the whole core interval (Fig. 4 – 26a), eccentricity cycles can be identified easier than obliquity and precession cycles. Since changes of summer insolation forcings of the A/C ratio were recognised above, the continuous wavelet transforms are shown for the first three sections (section 4 is too short) individually (Fig. 4 – 26

b – d). The analysis of these sections show that precession and obliquity forcings are clearly a driver for moisture availability in the NW Qaidam Basin as well, despite the reversals between high A/C and high 65°N summer insolation and high A/C and low 65°N summer insolation. The changing correlation between the A/C ratio and the direction of orbital forcing leads to the question, what the driver behind these changes is.

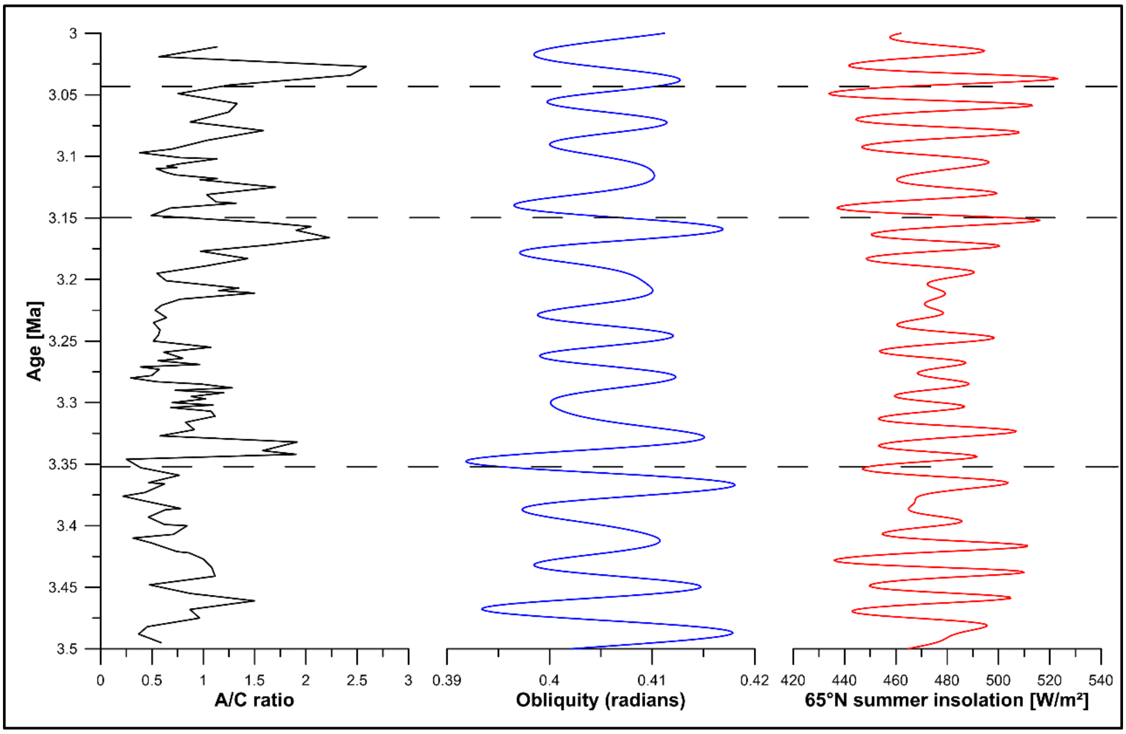

Fig. 4 - 25: Comparison of the A/C ratio with the 65°N summer insolation and obliquity solution from (Laskar et al., 2004). Dashed lines indicate the sections 1 (3.5 – 3.36 Ma), 2 (3.36 – 3.15 Ma), 3 (3.15 – 3.04 Ma) and 4 (3.040 – 3.011 Ma) of this SG-1b record interval. Section 1 and 3 show correlations with low 65°N summer insolation and obliquity whereas sections 2 and 4 are correlated to high 65°N summer insolation and obliquity.

Moisture availability is dependent mainly on precipitation and temperature (Komuscu et al., 1998), and hence changes in one climate parameter could drive changes in the effective moisture availability. However, co-variability between these two variables exist and increased warming can lead to an increase in atmospheric moisture and associated increase in precipitation (Dai, 2011; Trenberth et al., 2005; Trenberth and Shea, 2005). On the other hand, temperature and precipitation can also be negatively correlated in some areas, which leads to cooler and wetter or warmer and drier conditions (Dai, 2011; Nicholls et al., 2004). This study suggests that during sections 1 and 3 effective moisture increases with lower 65°N summer insolation (temperatures), whereas during sections 2 and 4 the effective moisture increases with higher 65°N summer insolation (temperatures). In order to explain the different forcing mechanisms in the moisture availability, the moisture source for the NW Qaidam Basin in the interval from 3.5 to 3.0 Ma needs to be further explored.

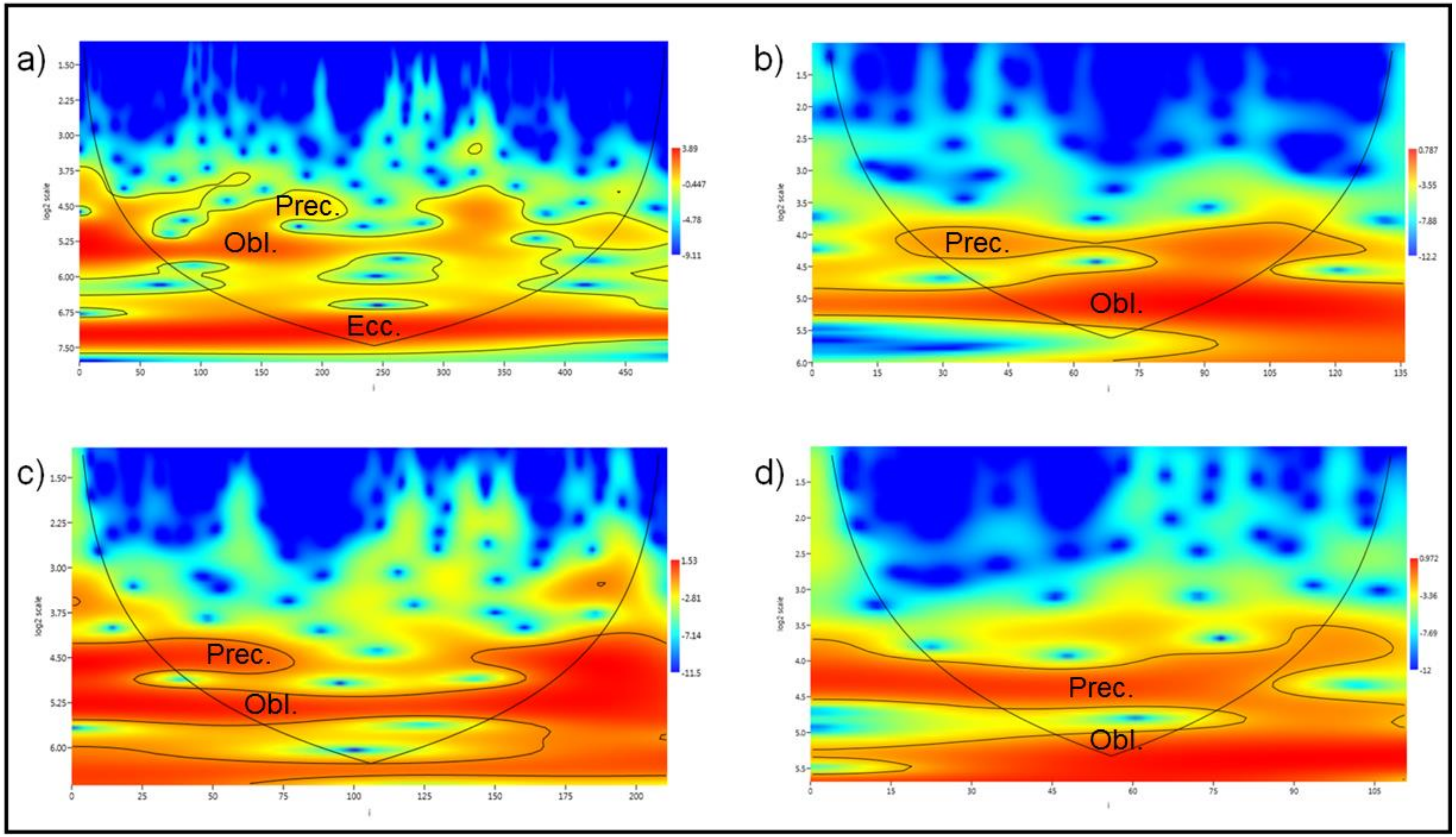

Fig. 4 - 26: Continuous wavelet transform of the A/C ratio for a) the whole core interval (3.5 – 3.011 Ma), b) section 1 (3.5 – 3.36 Ma), c) section 2 (3.36 – 3.15 Ma), d) section 3 (3.15 – 3.040 Ma). Prior to the wavelet analysis, the A/C ratio was linearly interpolated to 1 ka intervals using PAST (Hammer et al., 2001). Precession (~4.2 – 4.5 on log2 scale) and obliquity (~ 5.25 on log2 scale) forcings can be seen for all sections (1-3) whereas the eccentricity signal (~ 7 on log2 scale) is only visible in the whole core continuous wavelet transform due to the required longer time interval necessary to see such long cycles.

4.3.3 Palaeoclimate variability of NW Qaidam Basin during the Piacenzian

4.3.3.1 NW Qaidam Basin under the influence of the East Asian Summer and Winter Monsoon

Given the orographic barriers (Kunlun Mountains, Qilian Mountains, Altun Mountains) surrounding the Qaidam Basin, an intriguing question is from where moisture entered the Qaidam Basin. The three possibilities – ISM, EASM, westerlies – have already been discussed for modern day (see Chapter 2.1.2.1). Since there are ongoing discussions about the timing and uplift of the northeastern part of the Tibetan Plateau (Cui et al., 1998; DeCelles et al., 2007; Garzione et al., 2000; Zheng et al., 2000), a separate discussion for the Pliocene is necessary. Prior to the Pliocene, the central and southern parts of the Himalayan-Tibetan-Plateau had already been uplifted (Clift et al., 2002; Hoke et al., 2014; Spicer et al., 2003; Tapponnier et al., 2001) and thus, the rain shadow effect had most likely been established by that time (Dettman et al., 2003). Therefore, the ISM can be excluded as a source of moisture for NE Tibetan Plateau (Dettman et al., 2003). This is further supported by moisture pathway reconstructions for Central Asia based on carbonate $\delta^{18}O$ (Caves et al., 2015). However, due to similar isotopic signatures in carbonate $\delta^{18}O$ in eastern China and Central Asia, Caves et al. (2015) could not distinguish between westerly and EASM moisture source as the dominant regime in Central Asia.

The modern rainfall distribution in the Qaidam Basin shows that there is gradient from the SE parts, which receive higher amounts of precipitation, to the NW parts, which receive considerably less precipitation (Wang et al., 2014). As the precipitation is mainly occurring during the summer months, the EASM has a strong effect on the southeastern parts of the Qaidam Basin but only limited effect on the northwestern parts (Wang et al., 2014).

In combination with the EASM Index from Guo (2003), Xu et al. (2011) found that tree ring width and tree ring $\delta^{18}O$ data in the eastern Qaidam Basin are associated with changes in moisture availability as a result of changes in the EASM in the past 200 years. According to Guo (2003) and Xu et al. (2011), during times of weaker EASM index, precipitation in the Qaidam Basin was higher which resulted from different position of the Western North Pacific Subtropical High. Furthermore, Zhou et al. (2007) suggested that based on isotope analysis the

EASM reaches the western parts of the Qilian Mountains, which are also outside of the modern dashed line of monsoonal influence (Fig.4 – 27). Currently, recycling of water (evapotranspiration of water that already precipitated) is suggested to be the mechanism for transport of moisture into the Qaidam Basin coming originally from the EASM regime (Li et al., 2006; Xu et al., 2011)

In deep time, Herb et al. (2017) proposed the possible influence of a monsoonal source at the SG-1 study site in the NW Qaidam Basin between 1.9 and 1.3 Ma. Therefore, it seems that the NW Qaidam Basin could be influenced when the EASM was strong enough. To determine whether the westerlies were able to provide moisture to the Qaidam Basin during the Pliocene, the pathway of the westerlies has to be examined. The westerlies carry moisture derived mainly from the Atlantic Ocean over the Eurasian landmass towards the Himalayan Tibetan Plateau (Pamir Mountains and Tian Shan Mountains) before entering the Tarim Basin (north of Qaidam Basin). Multiple studies from the Tarim Basin reveal that this basin underwent drastic aridification between 5 and 7 Ma (Chang et al., 2017; Liu et al., 2014; Sun et al., 2015; Sun et al., 2017; Zhang et al., 2013; Zhang and Sun, 2011). Magnetostratigraphic data at the southern flank of the central Tian Shan mountains (N-Tarim Basin) indicate that increased uplift and also erosion took place in the Late Miocene (11 Ma until at least 5 Ma) (Charreau et al., 2006; Huang et al., 2006). This is consistent with pollen data from the southern Tian Mountains, which show that *Abies* abruptly increased after 7 Ma which implies that mountain ranges were higher allowing for growth of *Abies* (Zhang and Sun, 2011). Therefore, authors are arguing that the continued collision in the northern Tibetan Plateau closed the pathway of westerly moisture entering the Tarim Basin (Liu et al., 2014; Sun et al., 2017), which resulted in the onset of the Taklamakan desert in central Tarim Basin around 7 Ma ago (Sun et al., 2009) and 5.3 Ma ago in western Tarim Basin (Sun and Liu, 2006). Since the Altun Mountains separate the Tarim Basin from the Qaidam Basin since at least the Oligocene/Miocene (Hanson, 1999; Sobel et al., 2003), the westerlies would have to pass another, albeit lower, mountain range before entering the Qaidam Basin. Considering all the above, especially the formation of the Taklamakan desert in the Tarim Basin during Late Miocene/Early Pliocene (Sun et al., 2009), it seems unlikely that westerly winds contributed significant amounts of precipitation to the NW Qaidam

Basin (see also Fig. 4 – 27). Instead, periods of strong westerly winds could lead to increased dryness in the Qaidam Basin (Wang et al., 2013).

Pollen records from the NW Qaidam Basin (Cai et al., 2012; Miao et al., 2011; Miao et al., 2013) show that a long-term aridification trend exists, which is linked to global cooling (Zachos et al., 2001) since the Early Miocene. Due to synchronised cooling in all precipitation source areas – Atlantic Ocean (westerlies), Indian Ocean (ISM), Pacific Ocean (EASM) it was not possible to determine the specific wind system responsible for precipitation changes in the NW Qaidam Basin (Miao et al., 2013). In order to address this question and identify the wind system/precipitation source area for NW Qaidam Basin between 3.5 and 3.0 Ma, results from the SG-1b core are compared to different regional records. Fig. 4 – 28 shows the percentage of grasses in the record (Poaceae + Cyperaceae) from this study along with the eolian percentage of grain size recorded in sediments of core WEDP01 from the Tengger Desert (Li et al., 2018b), phases of increased input of coarser material at Lake Qinghai (Fu et al., 2013), magnetic susceptibility of sediments at Lake Qinghai (Fu et al., 2015) and TOC and $CaCO_3$ content from Lop Nor core in the Tarim Basin (Liu et al., 2014). The various regional proxies represent the following: The eolian content in the Tengger Desert sediments represents dryness in a study area north of the CLP, which becomes especially severe after 0.8 Ma, leading to the formation of the desert (Li et al., 2018b). A sediment record from Lake Qinghai to the southeast of the Qaidam Basin shows two phases of increased mean grain size which according to the authors could be due to uplift in the sediment source areas (Fu et al., 2013). However, the other sedimentological changes at Lake Qinghai are thought to be related to variability in the EASM (Fu et al., 2013). Thus, it might be possible that also the changes in grain size reflect EASM variability (weakening in this case) leading to a lake size reduction and the deposition of sediments with a coarser grain size at the coring position. Additionally, the magnetic susceptibility of Lake Qinghai is shown which can be used as a proxy for humidity with lower values representing drier phases (Ao et al., 2016; Fu et al., 2015; Maher et al., 1994; Nie et al., 2008).

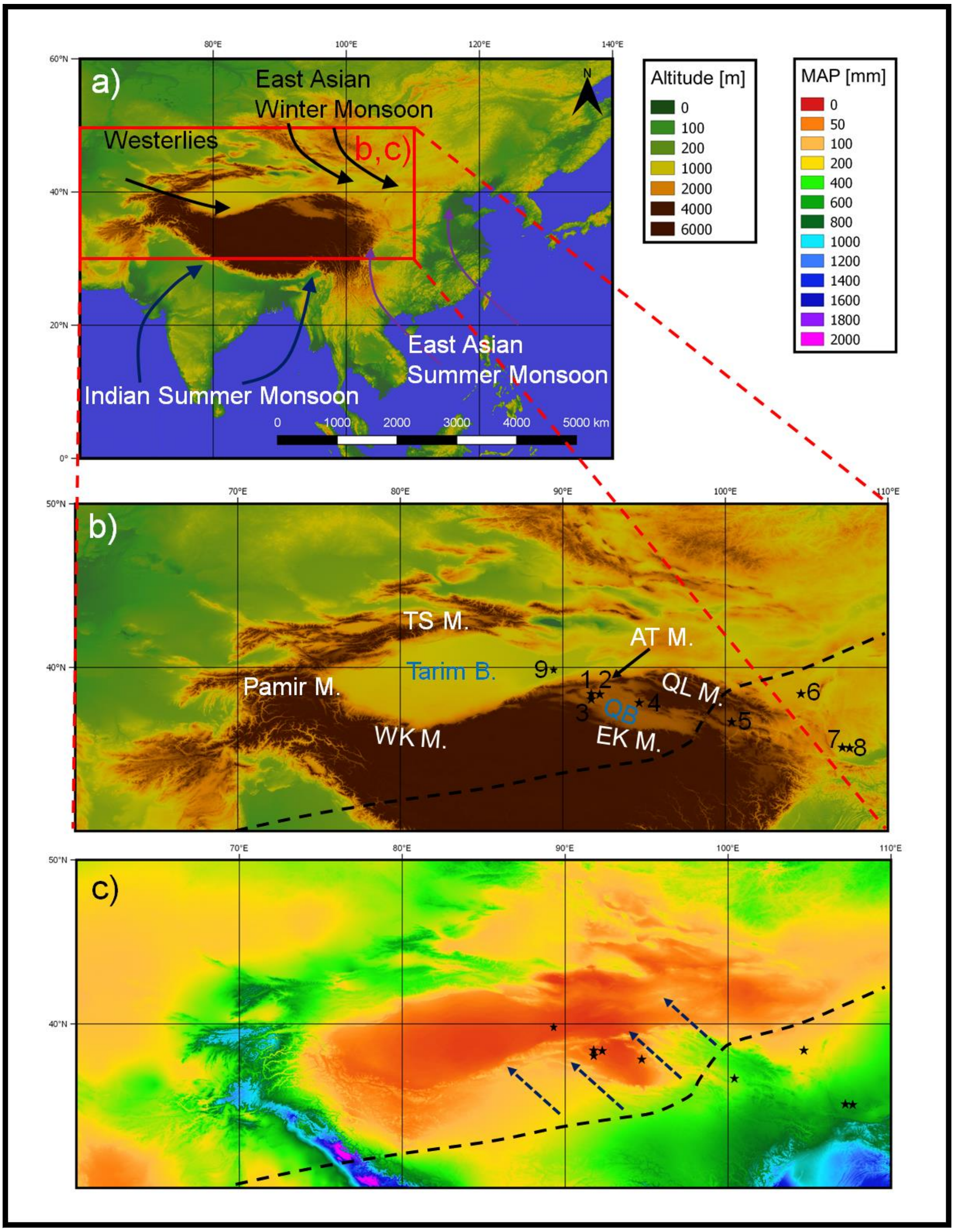

Fig. 4 - 27: a) Overview of relevant study sites for discussion of Pliocene climate evolution. 1 = SG-1b core (this study), 2 = SG-3 core (Cai et al., 2012), 3 = KC-1 core (Miao et al., 2011), 4 = Yahu Secton (Wu et al., 2011), 5 = Lake Qinghai (Fu et al., 2013), 6 = WEDP01 Core (Li et al., 2018b), 7 = Chaona (Ji et al., 2017), 8 = Lingtai (Sun et al., 2010), 9 = Lop Nor (Liu et al., 2014). b) Topographic overview about mountain ranges that block moisture coming from the westerlies and monsoon systems: Pamir Mountains, Tian Shan Mountains (TS M.), West Kunlun Mountains (WK M.), East Kunlun Mountains (EK M.), Altun Mountains (AT M.) and Qilian Mountains (QL M.). The dashed line represents the modern monsoonal limit (after Chen et al., 2008; Gao, 1962). c) MAP map of the same areas as in b). The dashed arrows indicate that the area under monsoonal (summer monsoon) influence shifted north and westwards into the Asian interior during the Pliocene compared to its modern position. The maps has been drawn using QGIS 2.18.4 (QGIS Development Team, 2016).

The TOC and $CaCO_3$ content at the Lop Nor coring site are an indicator for palaeoprecipitation in the Tarim Basin with higher TOC and $CaCO_3$ content suggesting wetter phases (Liu et al., 2014). The grass percentage in the SG-1b record represents changes in the palaeolake size as has been demonstrated previously by comparing their variability to lithological changes (Fig. 4 – 20). The varying dominance of the lakeshore vegetation in the pollen record suggested that palaeolake size was small between 3.5 and 3.35 Ma, large between 3.35 and 3.120 Ma and small again between 3.12 and 3.011 Ma. Dry periods between 3.5 and 3.35 Ma as well as between 3.12 and 3.011 Ma were also seen at Lake Qinghai where a rise in grain size and lower magnetic susceptibility suggest that the EASM weakened (Fu et al., 2013). Based on changes in the sedimentology, Fu et al. (2013) suggest that Lake Qinghai fully transitioned into a shallow lake by 3.06 Ma. The two characteristic drought intervals intervals were also observed in Tengger Desert, as indicated by the percentage of deposited sediments of eolian origin (Li et al., 2018b). Between 3.3 and 3.1 Ma, reduced eolian influx signals a wetter period and strengthened EASM precipitation in that region, which is also observed in this study by the increase of arboreal taxa, reduced input of lakeshore vegetation and the end of declining A/C values. The sediment records from Lake Qinghai and Tengger Desert clearly receive their precipitation from the EASM (Fig. 4 – 27 and Fig. 4 – 28). On the CLP, Sun et al. (2010) shows that the EASM has been relatively weak between 3.5 and 3.3 Ma, relatively strong between 3.3 and 3.08 Ma and relatively weak again from 3.08 to 3.0 Ma based on a summer monsoon stack that incorporates magnetic susceptibility and carbonate content. In contrast, the TOC and $CaCO_3$ values from Lop Nor (Tarim Basin) show a different trend (Fig. 4 – 28) (Liu et al., 2014). Lop Nor receives moisture through the westerlies, which has been significantly limited after the closure and uplift of the Pamir Mountains reducing the moisture transport into the Tarim Basin after 4.9 Ma (e.g. Liu et al., 2014; Sun et al., 2017 and references therein). The higher values and stronger fluctuations in the TOC and $CaCO_3$ data indicates that moisture transport of the westerlies into the Tarim Basin was comparatively high between 3.5 and 3.34 Ma and between ~ 3.2 and 3.050 Ma. Contrary, in the time interval lasting from 3.34 to 3.2 Ma low carbonate formation and organic matter contents suggest a drier period (Liu et al., 2014). Two important conclusions can be drawn from the data comparison. First of all, the moisture history between 3.5 and 3.0 Ma is not synchronous for the westerlies and EASM. A similar out-of-phase relationship between precipitation in the EASM region and westerly dominated Central Asia region has been recognised by Chen et al. (2008), which has been addressed as a result of different forcing mechanisms for moisture changes in the Pacific (summer insolation at low latitudes) and North Atlantic (North Atlantic SST and high latitude surface air temperatures) source regions. Secondly, identified phases of increased wetness and aridity in the NW Qaidam Basin, as presented here in this study, are in phase with other study sites from the EASM region. Therefore, it is reasonable to conclude that the changes in vegetation/precipitation at the SG-1b coring site and the further regional surroundings are due to changes in the EASM between 3.5 and 3.0 Ma.

Modern day Qaidam Basin is largely covered by deserts and tree pollen only account for less than 5% in surface samples (Zhao and Herzschuh, 2009). This study, however, shows that xerophytic shrubs were growing in the NW part of the Qaidam Basin and contained tree pollen of ~ 10% consistently. Therefore, this study proposes that the EASM shifted northwards during the Pliocene and reached its northernmost limit between 3.3 and 3.12 Ma (Fig. 4 – 27c).

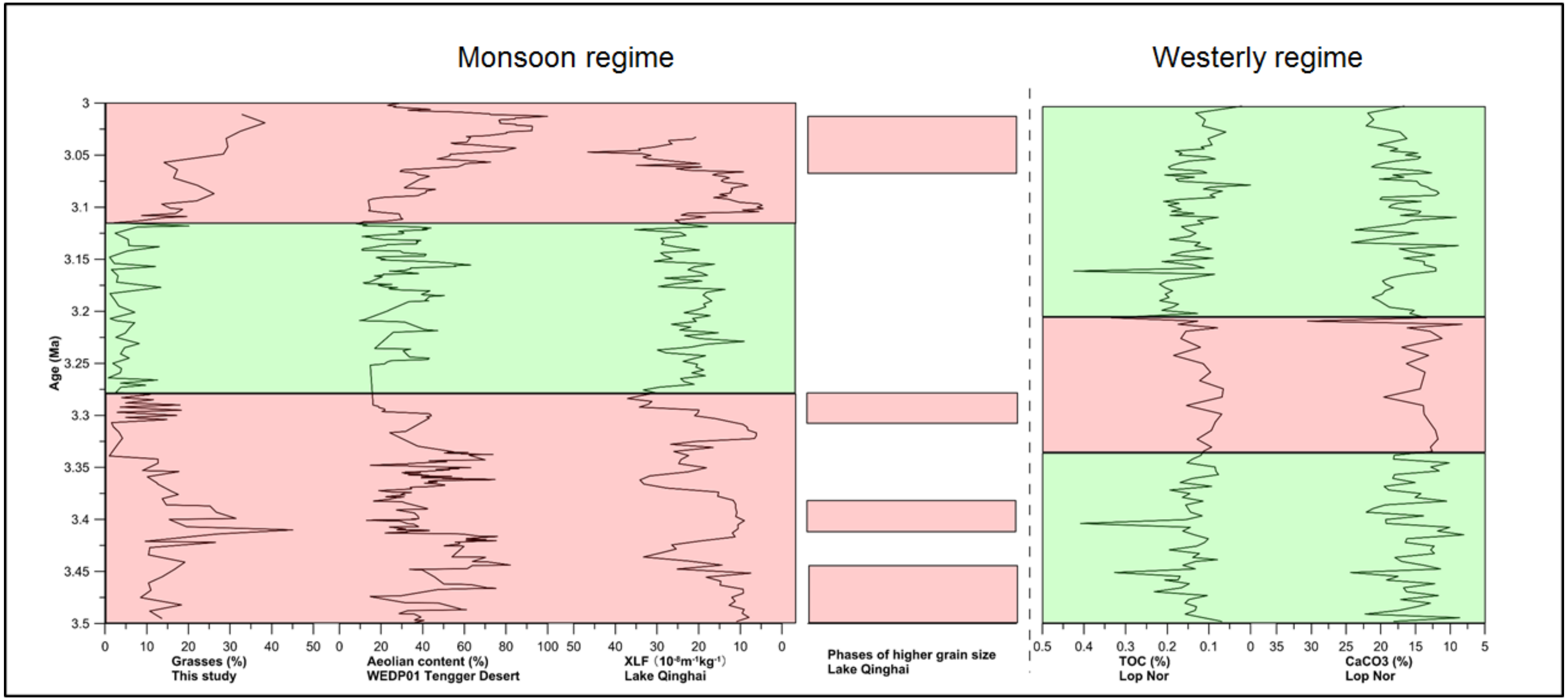

Fig. 4 - 28: Comparison of grasses (Poaceae + Cyperaceae) from this study with the eolian content in sediments at the WEDP01 core from the Tengger Desert (Li et al., 2018b), magnetic susceptibility of a Lake Qinghai core (Fu et al., 2015), phases of larger grain size (Fu et al., 2013) at Lake Qinghai and TOC and CaCO3 content in the Lop Nor core (Liu et al., 2014). Note, that the ages for the Lake Qinghai records were realised from the related published magnetostratigraphic figure since they were not published as raw data. The figure indicates that between 3.5 and 3.3 Ma the study sites were characterised by increased aridity, which was then followed by a wetter interval shaded in green. After ~ 3.12 Ma, the records were showing increased aridity trends again.

Influence of EAWM on the SG-1b palaeolake

The EAWM has been intensively studied using geochemical proxies (Sun et al., 2010; Wan et al., 2007) and dust accumulation rates (Rea et al., 1998; Zhang et al., 2018) to identify strengthening and weakening periods during the Pliocene. Furthermore, the connectivity of the EAWM to tectonic uplift of the Himalayan-Tibetan Plateau (An et al., 2001) and/or the onset of the NHG (Sun et al., 2010) were assessed. Based on a quartz grain size signal, Sun et al. (2010) indicate that the EAWM strengthened on the CLP in the time interval from 3.5 to 3.3 Ma and 3.15 to 3.0 Ma. The pattern matches the trend of strongly increased lakeshore vegetation as an indication for reduced lake size very well. However, the three other available high-resolution study sites (ODP 642B offshore Norway, Lake Baikal, Lake El'gygytgyn) also show cooling/drying trends during these time intervals (Andreev et al., 2014; Demske et al., 2002; Panitz et al., 2016). To identify particular strengthening episodes of the EAWM, time intervals need to be examined where trends in the palaeovegetation history suggests that cooling occurred, while other study sites, which are not affected by the EAWM, were not characterised by cooling. From 3.42 – 3.40 Ma, strong cooling/drying occurred at the SG-1b study site, Lake Baikal (Demske et al., 2002) and in northern Norway (Panitz et al., 2016) but not in NE Siberia (Andreev et al., 2014). Furthermore, the interval from 3.29 to 3.26 Ma was characterised by cooling and drying in this study and in the Lake Baikal area (Demske et al., 2002), whereas in northern Norway (Panitz et al., 2016) and NE Siberia (Andreev et al., 2014) higher temperatures and precipitation were concluded from changes in the vegetation. The similar climatic trends at Lake Baikal and the SG-1b core during these intervals could be explained by the fact that both study sites are further away from the marine regime compared to Lake El'gygytgyn and northern Norway (as represented in ODP 642B). However, another similarity between Lake Baikal and the SG-1b palaeolake is that both regions are influenced by the EAWM. Lake Baikal is located in the area where the Siberian High is forming during boreal winter months. As the strength of the EAWM depends on the thermal contrast between the Eurasian continent (Siberian High) and the warm Pacific (Shi et al., 2011), variations in the EAWM strength should be seen at both study sites.

Fig. 4 – 29 shows a comparison between the grain size proxy (ln Zr/Ti), the winter monsoon proxy (ln Sc/Ti) , the A/C ratio as a proxy for moisture availability, the

percentage of grasses (Poaceae and Cyperaceae) as a proxy for palaeolake size, and the weight percentage of potassium from IODP core U1422 from the Sea of Japan (Zhang et al., 2018). K (wt%) is interpreted to reflect the dominance of physical over chemical weathering in the Asian interior and is transported to the Sea of Japan mainly as dust by either the EAWM or the westerlies (Zhang et al., 2018). When K (wt%) rises, it is assumed that the Asian interior was drier compared to intervals with lower K (wt%) (Zhang et al., 2018). The diagram shows that four intervals exist, where elevated peaks in the grain size, winter monsoon proxy are matched with the aridity proxy from Zhang et al. (2018). Included are the two time intervals, highlighted above, during which cooling/drying in this study and Lake Baikal (Demske et al., 2002) was identified (high %grasses, low A/C) but was not seen at Lake El'gygytgyn (Andreev et al., 2014) and partially not seen at ODP Site 642B (Panitz et al., 2016). The MIS M2 event (~ 3.3 Ma) is characterised by higher aridity, although not as strong compared to the intervals from 3.42 to 3.40 Ma and 3.29 to 3.26 Ma. The grain size proxy, A/C ratio and grasses point to slightly drier conditions (palaeolake shrinking). Only the winter monsoon proxy seem to suggest a stronger cooling, however this proxy has reached maximum values numerous times before and after this interval, which indicates that the MIS M2 event has not been outstandingly cool/dry in the SG-1b record.

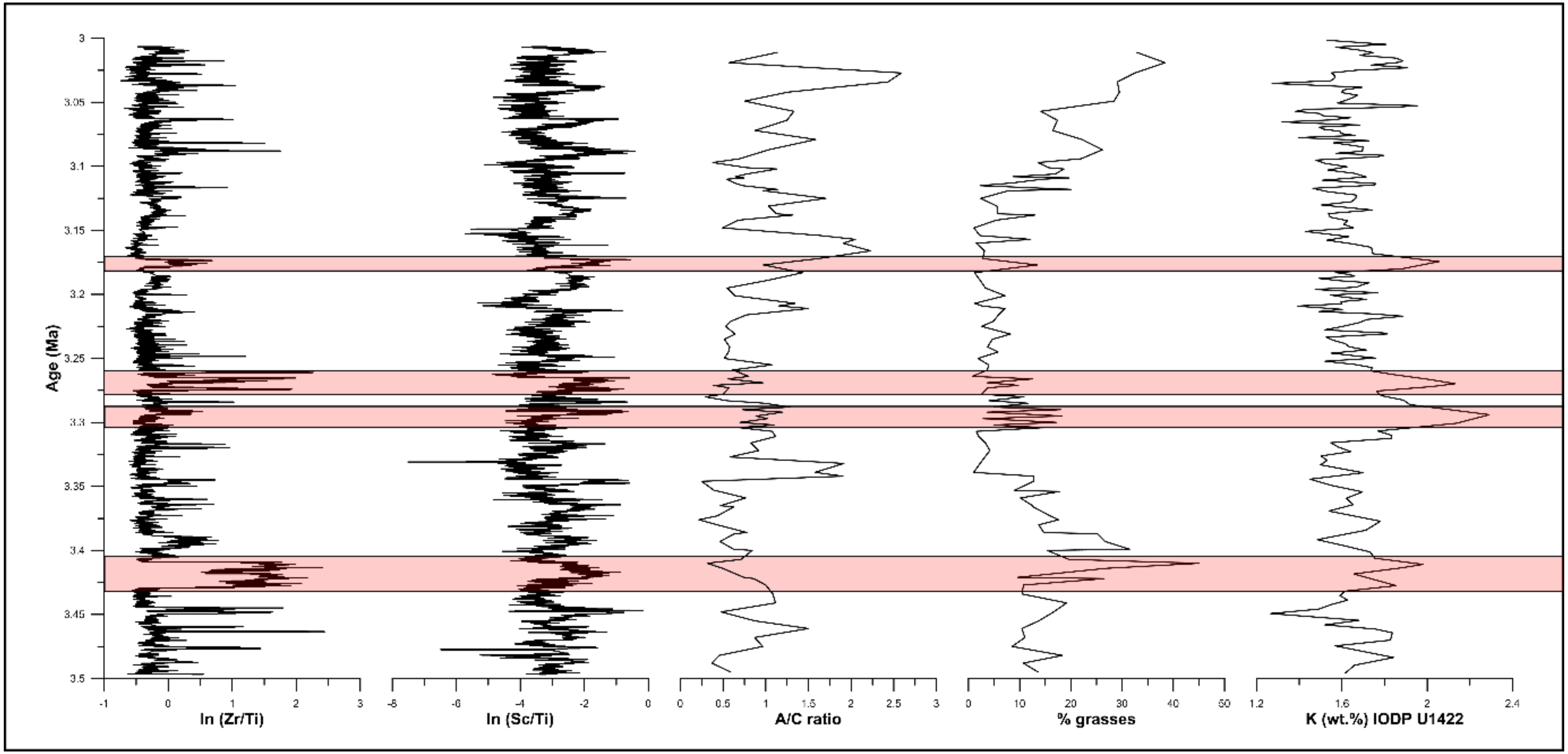

Fig. 4 - 29: Comparison of westerlies induced dust flux into the Sea of Japan, expressed as K (wt %) (Zhang et al., 2018) with grain size proxy (ln Zr/Ti), winter monsoon proxy I (ln Sc/Ti), A/C ratio and the percentage of grasses from this study. Red-shaded are intervals within the 3.5 to 3.0 record, which showed significantly increased aridity in the Asian interior and higher grain size/ potentially stronger winter monsoon activity in the SG-1b core area.

4.3.3.2 Climate estimates for the NW Qaidam Basin between 3.5 and 3.0 Ma

The results of the Coexistence Approach, semi-quantitative A/C ratio approach and transfer function are shown in Fig. 4 – 30, 4 – 31 and 4 – 32 respectively.

Based on the Coexistence Approach, Pliocene precipitation estimates in this study are very high compared to modern day Qaidam Basin (red lines) and for typical cold semi-deserts (Whittaker, 1975). This is supported by Zhang et al. (2015) findings that climate reconstructions based on the Coexistence Approach cannot reproduce the extremely low MAPs on the Qinghai-Tibetan Plateau. The temperature estimates also show higher values in the Pliocene compared to modern day, but their lower range is close to the modern value at the SG-1b site in strong contrast to the MAP reconstruction. Higher temperatures in the Pliocene could be expected because of higher global mean air temperatures from models (e.g. Haywood and Valdes, 2004). Both, temperature and precipitation, however, show almost no climate variability throughout the record. Initially for Tertiary European forests designed (Mosbrugger and Utescher, 1997), limitations of the Coexistence Approach have been identified in combination with cold climates, long-distance transport of taxa, strong altitudinal gradients in the study area, high-altitude study sites and a low variability because of common taxa sharing a large climate gradient (e.g. Grimm and Denk, 2012; Mosbrugger and Utescher, 1997; Zhang et al., 2015).

The A/C ratio as a semi-quantitative approach to calculate MAP ranges (Zhao et al., 2012) shows a different picture compared to the CoA reconstruction of MAP. Although confined to pre-set ranges (0 – 200 mm, 200 – 350 mm, 350 – 450 mm), stronger climate variability can be observed in the record (Fig. 4 – 31). The MAP reconstruction indicates that the climate in the NW Qaidam Basin was dry between 3.5 and 3.35 Ma except for two small intervals. This is in good agreement with the reconstruction of the palaeolake development that pointed out that a small lake size and depth characterised the SG-1b palaeolake in the lowermost interval. After 3.35 Ma, the consistently dry MAP estimates started to fluctuate more and became stronger especially after 3.22 Ma. The vegetation discussion emphasized that between 3.265 and 3.125 Ma the NW Qaidam Basin experienced a wet phase with less dominant palaeo lakeshore vegetation and a higher proportion of tree pollen in the record.

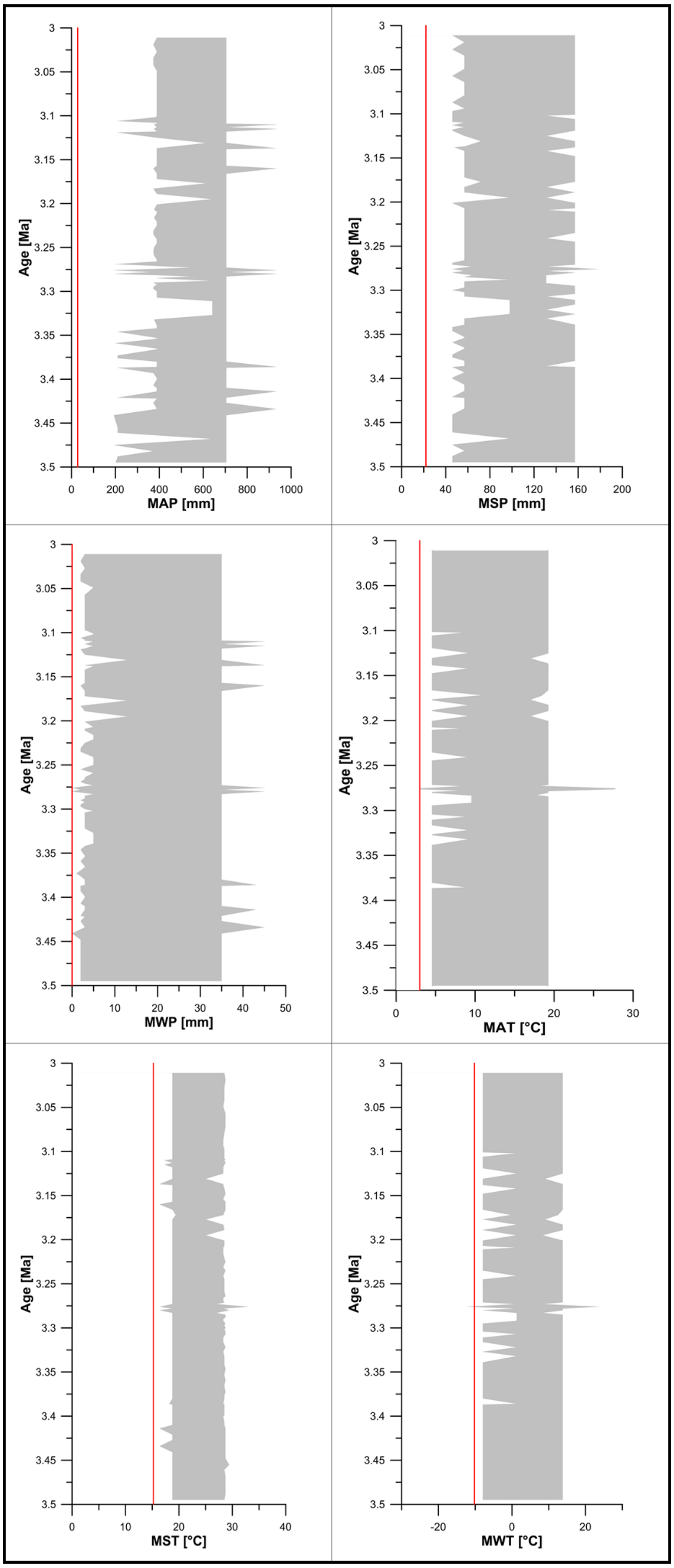

Fig. 4 - 30: Palaeoclimate estimates based on the Coexistence Approach from Mosbrugger and Utescher (1997). MAT = mean annual temperature, MST = mean summer temperature, MWT = mean winter temperature, MAP = mean annual precipitation, MSP = mean summer precipitation, MWP = mean winter precipitation. Palaeoclimate estimates are shown as ranges with lower and upper limit (grey). Modern values for the SG-1b coring site are shown as a red line.

After 3.125 Ma, the pollen record suggests that the climate became drier again, which can not be supported by the MAP reconstruction based on the semi-quantitative A/C ratio.

In contrast to the Coexistence Approach, the MAP ranges are smaller and have a higher variability. Since the A/C ratio is applied to semi-arid and arid areas (Zhao et al., 2012) with mostly open vegetation, this semi-quantitative estimate reflects actual precipitation changes in the Pliocene NW Qaidam Basin better than the Coexistence Approach. Although Zhao et al. (2012) reconstructed the semi-quantitative relationship of the A/C ratio with MAPs for semi-arid and arid China, the study from Zhao et al. (2008) suggests that the A/C ratio in the Qaidam Basin is even better correlated to changes in moisture availability. Since the actual A/C ratio shows more variability especially in the lowermost part of the record in comparison to the reconstructed MAP ranges and in light of the good orbital correlations of the A/C ratio shown in the previous sub-chapter, the actual A/C ratio should be used when characterising palaeoclimates, in order not to lose valuable information.

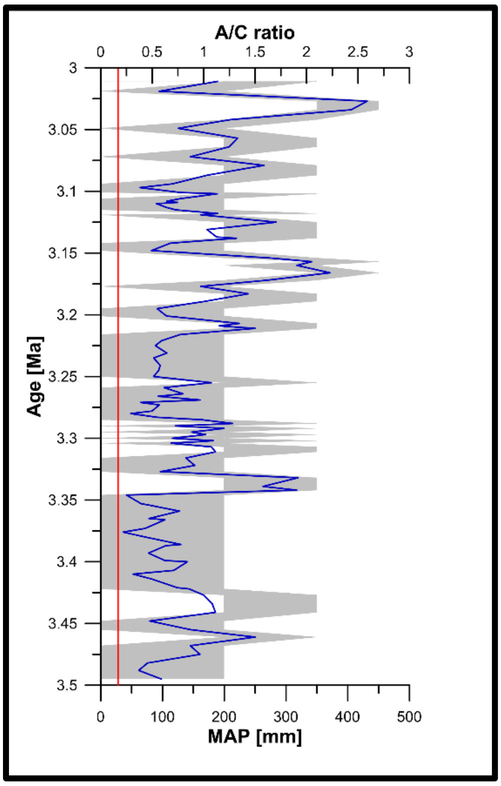

Fig. 4 - 31: Semi-quantitative estimate of MAP based on the A/C ratio after Zhao et al. (2012). Ranges for MAP are shown in grey, whereas the A/C ratio is shown in blue. The red line represents modern MAP values from the SG-1b coring site.

The climate estimates from the pollen – climate transfer functions (Fig. 4 – 32) show the narrowest range and highest climate variability from all three methodologies used. In contrast to the Coexistence Approach, the pollen – climate transfer functions are not based on presence/absence of taxa but rather the actual composition (Birks, 1995). Although Birks and Seppä (2004) and Rosén et al. (2003) suggest that long-distance transport of pollen have a negative effect on the quality of pollen – climate transfer functions, this does not apply for this study since also in the modern Qaidam Basin long-distance transport of trees (broadleaved and coniferous) is recorded (Zhao and Herzschuh, 2009). Limitations of the pollen – climate transfer functions exist though:

First of all, the modern pollen dataset does not consist of one uniform type of sediment sample (lake sediments, soil sediments, moss polsters, dust flux samples) which leads to significantly different pollen source areas between the modern sample sites (Birks and Seppä, 2004). Furthermore, the modern calibration set should consists of pollen taxa that are also found in the pollen record. In this study, however, a number of taxa (e.g. *Juglans*/*Pterocarya, Solanum,* partly *Alnus),* are not part of the final pollen – climate transfer functions either because they were not recorded in the modern pollen dataset or excluded from the calculations because of indifferent relationships to climate variables (see Chapter 3). A solution to this problem could be the inclusion of a larger modern pollen dataset expanding the geographical and climatic gradients, so that all taxa are included. A larger climatic range can increase the absolute error of the developed transfer function though (Cao et al., 2014) and increases the overestimation (underestimation) of very low (high) climate values. This is known as the edge effect and a direct result of applying WA-PLS (Birks, 1995; Birks and Seppä, 2004; Cao et al., 2014; ter Braak et al., 1993). In this study, the climate range was chosen to accommodate the modern climate conditions of the Qaidam Basin (i.e. focus on low precipitation sites and medium temperature sites). The temperature of the Qaidam Basin are well within the temperature of the modern calibration set, however, the modern precipitation is at the very low end of the modern calibration set. Therefore, overestimations of precipitation could be a factor in the climate records.

The precipitation estimates, especially MAP and MSP are significantly higher than their modern equivalents, however, they are not as high as suggested by the Coexistence Approach. The reconstructed MAPs range from ~ 100 to ~ 400 mm. Given that the Qaidam Basin has a very high potential evaporation rate and the pre-domination of semi-desert vegetation, the estimated MAPs seem to be plausible. Especially, the MAP record shows the previously mentioned three stages of high aridity (3.5 – 3.265 Ma), low aridity (3.265 – 3.125 Ma) and high aridity (3.125 – 3.011 Ma) in this record interval of the SG-1b core. This is in good agreement with the lithological and geochemical record, as the lowermost parts showed high amounts of chemical precipitates in the sediments (e.g. gypsum), whereas the middle part of this record was mainly characterised by mudstones. The top part, consisting of predominantly mudstones with the intercalation of sandstone intervals, also showed less wet conditions in the NW Qaidam Basin. The temperature records in the pollen – climate transfer functions do not show the three stages very well. They rather show a very slight increasing trend. The vegetation on the Tibetan Plateau, and especially in the drier parts of the Asian interior, are largely dependent on precipitation and less dependent on temperature changes (except high-altitudinal study sites) (Gessner et al., 2013 and references therein). Therefore, it might be that the transfer function does not reflect temperature changes very well, since most of the changes in palaeovegetation is dominated by precipitation. In terms of temperature estimates, the palaeorecord seems to have a similar MAT compared to modern-day. This could either be related to the temperature insensitivity of palaeovegetation changes in the Qaidam Basin (as mentioned above) or the temperature did not vary significantly between 3.5 and 3.0 Ma. Temperature estimates for the mPWP are suggested to be 2 – 3 °C higher during the Pliocene (Haywood and Valdes, 2004) compared to the preindustrial and even higher in the high latitudes (Ballantyne et al., 2010; Panitz et al., 2016). Therefore, the palaeotemperature estimates for the NW Qaidam Basin (mid-latitudes) are in contrast to these studies.

Model simulations from Li et al. (2018a) suggest that precipitation (MAP) in the Qaidam Basin was roughly 50 – 100 mm higher in the Pliocene compared to pre-industrial level. This is in a very good agreement with the climate estimates from the transfer functions in this study, and shows that the climate estimates, provided by this study, seem to be reasonable.

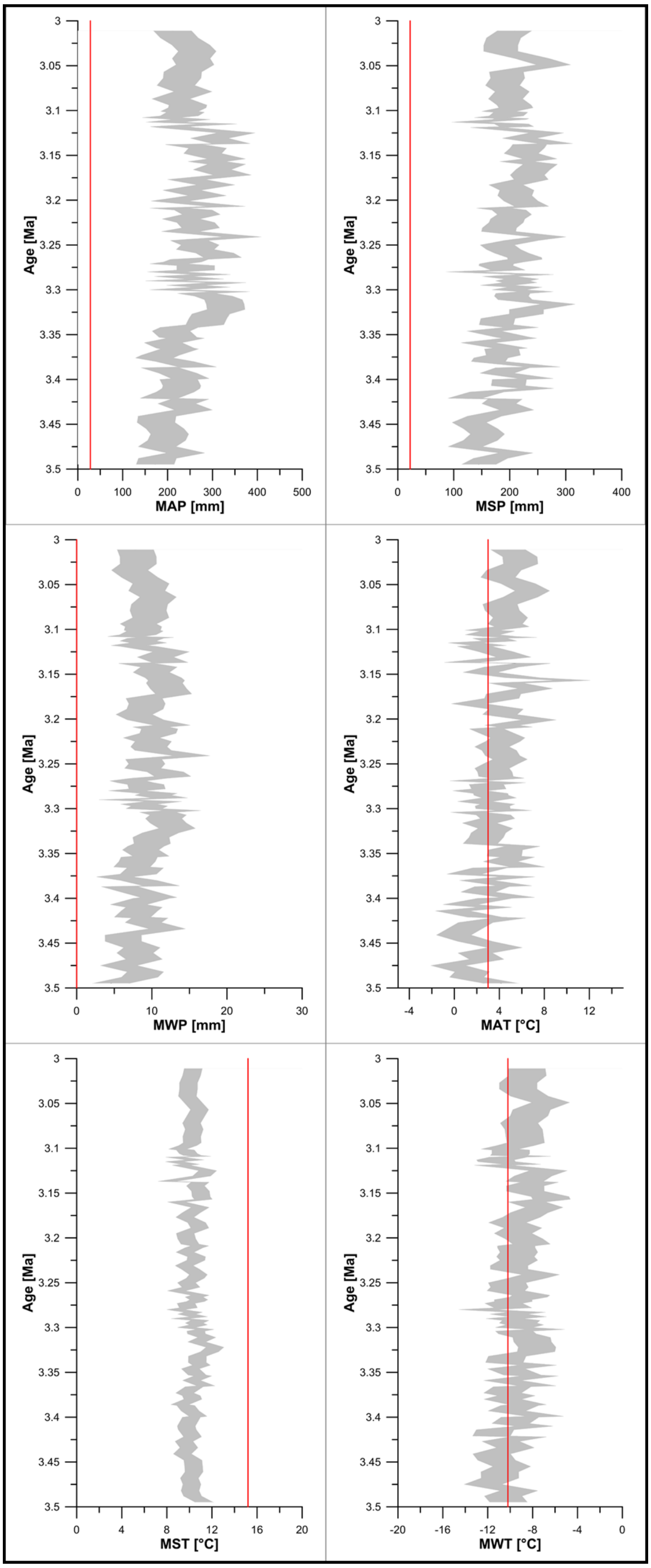

Fig. 4 - 32: Palaeoclimate estimates for the SG-1b core based on the established pollen – climate transfer functions. Ranges for the climate estimates are shown in grey. The red line represents modern values from the SG-1b coring site.

4.3.3.3 Link between moisture availability in NW Qaidam Basin and re-organisation of Pacific Ocean currents

Various studies reflected on the strength of both, the EASM and EAWM during the Pliocene. An et al. (2001) proposed that the EASM and EAWM were stronger between 3.6 and 2.6 Ma indicated by increased magnetic susceptibility, Rb/Sr ratios and Al flux on the CLP (Bajiazui section) and an increase of dust fluxes into the North Pacific which has been observed by Rea et al. (1998). An et al. (2001) suggests that uplift in the Tibetan Plateau played a role as a possible forcing mechanism for these changes in the EAM system. A higher Tibetan Plateau increases the area heated up (cooled down) during summer (winter) and thereby, forces stronger circulation in East Asia (An et al., 2001). Evidence for uplift on the eastern and northern parts of the Tibetan Plateau are based on increased sedimentation rates and the occurrence of molasse and conglomerate sediments in the record (An et al., 2001; Li et al., 1997; Métivier et al., 1998; Zheng et al., 2000). Ao et al. (2016), on the other hand, argues that an intensification of the EASM in the late Miocene and Pliocene is linked to ice sheet growth in Antarctica which caused an increase in the cross-equatorial SST gradient. Another explanation is related to the gradual closure of the CAS and the related reorganisation of the Pacific wind and ocean circulations (Nie et al., 2014). The study suggests that the closure of the Isthmus of Panama forced a freshening of equatorial Pacific waters (Haug and Tiedemann, 1998) which in turn lead to North Pacific and Arctic cooling, an increase in the North Pacific high pressure cell and thereby intensification of the EASM. In fact, the closure of the CAS is a major tectonic event during the Pliocene, which has been at the center of research related to changes in the thermohaline circulation and the onset of the NHG for decades. However, timings and consequences of the reorganisation of ocean current flow is still not fully understood. Haug and Tiedemann (1998) argue that diverging ocean carbon preservation in the Caribbean Sea (ODP Site 999) and in the Pacific (ODP Site 846) from 4.6 Ma onwards is a direct result of changing thermohaline circulation caused by the formation of the Isthmus of Panama. This is further supported by increased salt transportation to the North Atlantic and the intensification of the upper North Atlantic Deep Water (UNADW) (Haug and Tiedemann, 1998). Haug et al. (1999) showed that after 4.6 Ma, increased $\delta^{13}C$ values in the Caribbean Sea (ODP Site 999) correlate well with biogenic opal production in the northern subarctic Pacific (ODP Site 882). The authors related this to enhanced thermohaline circulation after a major step in closure of the CAS, causing increased nutrient supply to the subarctic Pacific where upwelling caused production of biogenic opal to rise steeply (Haug et al., 1999). After the onset of the NHG, though, increased sea-ice formation in the subarctic Pacific led to the establishment of a halocline leading to suppressed upwelling and a decline in biogenic opal production (Haug et al., 1999). Following the re-organisation of the thermohaline circulation, SST started to drop in the equatorial eastern Pacific after 4.2 Ma (Lawrence et al., 2006). Furthermore, Steph et al. (2010) concluded that the EEP cold tongue evolved around 4.0 Ma, during which for the first time the SST gradient between the western equatorial Pacific (WEP) and EEP was established. This has been based on comparisons of SST from ODP Sites 846 (Lawrence et al., 2006) and 806 (Wara et al., 2005). Fedorov et al. (2006), however, suggested that the onset of equatorial temperature gradient between the WEP and EEP has not occurred until 1.7 Ma by comparing ODP Sites 806 and 847. Steph et al. (2010) suggested that ODP Site 847 was not in the center of the EEP cold tongue during the early and middle Pliocene because of its similarities in mixed layer temperatures with ODP Site 1241 (East Pacific Warm Pool).

Fig. 4 – 33 shows the comparison of A/C ratios from this study with SST from ODP Site 846 in the EEP (Lawrence et al., 2006). The figure shows that the moisture availability in the NW Qaidam Basin increased during times of higher SST in the EEP. The higher SST in the EEP cause El Niño like conditions through reducing the equatorial temperature gradient across the Pacific (Steph et al., 2010), which results in EASM penetration into the NW Qaidam Basin. During Holocene times, Chavez et al. (1999) found that during the El Niño event in 1997-1998 weakening and reversal of trade winds in the WEP caused an eastwards extension of warm surface waters into the EEP and deepening of the thermocline by more than 90 m. The reversal of the trade winds caused local downwellings offshore South America, instead of the usual upwelling causing a decline in nutrient supply and bioproductivity (Chavez et al., 1999). In China, Lau and Weng (2001) indicated that during the 1997-1998 El Niño precipitation increased in parts of western China.

Furthermore, based on spatiotemporal tree ring information for the past centuries in East Asia, Cook et al. (2010) suggested that moisture availability increased over the eastern Tibetan Plateau when the SST increased in the EEP.

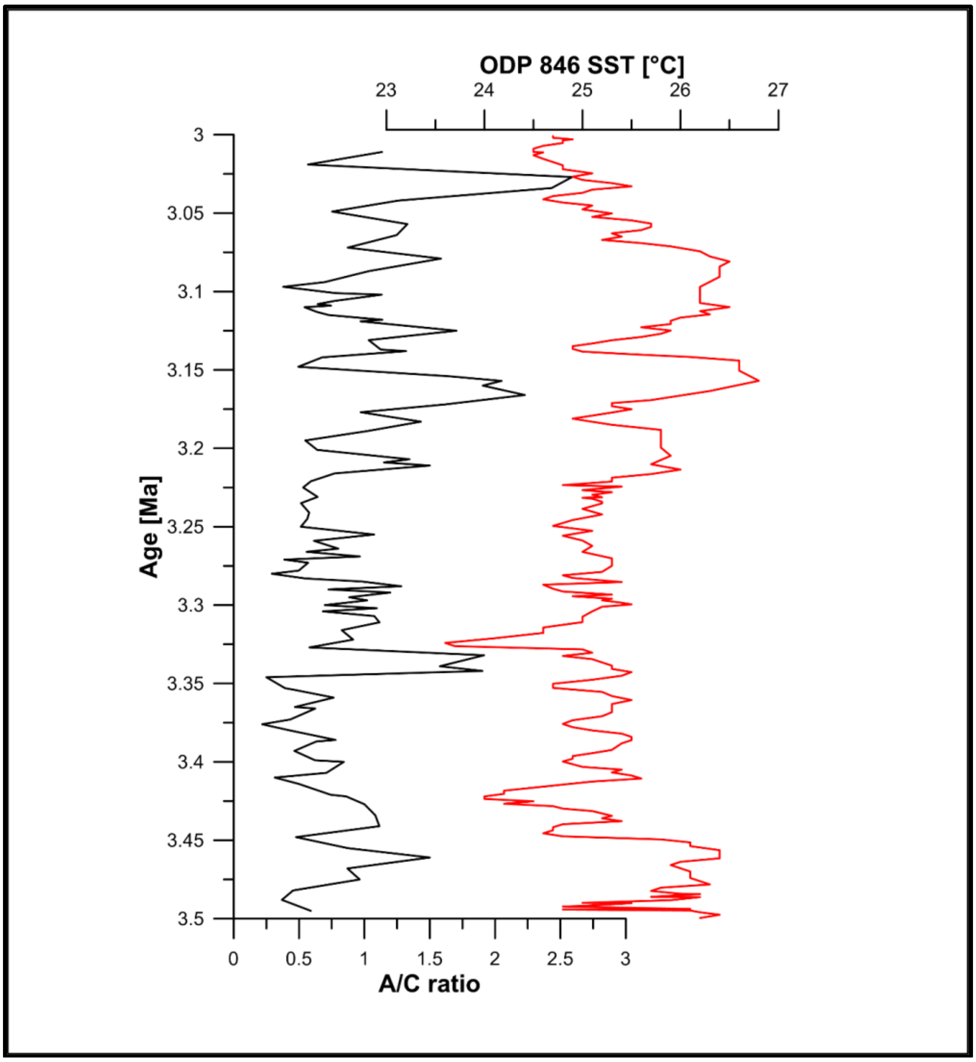

Fig. 4 - 33: Comparison of A/C ratios with SST reconstructions in the EEP (Lawrence et al., 2006) showing a good agreement for most of the record (except ~ 3.1 Ma).

Variability in intensity and distribution of EASM precipitation over China depending on the ENSO was discussed by additional studies (Hong et al., 2005; Shi et al., 2012; Zhang et al., 1996). Shi et al (2012) showed that in El Niño years (Niño 3.4 SST) compared to La Nina years summer precipitation, 500 hPa geopotential height and 850 hPa wind vectors increase at locations north of 30°N, whereas in southern East Asia (south of 30 °N) the opposing trend with enhanced drying has been observed. Similarly, data-model simulations from Brierley et al. (2009) propose that a reduced meridional temperature gradient between the EEP and California Margin in the Pliocene led to a decrease in precipitation intensities in the Intertropical Convergence Zones. Compared to modern day, the simulations suggest that southwestern and southeastern China were drier during the Pliocene whereas increased precipitation occurred north of 25 – 30°N between 80 and 110°E (Brierley et al., 2009).

Permanent El Niño conditions in the Pacific have been proposed to persist to at least ~ 3 Ma ago (Karas et al., 2009; Philander and Fedorov, 2003; Wara et al., 2005), which covers the whole SG-1b core interval from this study. Karas et al. (2009) suggested that termination of increased SST in the EEP (and therefore El Niño like conditions) occurred after 2.95 Ma as a result of oceanographic reorganisations caused by the constriction of the Indonesian Seaway between 3 and 4 Ma (Cane and Molnar, 2001). They found that gradual cooling and freshing at DSDP Site 214 (Tropical Eastern Indian Ocean) since 4.3 Ma was caused by a change from warm and salty South Pacific waters to cold and fresh North Pacific waters. The tectono-oceanographic development of the ITF is relevant for this study here, because according to Karas et al. (2009) and Rodgers et al. (2000) the northward movement of New Guinea caused a stronger Southern Ocean component in the Equatorial Undercurrent (EUC).

Modern and Late Pleistocene tracer studies, mineral fluxes and developments of $\delta^{14}C$ through the South and North Pacific led to the assumption that the EUC in the equatorial Pacific (Fig. 4 – 36) is being fed by Antarctic Intermediate Water (AAIW) and Subantarctic Mode Water (SAMW) originating from the SW and SE Pacific through the New Guinea Coastal Under Current, St. Georgen Under Current and New Ireland Undercurrent as well as a North Pacific source (Dugdale et al., 2002; Hu et al., 2016a; Leduc et al., 2010; Max et al., 2017; Rippert et al., 2017; Toggweiler et al., 1991; Wells et al., 1999). To identify changes in the feeding intermediate waters from the southern and Northern Hemisphere, marine proxies will be used to assess changes in high-latitude glaciation and intermediate water temperature changes that could drive changes in the equatorial thermocline (Fig. 4 – 34 and Fig. 4 – 35). Patterson et al. (2014) suggested that ice sheet forcings in Antarctica were driven by obliquity cycles until 3.5 Ma. Due to a combination of a low obliquity node and low eccentricity phase in the 400 ka cycles, orbital forcing of ice sheets could not be resolved sufficiently between 3.5 and 3.3 Ma, but the low obliquity node enhanced ice sheet growth (Patterson et al., 2014). Orbital forcing could also not be resovled for the period from 3.5 to 3.3 Ma in the SST reconstructions from Lawrence et al. (2006) in the EEP and in the A/C record from this study. The comparison of the A/C ratio in this study with insolation forcing indicates no consistent relationship with either northern or Southern Hemisphere forcing but rather constantly changing forcing.

After 3.3 Ma, Patterson et al. (2014) noticed a strong precessional forcing in the 65°S summer insolation driving changes in the Antarctic ice sheets causing the retreat of marine based ice to the Wilkes land (and causing the release of IRD) when warm ocean waters calved the marine ice sheets. From 3.3 Ma onwards, strong changes were also noted in the SW Pacific with a drop in δ^{18}O and increased δ^{13}C values (Caballero-Gill et al., 2019). The δ^{13}C signal at DSDP Site 594 also suggests that eccentricity and precessional forcing were the driving force for changes in AAIW temperature through modification of the Antarctic ice volume (Caballero-Gill et al., 2019).

The suggested warmer AAIW and SAMW waters in the SW Pacific have also also seen in reduced sand fractions (~ 3.3 – 3.2 Ma) of the sediments that Karas et al. (2011) use as an indicator for the migration or changes in strength (temperature/salinity) of AAIW and SAMW. In the EEP, where the EUC is fed by the AAIW and SAMW, a strong decrease in benthic δ^{18}O has been recognised post 3.3 Ma (until ca 3.15 Ma) (Shackleton et al., 1995) which indicates that the EUC warmed during this time period. The coherent phases of the benthic δ^{13}C signal at DSDP Site 594 and ODP Site 846 implies a strong correlation and only limited influence of North Pacific waters on the EEP during this time. In the time interval from 3.3 to 3.15 Ma, Karas et al. (2009) noticed a strong change in the subsurface of the Eastern Indian Tropical Ocean (EITO). The dominating trend from 3.5 Ma onwards at DSDP Site 214 is freshening and cooling of subsurface waters but has been interrupted by a period of warmer and saltier waters, which Karas et al. (2009) attributes to a change from predominantly North Pacific Waters to either increased influence of southern Indian Ocean or a return of South Pacific water through the Indonesian Seaway.

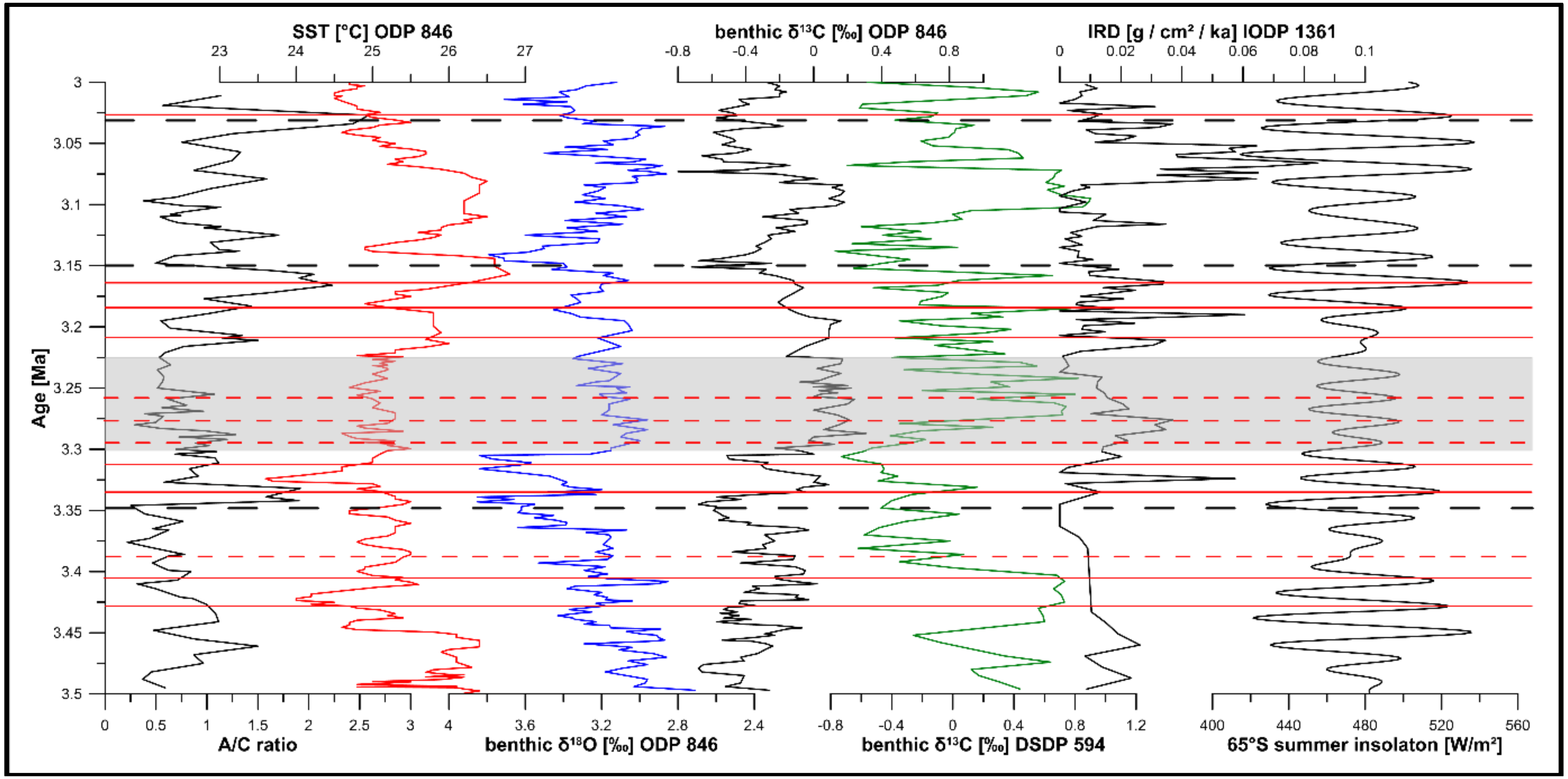

Fig. 4 - 34: Comparison of A/C ratio with SST from the EEP ODP 846 (Lawrence et al., 2006), benthic oxygen and carbon isotopes from ODP 846 (Shackleton et al., 1995), benthic carbon isotopes from DSDP 594 (Caballero-Gill et al., 2019), IRD from IODP 1361 (Patterson et al., 2014) and 65°S summer insolation (Laskar et al., 2004). The red lines show good agreements between the A/C ratios and the 65°S summer insolation. Slightly less good agreements are seen between 3.3 and 3.225 Ma (grey shaded interval) because no strong changes are seen in the A/C record as well as in the SST (Lawrence et al., 2006) and thermocline characteristics from ODP Site 846 (Shackleton et al., 1995). Despite the unclear/alternating forcing in the lowest interval (3.5 to 3.35 Ma), increasing SST in the EEP (Lawrence et al., 2006) are still well correlated to the A/C record. The relationship weakens around ~ 3.1 Ma, where thermocline waters ($\delta^{13}C$) in the EEP (Shackleton et al., 1995) still follow the signature of AAIW from DSDP Site 594 (Caballero-Gill et al., 2019) but A/C ratios were forced by NHG (see next figure).

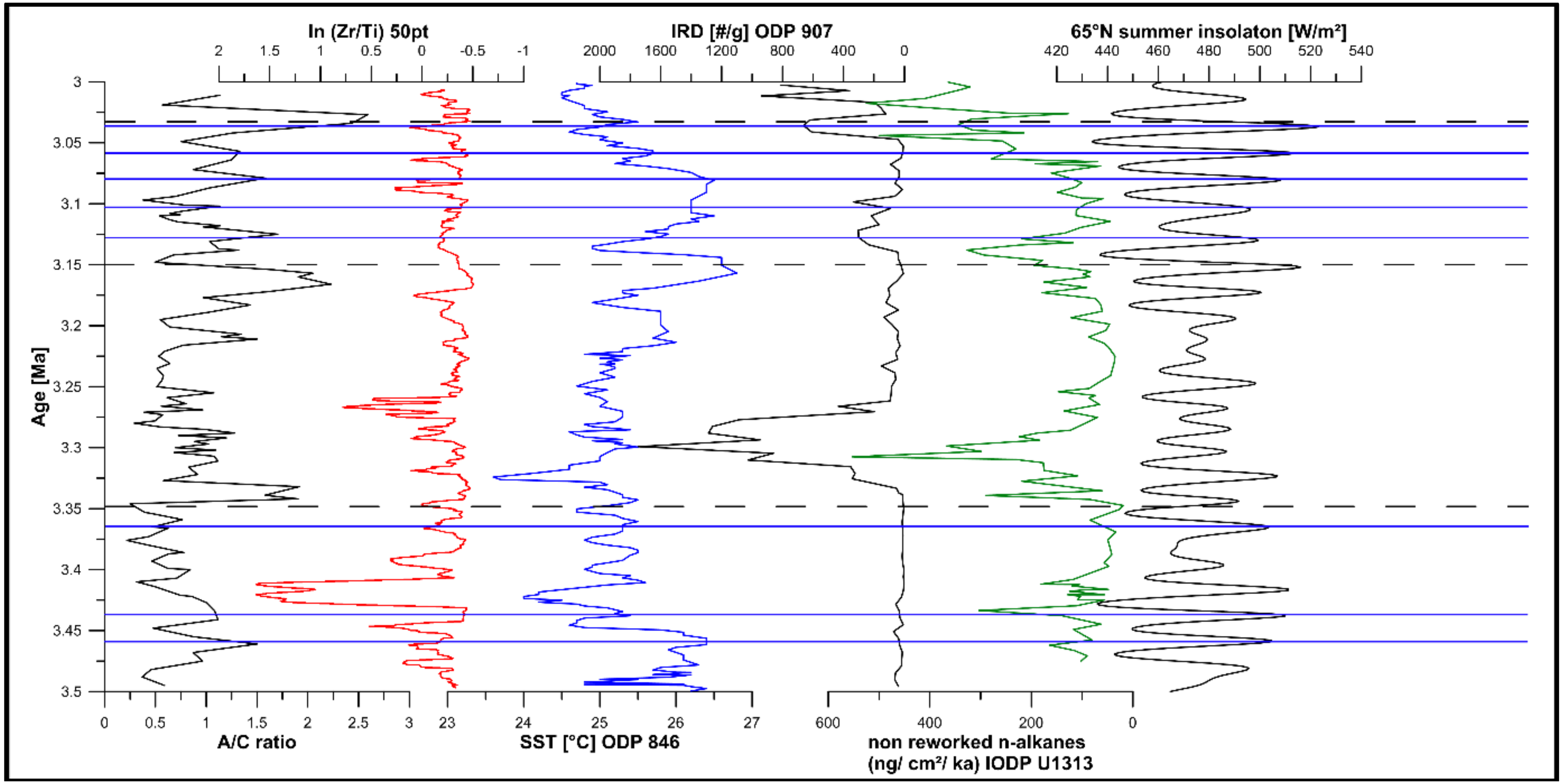

Fig. 4 - 35: Comparison of A/C ratio and grain size proxy with SST from the EEP ODP 846 (Lawrence et al., 2006), IRD from ODP 907 (Jansen et al., 2000), non-reworked n-alkanes from IODP 1313 (Naafs et al., 2012) and 65°N summer insolation (Laskar et al., 2004). The blue lines show good agreements between the A/C ratios and the 65°N summer insolation. A good agreement is also seen with increasing SST in the EEP (Lawrence et al., 2006) except around ~ 3.1 Ma. Non-reworked n-alkanes indicate increased eolian dust flux from North America into the Atlantic Ocean and are used as a proxy for increased NHG (Naafs et al., 2012). In the time interval from 3.5 to 3.35 Ma, only some peaks show a good agreement with the Northern Hemisphere summer insolation while matches were also found between A/C ratios and 65°S summer insolation (see previous figure).

South Pacific waters are strongly reduced from entering the EITO because of the northward movement of Guinea in the Pliocene (Cane and Molnar, 2001; Karas et al., 2009). However, it is not clear how the SAMW/AAIW could have entered the ITF. There are three possibilities: First of all, it is possible that passages opened/widened after 3.3 Ma, which led to a preferential flow from South Pacific Waters. Secondly, it is possible that the SAMW and AAIW were much stronger during this time interval, which led to a northward expansion of South Pacific Waters. Although Karas et al. (2011) suggest that SAMW and AAIW migrated northwards and/or freshened and cooled after 3.5 Ma, the resolution of the ODP Site 590B is not high enough to explicitely suggest such a development. Indeed, sand fractions of the sediment decreased after 3.3 Ma suggesting a southward retreat of SAMW and AAIW. Furthermore, McClymont et al. (2016) showed that temperatures in the subsurface were higher post 3.3 Ma. Instead, the timing of return towards South Pacific Waters through the Indonesian Seaway could be explained by strongly reduced North Pacific Waters as a consequence of ice sheet collapse in the Northern Hemisphere and subsequent lower production of NPIW, which has been suggested during deglaciation periods in the Late Pleistocene (Max et al., 2017; Rippert et al., 2017). At ODP Site 1208, strong warming of North Pacific Deep Waters (NPDW) was recognised between 3.3 and 3.15 Ma (Woodard et al., 2014), which could have been a direct consequence of ice sheet melting after MIS M2 and different ocean circulation (Woodard et al., 2014). The deepening of the thermocline in the EEP and the increase in SST after ~ 3.225 Ma is in good agreement with an increase in precipitation in the NW Qaidam Basin. Not only is the 65°S summer insolation forcing noticed in the Southern Ocean, EEP benthic isotopes and SST (Lawrence et al., 2006; Patterson et al., 2014; Shackleton et al., 1995), but also in the A/C ratio of this study. When ice sheets retreated during insolation maxima in the Southern Hemisphere, AAIW water becomes warmer, which then heats up the equatorial intermediate water causing a deeper thermocline and more El Niño like conditions in the EEP. This has a positive effect on the precipitation in the NW Qaidam Basin. After MIS M2, the strongly reduced Northern Hemisphere glaciers and ice sheets do not have a lasting effect on this connection.

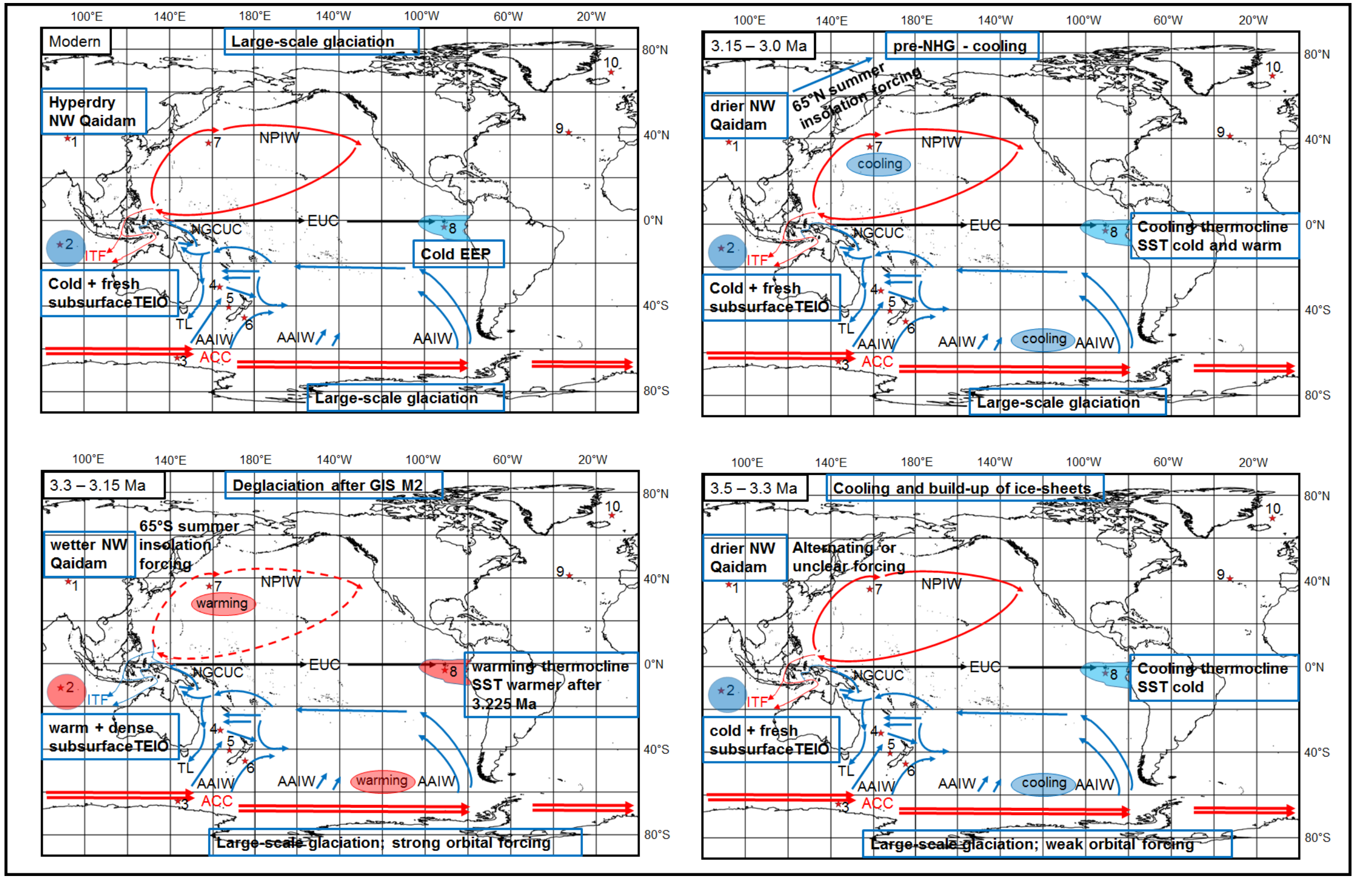

Fig. 4 - 36: The map overview shows a simplified relationship between Pacific Ocean currents on the Equatorial Undercurrent (EUC) and subsequently the EEP. Modern ocean currents direction taken from a compilation of sources (Bostock et al., 2010; Bostock et al., 2013; Gordon and Fine, 1996; Harper, 2000; Kawabe and Fujio, 2010; McCreary et al., 2007; Yang et al., 2017). During the intervals from 3.5 to 3.3 and 3.15 to 3.0 Ma, cooling in both high latitudes was observed which had a profound effect on the formation of AAIW and NPIW and the thermocline (+SST) in the EEP. During these intervals MAPs in the NW Qaidam Basin were lowest and no clear forcing (3.5 – 3.3 Ma) or Northern Hemisphere forcing (3.15 – 3.0 Ma) was observed in the A/C ratio. During the interval from 3.3 to 3.15 Ma, warming took place after MIS M2 which caused a warming in the AAIW and North Pacific Deep Waters (NPDW, no NPIW record available for this interval). Weakened North Pacific subsurface waters are assumed from the change of ITF at DSDP Site 214 (Karas et al., 2009). Strong warming in the EEP led to wetter conditions in the NW Qaidam Basin and forcing through Southern Hemisphere summer insolation (minima ice sheet extents). 1 = SG-1b core (this study), 2 = DSDP 214 (Karas et al., 2009), 3 = IODP U1361, 4 = DSDP 590B (Karas et al., 2011), 5 = DSDP 593 (McClymont et al., 2016), 6 = DSDP 594 (Caballero-Gill et al., 2019), 7 = ODP 1208 (Woodard et al., 2014), 8 = ODP Site 846 (Lawrence et al., 2006; Shackleton et al., 1995), 9 = IODP 1313 (Naafs et al., 2012), 10 = ODP 907 (Jansen et al., 2000).

After 3.15 Ma, the driving force of the A/C ratio changes from 65°S summer insolation to 65°N summer insolation. The records from the Southern Pacific, Antarctica and EEP, however, do not see such a change (Caballero-Gill et al., 2019; Lawrence et al., 2006; Patterson et al., 2014; Shackleton et al., 1995). The benthic $\delta^{13}C$ signal in the Southern Ocean still propagates through the EUC towards the EEP in the benthic $\delta^{13}C$ and SST (Caballero-Gill et al., 2019; Lawrence et al., 2006; Shackleton et al., 1995). Associated with a weakened connection to the EEP are increasingly dry conditions in the NW Qaidam Basin, which could be related to reduced EASM precipitation in the study area. The A/C ratios are linked to the Northern Hemisphere build-up of glaciers and increases during times of increased 65°N summer insolation when ice sheets retreated (Jansen et al., 2000; Kleiven et al., 2002) and climate conditions were less dry in the Northern Hemisphere (Naafs et al., 2012). Isotope analysis from Heermance et al. (2013) suggested that enhanced drying and a change in palaeocurrents occurred in the Qaidam Basin around 3.1 Ma which opens the possibility that atmospheric circulations changed. Clemens et al. (2008) and Sun et al. (2010) suggested that around 3.15 – 2.75 Ma major changes in EASM and EAWM interplay began. During the interval before 3.15 Ma, stronger EASM phases were occurring during stronger phases of EAWM, whereas after 3.15 Ma, stronger phases of EASM were antiphased to stronger phases of EAWM. Furthermore, the intensity of the EAWM increased strongly after 3.15 Ma. These observations are in good agreement with the findings of this study. The changes of high moisture availability during weak Northern Hemisphere summer insolations (colder intervals) to high moisture availability during strong Northern Hemisphere summer insolations (warmer intervals) show that Northern Hemisphere cooling after 3.15 Ma had a profound effect on atmospheric-ocean interactions related to monsoonal strength and variability (Clemens et al., 2008).

In order to assess the impact of the orbital forcing changes in the NW Qaidam Basin on the precipitation, Fig.4 – 37 shows a comparison of the reconstructed MAPs for the SG-1b core with changes in the EEP surface and thermocline conditions. During the grey-shaded interval from 3.3 to 3.15 Ma where the thermocline deepened (Shackleton et al., 1995) and SST underwent warming (Lawrence et al., 2006), MAP estimates are higher than in the previous or subsequent interval. However, this high-resolution study suggests that the onset of higher MAPs already started slightly earlier and lasted longer (~ 3.35 – 3.120 Ma) covering most of the mPWP.

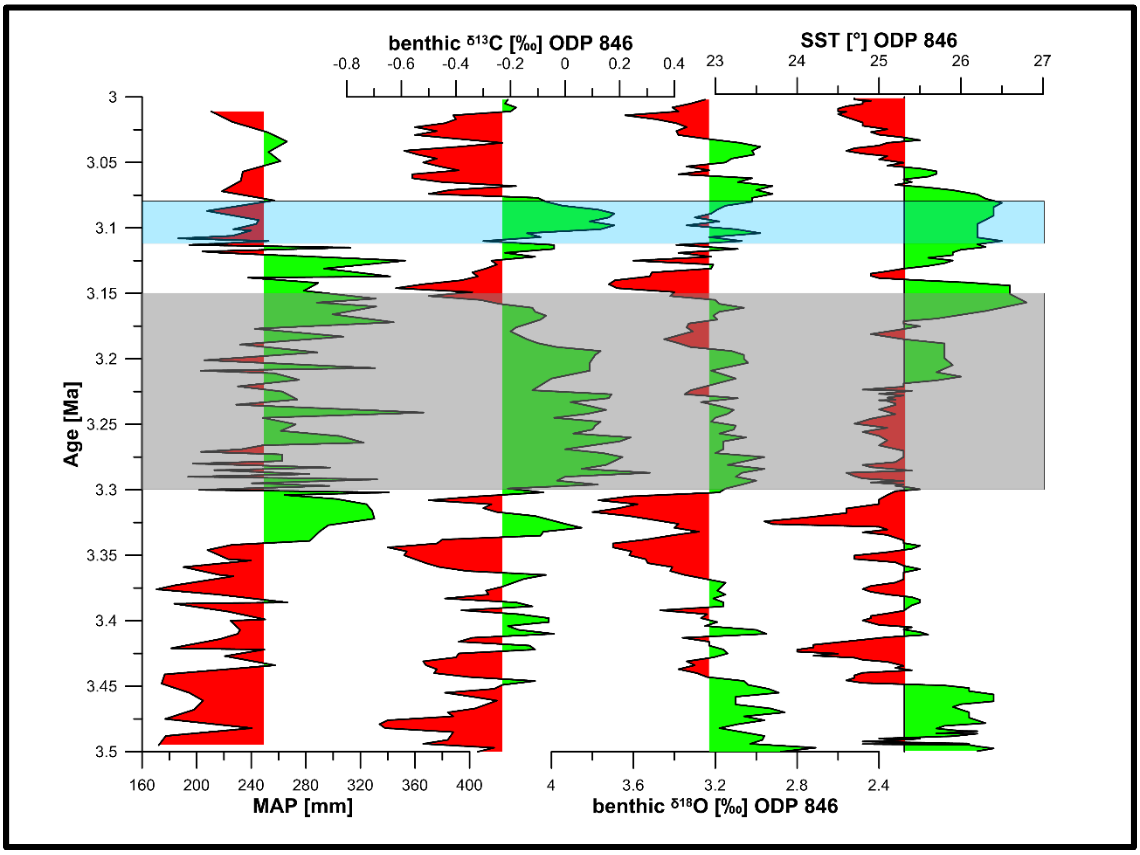

Fig. 4 - 37: Comparison of reconstructed precipitation estimates in NW Qaidam Basin with the evolution of the EEP, as expressed by thermocline conditions ($\delta^{18}O$, $\delta^{13}C$) (Shackleton et al., 1995) and SST (Lawrence et al., 2006). The grey shaded interval outlines the supposedly warmer conditions after MIS M2. The blue shaded interval depicts the onset of palaeocurrent changes and enhanced drying in the Qaidam Basin from Heermance et al. (2013).

Ji et al. (2017) proposed that the climate in Chaona, CLP, was drier during the mPWP and that drier conditions could be expected during periods of global warmth. Other low resolution studies from the CLP, also indicate that the mPWP was drier (Li et al., 2011). However, the results from this study show wetter conditions during the mPWP. Since the ENSO related precipitation patterns over East Asia vary from area to area (Cook et al., 2010; Lau and Weng, 2001; Shi et al., 2012), the results from this study and Ji et al. (2017), do not necessarily have to contradict each other. In order to see a full impact of the ENSO (or warming in EEP in general) on precipitation in East Asia, many more high-resolution studies all over China are needed.

4.4 Summary & Conclusions

The multi-proxy analysis of the SG-1b core for the time interval between 3.5 and 3.0 Ma revealed the following important findings:

- The NW Qaidam Basin underwent three major climatic stages: 3.5 – 3.285 Ma dry, 3.285 – 3.125 Ma wet and 3.125 – 3.011 Ma dry.

- The comparison to other high-resolution studies (Andreev et al., 2014; Demske et al., 2002; Panitz et al., 2016) showed that cooling and drying around 3.42 – 3.40 Ma and 3.28 – 3.265 Ma is specifically related to changes in the EAWM strength. Both, this study and the record from Lake Baikal (Demske et al., 2002) do not see drastic changes in the palaeovegetation around MIS M2 in contrast to the studies offshore Norway (Panitz et al., 2016) and in NE Siberia (Andreev et al., 2014). This seem to suggest that despite the characteristic cooling and build-up of ice sheets in the Northern Hemisphere MIS M2 has only a profound effect on palaeovegetation at study sites which are close to oceans. This has to be confirmed by more high-resolution studies that are close/far from marine sites though.

- The comparison of the results from the SG-1b core and other records from China (Fu et al., 2013; Fu et al., 2015; Li et al., 2018b; Liu et al., 2014) showed that the NW Qaidam Basin was strongly influenced from the EASM. The presence of a palaeolake and semi-desert vegetation suggests that the EASM penetrated further into NW China during the Pliocene compared to modern-day.

- Stronger EASM precipitation int the NW Qaidam Basin is related to warming in the EEP during times of orbital forced Antarctic ice sheet retreat (especially before 3.15 Ma).

- The A/C ratio indicates that major atmospheric changes took place around 3.15 Ma when the driving force for moisture in the NW Qaidam Basin changed from 65°S summer insolation forcing to 65°N summer insolation. Previous studies (Clemens et al., 2008; Sun et al., 2010) have suggested that before 3.15 Ma strong EAWM was occuring during phases of strong EASM, which then changes into strong (weak) EAWM being coupled with weak (strong) EASM. This study is able to provide palynological evidence for the conclusion of Clemens et al. (2008) that the onset of the NHG changed the timings between the EASM and EAWM. However, the studies suggest that the final change occurred at 2.75 Ma (Clemens et al., 2008; Sun et al., 2010) with a preceding transition period between 3.15 and 2.75 Ma (Sun et al., 2010). The A/C record, though, demonstrates that the change of phases between EASM and EAWM could have happened sharply at ~ 3.15 Ma.

- The palaeoclimate estimates based on the pollen – climate transfer functions indicate that the NW Qaidam Basin received about four to twentyfold precipitation (MAP ~ 120 – 400 mm) compared to modern-day. This estimate is in good agreement to a recently published modelling study of precipitation changes during the mPWP from Li et al. (2018a). The temperature estimates do not indicate much variability over the interval from 3.5 to 3.0 Ma. While the MAT do not show any similarities to the dry-wet-dry succession, MST and MWT indicate that the period from 3.3 to 3.125 was slightly warmer than the interval from 3.5 to 3.3 Ma and 3.125 to 3.0 Ma. The MAT reconstructions are similar to modern-day MATs in the NW Qaidam Basin and show no strong Pliocene warming compared to other high-latitude study sites (Panitz et al., 2016). Since the vegetation in arid Central Asia is mostly determined by precipitation and not temperature (Gessner et al., 2013), such an outcome (higher precipitation, similar temperature) might be an expression of the Pliocene warming over the oceans.

Chapter 5: Plio-Pleistocene vegetation and climate history of the Kunlun Pass Basin: An example of late Neogene tectonic uplift on the NE Tibetan Plateau?

5.1 Introduction

The uplift history of the northeastern part of the Tibetan Plateau has been subject to controversy for at least twenty years. An overview over the timing of uplift on the Himalayan-Tibetan Plateau is shown by the map from Tapponnier et al. (2001), which suggests that the northeastern and northwestern parts of the Tibetan Plateau are the youngest parts of the mountain range (Fig. 5 – 1). While Tapponnier et al. (1986) and Molnar et al. (1993) suggest that most of the uplift has been completed prior to the Late Miocene, others suggested that main tectonic uplift movements occurred during Plio-Pleistocene times (An et al., 2001; Cui et al., 1998; Hsü, 1976; Li et al., 1981; Zheng et al., 2000). The uncertainty in the uplift history also manifests itself in estimates of the Kunlun Pass Basin altitude during the Late Pliocene which ranges from 1000 – 1500 m based on ostracods and pollen data (Wu et al., 2001), 400 - 3600 m based on stable isotopes (Wang et al., 2008b) and 3200 – 4200 m based on the identification of fish species (Wang and Chang, 2010). All these studies have in common that their palaeoaltitudinal estimate of the Kunlun Pass Basin is lower than the modern height (4700 – 5300 m). Based on the identification and dating of the Kunlun Yellow River movement, Cui et al. (1998) even suggested that the Kunlun Pass Basin was still at a height of ~ 1000 – 1500 m until 1.1 Ma and has only since then been significantly uplifted to its modern altitude. By recording palaeovegetation changes at this high-altitude site during the warmer Pliocene and the Plio-Pleistocene transition, this study presents a palynological view into the palaeoaltitudinal discussion of this part of the Tibetan Plateau. The palynological data will be compared to isotope data from the same samples provided by project partners (Prof. Carmala N. Garzione, Feng Cheng; University of Rochester, United States) to distinguish changes in palaeovegetation related to tectonics or climate evolution. For this purpose, the Kunlun Pass Basin record will also be compared to the Qaidam Basin record (SG-1b core, Chapter 4), which at a lower modern elevation, should provide insights into whether changes in the vegetation composition were similar or diverged between the two study sites during the Pliocene.

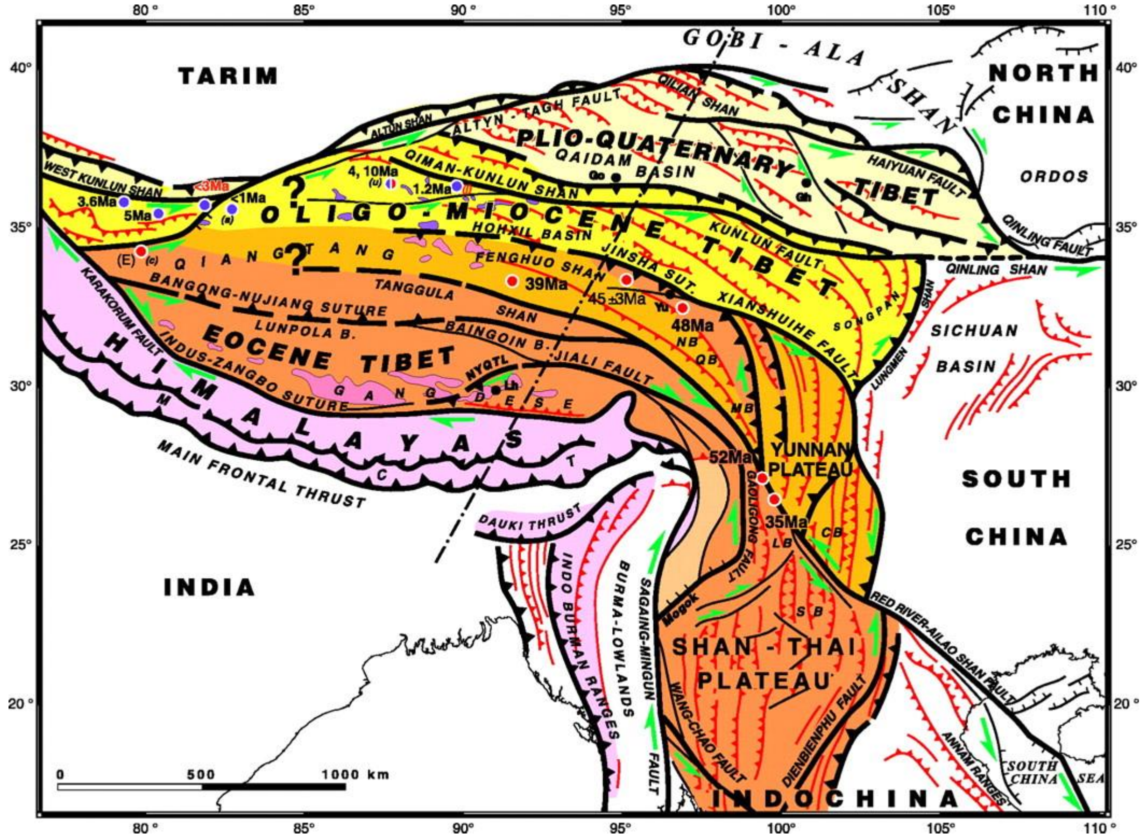

Fig. 5 - 1: Map overview for uplifted areas on the Tibetan Plateau from Tapponnier et al. (2001).

5.2 Results

A total of 154 pollen samples were counted from the Kunlun Pass Basin outcrop that relates to an age range of 4.314 to 0.852 Ma (see Age Model in Chapter 3.2.2). The pollen and spore concentrations ranged between 68 and 10,000 grains/g sediment (wet) for all samples, however concentrations over 4,000 grains / g sediment (wet) only occurred rarely. Based on CONISS (Grimm, 1987), the pollen assemblages from the Kunlun Pass Basin record (Fig. 5 – 2 and Fig. 5 – 3) can be divided into 4 main and 12 subzones. Generally, the pollen assemblage of the Kunlun Pass Basin is dominated by xerophytic shrub taxa, such as Chenopodiaceae, *Artemisia*, Caryophyllaceae, Asteraceae and *Ephedra* *spp.* The grasses Poaceae and Cyperaceae occurred consistently around 10% throughout the record, however increased strongly in pollen zone 4-A (after 2.6 Ma). The broadleaved trees occurred in higher abundances in the lowermost part of the record and declined thereafter whereas coniferous trees occurred in higher abundances during some intervals throughout the record. A more detailed description of the PAZ is given below.

The PAZ 1-A (4.314 – 4.157 Ma) is characterised by high percentages of Chenopodiaceae (22.92 – 61.68%) with lower contributions from *Artemisia* (5.88 – 33.23%). The grasses Poaceae (2.99 – 29.33%) and Cyperaceae (1.20 – 20.16%) are abundant. Other herbaceous taxa which are present are Asteraceae (0 – 14.04%), Caryophyllaceae (1.23 – 7.02%) and *Ephedra spp*. (0 – 4.10%).Since changes in *Ephedra spp.* are not significant throughout the record, it will not be specified further. Coniferous trees are low (0 – 15.28%) compared to the whole record with *Pinus* being the most abundant. Broadleaved trees (1.68 – 27.22%) are highest in PAZ 1-A compared to the whole record with several *Betula* spikes visible in this zone.

Most notably in PAZ 1-B (4.157 – 4.030 Ma) is the drop in broadleaved trees (0.65 – 6.48%). Compared to pollen assemblage zone 1-A, they do only comprise half of the average pollen percentage. Simultaneously to the decrease in broadleaved trees, abundances in coniferous trees (2.26 – 30.77%) increase significantly, along with Asteraceae (1.75 – 16.82%), Caryophyllaceae (0 – 24.52%) and Cyperaceae (0 – 13.74%). Poaceae (0 – 20.55%) decrease gradually throughout this zone. *Artemisia* (6.77 – 47.74%) and Chenopodiaceae (8.71 – 41.10%) remain largely unchanged compared to PAZ 1-A.

In PAZ 2-A (4.030 – 3.857 Ma) coniferous trees remain on an elevated level (2.68 – 47.21%) whereas no significant changes for broadleaved trees are recorded (0 – 12.77%). Asteraceae (0.63 – 5.20%), and Caryophyllaceae (0 – 9.32%) return to lower values. Poaceae (3.19 – 27.45%) and especially Cyperaceae (2.13 – 24.13%) increase along with *Artemisia* (9.15 – 34.60%), whereas Chenopodiaceae (6.69 – 50.00%) decrease.

The PAZ 2-B (3.857 – 3.563 Ma) is characterised by a sharp decrease in coniferous trees (0 – 18.55%) and to a minor extent broadleaved trees (0 – 7.61%). *Artemisia* (9.64 – 38.37%), Asteraceae (0.31 – 18.07%), Caryophyllaceae (0 – 7.14%), Poaceae (3.57 – 18.07%) and Cyperaceae (3.23

– 20.48%) remain at their previous level. Chenopodiaceae (19.28 – 64.15%) increases strongly at the onset of this PAZ.

PAZ 2-C (3.563 – 3.279 Ma) is very similar to PAZ 2-B. Chenopodiaceae (25.93 – 66.67%) is very high whereas *Artemisia* (8.08 – 35.73%) is slightly lower. Poaceae (5.58 – 22.81%), Cyperaceae (1.39 – 27.49%), Asteraceae (0 – 7.41%), and Caryophyllaceae (0 – 7.04%) remain unchanged. Coniferous (0 – 11.63%) and broadleaved trees (0 – 5.26%) decrease further in this PAZ.

PAZ 2-D (3.279 – 3.025 Ma) is characterised by a strong increase in *Artemisia* (11.46 – 48.00%) at the expense of Chenopodiaceae (31.33 – 59.14%), Poaceae (3.59 – 23.25%), Cyperaceae (0 – 12.00%), Asteraceae (0 – 6.77%), Caryophyllaceae (0 – 6.35%) and coniferous trees (0 – 8.40%) are all dropping slightly. Broadleaved trees (0 – 3.27%) remain unchanged at low values.

PAZ 3-A (3.025 – 2.974 Ma) is characterised by a very strong increase in coniferous trees (6.90 – 34.32%). *Artemisia* (28.92 – 48.22%) continues to increase whereas Chenopodiaceae (15.43 – 28.97%) drop to their lowest values in the entire Kunlun Pass Basin record. Poaceae (3.56 – 9.66%), Cyperaceae (0.86 – 9.66%), Asteraceae (0.27 – 2.07%) and Caryophyllaceae (0 – 0.81%) occur with slightly lower percentages. Broadleaved trees (0.69 – 3.45%) increase, however, not as strongly as the coniferous trees.

The coniferous trees decrease (2.11 – 12.00%) steeply at the onset of PAZ 3-B (2.974 – 2.741 Ma). *Artemisia* (15.91 – 48.61%) also decreases in this zone whereas Chenopodiaceae (24.00 – 60.81%) recovers to its levels from PAZ 2-D. Asteraceae (0.33 – 3.57%), Poaceae (4.97 – 15.91%), Cyperaceae (0 – 21.33%) and Caryophyllaceae (0 – 4.00%) increase slightly. The broadleaved trees remain unchanged between 0 and 4.55%.

The PAZ 3-C (2.741 – 2.609 Ma) is characterised by a strong rise in *Artemisia* (16.67 – 58.66%) at the onset of this interval. However, subsequently *Artemisia* is declining to the levels of the previous PAZ (3-B). In contrast, Chenopodiaceae (8.02 – 52.51%) is increasing as well as Poaceae (3.77 – 21.67%) and Cyperaceae (3.77 – 21.67 %). Caryophyllaceae (0 – 2.53%) and Asteraceae (0 – 6.67%) are present. Coniferous trees (1.12 – 46.41%) occur in low abundances except for the uppermost sample, which showed a very high value. The broadleaved trees increase slightly in this zone (0 – 6.67%).

The PAZ 4-A (2.609 – 2.183 Ma) is characterised by a sharp decrease in broadleaved trees (0 – 5.41%), which remained at very low levels hereafter. This decline marks the second abrupt decrease in broadleaved trees after the change from PAZ 1-A to 1-B. *Artemisia* (11.01 – 25.00%) and Chenopodiaceae (10.05 – 67.74%) decrease to low levels in this zone, whereas Poaceae (7.45 – 30.19%) and especially Cyperaceae (1.92 – 37.67%) steeply increase at ~ 2.50 Ma. Afterwards, the abundances in Cyperaceae start to decline gradually while Poaceae levels stay high. Asteraceae (0 – 8.33%) and Caryophyllaceae (0 – 3.77%) remain unchanged. The coniferous trees (0 – 21.47%) increase after 2.5 Ma towards the top of this zone.

PAZ 4-B (2.183 – 1.789 Ma) is characterised by an abrupt increase of Chenopodiaceae (46.70 – 70.74%) and simultaneously sharp decrease in Poaceae (7.45 – 22.80%), Cyperaceae (1.06 – 18.15%) and coniferous trees (1.20 – 5.95%). In contrast to Chenopodiaceae, *Artemisia* (4.85 – 14.89%) does not show a strong change at the beginning of this zone but rather declines gradually. Asteraceae (0.52 – 2.80%), and Caryophyllaceae (0 – 3.08%) decrease and become partly absent in some samples. Only few broadleaved trees were found in this zone (0 – 0.44%).

In PAZ 4-C (1.789 – 0.852 Ma) *Artemisia* (20.19 – 24.88%) increases gradually whereas Chenopodiaceae (35.21 – 44.79%) declines. Poaceae (7.93 – 16.90%) decreases significantly at the onset of this zone, whereas Cyperaceae (8.74 – 17.31%) becomes more abundant. They generally show opposing trends since ~ 2.4 Ma which also continues in this interval. Asteraceae (0.47 – 3.07%), Caryophyllaceae (0 – 3.13%), coniferous (1.71 – 7.67%) and broadleaved trees (0.31 – 1.71%) do not change significantly and only occur at a very low levels.

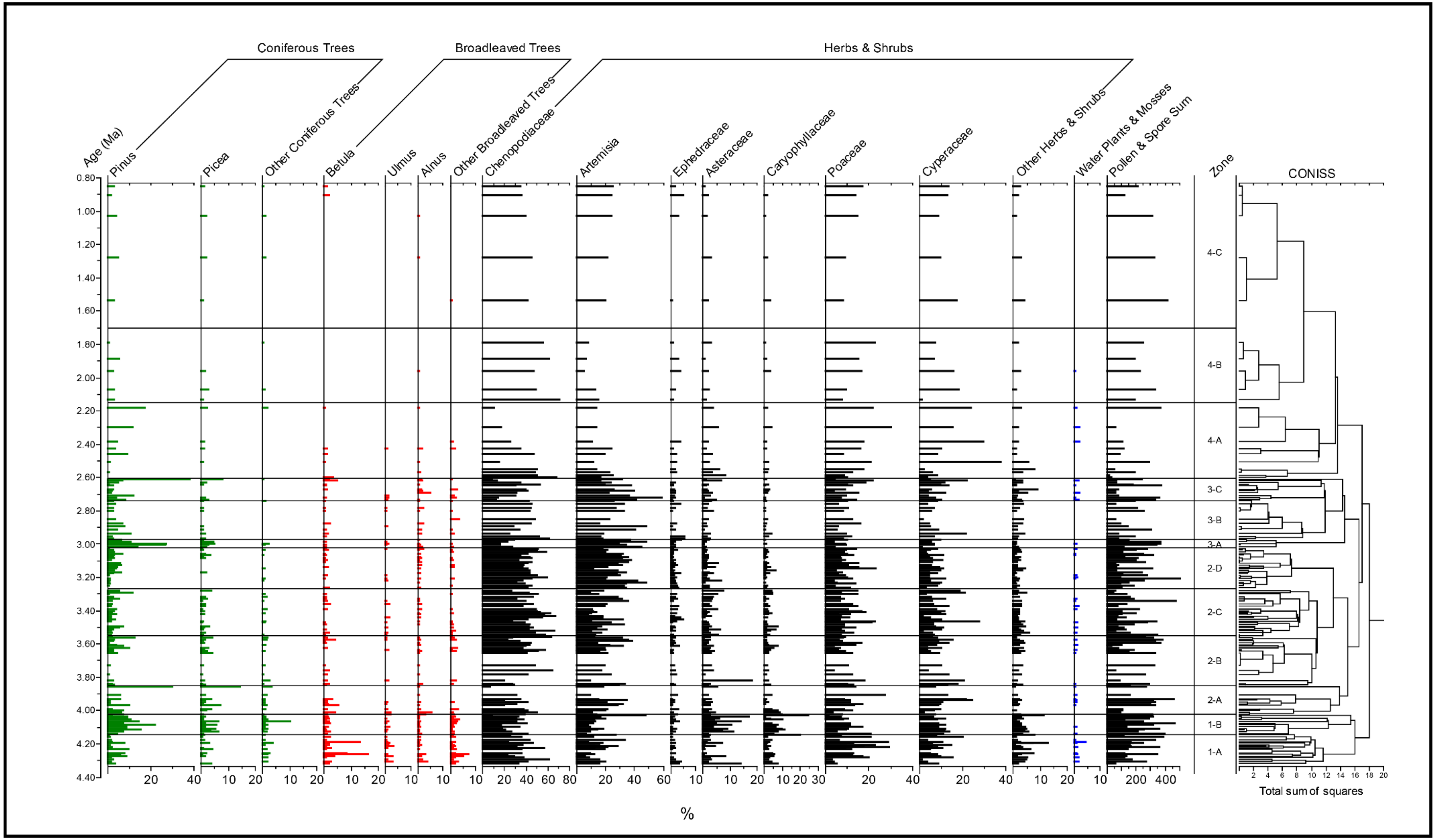

Fig. 5 - 2: Pollen diagram of the Kunlun Pass Basin (main taxa).

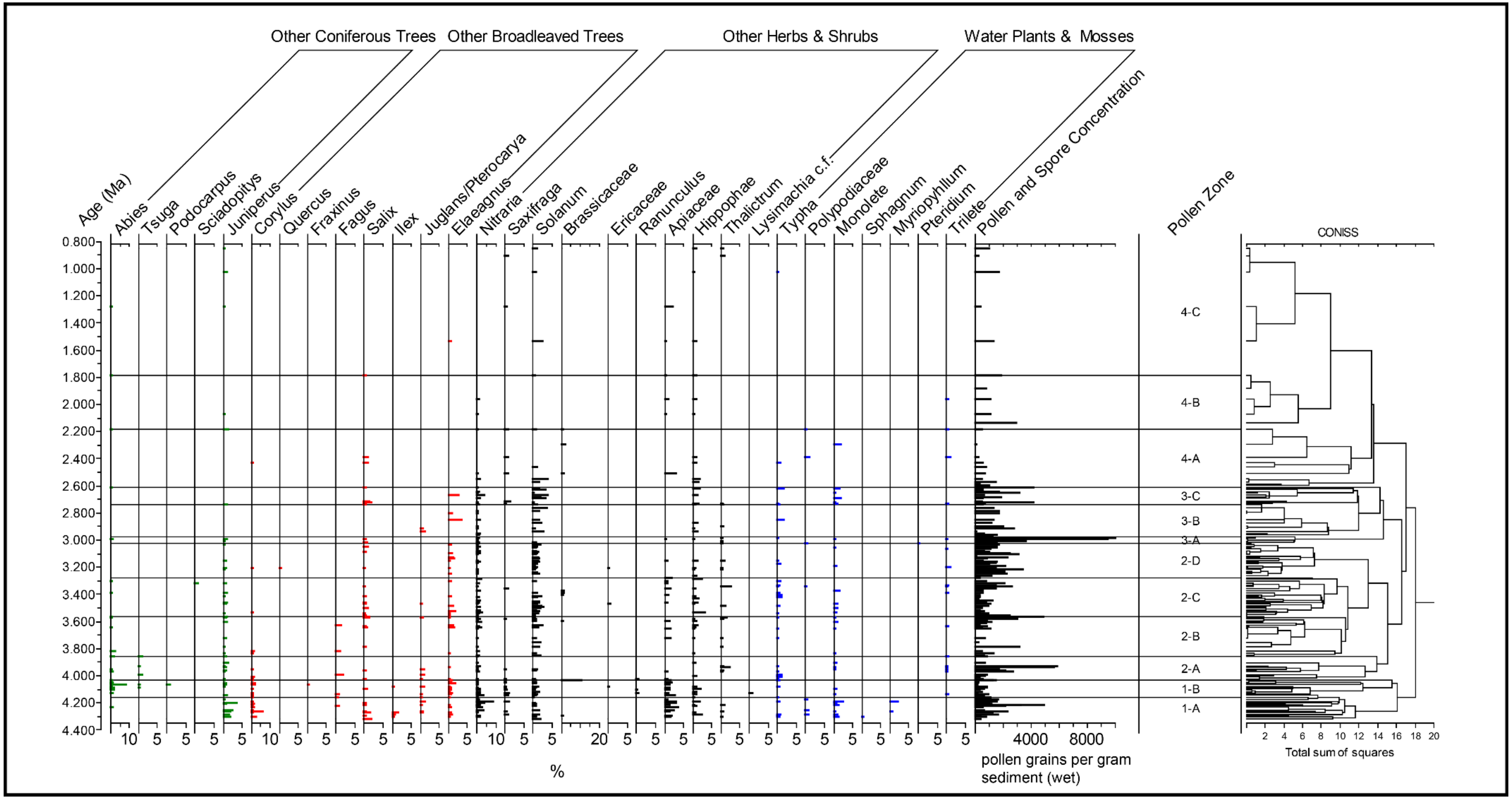

Fig. 5 - 3: Pollen diagram of the Kunlun Pass Basin (all other taxa).

5.3 Discussion

5.3.1 Kunlun Pass Basin and SG-1b core: similar pollen assemblages – same interpretation of the pollen signal?

Although the Kunlun Pass Basin palynological record has similar pollen assemblages as the SG-1b core from the NW Qaidam Basin (Chapter 4.3.2.1), a separate interpretation is required because the Kunlun Pass Basin is located at the top of a mountain range whereas the SG-1b core is located in an intramontane basin (surrounded by mountains).

Mountainous broadleaved and coniferous forest vegetation

The broadleaved pollen in the Kunlun Pass Basin record represent patches of broadleaved dominated woodlands and cool- or cold-temperate mixed broadleaved and coniferous forests. Especially at the base of the pollen record, broadleaved tree pollen occur in high amounts (up to 27.2 %), which indicates that patches of broadleaved forests were growing close to the study site. These broadleaved forests were mainly consisting of *Betula*, *Ulmus*, *Corylus*, *Salix* and *Alnus*. *Juniperus* occurred in high amounts in the first pollen zone with the other broadleaved trees (and declined afterwards), which indicates that it grew in the cool- or cold-temperate mixed broadleaved and coniferous forests and not in the cold-temperate coniferous forests.

The coniferous tree pollen (especially *Pinus*, *Picea*, *Abies*) represent cold-temperate coniferous forests or mountain forests. In contrast to the broadleaved forests which retreated after PAZ 1-A, *Pinus*-*Picea* coniferous forests expanded multiple times into the Kunlun Pass Basin area. The absence of such advances by broadleaved forests into the Kunlun Pass Basin likely reflects that temperatures were too low for broadleaved trees (after PAZ 1-A) while coniferous forests were able to grow in the area during times of increased precipitation.

Xerophytic Shrublands

The xerophytic taxa in the Kunlun Pass Basin record include Chenopodiaceae, *Artemisia*, *Ephedra*, *Nitraria*, Asteraceae and Caryophyllaceae. In contrast to the NW Qaidam Basin pollen record, in which these taxa characterise a temperate semi-desert vegetation, the Kunlun Pass Basin pollen record exhibits some distinct differences. First of all, *Ephedra spp.* is less represented in the Kunlun Pass Basin record and generally comprises between 1.10 and 2.15%, whereas *Ephedra spp.* percentages in the SG-1b record ranged usually between 5.20 and 12.80%. Tab. 5 – 1 and Fig. 5 – 4 show the general altitudinal relationship of *Ephedra* in NW China based on the dataset provided by Prof. Jian Ni (Chen et al., 2010b; Ni et al., 2014). Averaged for 500 m intervals, the figure shows that *Ephedra* percentages drop significantly above 3000 m. In addition, Cour et al. (1999) found that *Ephedra* occurred in high abundances in low elevation semi-deserts in the Western Kunlun and Taklamakan Mountains, while *Ephedra* typically dropped to 2% in high mountainous areas (Karakorum Mountains). Cour et al. (1999) also suggested that in alpine locations in western China, Asteraceae almost exclusively consist of Tubuliflorae type whereas Liguliflorae type has been very rare. Liguliflorae type make up to 2.87% and 6.74% of Asteraceae in the Kunlun Pass Basin and SG-1b record, respectively, which suggests that the Kunlun Pass Basin record is situated at a higher elevation. High abundances of Asteraceae and Caryophyllaceae are recorded at the onset of the Kunlun Pass Basin record (pollen zones 1-A, 1-B, 2-A, 2-B) coinciding with higher percentages of broadleaved and coniferous tree pollen. During present-day, Yu et al. (2001) found Caryophyllaceae in higher abundances in high-altitude sites, which is supported by the modern pollen dataset that shows a strong increase of Caryophyllaceae above 4500 m (Tab. 5 – 1).

Taking these differences between the SG-1b record and the Kunlun Pass Basin into account, the xerophytic shrublands represent alpine and not temperate semi-deserts in this record.

Tab. 5 - 1: Altitudinal distribution of *Ephedra* and Caryophyllaceae (averages per elevation interval). Based on provided modern pollen dataset from Prof. Jian Ni (Chen et al., 2010b; Ni et al., 2014).

Altitude - low [m]	Altitude - high [m]	Nr. of sites	*Ephedra* [%]	Caryophyllaceae [%]
0	500	14	4.46	0.02
500	1000	36	6.38	0.02
1000	1500	48	7.61	0.21
1500	2000	42	11.25	0.19
2000	2500	50	3.12	0.28
2500	3000	82	7.41	0.23
3000	3500	190	2.40	0.55
3500	4000	112	2.57	0.69
4000	4500	164	1.10	0.37
4500	5000	156	0.55	2.20
5000	5500	13	1.27	10.42

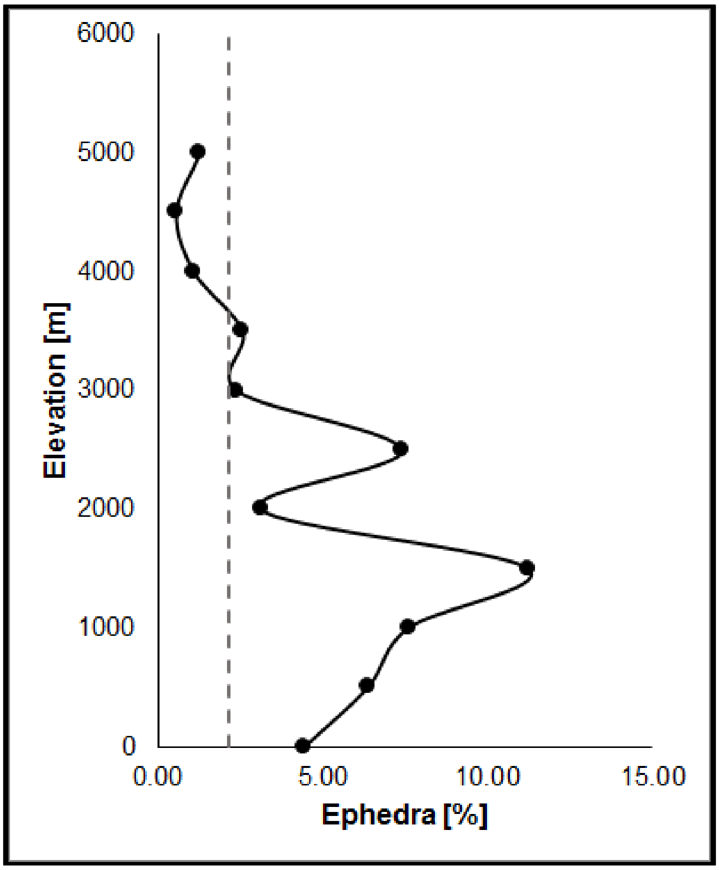

Fig. 5 - 4: Elevation profile of *Ephedra* in modern pollen samples (Dataset from Prof. Jian Ni, same as used for developing the modern pollen-climate dataset). *Ephedra* percentages were averaged in 500 m intervals. Elevations on the y axis show lower part of that interval (e.g. 2000 m refers to 2000 – 2500 m interval). Grey dashed line shows the maximum average of *Ephedra* in pollen assemblage zones of the Kunlun Pass Basin record.

Alpine steppes and meadows

The interpretation of Poaceae and Cyperaceae is slightly more challenging in the Kunlun Pass Basin record compared to the SG-1b core, because no additional information (lithology, XRF facies) are available for these outcrop samples. It is possible that Poaceae and Cyperaceae are representing lakeshore grasses similar to the SG-1b palaeolake. In contrast to the SG-1b core though, *Typha* is not present consistently in the pollen record, which could point to a reduced lakeshore vegetation or a reduced importance of local lakeshore pollen on the pollen assemblage in case of a large lake size (Vincens et al., 2005). Poaceae and Cyperaceae consistently have combined values of ~ 20 – 25% for most pollen zones in the Kunlun Pass Basin record, whereas in the SG-1b record Poaceae and Cyperaceae comprised less than 10% for most intervals. Therefore, instead of being interpreted as lakeshore vegetation, Poaceae and Cyperaceae represent steppe/meadow elements in this record. The higher Poaceae and Cyperaceae occurrences are also in good agreement with the modern vegetation on the Tibetan Plateau (Fig.5 – 5), where large parts of the central Tibetan Plateau are covered by alpine steppes and alpine meadows (Ni, 2001; Ni and Herzschuh, 2011; Song et al., 2005b; Yu et al., 2001).

PCA

In Fig. 5 – 6 the PCA of the Kunlun Pass Basin pollen record is shown. A distinction can be made between xerophytic shrubs I, xerophytic shrubs II + other herbs, broadleaved trees, coniferous trees and the grasses Poaceae and Cyperaceae. The xerophytic shrubs I group consist of Chenopodiaceae, *Ephedra* and *Artemisia.* They have the lowest PCA Axis 1 values which suggests that the first PCA Axis represents a precipitation gradient from dry conditions (low PCA Axis 1 values) to wet conditions (high PCA Axis 1 values). This is further supported by the relatively higher PCA Axis 1 value of *Artemisia* in comparison to Chenopodiaceae which can be explained by the higher moisture need of *Artemisia* (El-Moslimany, 1990; Zhao et al., 2012; Zhao et al., 2007).

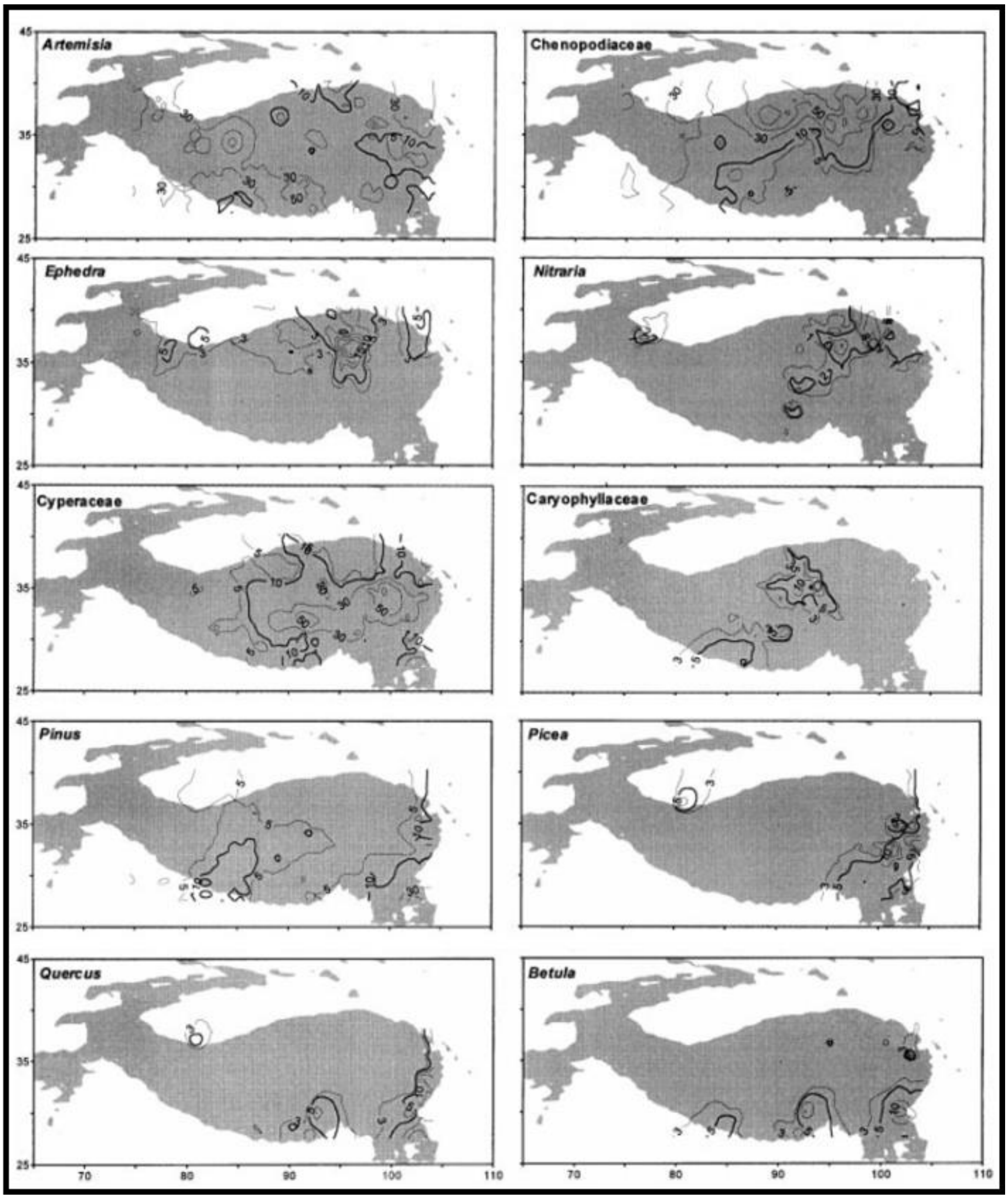

Fig. 5 - 5: Modern pollen distributions on the Tibetan Plateau taken from Yu et al. (2001).

Asteraceae and Caryophyllaceae are the two members of the xerophytic shrubs II + other herbs group in this pollen record. Their clear difference from the xerophytic shrubs I group along PCA Axis 1 indicates different preferable climate conditions (higher precipitation / moisture availability). Moreover, the coniferous trees, broadleaved trees and grasses have positive PCA Axis 1 values which indicates that these groups occurred during wetter conditions. Along PCA Axis 2 there is a clear gradient from grasses (negative PCA Axis 2 values) to xerophytic shrubs II + other herbs and coniferous trees (~ slightly negative/positive PCA Axis 2 values) and broadleaved trees (positive PCA Axis 2 values). This sequence can be interpreted as a temperature gradient from alpine steppe/meadow elements towards broadleaved trees.

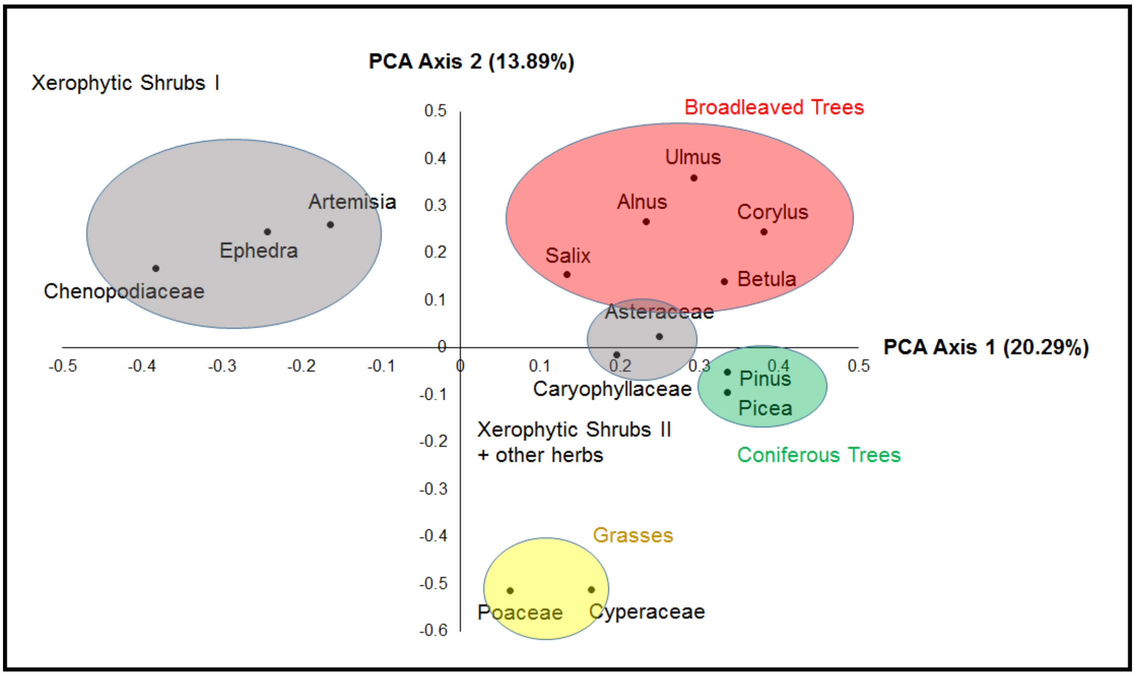

Fig. 5 - 6: PCA of the major pollen taxa/families from the Kunlun Pass Basin. PCA Axis 1 explains 20.29% of the total variance and separates the xerophytic shrubs I from all other groups of pollen. Since these xerophytic shrubs are less reliant on water availability, this suggests that precipitation is controlling Axis 1. PCA Axis 2 explains 13.89% of the total variance. Major differences are between the grasses (low PCA Axis 2 values), coniferous trees and xerophytic shrubs II + other herbs (medium PCA Axis 2 values) and broadleaved trees (high PCA Axis 2 values). This points to a temperature led control of PCA Axis 2 distribution with high PCA Axis 2 values representing warmest conditions.

5.3.2. Vegetation history

Vegetation between 4.314 and 4.030 Ma

From 4.314 to 4.030 Ma the Kunlun Pass Basin record is characterised by open woodland vegetation. Since the broadleaved tree pollen did not continuously reach high values, the patches of broadleaved forests expanded and retreated frequently during this time interval. The cool and cold-temperate mixed broadleaved and coniferous forests were composed of *Betula*, *Ulmus*, *Alnus*, *Elaeagnus*, *Salix, Juniperus* and *Corylus* with some minor appearances of *Ilex* and *Juglans*/*Pterocarya*. In two subsequent cooling steps at 4.157 and 4.030 Ma, the broadleaved forests substantially decreased in the Kunlun Pass Basin area and the composition of the thinned broadleaved forest patches changed. Warm-temperate taxa, such as *Ilex*, *Juglans*/*Pterocarya* and *Corylus*, occurred only rarely after 4 Ma in the pollen record, whereas taxa capable of surviving colder conditions, such as *Betula*, *Alnus*, *Salix*, *Elaeagnus, Juniperus* and *Ulmus*, continued to appear in the pollen record. Despite the occurrence of forest patches, xerophytic shrublands were still dominating in the Kunlun Pass Basin area (Fig. 5 – 7). After 4.157 Ma, a major transition took place as the broadleaved forest patches were replaced by *Pinus-Picea* coniferous forest patches, whereas Asteraceae and Caryophyllaceae replaced Chenopodiaceae in the xerophytic shrublands. These palaeovegetation changes indicate that the climate in the Kunlun Pass Basin area became significantly colder causing the retreat of broadleaved forest patches to warmer areas on the Tibetan Plateau. At the same time, the climate conditions were still wet or even wetter than before 4.157 Ma.

Large distributions of broadleaved and coniferous forests were recorded across multiple study sites all over China for the Early Pliocene: Wang et al. (2006a) shows that both coniferous and broadleaved forests existed in Xifeng, CLP, but that the trees thinned drastically around 4.2 Ma. While *Pinus* still prevailed in the area, most of the broadleaved trees such as *Betula*, *Quercus* and *Juglans* became almost absent after ~ 4.0 to 3.8 Ma. An increase in the xerophytic shrubs Chenopodiaceae and *Ephedra* indicates that between 4.2 and 4.0 Ma climate conditions became colder and drier. In Baode, northern CLP, broadleaved forests also started to decline after 4.4 Ma and subtropical taxa became extinct (Li et al., 2011). In the Yushe Basin, Shi et al. (1993) noted that after 4.5 Ma climate cooling caused a transition from subtropical to warm-temperate taxa in the broadleaved forests. Between 4.3 and 4.1 Ma, broadleaved forests declined and were replaced by coniferous forests, a similar change that has been observed in the Kunlun Pass Basin record. In the SW parts of the Tibetan Plateau (Zanda Basin), Wu et al. (2014a) showed that sub-alpine dark coniferous forests persisted throughout the Early Pliocene, however, changes in the assemblage point to an expansion of *Pinus* at the expense of *Abies* around 4.3 – 4.4 Ma.

Vegetation between 4.030 and 3.4 Ma

After 4.030 Ma the open woodland / patchy forest vegetation was replaced by alpine steppes/meadows and subsequently xerophytic shrublands. The alpine steppe/meadow vegetation in the Kunlun Pass Basin area persisted between ~

4.030 – 3.8 Ma and was characterised by large abundances in Poaceae, Cyperaceae and *Artemisia*. Although *Artemisia* shows high similarities with Chenopodiaceae and *Ephedra* over the entire palynological record (Fig. 5 – 6), *Artemisia* is also known to occur besides Poaceae and Cyperaceae in alpine steppes and meadows on the Tibetan Plateau (Zhao and Herzschuh, 2009). The transition into steppe/meadow vegetation marks a further cooling step of the Kunlun Pass Basin area.

After 3.8 Ma, the Kunlun Pass Basin area was characterised by an expansion of Chenopodiaceae dominated xerophytic shrublands, which indicates that dry climatic conditions prevailed. Since *Artemisia* and Chenopodiaceae consistently contained more than 45 – 50% of the total pollen sum after 3.8 Ma (until ca 2.6 Ma), the A/C ratio can be applied as an indicator for changes in the moisture availability (Zhao et al., 2012). From 3.8 to 3.4 Ma, a clear trend towards lower A/C ratios can be seen (Fig. 5 – 8) which can be interpreted as an intensification of dry conditions. Between ca. 3.6 and 3.4 Ma, the lowest A/C ratios were observed in the Pliocene section of the Kunlun Pass Basin record. Although the transition from alpine steppes/meadows to xerophytic shrublands should be primarily interpreted as a shift in precipitation, it is possible that the palaeovegetation changes also suggest warming of the Kunlun Pass Basin.

An expansion of Chenopodiaceae shrublands was also observed on the CLP and in the Yushe Basin (Li et al., 2011; Shi et al., 1993; Wang et al., 2006a). In the Yushe Basin, the expansion of Chenopodiaceae was characterised as a short cool and dry period (Shi et al, 1993). In contrast, records on the CLP show that Chenopodiaceae increased strongly after 4.4 Ma (Li et al., 2011) on the northern CLP and after ~ 3.8 Ma (Wang et al., 2006a) on the southern CLP.

Vegetation between 3.4 and 2.75 Ma

After 3.4 Ma, the A/C ratios started to increase until ~ 2.75 Ma. Although xerophytic shrublands still prevailed in the Kunlun Pass Basin area, the climate conditions were characterised by increased moisture. In the short time interval from 3.025 to 2.974 Ma, coniferous forests again expanded into the study area, which indicates an increase in precipitation at the Kunlun Pass Basin.

On the CLP, changes in the composition of xerophytic shrublands towards higher abundances of *Artemisia* have also been observed in Baode (~ 3.5 Ma) and Xifeng (~ 3.5 – 3.6 Ma) (Wang et al., 2006a, Li et al., 2011). Since forests retreated from Baode concomitantly with the increase in *Artemisia*, a simple increase in precipitation cannot be used as an explanation for the northern CLP (Li et al., 2011). On the southern CLP, no reduction of tree pollen was recorded (Wang et al., 2006a). Instead, from 3.6 to 2.7 Ma, *Ephedra* disappeared in the pollen record from Xifeng, which indicates that climate conditions were wetter during this time period (Wang et al., 2006a).

Vegetation between 2.75 and 0.853 Ma

The onset of the NHG (~ following 2.75 Ma) was characterised by a decrease in the A/C ratio, which points to drier conditions in the Kunlun Pass Basin area.

After 2.6 Ma, the second sharp reduction of broadleaved tree pollen in the entire Kunlun Pass Basin suggests that temperature significantly declined. The vegetation was transitioning into steppes/meadows, which is indicated by the strong increase of Poaceae and Cyperaceae after ~ 2.5 Ma. The decrease of xerophytic shrublands from 2.5 Ma to ~ 2.15 Ma suggests that the climate conditions were cold and wet after the initial phase of the NHG. Coniferous forest patches persisted in the Kunlun Pass Basin area between 2.6 and 2.15 Ma.

After 2.15 Ma, the palaeovegetation suggests that intense drying occurred in the Kunlun Pass Basin area, because steppes/meadows were replaced by Chenopodiaceae dominated xerophytic shrublands.

In the nearby Qaidam Basin (SG-3 core), Cai et al. (2012) concludes that drying and cooling became intensified around 2.6 Ma when A/C ratios and broadleaved trees decreased. However, their pollen diagram suggest gradual rather than sharp changes in the palaeovegetation, which is contrary to the Kunlun Pass Basin record. Furthermore, the SG-3 pollen record does not support the notion of a wetter NW Qaidam Basin between 2.5 and 2.15 Ma (Cai et al., 2012).

In NE Siberia, the Lake El'gygytgyn palynological record (Andreev et al., 2014) indicates that the onset of the NHG was characterised by a retreat of coniferous forests and expansion of tundra vegetation which led to the conclusion that colder and drier conditions persisted between 2.733 and 2.698 Ma. Furthermore, Andreev et al. (2014) found that re-advances of cold deciduous forests occurred after 2.55 Ma during warm intervals. Although Andreev et al. (2014) suggest that enhanced deforestation occurred at Lake El'gygytgyn after 2.158 Ma due to very dry and cold conditions, Zhao et al. (2015) showed that forest vegetation re-advanced around Lake El'gygytgyn once again when Northern Hemisphere summer insolation was providing more favourable warm conditions. However, the authors only focussed on a very small time interval (2.15 – 2.10 Ma).

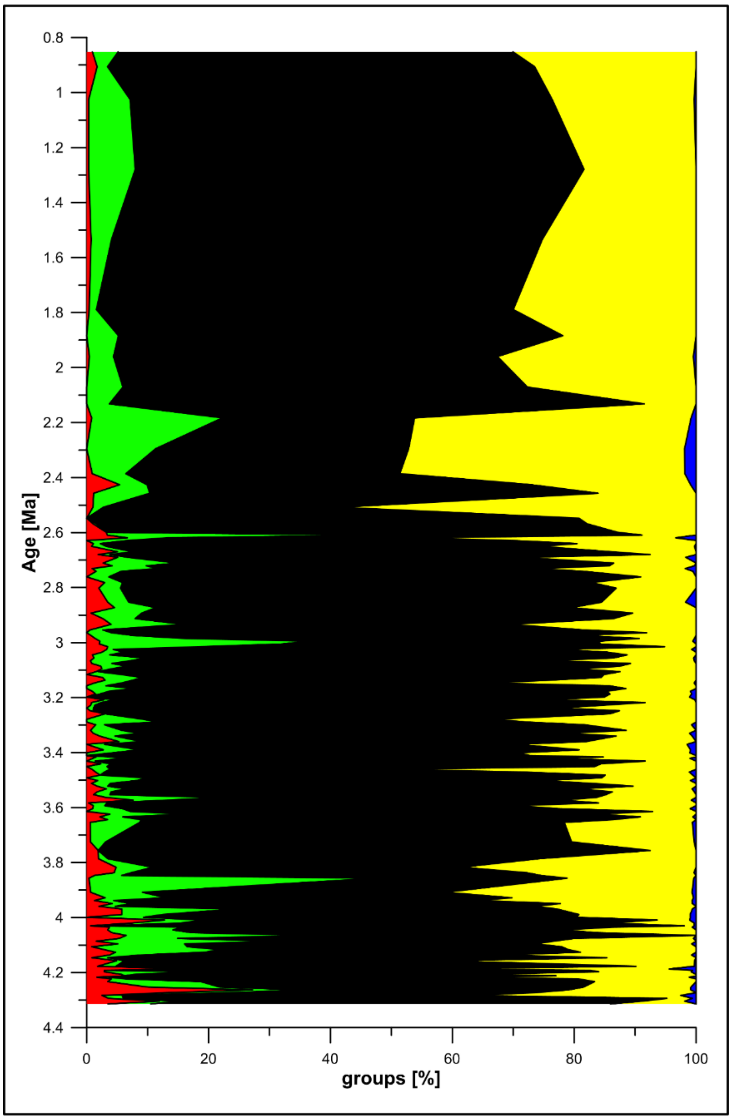

Fig. 5 - 7: Age profile of broadleaved trees (red), coniferous trees (green), herbs & shrubs (black), Poaceae + Cyperaceae (yellow), water plants, ferns & mosses (blue) for the Kunlun Pass Basin. Note that above ~ 2.4 Ma the sample resolution is significantly lower.

The Kunlun Pass record indicates a re-occurrence of coniferous forests during the Early Pleistocene followed by a decline between 2.183 and 2.132 Ma (alongside alpine steppes/meadows). A contemporaneous rise in Chenopodiaceae shrublands suggest drier climates during this time interval. A further interpretation of this section is hampered by the lower resolution of the Early Pleistocene section.

5.3.3 Palaeoclimate variability of the Kunlun Pass Basin during the Pliocene and Early Pleistocene

5.3.3.1 Qualitative interpretation of temperature, precipitation and wind regimes changes

Based on the palaeovegetation reconstruction, several temperature and precipitation trends of the Kunlun Pass Basin record were identified:

From 4.314 to ~ 3.8 Ma a distinct trend towards colder conditions can be interpreted after which temperatures appear to remain largely unchanged until ca. 2.7 – 2.5 Ma. Following the onset of the NHG (~ 2.75 Ma) (Haug et al., 2005), broadleaved forests further declined while alpine steppes/meadows became dominant, and thus, another cooling step took place in the Kunlun Pass Basin area. Severe drying occurred in the Kunlun Pass Basin from ~ 3.8 until 3.4 Ma and after 2.183 Ma. At both times, Chenopodiaceae dominated xerophytic shrublands became the dominant vegetation type in the Kunlun Pass basin area coinciding with a retreat of broadleaved and coniferous forest patches and a decrease in alpine steppe/meadow vegetation. Tab. 5 – 2 summarises how the palaeovegetation changes relate to climate changes in the Kunlun Pass Basin area from the Early Pliocene to the Middle Pleistocene.

In addition to the decline of broadleaved forests on the CLP around ca 4.5 to 4.0 Ma (Li et al., 2011; Wang et al., 2006a), also terrestrial mollusc assemblages on the CLP (Xifeng, Dongwan) indicate that temperatures decreased during this time because thermo-humidophilous taxa were largely replaced by meso-xerophilous taxa (Li et al., 2008; Wu et al., 2006) (Fig. 5 – 8). A temperature decrease following the Early Pliocene is not confined to Chinese records, but has also been recognised in oxygen isotope records from benthic foraminifera, which show that deep ocean conditions were cooling throughout the Pliocene with superimposed warmer and colder intervals (Lisiecki and Raymo, 2005; Williams et al., 2009; Zachos et al., 2001). During the Early Pliocene, MIS Gi26 (ca. 4.15 Ma; Lisiecki and Raymo, 2005) and especially MIS Gi20 (ca. 4.0 Ma; Lisiecki and Raymo, 2005) mark strong cooling intervals. In the Kunlun Pass Basin record, patches of broadleaved forests were replaced by coniferous forests around 4.157 Ma coinciding with MIS Gi26. Around 4.030 Ma a further cooling step was recorded, which was characterised by the development of steppe/meadow vegetation and a decline in coniferous forests and warm-temperate broadleaved trees. The vegetation change in the Kunlun Pass Basin record could have been triggered by the pronounced cooling associated with MIS Gi20.

Tab. 5 - 2: Overview of climate changes in the Kunlun Pass Basin between 4.314 and 0.853 Ma.

Age (Ma)	**Vegetation Change**	**Climate Interpretation**
4.314 – 4.157	High broadleaved forests, existing warm taxa	Warm-wet
4.157 – 4.030	Decline in broadleaved forests, increase in coniferous forests, replacement of Chenopodiaceae with Asteraceae and Caryophyllaceae	Cool-wet
4.030 – 3.800	Decline in broadleaved and coniferous forests, expansion of alpine steppes/meadows	Cold-wet
3.800 – 3.400	Expansion of Chenopodiaceae dominated xerophytic shrublands at the expense of alpine steppes/meadows	Cold-dry
3.400 – 2.721	Increase of *Artemisia* in xerophytic shrublands, increase in coniferous forests	Cold-wet
2.721 – 2.609	Decrease in coniferous forests, decrease of *Artemisia* in xerophytic shrublands	Cold-dry
2.609 – 2.183	Expansion of alpine steppes/meadows, decrease in xerophytic shrublands, increase in coniferous forests, decrease in broadleaved forests	Cold-wet
2.183 – 0.853	Decrease in broadleaved and coniferous forests, Poaceae dominated alpine steppes/meadows, expansion of Chenopodiaceae dominated shrublands	Cold-dry

Palaeoclimate models suggest that global temperatures were up to 4°C warmer during the Early Pliocene (4.2 – 4.0 Ma) compared to pre-industrial level (Brierley et al., 2009) and 2.39 to 2.92°C degrees warmer during the mPWP compared to pre-industrial level (Haywood et al., 2009; Haywood and Valdes, 2004). The implied global temperature decrease of up to 1.61°C and concurrent decline in atmospheric carbon dioxide concentrations (Pagani et al., 2010; Seki et al., 2010) deliver a probable explanation for the vegetation and climate changes in the Kunlun Pass Basin area for the early part of the record.

In contrast to the predominantly temperature controlled vegetation changes between 4.314 and 3.8 Ma, the expansion of Chenopodiaceae dominated xerophytic shrublands after ~ 3.8 Ma represents a shift in precipitation. Patchy forest vegetation and alpine steppes/meadows characterise wet conditions, whereas the xerophytic shrublands and specifically those that are dominated by Chenopodiaceae over *Artemisia* (El-Moslimany, 1990; Zhao et al., 2012) represent dry conditions. The Pliocene aridification was also recorded at Lake Qinghai and the CLP (Ao et al., 2016; Fu et al., 2013). Based on the formation and expansion of Lake Qinghai, Fu et al. (2013) suggested that the EASM was strong between 4.4 and 3.6 Ma. Additionally, Ao et al. (2016) created an EASM stack for the CLP which shows that a first peak in monsoon strength occurred around 4.1 Ma. However, around 3.8 to 3.6 Ma changes in sedimentation and ostracod assemblages at Lake Qinghai point to drying of the area (Fu et al., 2013; Lu et al., 2017). Lu et al. (2017) found that the abundances and diversity of the ostracod assemblage in Lake Qinghai decreased sharply around 3.74 Ma, which led the authors to conclude that Lake Qinghai was shallowing. After 3.6 Ma, ostracods disappeared and the lithology changed from dark silts and sandy silts to grey sands and silty sands (Fu et al., 2013; Lu et al., 2017). Although Fu et al. (2013) hypothesizes that tectonic uplift has been responsible for these sediment changes, a reduced strength of the EASM could be a good alternative explanation. A weaker summer monsoon was also observed in the EASM stack from the CLP between 4.0 and 3.6 Ma (Ao et al., 2016) and can be concluded from the strong increase of Chenopodiaceae shrublands on the CLP at Xifeng around that time (Wang et al., 2006a). Taking into account that the aridification also took place in other parts of China after 3.8 Ma, it seems likely that the replacement of steppes/meadows in the Kunlun Pass Basin area by xerophytic shrublands was forced by weakening of the EASM.

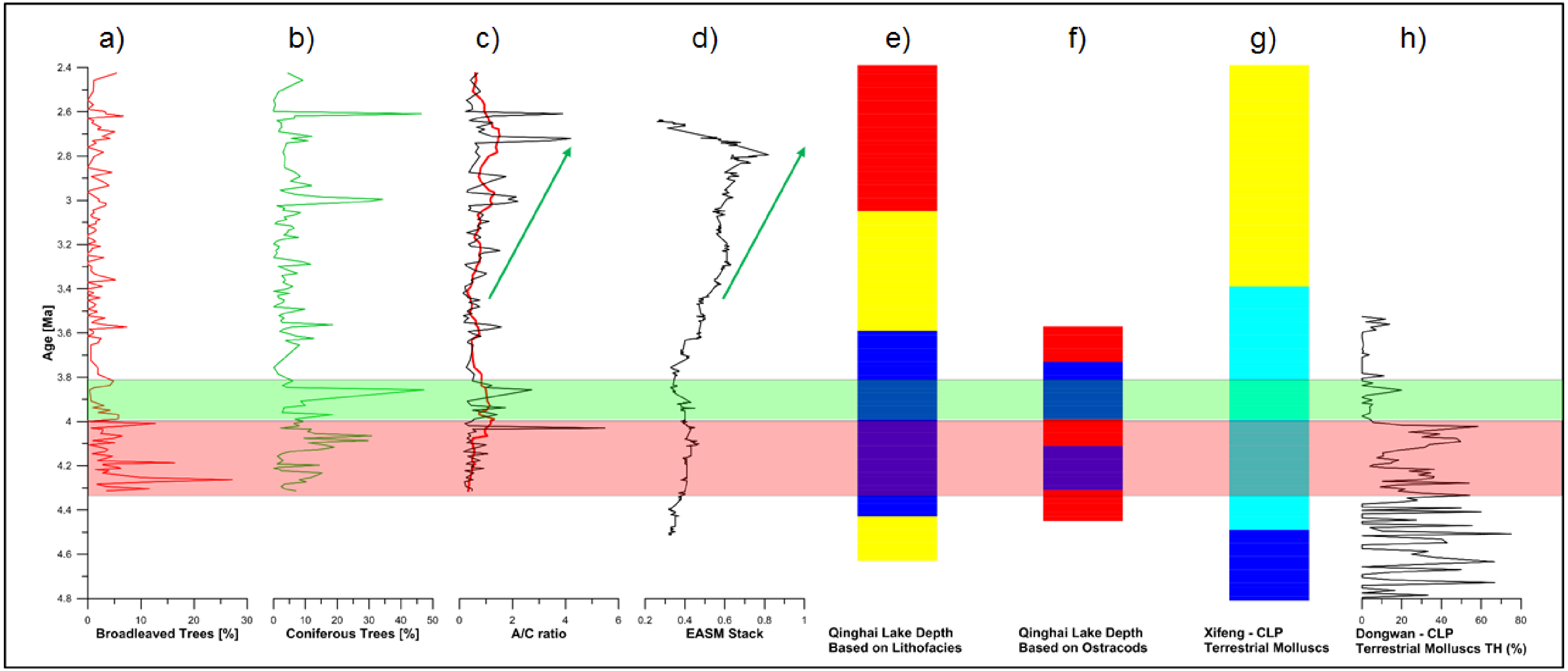

Fig. 5 - 8: a-c) Comparison of pollen data from the Kunlun Pass Basin (this study) with other records. The A/C ratio (c) has been smoothed in order to compare the development of moisture availability with the lower resolution EASM stack (d) from Ao et al. (2016) e) Lake depth estimation (blue = deep lake, yellow = transition period, red = shallow lake) of Qinghai Lake from Fu et al. (2013). f) Lake depth estimation of Qinghai Lake based on ostracod analysis (blue = deep lake, red = shallow lake) from Lu et al. (2017). No ostracods have been recorded after 3.58 Ma. g) Terrestrial mollusc record from Xifeng, CLP Wu et al. (2006) showing phases where thermo-humidiphilous dominate together with meso-xerophilous taxa (dark blue), meso-xerophilous taxa dominate mollusc assemblage with lower contributions from thermo-humidiphilous and rare contributions from cold-aridiphilous taxa (light blue) and a phase of mixed assemblage with dominating meso-xerophilous taxa but strongly increased cold-aridiphilous taxa and rare occurrences of thermo-humidiphilous taxa. h) Percentage of thermo-humidiphilous taxa on the molluscan assemblage in Dongwan, CLP (Li et al., 2008).

Based on the A/C ratio, the driest climate conditions of the Pliocene in the Kunlun Pass basin area was recorded between 3.6 and 3.4 Ma. This is in good agreement with the aforementioned higher sediment grain size and low magnetic susceptibility at Lake Qinghai (Fu et al., 2013; Fu et al., 2015), which support drier conditions during the Early Piacenzian. After 3.4 Ma, the sediment proxies from Lake Qinghai suggest that the EASM strengthened (Fu et al., 2013; Fu et al., 2015). A return to wetter conditions was also indicated by the eolian content from the WEDP01 core in the Tengger Desert (Li et al., 2018b) and the SG-1b palynological record presented in the previous chapter. After 3.5 – 3.4 Ma, the peaks of A/C ratios are increasing until ca 2.72 Ma, which are best shown by the smoothed A/C ratios (Fig. 5 – 8, red curve). Both curves show similar trends, however, the A/C ratio shows an offset. Other Chinese records also do not show a coherent picture for the climate evolution during the Late Pliocene. In Xifeng, the terrestrial molluscan fauna changed from meso-xerophilous taxa to cold-aridiphilous taxa suggesting cooling and/or drying of the area (Wu et al., 2006). Mixed signals were also derived from the pollen record from Baode (Li et al., 2011). Between 3.5 and 3.05 Ma, *Artemisia* increases at the expense of Chenopodiaceae which could be interpreted as a moister xerophytic shrubland, however at the same time broadleaved trees decline and the openness of the vegetation is at a maximum (Li et al., 2011).

It seems that the mostly synchronous climate developments from the Early Pliocene to Late Pliocene (temperature decrease around 4.5 – 4.0 Ma; weakening of the EASM around 3.8 Ma) did not follow through uniformly in the Late Pliocene. Instead, the Chinese records used here for comparison purposes show greater variations from each other after ~ 3.6 – 3.4 Ma. In Chapter 4.3.3.3, it was shown that the EASM related precipitation in China can vary depending on temperature conditions in the EEP and distribution and extent of high latitude ice sheets. Thus, it seems likely that the beginning breakdown of so-called permanent El Niño conditions (Wara et al., 2005) led to stronger differentiation of climate evolution in various parts in China after ~ 3.5 Ma.

In the Kunlun Pass Basin area, the Plio-Pleistocene transition is characterised by multiple steps of vegetation and climate change. After 2.721 Ma, *Artemisia* starts to decline substantially, which led to drier conditions in the Kunlun Pass Basin until ca 2.5 Ma. The decline in A/C values come shortly after large-scale glaciations started to occur in the North Atlantic and North Pacific (Bartoli et al., 2005; Haug et al., 2005; Jansen et al., 2000; Jansen and Sjøholm, 1991; Kleiven et al., 2002). Cooling of oceanic SST can have a profound negative impact on moisture availability transported to land areas via atmospheric transport as shown by Meehl et al. (2005) and could therefore, be a possible explanation for reduced moisture availability in the Kunlun Pass Basin during that time. After 2.6 Ma, thinning of coniferous forests and broadleaved forests indicates that strong cooling took place. Around 2.5 Ma, the xerophytic shrublands were replaced by alpine steppe/meadow vegetation marking a further cooling but also the return of wetter conditions in Kunlun Pass Basin area. Increasingly wet conditions were also seen by the re-advance of coniferous forests after ~ 2.450 Ma, which seem to increase from 2.4 towards 2.183 Ma when glacial stages became weaker (after MIS 96, 98, 100) (Lisiecki and Raymo, 2005).

Despite the lower resolution in the Pleistocene pollen record, a sharp change in the composition was observed between 2.183 and 2.132 Ma, which can be primarily interpreted as strong drying and cooling. Although broadleaved forests already thinned prior to 2.132 Ma, they became very rare after that time. The sharp shift towards Chenopodiaceae dominated xerophytic shrublands reveals that the Kunlun Pass Basin area underwent significant drying during this time. Drying and cooling were also observed by Andreev et al. (2014) in the Lake El’gygytgyn record after 2.164 Ma, where coniferous trees retreated and tundra vegetation expanded. Zhao et al. (2015) showed that forest vegetation re-advanced around Lake El’gygytgyn when Northern Hemisphere summer insolation was providing more favourable warm conditions, however, the authors only focussed on a very short time interval (2.15 – 2.10 Ma). Significant changes around 2.15 Ma (MIS 82) were also been observed in other records: Fu et al. (2013) interpreted that lithology changes in Qinghai Lake at 2.15 Ma from primarily silts to silts, sands and fine gravel represent a shift towards a weakened EASM and/or strengthened EAWM. On the CLP, Ding et al. (2002) found that a thick and coarse loess layer had been deposited during MIS 82, which indicates that EAWM has been comparatively stronger than earlier and later intervals. Raymo et al. (1986), Hodell and Channell (2016) and Rohling et al. (2014) noticed that MIS 82 (2.15 Ma; Lisiecki and Raymo, 2005) was particularly colder compared to the previous MIS (84, 86, 88, 90, 92, 94). Rohling et al. (2014) stated that MIS 82 was the first deep glaciation stage with a low stand of relative sea level ~ - 70 m compared to modern. A stronger cooling during MIS 82 was also noticed across tropical SSTs (Herbert et al., 2010) with the largest drop of SSTs in the EEP (Lawrence et al., 2006). Thus, the extreme cooling of MIS 82 could have been a trigger for the onset of cold-dry conditions in the Kunlun Pass Basin area through changes to the monsoonal system. In order to prove this, a higher resolution analysis of the Pleistocene section is required, which is beyond the scope of this study.

5.3.3.2 Palaeoclimate estimates for the Kunlun Pass Basin record

In Fig. 5 – 9 and Fig. 5 – 10 palaeoclimate estimates based on the Coexistence Approach (Mosbrugger and Utescher, 1997) and the pollen – climate transfer functions are shown for the Kunlun Pass Basin record. The climate estimates which are based on the coexistence approach (Mosbrugger and Utescher, 1997) show similar disadvantages as in the SG-1b record – a missing variability and large ranges. Despite the fact that the palaeovegetation of the Kunlun Pass Basin record suggest two strong cooling intervals (4.314 - ~ 3.8 Ma and ~ 2.6 – 2.15 Ma) and two strong drying intervals (3.8 – 3.4 Ma and 2.15 – 0.853 Ma), these trends cannot be reproduced by the palaeoclimate estimates based on the Coexistence Approach.

In contrast, the temperature and precipitation reconstructions based on the pollen-climate transfer functions are able to capture these palaeovegetation changes. Therefore, all subsequent palaeoclimate estimates are based on the calculations from the pollen – climate transfer functions. In general, the estimated temperature ranges (MAT, MST and MWT) are considerably warmer than their modern-day equivalent. The minimum estimates do not change much considering that the record comprises the warmer Early Pliocene, Late Pliocene and Plio-Pleistocene transition. The lowest MAT estimates are ~ -3.5 to -2.5°C, which is still significantly warmer than the present Kunlun Pass Basin MAT value of ~ -6.1°C. It does not seem plausible that climate conditions during the Plio-Pleistocene transition were 2.5°C higher than modern day. Since the modern pollen dataset had only a few study sites included, where present annual temperatures are lower than in the Kunlun Pass Basin area, it seems likely that the temperature estimates have a consistent warm bias due to the edge effect

(Seppä et al., 2004; ter Braak et al., 1993). In contrast to the temperature estimates, the precipitation estimates (MAP, MSP and MWP) do not show consistently higher values. Since many pollen assemblages in the modern pollen dataset are derived from study sites, which experience drier conditions than the modern Kunlun Pass Basin, a consistent bias towards higher or lower values is unlikely.

In the lowermost interval (4.314 – 4.03 Ma) the climate was characterised by high temperatures (~ -2.5 to +9°C MAT) and high precipitation (~ 150 to 400 mm MAP). Based on the pollen – climate transfer functions the decrease in coniferous and especially broadleaved trees after 4.030 Ma suggest that MAT were lowered to a range between ~ -3 to +7°C. This MAT range did not change significantly until ca. 2.7 Ma. However, the lower range estimates were slightly higher after ~ 3.1 Ma, which will be discussed separately in Chapter 5.3.3.3. After the transition towards Chenopodiaceae dominated xerophytic shrublands around 3.8 Ma, the MAP estimates show a strong decline to a range between 100 and 300 mm. The increase in A/C ratios after 3.6 to 3.4 Ma, is not reflected by the transfer function-based MAP estimates. MAPs remain range-bound until ca 2.5 Ma. As previously mentioned, the onset of the NHG around 2.75 Ma (Haug et al., 2005) had a significant influence on the Kunlun Pass Basin area. Despite the fact that the A/C ratio decrease with the onset of large-scale glaciers in the Northern Hemisphere, which suggests a reduction in moisture availability (El-Moslimany, 1990; Zhao et al., 2012), the MAP estimates only see a slight trend towards lower precipitation from 2.75 to ~ 2.55 Ma. Since this slight decrease stays within the MAP range, which was established after 3.8 Ma, a lower moisture availability is not recorded in the MAP reconstruction based on the pollen – climate transfer functions.

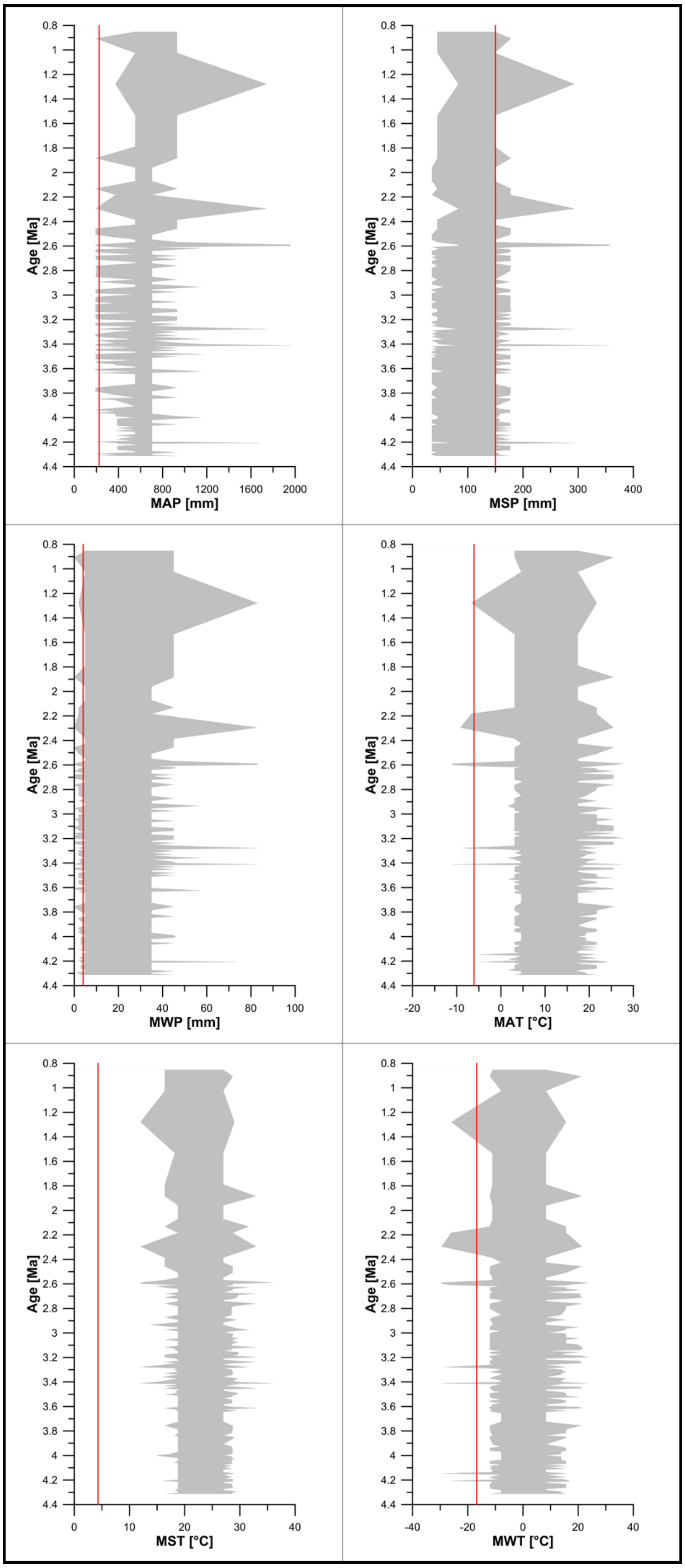

Fig. 5 - 9: Climate reconstructions based on the Coexistence Approach (Mosbrugger and Utescher, 1997).

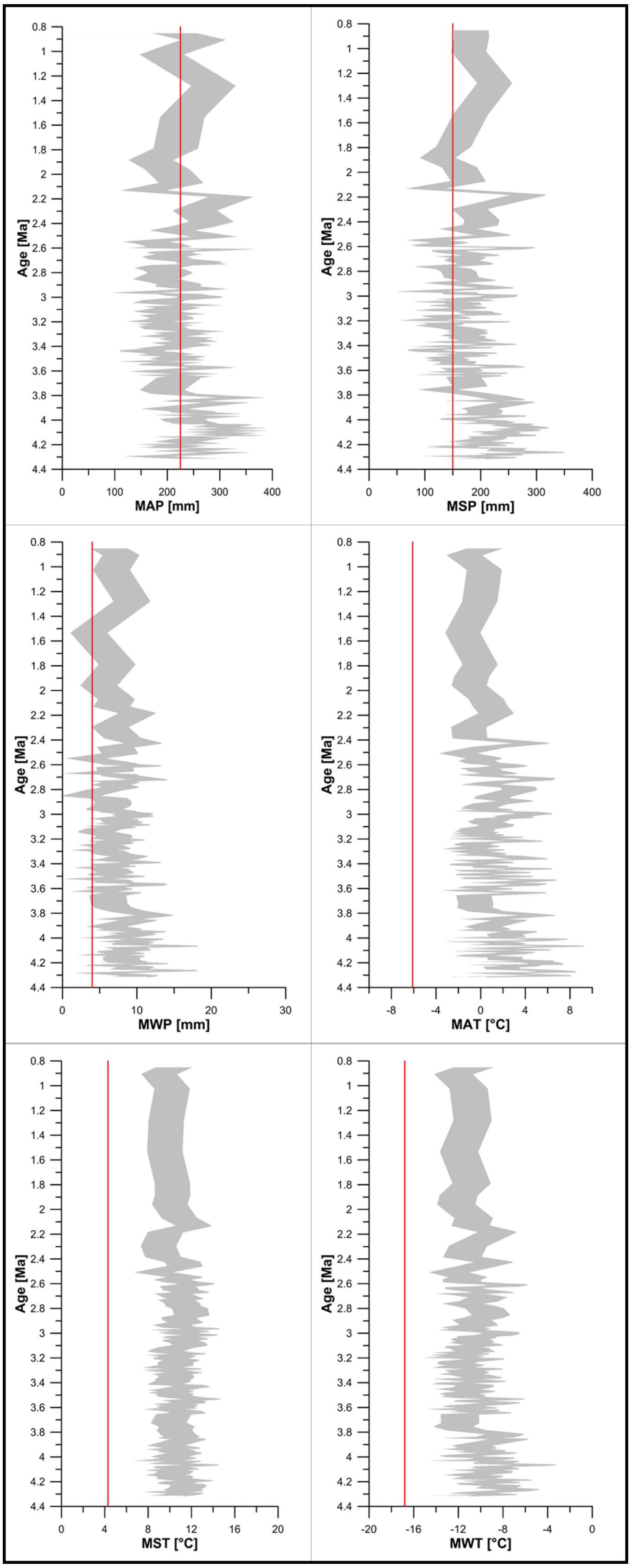

Fig. 5 - 10: Climate reconstructions based on the pollen – climate transfer function.

The temperature reconstructions show that MAT dropped from a maximum of +6.6°C (2.711 Ma) to a range of -3.6 to +4.1°C. One sample (2.426 Ma) showed a higher MAT estimate (6.1°C), which is related to a higher broadleaved tree pollen percentage in that specific sample (~ 5%). Since total pollen sums of the Pleistocene part of the record were generally low, this could either be a too high estimate or the sample represents an outlier. The pollen – climate transfer functions suggest that the MAPs fluctuated in a higher range between 150 and 350 mm, when the vegetation changed from xerophytic shrublands to steppes/meadows in the time interval from ~ 2.5 to 2.15 Ma. After MIS 82, the MAP estimates returned to the lower range of 100 to 300 mm.

In the following, the reconstructed temperatures will be compared to the global temperature estimates for the Early Pliocene (4.2 – 4.0 Ma; +4°C) (Brierley et al., 2009) and mPWP (3.3 – 3.0 Ma; +2.39 – 2.92°C) (Haywood et al., 2009; Haywood and Valdes, 2004) to infer if the Kunlun Pass Basin as a high latitude study site also experienced amplified warming similar to high latitude study sites (Panitz et al., 2016). Since the lower range is likely to be biased towards higher temperatures as discussed above, maximum and average values of the best estimate should track the palaeotemperature trend better. In Tab. 5 – 3 an overview of minimum, maximum and average MAT estimates is given for the Kunlun Pass Basin record based on the best estimate from the pollen – climate transfer functions.

Between the Early and Middle Pliocene interval the temperature dropped ~ 2.26°C on average and the maximum reconstructed MAT are 3.68°C lower in the 3.3 to 3.0 Ma interval compared to the 4.314 to 4.000 Ma interval. These temperature declines are higher than the averaged global estimate cooling of ~ 1.08 to 1.71°C for the same time intervals (Brierley et al., 2009; Haywood et al., 2009; Haywood and Valdes, 2004; Pagani et al., 2010).

Tab. 5 - 3: Palaeotemperature estimates (MAT) for the Kunlun Pass Basin for selected time intervals. The temperatures are based on the best estimate (lower and upper ranges as shown by grey border in Fig. 5 – 10 are minimum/maximum values based on the RMSEP). The numbers in brackets indicate the difference between the palaeotemperature estimates and the modern MAT of the Kunlun Pass Basin (-6.1°C).

Time interval	Min (°C)	Max (°C)	Average (°C)
4.314 – 4.000 Ma	-1.61 (+4.49)	+7.63 (+13.73)	+2.81 (+8.91)
3.300 – 3.000 Ma	-1.82 (+4.28)	+3.95 (+10.05)	+0.55 (+6.65)
2.700 – 2.500 Ma	-2.15 (+3.95)	+2.56 (+8.66)	+0.47 (+6.57)

Since high latitude and high altitude sites are more sensitive to changes in global temperatures (Solomon et al., 2007), these estimates indicate that the Kunlun Pass Basin underwent amplified cooling from the Early Pliocene to the middle Pliocene. MAT estimates for the 3.3 to 3.0 Ma interval indicates that temperatures were ~ 4.28 – 10.05°C higher than modern day.

Model simulations from Yan et al. (2019) suggest that the Tibetan Plateau was between 0.5 and 4.0 °C warmer in the Late Pliocene compared to the pre-industrial (Fig. 5 – 11). Therefore, the temperature estimates from this thesis indicate that the warming has been more intense in the Kunlun Pass Basin during the mPWP than models suggest. Despite the very heterogeneous warming (Fig. 5 – 11), the temperatures on the Tibetan Plateau were supposedly higher than in southeastern and northeastern China and the Tarim Basin, which all lie at a much lower elevation but similar latitude. A slightly increased warming of the Tibetan Plateau (5 – 7 °C) compared to similar latitudinal regions is also postulated in the future global warming scenario from Feng et al. (2014) (Fig. 5 – 12), which conclude that only the high latitudes (> 8°C) experience a stronger warming on an annual basis.

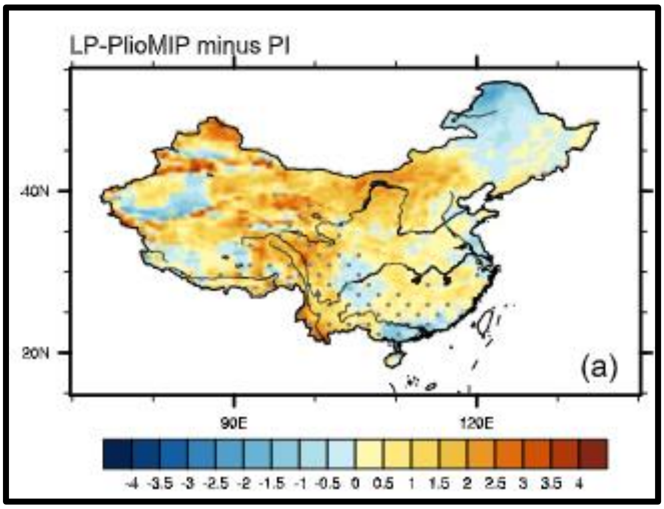

Fig. 5 - 11: Modelled temperature differences between the Late Pliocene and pre-industrial (Yan et al., 2019).

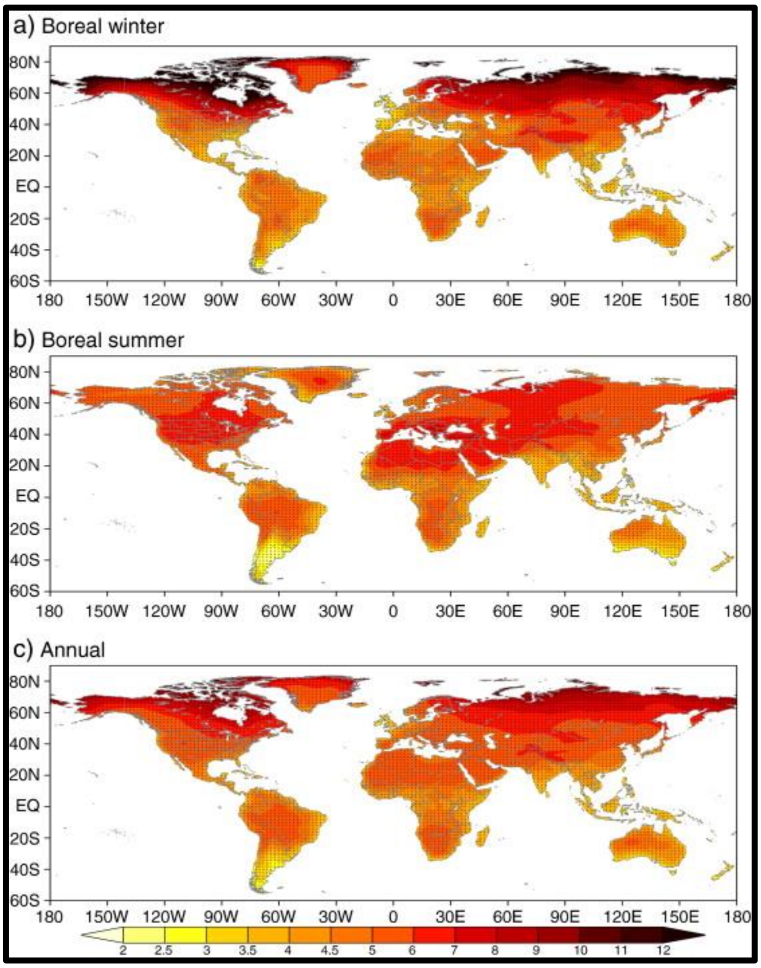

Fig. 5 - 12: Projected temperature changes during 2071–2100 relative to 1961–90 under RCP8.5 scenario (Feng et al., 2014).

In fact, Panitz et al. (2016) found that temperatures were 5 to 14°C higher in Norway during the Piacenzian based on the Coexistence Approach, while in the Canadian Arctic higher MATs of up to 19°C were inferred by Ballantyne et al.

(2010), which supports the modelling of projection of Feng et al. (2014) that MAT estimates from Kunlun Pass Basin (i.e. Tibetan Plateau) are slightly below the estimates from high latitude sites during intervals of global warmth.

5.3.3.3 What do the Kunlun Pass Basin and SG-1b record (NW Qaidam Basin) tell us about the Late Pliocene evolution of the EASM?

Despite the different palaeovegetation history in the NW Qaidam Basin and in the Kunlun Pass Basin area, a comparison of the palaeoclimate estimates and A/C ratios from both sites might reveal similarities or differences, from which conclusions about the EASM evolution can be drawn (Fig. 5 – 13).

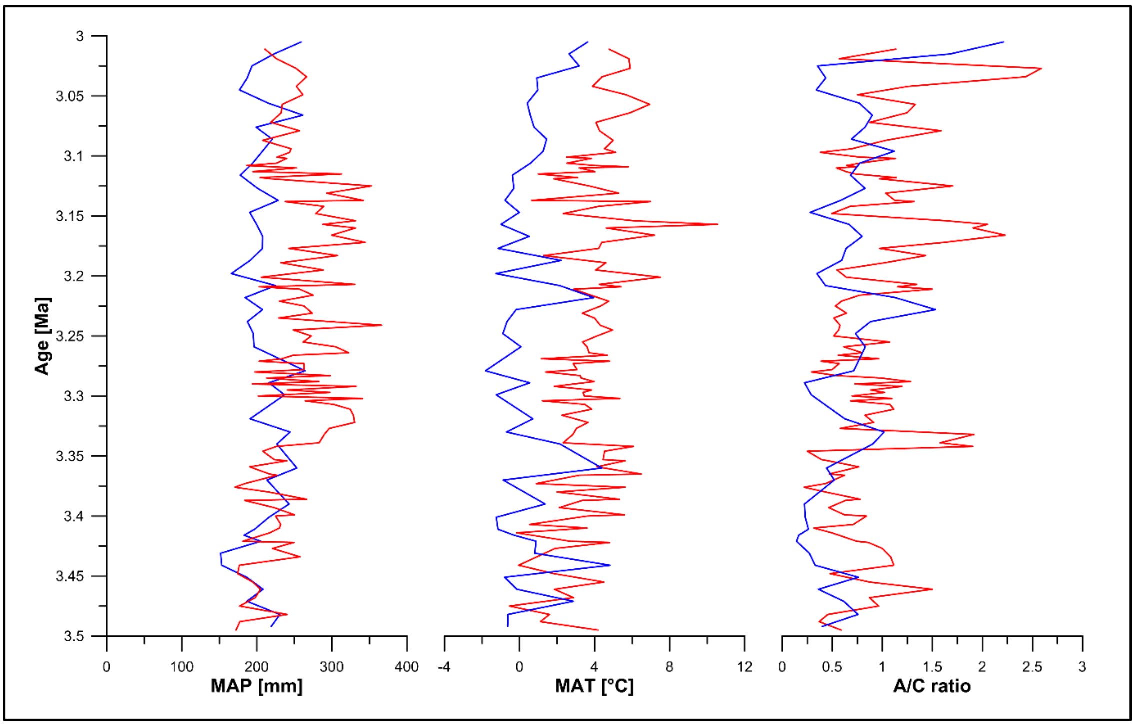

Fig. 5 - 13: Palaeoclimate estimates and A/C ratios of Kunlun Pass Basin (blue) and SG-1b core from the NW Qaidam Basin (red). The MAP reconstructions and A/C ratios (except 3.2 – 3.1 Ma) indicate opposite trends after 3.35 Ma in the Kunlun Pass Basin and Qaidam Basin record. No consistent trend was observed for MAT reconstructions.

The comparison between the two study sites show that the quantitative precipitation estimates are similar. However, whereas there are strong fluctuations and a clear dry-wet-dry structure in the NW Qaidam Basin (red), the Kunlun Pass Basin precipitation estimates do not vary significantly over that time period and are within the estimated error (RMSEP; see the grey ranges; Fig. 5 – 10 and Fig. 4 – 32). The MAP estimates and A/C ratios for the Kunlun Pass Basin show opposing trends to the NW Qaidam Basin, which becomes especially apparent after 3.35 Ma.

In order to explain this phenomenon of stronger EASM in the NW Qaidam Basin and weaker EASM in the Kunlun Pass Basin (and vice versa), at least one more study site at the western limit of the EASM would be necessary to cover the time interval from 3.5 to 3.0 Ma. Since this is beyond the scope of this thesis, only a first speculation can be made: It might be possible that when the precipitation from the EASM at the western limit is strongest (weakest) in northern positions, it became weakest (strongest) in southern positions.

The MAT reconstructions show that the Kunlun Pass Basin was colder than the NW Qaidam Basin during most of the 3.5 to 3.0 Ma interval, which is in good agreement with the modern altitudinal difference between these two locations. However, in contrast to the MAP reconstructions and A/C ratios, temperature reconstructions from both sites do not seem to be correlated.

5.3.4 Has the Kunlun Pass Basin been uplifted during or after the Pliocene? – A palynological perspective.

The MAT and MAP distribution in China (Fig. 2 – 2 and Fig. 2 – 3) highlights the strong temperature gradient between high mountainous areas on the Tibetan Plateau and the surrounding lowlands and basins. In response to a potential tectonic uplift, the palaeovegetation should show a decrease of warm loving taxa, such as broadleaved trees. In Chapter 5.3.2 the palaeoclimate estimates for the Kunlun Pass Basin record were shown (Fig. 5 – 10), which illustrated that two phases of cooling occurred in the study area (~ 4.314 – 3.8 Ma and 2.6 – 2.15 Ma) where broadleaved trees declined significantly.

Additionally, the carbonate $\delta^{18}O$ record (F.Cheng, in prep.) of the Kunlun Pass Basin will be used as an independent proxy. Carbonate $\delta^{18}O$ are a common proxy to trace changes in palaeoelevation based on the different isotopic signature of meteoric water which is incorporated into carbonates (Garzione et al., 2008). In Fig. 5 – 14A the relationship between altitude and $\delta^{18}O$ values from the Dudh Koshi watershed (Southern Himalayas) and the Niyang watershed (Tibetan Plateau) from Florea et al. (2017) are shown to illustrate that $\delta^{18}O$ values decline with increasing elevation. Additionally, in Fig. 5 – 14B – D, examples of palaeoelevation studies are shown where decreases in $\delta^{18}O$ values are used to characterise phases of tectonic uplift (Garzione et al., 2008; Kar et al., 2016; Li et al., 2016).

In Fig. 5 – 15 a comparison between the carbonate $\delta^{18}O$ values (F. Cheng, in prep.) and reconstructed MAT and MAP estimates based on the pollen – climate transfer functions are shown. The good agreement between the carbonate $\delta^{18}O$ record, which can be interpreted as a proxy for temperature (Garzione et al., 2008), and the MAT record indicates that the established pollen-climate transfer function for the MATs is robust and can track changes in temperature. Although the general trends are collinear between the carbonate $\delta^{18}O$ values and the reconstructed MATs, there is no obvious correlation with regard to the strength of each signal. In contrast to the two cooling intervals in the Kunlun Pass Basin vegetation and climate record, the carbonate $\delta^{18}O$ record only captures a strong drop around 2.6 Ma. Although previous studies suggested that tectonic uplift could have occurred at 2.6 Ma (e.g. Cai et al., 2012; Song et al., 2005a) causing changes in sediment deposition or palaeovegetation, a much simpler explanation for a temperature decrease around 2.6 Ma would be the onset of the NHG (Haug et al., 2005). Henceforth, no tectonic uplift will be concluded for the cooling from 2.6 to 2.15 Ma.

Between 4.314 and 4.0 Ma (Fig. 5 – 15; red shaded area) MAT estimates and carbonate $\delta^{18}O$ values show a striking mismatch (especially in the first 100 ka) where carbonate $\delta^{18}O$ values increase while the reconstructed MATs decline. As the pollen transfer function derived estimates of higher temperatures based on a robust increase of warm loving broadleaved trees between 4.314 and 4.0 Ma, it seems likely that the carbonate $\delta^{18}O$ values might not be temperature controlled in this time interval. Alternatively, the missing drop of carbonate $\delta^{18}O$ values could suggest that no tectonic uplift occurred during this time interval. Since the earliest interval of this record represents the highest temperatures, it will be examined further if the drop in temperature (and broadleaved trees) and anomalous $\delta^{18}O$ values might have been caused by tectonic uplift.

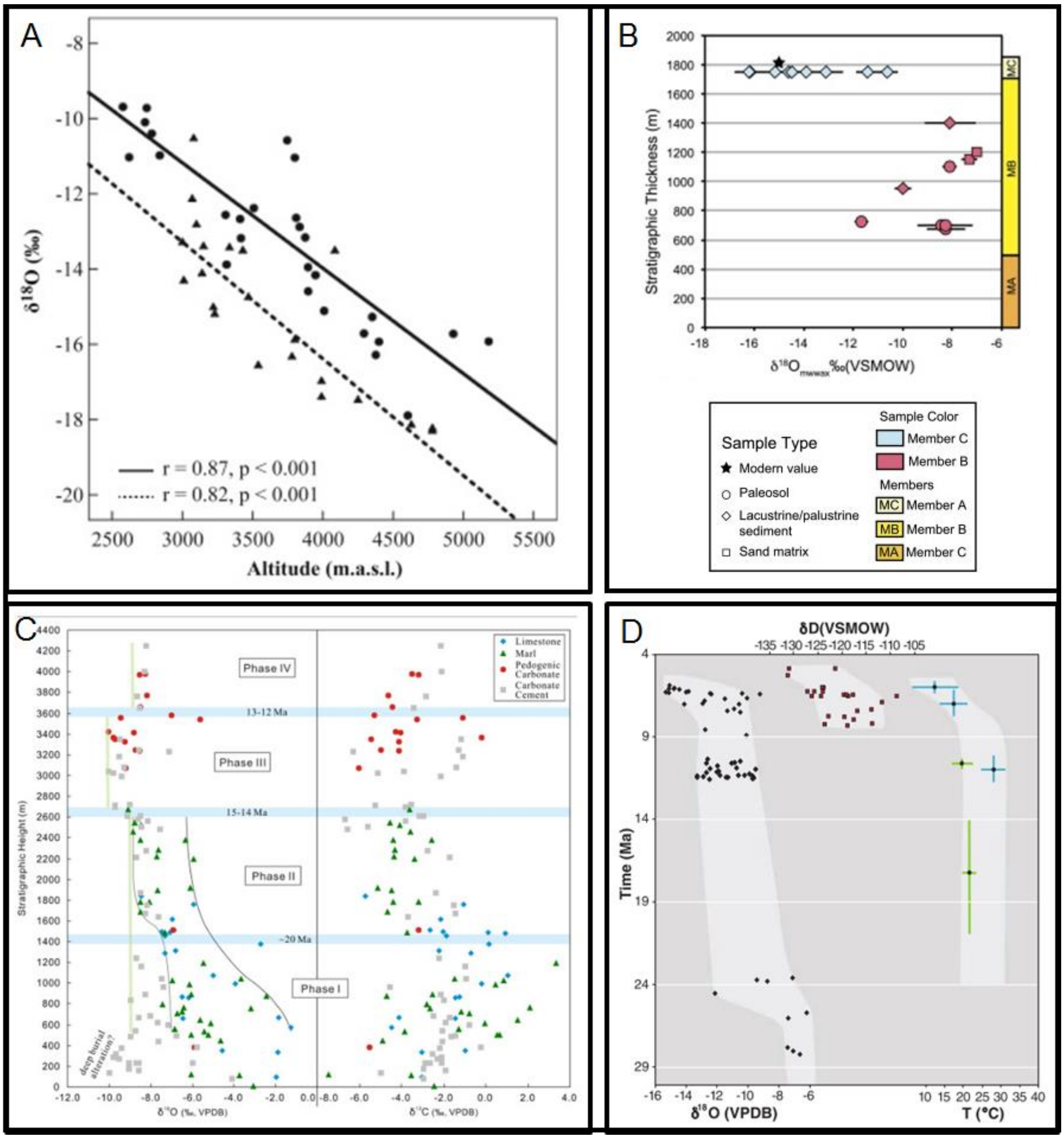

Fig. 5 - 14: A) Relationship between altitude and stream water δ^{18}O values from the Dudh Koshi watershed (Southern Himalayas) and the Niyang watershed (Tibetan Plateau) from Florea et al. (2017). B) Isotopic data from central Altiplano (Andes) suggest strong uplift after sediment member B (MB) (Kar et al., 2016). C) Isotopic data from the SW Qaidam Basin illustrating that the northeastern Tibetan Plateau was uplifted around 15 to 14 Ma (Li et al., 2016). D) Isotopic data from the Central Andes suggesting that only slight uplift took place until ~ 10 Ma after which steep rise of the mountain range took place (Garzione et al., 2008).

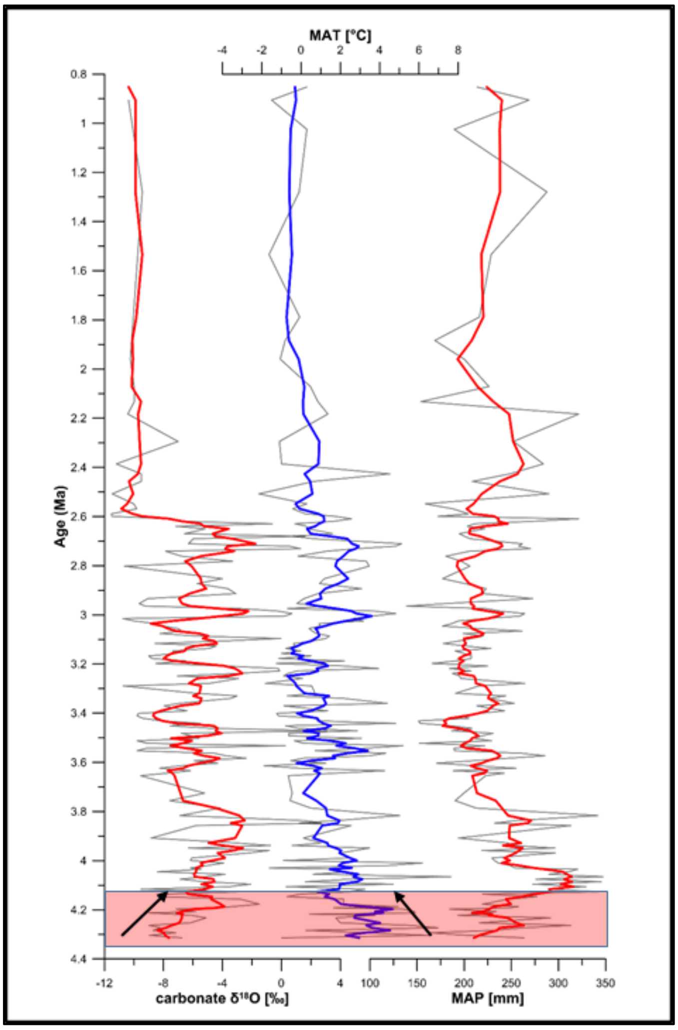

Fig. 5 - 15: Comparison of carbonate δ^{18}O values with reconstructed MAT and MAP estimates based on the established transfer functions. The figure shows only data where both, isotope and pollen data, is available. The grey lines represent the actual data points whereas the thick red and blue lines represent 5pt averages of each proxy.

The regional climate records shown in Fig. 5 – 8 and the higher amounts of broadleaved forests on the CLP (Li et al., 2011; Wang et al., 2006a) highlight that during the time interval from 4.4 to 4.0 Ma, high temperatures and precipitation characterised multiple study areas across China that were unaffected by tectonic uplift. This would indicate that the higher broadleaved tree pollen in the record are a climate and not a tectonic signal.

Furthermore, the altitudinal distribution of *Ephedra* and Caryophyllaceae in the modern pollen samples (Tab. 5 – 1) shows two characteristic trends (Fig. 5 – 16). The average percentage of *Ephedra* peaks at an elevation of 1500 to 2000 m and 2500 to 3000 m, and declines thereafter. On the other hand, average percentages of Caroyphyllaceae remain very low until the highest elevation intervals (4500 to 5000 m and 5000 to 5500 m). Based on the comparison of average *Ephedra* and

Caryophyllaceae percentages from the main PAZs of the Kunlun Pass Basin pollen record and the modern altitudinal distribution, a very simplistic elevation estimation is possible. The abundance of *Ephedra* suggest that the elevation of the Kunlun Pass Basin was between 3000 to 3500 m and 5000 to 5500 m. The percentages of Caryophyllaceae in PAZ 1 and 2 indicate that the Kunlun Pass Basin was already elevated to its modern height in the 4500 to 5000 m interval. Although, PAZ 3 and 4 could potentially represent lower elevation levels, there are no indications of a subsidence from PAZ 1 to PAZ 3 in that region. Most likely, the differences in Caryophyllaceae abundance rather represent changes in climate that were not triggered by tectonics.

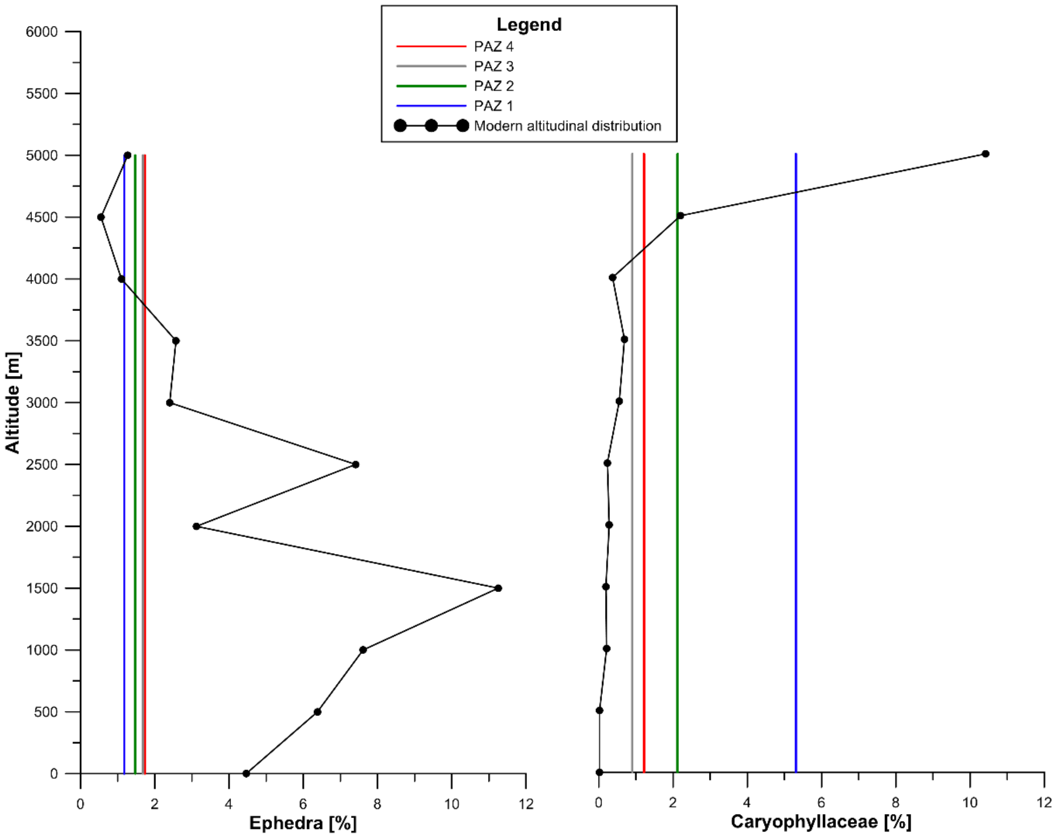

Fig. 5 - 16: Elevation profile of *Ephedra* and Caryophllaceae (black line with dots) in modern pollen samples (Dataset from Prof. Jian Ni, same as used for developing the modern pollen-climate dataset). *Ephedra* and Caroyphallaceae percentages were averaged in 500 m intervals. Elevations on the y axis show lower part of that interval (e.g. 2000 m refers to 2000 – 2500 m interval). The averaged pollen percentages from the main PAZs of the Kunlun Pass Basin record are shown in blue (PAZ 1), green (PAZ 2), grey (PAZ 3) and red (PAZ 4) for comparison.

The modern pollen distribution from Yu et al. (2001) shows that the broadleaved and coniferous tree pollen are mostly found in the warm and wet southeastern parts of the Tibetan Plateau where respective forests grow (Fig. 5 – 5). Hence, the high broadleaved and coniferous tree pollen in the oldest part of the Kunlun Pass Basin record might have been caused by the expansion of forests from the southeastern Tibetan Plateau during increased temperatures. Multiple BIOME4 projections for future global warming show that under higher atmospheric carbon dioxide concentrations and higher temperatures a northward expansion of coniferous and broadleaved forests (Fig. 5 – 17 and Fig. 5 – 18) from the southern Tibetan Plateau can be expected (Song et al., 2005b; Wang et al., 2011; Zhao et al., 2011). Furthermore, shrublands are largely increasing at the expense of alpine meadows on the central Tibetan Plateau (Fig. 5 – 17). This modelled temperature dependent shift of vegetation on the Tibetan Plateau is in line with the PCA from the Kunlun Pass Basin record, where Poaceae and Cyperaceae as elements of alpine steppes/meadows reflect coldest conditions. Similarly, Wang et al. (2011) showed that forest vegetation expanded towards the Kunlun Pass Basin with temperature increases of 5°C (Fig. 5 – 18).

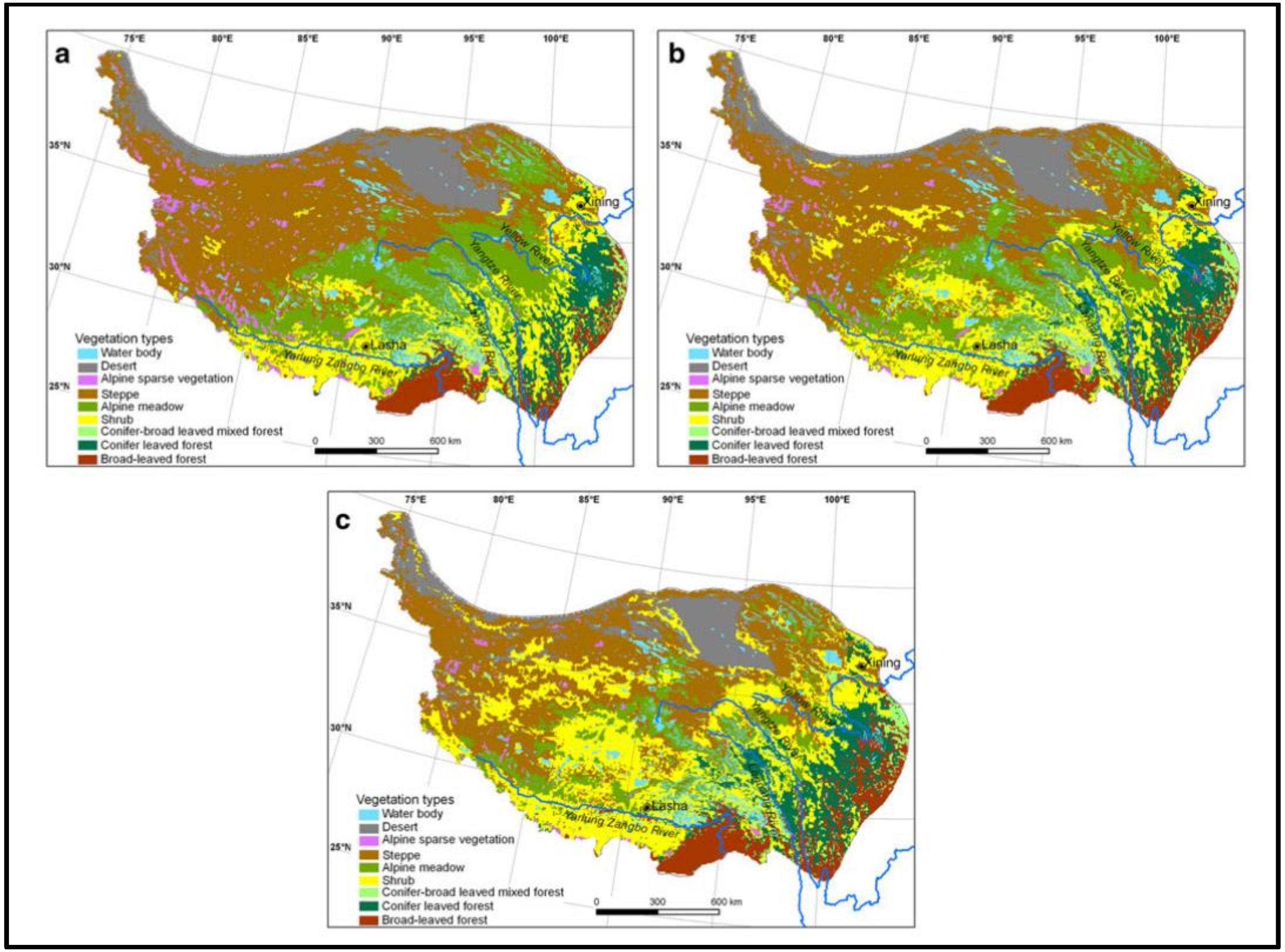

Fig. 5 - 17: Vegetation distribution on the Tibetan Plateau at three climate change stages (a 1991 – 2020, b 2021 – 2050, c 2051 – 2080) (Zhao et al., 2011).

Since the MAT reconstructions showed that temperatures were 4.49°C higher during the Early Pliocene as a lower estimate (Tab.5 – 3), the modelled vegetation distribution from Wang et al. (2011) on the Tibetan Plateau supports the assumption of this study that no tectonic uplift is necessary for the past 4.314 Ma to explain the vegetation changes. The good agreement of palaeoclimate reconstructions of the Kunlun Pass Basin record with global climate indicators can also be seen in Fig. 5 – 18. For the Kunlun Pass Basin record, higher A/C ratios (moisture) and temperatures (higher carbonate $\delta^{18}O$ values and reconstructed MATs) correspond well with each other with the prominent exception of the first 300 ka, which is being examined further by the project partners (e.g. clumped isotope palaeothermometry, Uk'37 temperature estimates).

The reconstructed MAT estimates show a decrease in temperatures from 4.3 to ~ 3.2 Ma, which is also seen in the SST estimates from ODP Site 846 (Lawrence et al., 2006) as well as in the benthic oxygen isotope record from Zachos et al. (2001). From 3.2 to 2.7 Ma, the reconstructed MATs and carbonate $\delta^{18}O$ values increase slightly which occurs at a time where there seems to be a pause in the decline of SST at ODP Site 846 (Lawrence et al., 2006) and benthic foraminifera $\delta^{18}O$ (Zachos et al., 2001). After 2.75 Ma, the MATs and carbonate $\delta^{18}O$ values decrease again. It is difficult to say whether the MATs remain at a low level without much fluctuation as indicated by Fig. 5 – 19 or if they continue to fluctuate. This is due to the low resolution of counted pollen samples in this time interval. The MAT reconstructions also show a good anti-correlation to the alkane dust record from IODP Site U1313 that reflects increased aridity on the North American continent during cold periods (Naafs et al., 2012).

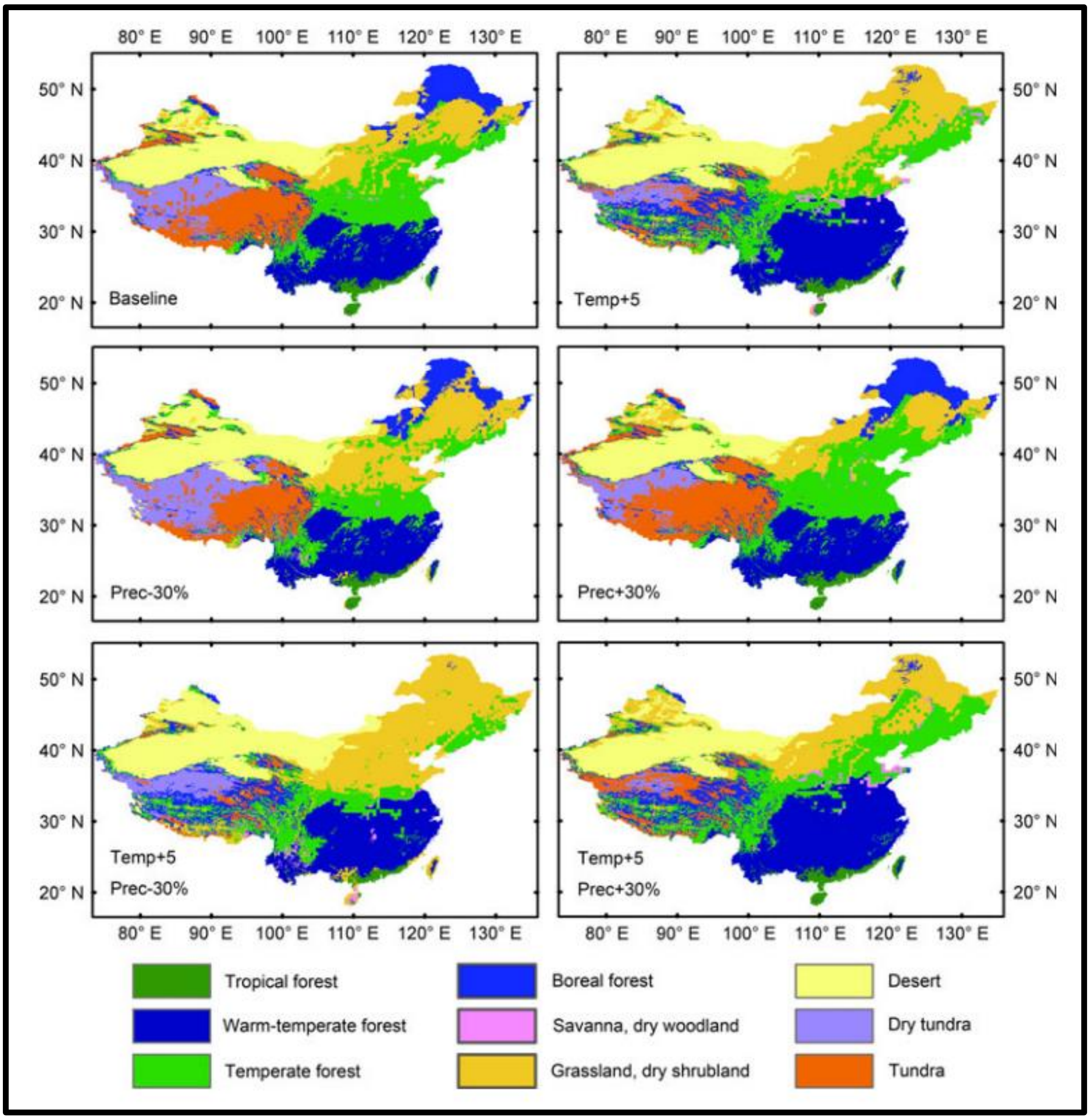

Fig. 5 - 18: Mega-Biome changes in China based on climate changes under recent atmospheric carbon dioxide concentrations (Wang et al., 2011).

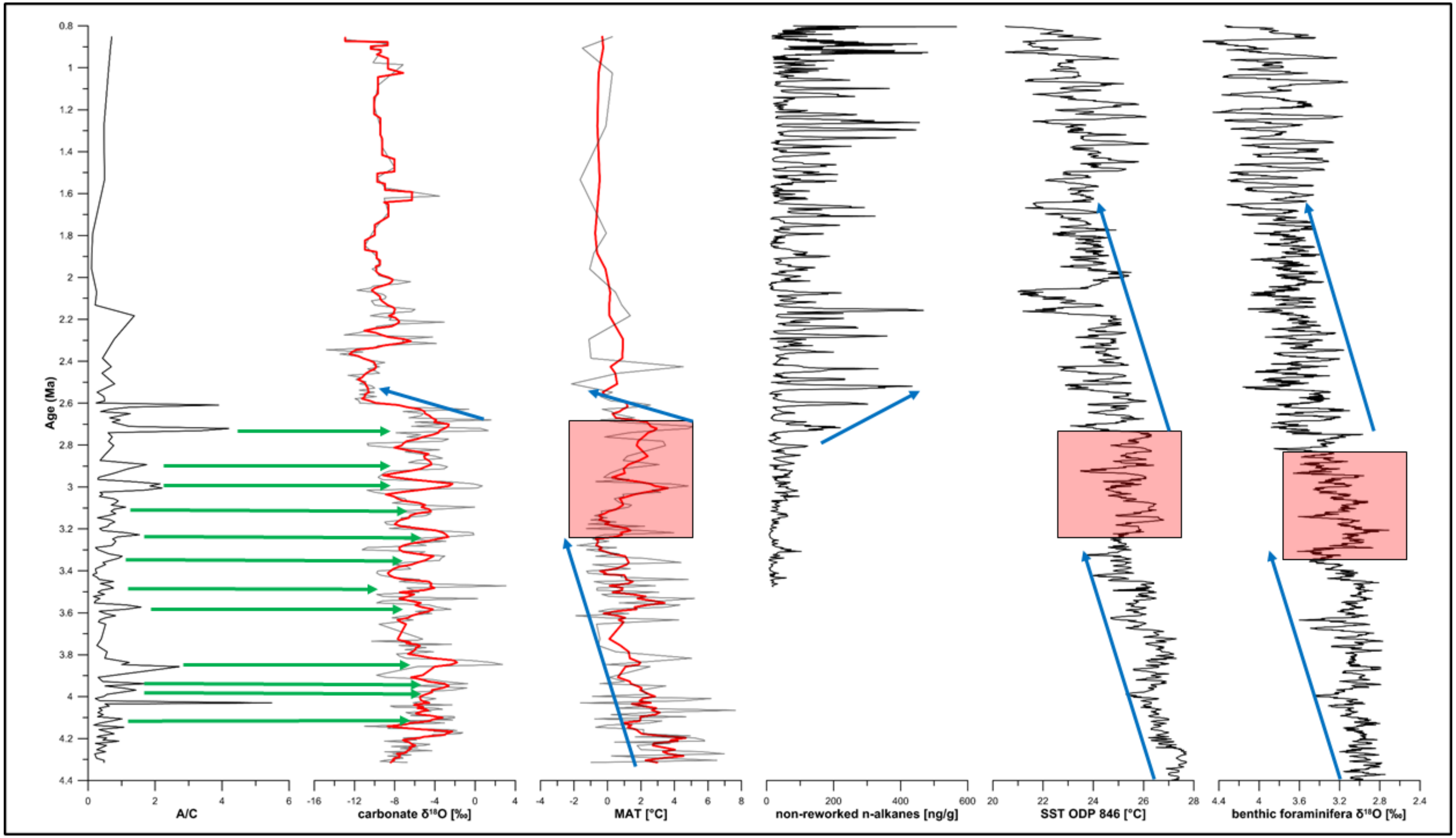

Fig. 5 - 19: Comparison of A/C ratio, carbonate $\delta^{18}O$ values and reconstructed MATs from this study with alkane dust record from IODP Site U1313 (Naafs et al., 2012), SST from ODP Site 846 (Lawrence et al., 2006) and benthic oxygen isotopes from Zachos et al. (2001). The green arrows indicate co-occurring peaks in the A/C ratio and carbonate $\delta^{18}O$ values.

5.3.5. Orbital forcing of palaeovegetation and palaeoclimate variability in the Kunlun Pass Basin

In Fig. 5 – 20, the Lomb Periodograms for the A/C ratio, broadleaved trees, coniferous trees, reconstructed MAPs and reconstructed MATs are shown. Since broadleaved trees show a strong decline after the initial 300 ka of the pollen record, their orbital cycles show the lowest powers compared to the other proxies. Eccentricity forcing is the strongest signal in all indicators whereas obliquity cycles are not always visible. However, stronger powers have been noticed for cycles ~ 58 ka which have been suggested to be a combination of obliquity and precessional forcing (Berger, 1977; Bordiga et al., 2014). Since the resolution of samples is too low to directly test if precession has a strong influence on the Kunlun Pass Basin palaeovegetation and palaeoclimate evolution, the 58 ka cycles could be an indicator that precession had a profound impact.

In the SG-1b core, eccentricity, obliquity and precession signals were recorded by the continuous wavelet transform. Despite the lower resolution, it should still be possible to detect obliquity cycles in the Kunlun Pass Basin record. Whereas the NW Qaidam Basin showed a strong obliquity forcing during times of low obliquity for most of the interval, no strong obliquity cyclicity is seen in the Kunlun Pass Basin record. Instead, eccentricity forcing had the highest impact on the palaeovegetation and palaeoclimate evolution.

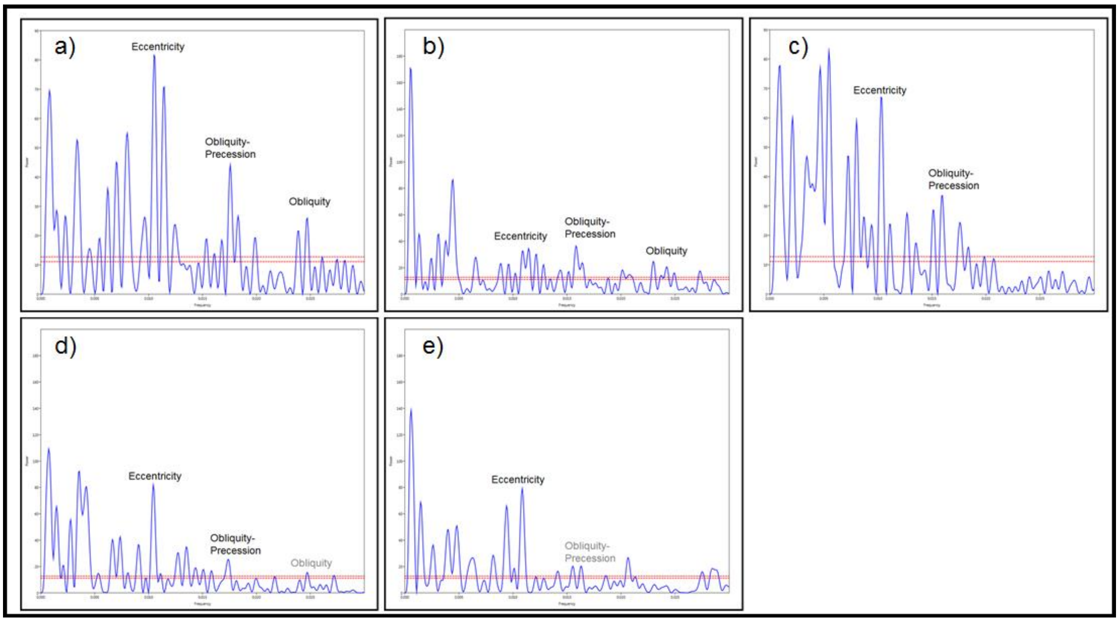

Fig. 5 - 20: Lomb Periodogram of A/C ratio (a), broadleaved trees (b), coniferous trees (c), MAPs (d) and MATs (e) for the interval from 4.314 to 2.6 Ma. The figure has been drawn using PAST3 (Hammer et al., 2001). The resolution of samples after 2.6 Ma is too low for a longer examination of orbital forcings.

5.4 Summary & Conclusions

The Kunlun Pass Basin record show multiple vegetation and climate changes between 4.314 and 0.853 Ma,

- The palaeovegetation history of the Kunlun Pass Basin reveals that two strong cooling phases took place. During the Early Pliocene from 4.314 to ~ 3.8 Ma broadleaved and coniferous forest patches were replaced by xerophytic shrublands. According to the pollen-climate transfer functions, the MAT dropped by ca. 3.0 ± 0.7°C between the time intervals 4.3 – 4.0 Ma to 3.3 – 3.0 Ma, which is larger than the modelled decline of global temperatures (~ 1.08 – 1.71°C) for the same time intervals (Brierley et al., 2009; Haywood et al., 2009; Haywood and Valdes, 2004). After the onset of the NHG, a change from xerophytic shrublands to alpine steppe/meadow vegetation suggests another period of strong temperature decline.

- The strong expansion of xerophytic shrublands after 3.8 Ma and after ~ 2.15 Ma indicates intervals of aridification in the Kunlun Pass region in the Late Pliocene and Early Pleistocene.

- A good correlation of temperature estimates from two independent proxies (pollen and carbonate δ^{18}O values) indicate that no tectonic uplift occurred in the studied interval. Despite the missing match between the pollen and isotope proxies in the first 100 – 300 ka, there is no characteristic drop in carbonate δ^{18}O values, which would indicate tectonic uplift. Additionally, the high percentages of Caroyphyllaceae and low percentages of *Ephedra* in PAZ 1 imply that the Kunlun Pass Basin already reached an elevation interval of ~ 4500 to 5000 m in the Early Pliocene based on a comparison to their modern altitudinal distribution in NW China. Furthermore, a higher reconstructed temperature during this time interval is also suggested by other Chinese records which were unaffected by tectonic uplift.

- The temperature reconstruction for the time interval 3.3 to 3.0 Ma reveals that Pliocene temperatures were 4.28 – 10.05°C higher than present-day. This is in good agreement with other temperature reconstructions from high latitudinal sites which suggested temperatures of up to 19°C higher during the mPWP (Ballantyne et al., 2010; Panitz et al., 2016). These palaeotemperature estimates from the Kunlun Pass Basin exceed current modelling results for the mPWP which indicate that temperatures were only 0.5 – 4.0°C higher on the Tibetan Plateau compared to the pre-industrial (Yan et al., 2019).

- Although strong cooling and advances of ice sheets were already recognised after 3.15 Ma in the North Atlantic region (Jansen et al., 2000; Kleiven et al., 2002), palaeotemperature estimates in the NW Qaidam Basin and Kunlun Pass Basin together with elevated carbonate $\delta^{18}O$ values (Kunlun Pass Basin samples) indicate that temperatures in NW China were not declining until 2.75 Ma. Furthermore, the comparison between MAPs and A/C ratios from the Kunlun Pass Basin and the NW Qaidam Basin seem to suggest that when the EASM caused wetter conditions in the NW Qaidam Basin (northwestward extension of EASM), the Kunlun Pass Basin became drier (less intense EASM). Since the sample resolution of this study is different for the Kunlun Pass Basin and the NW Qaidam Basin record and the studied comparison interval (3.5 – 3.0 Ma) is rather short, further investigation into this pattern (extended EASM into NW Qaidam Basin while less intense EASM at Kunlun Pass Basin) is required.

- A sharp change from steppe/meadow vegetation and patches of coniferous forests to Chenopodiaceae dominated xerophytic shrublands between 2.183 and 2.132 Ma is most likely related to increased glaciation and changes in sea-level after MIS 82 (Raymo et al., 1986; Rohling et al., 2014). Since the palaeovegetation did not return to steppes/meadows or patchy forest vegetation after 2.132 Ma in the Kunlun Pass Basin record, sea level lowering and increased glaciation could have had a long-lasting effect on the region. The changes after MIS 82 should be followed up with a higher resolution counting.

Chapter 6: Conclusions

6.1 NW Qaidam Basin

6.1.1 Summary

This thesis examined the vegetation and climate variability of the NW Qaidam Basin between 3.5 and 3.0 Ma (including the mPWP), the main source of precipitation during this warm period and the forcing mechanisms for the climate variability. Palaeovegetation and palaeoclimate reconstructions for the mPWP are fundamentally important in order to understand how our environment might change under future global warming scenarios (Haywood et al., 2009; Haywood et al., 2016; Salzmann et al., 2013; Seki et al., 2010). Previous studies from the NW Qaidam Basin suggested that aridification as a consequence of global cooling and/or uplift of the Tibetan Plateau led to the formation of xerophytic shrublands between the Miocene and Pleistocene (Cai et al., 2012; Miao et al., 2011; Miao et al., 2013). In order to understand, how the precipitation and thereby, vegetation and climate, in a warmer world changes at the western limit of the EASM, the mPWP of the NW Qaidam Basin provides a good opportunity to study palaeovegetation and palaeoclimate variability.

This thesis presents the first high resolution palynological record from the NW Qaidam Basin covering 3.5 and 3.0 Ma which demonstrates that the regional vegetation was dominated by xerophytic shrublands composed of Chenopodiaceae, *Artemisia*, *Ephedra*, *Nitraria* and Caryophyllaceae. The frequent occurrences of coniferous and broadleaved trees, such as *Betula*, *Corylus*, *Ulmus*, *Alnus*, *Juglans*/*Pterocarya*, *Pinus*, *Picea* and *Abies*, illustrates that the Late Pliocene in the NW Qaidam Basin was much wetter than modern day. The lithology, X-ray fluorescence and C/N data point to the existence of a semi-large and semi-deep palaeolake that underwent frequent changes in lake size and depth while nowadays this area is characterised by a desert landscape. The wetter conditions during the Pliocene are supported by palaeoclimate estimates based on pollen – climate transfer functions which indicate that the MAPs are more than 100 mm higher than present day. Although many studies suggest that the temperature during the mPWP was significantly higher

(Haywood et al., 2009; Haywood and Valdes, 2004; Martinez-Boti et al., 2015), the palaeoclimate reconstruction of MATs at the SG-1b coring site does not indicate significantly warmer conditions.

The comparison of sedimentological analyses and lakeshore grass percentages to other Chinese records from the EASM (Fu et al., 2013; Fu et al., 2015; Li et al., 2018b) and westerlies (Liu et al., 2014) dominated precipitation regimes showed that the main source of precipitation in the NW Qaidam Basin was delivered by the EASM. Using the A/C ratio (El-Moslimany, 1990; Zhao et al., 2012), it was possible to link the moisture availability in the NW Qaidam Basin to warming in the EEP (Lawrence et al., 2006) and orbital forcings of high latitude ice sheets. During the cooling from 3.5 to 3.3 Ma, which culminated in the MIS M2 cooling event (Lisiecki and Raymo, 2005), and after 3.15 Ma (until ca. 3.025 Ma) the A/C curve fits well with Northern Hemisphere summer insolation suggesting that the EASM was stronger during boreal summer when ice sheets existed in the Northern Hemisphere. Between ~ 3.35 and 3.15 Ma, however, the A/C curve fits well with the Southern Hemisphere summer insolation which indicates that Antarctic ice sheet variability significantly influenced the EASM and thereby the moisture availability in the NW Qaidam Basin. This study described for the first time the impact of hemisphere change of EASM forcing (Clemens et al., 2008; Sun et al., 2010) during the Late Pliocene on the vegetation in the Asian interior.

6.1.2 Main findings

- The new results from the SG-1b core show that between 3.5 and 3.0 Ma the main source of precipitation in the NW Qaidam Basin was provided by the EASM. The presence of a palaeolake and semi-desert vegetation suggests that the EASM penetrated further into NW China during the Pliocene compared to modern-day. Stronger EASM precipitation in the NW Qaidam Basin was related to warming in the EEP during times of orbital forced ice sheet retreat.

- The palaeovegetation and palaeoclimate reconstruction indicates that the NW Qaidam Basin underwent three major climatic stages: 3.5 – 3.285 Ma dry, 3.285 – 3.125 Ma wet and 3.125 – 3.011 Ma dry. Despite the two drier intervals at the top and bottom of this time interval, the palaeoclimate estimates, which are based on pollen – climate transfer functions, indicate that the NW Qaidam Basin received about four to twentyfold precipitation (MAP ~ 120 – 400 mm) compared to modern-day.

- Continuous wavelet transform analysis of the A/C ratio as a moisture indicator suggests that the precipitation in the Qaidam Basin was controlled by precession, obliquity and eccentricity cycles. However, increased moisture availability in the NW Qaidam Basin shifts from southern to Northern Hemisphere summer insolation during intervals of significant ice sheet build-up in the Northern Hemisphere.

6.2. Kunlun Pass Basin

6.2.1 Summary

This thesis presents the first well-dated palynological record from the Kunlun Pass Basin for the Early Pliocene until the Pleistocene (4.314 – 0.853 Ma), which illustrates palaeovegetation and -climate changes on the high mountainous Tibetan Plateau at orbital resolution.

The palynology record shows that the study area was characterised by patchy broadleaved and coniferous forest vegetation during the Early Pliocene until ca 4.0 Ma which implies much warmer conditions since forests on the Tibetan Plateau are restricted to southern and southeastern regions during present-day (Hou, 2001; Ni and Herzschuh, 2011; Wang et al., 2011). After a brief steppe/meadow transition period, which marked the end of a first cooling phase, xerophytic shrublands dominated the Kunlun Pass Basin until ca. 2.5 Ma with changing abundances of mainly Chenopodiaceae and *Artemisia* as a result of fluctuating moisture availability. The onset of the NHG (Haug et al., 2005) was characterised by initial drying around 2.75 Ma with a subsequent cooling at 2.6 and 2.5 Ma. The establishment of steppes/meadows with re-advancing coniferous forests display the coldest conditions from 2.5 to 2.15 Ma. Re-occuring expansion of Chenopodiaceae shrublands after the “deep glaciation” of MIS 82 (Ding et al., 2002; Hodell and Channell, 2016; Rohling et al., 2014) indicates sustained drying of the Kunlun Pass Basin area.

Based on pollen – climate transfer functions, the palaeoclimate estimates suggest that the temperatures were 4.49 to 13.73°C higher than modern-day in the Early Pliocene and 4.28 to 10.05°C higher than modern-day during the mPWP. Although the palaeovegetation, palaeoclimate estimates and carbonate δ^{18}O record of the Kunlun Pass Basin suggest that cooling occurred in the study area, tectonic uplift seems unlikely since the cooling periods were also observed in other Chinese records (Li et al., 2011; Wang et al., 2006a; Wu et al., 2006) unaffected by changes in palaeoelevation.

6.2.2 Main findings

- The palaeovegetation history of the Kunlun Pass Basin reveals that two strong cooling phases took place. During the Early Pliocene from 4.314 to ~ 3.8 Ma broadleaved and coniferous forest patches were replaced by steppes/meadows and subsequently xerophytic shrublands. After the onset of the NHG, a change from xerophytic shrublands to alpine steppe/meadow vegetation suggests another period of strong temperature decline (~ 2.6 to 2.15 Ma).

- The strong expansion of xerophytic shrublands after 3.8 Ma and after ~ 2.15 Ma indicates intervals of aridification in the Kunlun Pass region in the Late Pliocene and Early Pleistocene.

- The pollen – climate transfer function based temperature estimates show a good correlation to carbonate δ^{18}O values except for the initial 300 ka. Although carbonate δ^{18}O values point to strongly lowered values around 2.6 Ma, which could potentially represent tectonic uplift, the onset of the NHG seems to be a more likely explanation for the different isotope signal.

- Although the palaeovegetation and palaeoclimate estimates in the Early Pliocene suggest a strong cooling period from 4.314 to ~ 3.8 Ma, the carbonate $\delta^{18}O$ values do not show lowered values that are characteristic of period of tectonic uplift. Additionally, the comparison of *Ephedra* and Caryophyllaceae percentages from the pollen record with their modern-day elevation-dependent distribution shows that the modern height of the Kunlun Pass Basin was probably already reached in the Early Pliocene. Therefore, this thesis indicates that tectonic uplift unlikely occurred in the studied time interval.

- The comparison between MAPs and A/C ratios from the Kunlun Pass Basin and the NW Qaidam Basin seem to suggest that when the EASM caused wetter conditions in the NW Qaidam Basin (northwestward extension of EASM), the Kunlun Pass Basin became drier (less intense EASM). The underlying mechanism for this observation are unknown. Since at least three study sites are necessary to evaluate spatial information about the extent and intensity of the EASM, more high-resolution studies are required to make qualitative assumptions about the relative strength of the EASM in regions at the western limit. A working hypothesis could be that stronger precipitation in the NW Qaidam Basin is related to a weaking of precipitation in the Kunlun Pass Basin.

- Spectral analysis of vegetation and climate proxies indicates that eccentricity had the most significant effect on the palaeoenvironmental evolution of the Kunlun Pass Basin between 4.314 and 2.6 Ma.

6.3 Concluding remarks

In the Introduction Chapter, the need for high-resolution pollen records in NW China for the mPWP was outlined in order to improve our understanding of palaeovegetation and palaeoclimate variability in a warmer world. In the concluding remarks, I refer back to the question of what implications the main findings of this thesis have for modelling of the Pliocene as well as modelling of future climate during times of global warmth.

This thesis has shown that the NW Qaidam Basin becomes significantly wetter when global temperatures increase, the EEP warms and ice sheets shrink in both hemispheres. Although recently published, the modelling results from Yan et al. (2019) and Li et al. (2018a) are fundamentally different for the Qaidam Basin, which underlined the need for hard data. The results of this study are in good agreement with the suggested results from Li et al. (2018a).

Wetter climate conditions in this region will have a direct impact on the dust transport within China as it is one of the source regions (e.g. Pullen et al., 2011; Wang et al., 2006c). Depending on the scale of the global warming and climate amelioration in the Qaidam Basin, Chinese environmental policies, which are focused on improving palaeoenvironmental conditions in NW China with a sustainable land usage, could be influenced.

With regard to the Kunlun Pass Basin, this study showed strongly increased temperatures during the Early Pliocene and the mPWP, which has not been reproduced by recent modelling (Yan et al., 2019). In contrast, future modelling results (Feng et al., 2014; Wang et al., 2011) are in good agreement with the palaeotemperature estimates of this thesis.

This study presented the first palaeoclimate estimates for the Pliocene NW China. While the reconstructed temperature and precipitation records are a great improvement compared to traditional estimations based on methods, such as the Coexistence Approach (Mosbrugger and Utescher, 1997), the lack of sample sites from extremely cold and dry climates caused overestimation for the NW Qaidam Basin (precipitation) and Kunlun Pass Basin (temperature). As such, an increase in modern pollen rain data from these extreme environments (ideally from lake sediments only), is necessary to improve climate estimates of past geological times.

References

Adams, K.D., 2007. Late Holocene sedimentary environments and lake-level fluctuations at Walker Lake, Nevada, USA. Geological Society of America Bulletin 119, 126-139.

Agnihotri, R., Dutta, K., Bhushan, R., Somayajulu, B.L.K., 2002. Evidence for solar forcing on the Indian monsoon during the last millennium. Earth and Planetary Science Letters 198, 521-527.

Aichner, B., Feakins, S.J., Lee, J.E., Herzschuh, U., Liu, X., 2015. High-resolution leaf wax carbon and hydrogen isotopic record of the late Holocene paleoclimate in arid Central Asia. Climate of the Past 11, 619-633.

Aitchison, J.C., Ali, J.R., Davis, A.M., 2007. When and where did India and Asia collide? Journal of Geophysical Research: Solid Earth 112, n/a-n/a.

Almogi-Labina, A., Schmiedl, G., Hemleben, C., Siman-Tov, R., Segl, M., Meischner, D., 2000. The influence of the NE winter monsoon on productivity changes in the Gulf of Aden, NW Arabian Sea, during the last 530 ka as recorded by foraminifera. Marine Micropaleontology 40, 295-319.

Amidon, W.H., Hynek, S.A., 2010. Exhumational history of the north central Pamir. Tectonics 29.

An, Z., Kutzbach, J.E., Prell, W.L., Porter, S.C., 2001. Evolution of Asian monsoons and phased uplift of the Himalaya-Tibetan plateau since Late Miocene times. Nature 411, 62-66.

Andreev, A.A., Tarasov, P.E., Wennrich, V., Raschke, E., Herzschuh, U., Nowaczyk, N.R., Brigham-Grette, J., Melles, M., 2014. Late Pliocene and Early Pleistocene vegetation history of northeastern Russian Arctic inferred from the Lake El'gygytgyn pollen record. Clim. Past 10, 1017-1039.

Andrews, P., Bamford, M., 2008. Past and present vegetation ecology of Laetoli, Tanzania. Journal of Human Evolution 54, 78-98.

Ao, H., Roberts, A.P., Dekkers, M.J., Liu, X., Rohling, E.J., Shi, Z., An, Z., Zhao, X., 2016. Late Miocene–Pliocene Asian monsoon intensification linked to Antarctic ice-sheet growth. Earth and Planetary Science Letters 444, 75-87.

Badger, M.P.S., Chalk, T.B., Foster, G.L., Bown, P.R., Gibbs, S.J., Sexton, P.F., Schmidt, D.N., Pälike, H., Mackensen, A., Pancost, R.D., 2019. Insensitivity of alkenone carbon isotopes to atmospheric CO2 at low to moderate CO2 levels. Clim. Past 15, 539-554.

Ballantyne, A.P., Greenwood, D.R., Sinninghe Damsté, J.S., Csank, A.Z., Eberle, J.J., Rybczynski, N., 2010. Significantly warmer Arctic surface temperatures during the Pliocene indicated by multiple independent proxies. Geology 38, 603-606.

Ballantyne, A.P., Rybczynski, N., Baker, P.A., Harington, C.R., White, D., 2006. Pliocene Arctic temperature constraints from the growth rings and isotopic composition of fossil larch. Palaeogeography, Palaeoclimatology, Palaeoecology 242, 188-200.

Bartoli, G., Sarnthein, M., Weinelt, M., Erlenkeuser, H., Garbe-Schönberg, D., Lea, D.W., 2005. Final closure of Panama and the onset of northern hemisphere glaciation. Earth and Planetary Science Letters 237, 33-44.

Beaufort, L., de Garidel-Thoron, T., Linsley, B., Oppo, D., Buchet, N., 2003. Biomass burning and oceanic primary production estimates in the Sulu Sea area over the last 380 kyr and the East Asian monsoon dynamics. Marine Geology 201, 53-65.

Behre, K.-E., 1981. The interpretation of anthropogenic indicators in pollen diagrams. Pollen et spores 23, 225-245.

Berger, A., 1977. Support for the astronomical theory of climatic change. Nature 269, 44.

Bershaw, J., Penny, S.M., Garzione, C.N., 2012. Stable isotopes of modern water across the Himalaya and eastern Tibetan Plateau: Implications for estimates of paleoelevation and paleoclimate. Journal of Geophysical Research: Atmospheres 117, n/a-n/a.

Beug, H.-J., 2004. Leitfaden der Pollenbestimmung fur Mitteleuropa und angrenzende Gebiete. Verlag Friedrich Pfeil, Munich.

Birks, H., 1995. Quantitative palaeoenvironmental reconstructions. Statistical modelling of Quaternary science data. Technical Guide 5, 161-254.

Birks, H.J.B., Heiri, O., Seppä, H., Bjune, A.E., 2010. Strengths and weaknesses of quantitative climate reconstructions based on late-quaternary biological proxies. Open Ecology Journal 3, 68-110.

Birks, H.J.B., Seppä, H., 2004. Pollen-based reconstructions of late-Quaternary climate in Europe–progress, problems, and pitfalls. Acta Palaeobotanica 44, 317-334.

Blais, J.M., Kalff, J., 1995. The influence of lake morphometry on sediment focusing. Limnology and Oceanography 40, 582-588.

Blisniuk, P.M., Stern, L.A., Chamberlain, C.P., Idleman, B., Zeitler, P.K., 2005. Climatic and ecologic changes during Miocene surface uplift in the Southern Patagonian Andes. Earth and Planetary Science Letters 230, 125-142.

Boës, X., Rydberg, J., Martinez-Cortizas, A., Bindler, R., Renberg, I., 2011. Evaluation of conservative lithogenic elements (Ti, Zr, Al, and Rb) to study anthropogenic element enrichments in lake sediments. Journal of Paleolimnology 46, 75-87.

Bonnefille, R., 2010. Cenozoic vegetation, climate changes and hominid evolution in tropical Africa. Global and Planetary Change 72, 390-411.

Bookman, R., Enzel, Y., Agnon, A., Stein, M., 2004. Late Holocene lake levels of the Dead Sea. GSA Bulletin 116, 555-571.

Bordiga, M., Cobianchi, M., Lupi, C., Pelosi, N., Venti, N.L., Ziveri, P., 2014. Coccolithophore carbonate during the last 450 ka in the NW Pacific Ocean (ODP site 1209B, Shatsky Rise). Journal of Quaternary Science 29, 57-69.

Bostock, H.C., Opdyke, B.N., Williams, M.J.M., 2010. Characterising the intermediate depth waters of the Pacific Ocean using δ13C and other geochemical tracers. Deep Sea Research Part I: Oceanographic Research Papers 57, 847-859.

Bostock, H.C., Sutton, P.J., Williams, M.J.M., Opdyke, B.N., 2013. Reviewing the circulation and mixing of Antarctic Intermediate Water in the South Pacific using evidence from geochemical tracers and Argo float trajectories. Deep Sea Research Part I: Oceanographic Research Papers 73, 84-98.

Bradshaw, R.H.W., Webb, T., 1985. Relationships between Contemporary Pollen and Vegetation Data from Wisconsin and Michigan, USA. Ecology 66, 721-737.

Brierley, C.M., Fedorov, A.V., Liu, Z., Herbert, T.D., Lawrence, K.T., LaRiviere, J.P., 2009. Greatly Expanded Tropical Warm Pool and Weakened Hadley Circulation in the Early Pliocene. Science 323, 1714-1718.

Brodie, C.R., Leng, M.J., Casford, J.S.L., Kendrick, C.P., Lloyd, J.M., Yongqiang, Z., Bird, M.I., 2011. Evidence for bias in C and N concentrations and δ13C composition of terrestrial and aquatic organic materials due to pre-analysis acid preparation methods. Chemical Geology 282, 67-83.

Budziak, D., Schneider, R.R., Rostek, F., Muller, P.J., Bard, E., Wefer, G., 2000. Late Quaternary insolation forcing on total organic carbon and C-37 alkenone variations in the Arabian Sea. Paleoceanography 15, 307-321.

Caballero-Gill, R., Herbert, T.D., Dowsett, H.J., 2019. 100-kyr paced climate change in the Pliocene warm period, Southwest Pacific. . Paleoceanography and Paleoclimatology.

Cai, M., Fang, X., Wu, F., Miao, Y., Appel, E., 2012. Pliocene–Pleistocene stepwise drying of Central Asia: Evidence from paleomagnetism and sporopollen record of the deep borehole SG-3 in the western Qaidam Basin, NE Tibetan Plateau. Global and Planetary Change 94–95, 72-81.

Cane, M.A., Molnar, P., 2001. Closing of the Indonesian seaway as a precursor to east African aridification around 3–4 million years ago. Nature 411, 157.

Cao, X.-y., Herzschuh, U., Telford, R.J., Ni, J., 2014. A modern pollen–climate dataset from China and Mongolia: Assessing its potential for climate reconstruction. Review of Palaeobotany and Palynology 211, 87-96.

Cao, X.-y., Ni, J., Herzschuh, U., Wang, Y.-b., Zhao, Y., 2013. A late Quaternary pollen dataset from eastern continental Asia for vegetation and climate reconstructions: Set up and evaluation. Review of Palaeobotany and Palynology 194, 21-37.

Carroll, A.R., Bohacs, K.M., 1999. Stratigraphic classification of ancient lakes: Balancing tectonic and climatic controls. Geology 27, 99-102.

Caves, J.K., Winnick, M.J., Graham, S.A., Sjostrom, D.J., Mulch, A., Chamberlain, C.P., 2015. Role of the westerlies in Central Asia climate over the Cenozoic. Earth and Planetary Science Letters 428, 33-43.

Chang, C.-W., Iizuka, Y., Tzeng, W.-N., 2004. Migratory environmental history of the grey mullet Mugil cephalus as revealed by otolith Sr:Ca ratios.

Chang, H., An, Z., Wu, F., Jin, Z., Liu, W., Song, Y., 2013. A Rb/Sr record of the weathering response to environmental changes in westerly winds across the Tarim Basin in the late Miocene to the early Pleistocene. Palaeogeography, Palaeoclimatology, Palaeoecology 386, 364-373.

Chang, H., An, Z.S., Wu, F., Song, Y.G., Qiang, X.K., Li, L.Y., 2017. Late Miocene - early Pleistocene climate change in the mid-latitude westerlies and their influence on Asian monsoon as constrained by the K/Al ratio record from drill core Ls2 in the Tarim Basin. Catena 153, 75-82.

Chang, L., Guo, Z.T., Deng, C.L., Wu, H.B., Ji, X.P., Zhao, Y., Zhang, C.X., Ge, J.Y., Wu, B.L., Sun, L., Zhu, R.X., 2015. Pollen evidence of the palaeoenvironments of Lufengpithecus lufengensis in the Zhaotong Basin, southeastern margin of the Tibetan Plateau. Palaeogeography Palaeoclimatology Palaeoecology 435, 95-104.

Charreau, J., Gilder, S., Chen, Y., Dominguez, S.p., Avouac, J.-P., Sen, S., Jolivet, M., Li, Y., Wang, W., 2006. Magnetostratigraphy of the Yaha section, Tarim Basin (China): 11 Ma acceleration in erosion and uplift of the Tian Shan mountains. Geology 34, 181-184.

Chavez, F.P., Strutton, P.G., Friederich, G.E., Feely, R.A., Feldman, G.C., Foley, D.G., McPhaden, M.J., 1999. Biological and Chemical Response of the Equatorial Pacific Ocean to the 1997-98 El Niño. Science 286, 2126-2131.

Chen, F.-H., Chen, J.-H., Holmes, J., Boomer, I., Austin, P., Gates, J.B., Wang, N.-L., Brooks, S.J., Zhang, J.-W., 2010a. Moisture changes over the last millennium in arid central Asia: a review, synthesis and comparison with monsoon region. Quaternary Science Reviews 29, 1055-1068.

Chen, F., Yu, Z., Yang, M., Ito, E., Wang, S., Madsen, D.B., Huang, X., Zhao, Y., Sato, T., John B. Birks, H., Boomer, I., Chen, J., An, C., Wünnemann, B., 2008. Holocene moisture evolution in arid central Asia and its out-of-phase relationship with Asian monsoon history. Quaternary Science Reviews 27, 351-364.

Chen, J., An, Z., Head, J., 1999. Variation of Rb/Sr Ratios in the Loess-Paleosol Sequences of Central China during the Last 130,000 Years and Their Implications for Monsoon Paleoclimatology. Quaternary Research 51, 215-219.

Chen, J., Chen, F., Zhang, E., Brooks, S.J., Zhou, A., Zhang, J., 2009. A 1000-year chironomid-based salinity reconstruction from varved sediments of Sugan Lake, Qaidam Basin, arid Northwest China, and its palaeoclimatic significance. Chin.Sci.Bull. 54, 3749.

Chen, J., Chen, Y., Liu, L., Ji, J., Balsam, W., Sun, Y., Lu, H., 2006. Zr/Rb ratio in the Chinese loess sequences and its implication for changes in the East Asian winter monsoon strength. Geochimica et Cosmochimica Acta 70, 1471-1482.

Chen, Y., Ni, J., Herzschuh, U., 2010b. Quantifying modern biomes based on surface pollen data in China. Global and Planetary Change 74, 114-131.

Clark, M.K., Farley, K.A., Zheng, D., Wang, Z., Duvall, A.R., 2010. Early Cenozoic faulting of the northern Tibetan Plateau margin from apatite (U–Th)/He ages. Earth and Planetary Science Letters 296, 78-88.

Clemens, S.C., Murray, D.W., Prell, W.L., 1996. Nonstationary phase of the plio-pleistocene Asian monsoon. Science 274, 943-948.

Clemens, S.C., Prell, W.L., 1991. Late Quaternary forcing of Indian Ocean - Summer Monsoon winds - A comparison of fourier model and general circulation model results Journal of Geophysical Research-Atmospheres 96, 22683-22700.

Clemens, S.C., Prell, W.L., Sun, Y., Liu, Z., Chen, G., 2008. Southern Hemisphere forcing of Pliocene δ18O and the evolution of Indo-Asian monsoons. Paleoceanography 23.

Clift, P.D., Carter, A., Krol, M., Kirby, E., 2002. Constraints of India Eurasia collision in the Arabian Sea region taken from the Indus Group, Ladakh Himalaya, India, in: Clift, P.D., Kroon, D., Gaedicke, C., Craig, J. (Eds.), The tectonic and climatic evolution of the Arabian Sea region. J Geol Soc Special Publication.

Cohen, A., 2003. Age determination in lake deposits, Paleolimnology-The History and Evolution of Lake Systems. Oxford University Press.

Colin, C., Kissel, C., Blamart, D., Turpin, L., 1998. Magnetic properties of sediments in the Bay of Bengal and the Andaman Sea: impact of rapid North Atlantic Ocean climatic events on the strength of the Indian monsoon. Earth and Planetary Science Letters 160, 623-635.

Collins, L.S., Coates, A.G., Berggren, W.A., Aubry, M.-P., Zhang, J., 1996. The late Miocene Panama isthmian strait. Geology 24, 687-690.

Cook, B.I., Smerdon, J.E., Seager, R., Coats, S., 2014. Global warming and 21st century drying. Clim Dyn 43, 2607-2627.

Cook, E.R., Anchukaitis, K.J., Buckley, B.M., D'Arrigo, R.D., Jacoby, G.C., Wright, W.E., 2010. Asian Monsoon Failure and Megadrought During the Last Millennium. Science 328, 486-489.

Cour, P., Zheng, Z., Duzer, D., Calleja, M., Yao, Z., 1999. Vegetational and climatic significance of modern pollen rain in northwestern Tibet. Review of Palaeobotany and Palynology 104, 183-204.

Crowe, J.C., Sharp Jr., J.M., 1997. Hydrogeologic delineation of habitats for endangered species: the Comal Springs/River System. Environmental Geology 30, 17-28.

Csank, A.Z., Fortier, D., Leavitt, S.W., 2013. Annually resolved temperature reconstructions from a late Pliocene–early Pleistocene polar forest on Bylot Island, Canada. Palaeogeography, Palaeoclimatology, Palaeoecology 369, 313-322.

Cui, Z., Wu, Y., Liu, G., 1998. Discovery and character of the Kunlun-Yellow River Movement. Chin.Sci.Bull. 43, 833-836.

Cuven, S., Francus, P., Lamoureux, S.F., 2010. Estimation of grain size variability with micro X-ray fluorescence in laminated lacustrine sediments, Cape Bounty, Canadian High Arctic. Journal of Paleolimnology 44, 803-817.

Dai, A., 2011. Drought under global warming: a review. Wiley Interdisciplinary Reviews: Climate Change 2, 45-65.

Dai, A., 2012. Increasing drought under global warming in observations and models. Nature Climate Change 3, 52.

Dean, W.E., Fouch, T.D., 1983. Lacustrine Environment: Chapter 2: PART 1.

Dearing, J.A., 1997. Sedimentary indicators of lake-level changes in the humid temperate zone: a critical review. Journal of Paleolimnology 18, 1-14.

DeCelles, P.G., Kapp, P., Gehrels, G.E., Ding, L., 2014. Paleocene-Eocene foreland basin evolution in the Himalaya of southern Tibet and Nepal: Implications for the age of initial India-Asia collision. Tectonics 33, 824-849.

DeCelles, P.G., Quade, J., Kapp, P., Fan, M., Dettman, D.L., Ding, L., 2007. High and dry in central Tibet during the Late Oligocene. Earth and Planetary Science Letters 253, 389-401.

DeConto, R.M., Pollard, D., Wilson, P.A., Palike, H., Lear, C.H., Pagani, M., 2008. Thresholds for Cenozoic bipolar glaciation. Nature 455, 652-U652.

Dekens, P.S., Ravelo, A.C., McCarthy, M.D., 2007. Warm upwelling regions in the Pliocene warm period. Paleoceanography 22.

Demske, D., Mohr, B., Oberhänsli, H., 2002. Late Pliocene vegetation and climate of the Lake Baikal region, southern East Siberia, reconstructed from palynological data. Palaeogeography, Palaeoclimatology, Palaeoecology 184, 107-129.

Demske, D., Tarasov, P.E., Nakagawa, T., 2013. Atlas of pollen, spores and further non-pollen palynomorphs recorded in the glacial-interglacial late Quaternary sediments of Lake Suigetsu, central Japan. Quaternary International 290-291, 164-238.

Deng, T., Ding, L., 2015. Paleoaltimetry reconstructions of the Tibetan Plateau: progress and contradictions. National Science Review 2, 417-437.

Dettman, D.L., Fang, X., Garzione, C.N., Li, J., 2003. Uplift-driven climate change at 12 Ma: a long δ18O record from the NE margin of the Tibetan plateau. Earth and Planetary Science Letters 214, 267-277.

Ding, Z.L., Derbyshire, E., Yang, S.L., Yu, Z.W., Xiong, S.F., Liu, T.S., 2002. Stacked 2.6-Ma grain size record from the Chinese loess based on five sections and correlation with the deep-sea δ18O record. Paleoceanography 17, 5-1-5-21.

Ding, Z.L., Liu, T.S., Rutter, N.W., Yu, Z.W., Guo, Z.T., Zhu, R.X., 1995. Ice-Volume forcing of East Asian Winter Monsoon variations in the past 800,000 years. Quaternary Research 44, 149-159.

Dissard, D., Nehrke, G., Reichart, G.J., Bijma, J., 2010. The impact of salinity on the Mg/Ca and Sr/Ca ratio in the benthic foraminifera Ammonia tepida: Results from culture experiments. Geochimica et Cosmochimica Acta 74, 928-940.

Dolan, A.M., Haywood, A.M., Hill, D.J., Dowsett, H.J., Hunter, S.J., Lunt, D.J., Pickering, S.J., 2011. Sensitivity of Pliocene ice sheets to orbital forcing. Palaeogeography, Palaeoclimatology, Palaeoecology 309, 98-110.

Donald, D.B., Bogard, M.J., Finlay, K., Leavitt, P.R., 2011. Comparative effects of urea, ammonium, and nitrate on phytoplankton abundance, community composition, and toxicity in hypereutrophic freshwaters. Limnology and Oceanography 56, 2161-2175.

Douglas, S., Perry, M.E., Abbey, W.J., Tanaka, Z., Chen, B., McKay, C.P., 2015. The structure and chemical layering of Proterozoic stromatolites in the Mojave Desert. International Journal of Astrobiology 14, 517-526.

Dowsett, H.J., Barron, J.A., Poore, R.Z., Thompson, R.S., Cronin, T.M., Ishman, S.E., Willard, D.A., 1999. Middle Pliocene paleoenvironmental reconstruction: PRISM2. US Geological Survey open file report 99, 535.

Dowsett, H.J., Foley, K.M., Stoll, D.K., Chandler, M.A., Sohl, L.E., Bentsen, M., Otto-Bliesner, B.L., Bragg, F.J., Chan, W.L., Contoux, C., Dolan, A.M., Haywood, A.M., Jonas, J.A., Jost, A., Kamae, Y., Lohmann, G., Lunt, D.J., Nisancioglu, K.H., Abe-Ouchi, A., Ramstein, G., Riesselman, C.R., Robinson, M.M., Rosenbloom, N.A., Salzmann, U., Stepanek, C., Strother, S.L., Ueda, H., Yan, Q., Zhang, Z.S., 2013. Sea Surface Temperature of the mid-Piacenzian Ocean: A Data-Model Comparison. Scientific reports 3.

Dugdale, R., Wischmeyer, A., Wilkerson, F., Barber, R., Chai, F., Jiang, M.-S., Peng, T.-H., 2002. Meridional asymmetry of source nutrients to the equatorial Pacific upwelling ecosystem and its potential impact on ocean–atmosphere CO2 flux; a data and modeling approach. Deep Sea Research Part II: Topical Studies in Oceanography 49, 2513-2531.

El-Moslimany, A.P., 1990. Ecological significance of common nonarboreal pollen: examples from drylands of the Middle East. Review of Palaeobotany and Palynology 64, 343-350.

Endlicher, W., 1993. Klimatische Aspekte der Weidedegradation in Ost-Patagonien. Beiträge zur Kultur-und Regionalgeographie. Festschrift für Ralph Jätzold. Geographische Gesellschaft Trier, Trier, 91-103.

Fang, X., Gao, J., Zhang, W., Wang, Y., Liu, D., 2006. Detailed evolution of Qigequan-Yueyashan tectonics in the front of Altyn Tagh and western Qaidam Basin and selection of prospective targets. Report of Academy, 1-122.

Fang, X., Li, M., Wang, Z., Wang, J., Li, J., Liu, X., Zan, J., 2016. Oscillation of mineral compositions in Core SG-1b, western Qaidam Basin, NE Tibetan Plateau. Scientific reports 6, 32848.

Fang, X., Zhang, W., Meng, Q., Gao, J., Wang, X., King, J., Song, C., Dai, S., Miao, Y., 2007. High-resolution magnetostratigraphy of the Neogene Huaitoutala section in the eastern Qaidam Basin on the NE Tibetan Plateau, Qinghai Province, China and its implication on tectonic uplift of the NE Tibetan Plateau. Earth and Planetary Science Letters 258, 293-306.

Fedorov, A.V., Dekens, P.S., McCarthy, M., Ravelo, A.C., deMenocal, P.B., Barreiro, M., Pacanowski, R.C., Philander, S.G., 2006. The Pliocene Paradox (Mechanisms for a Permanent El Niño). Science 312, 1485-1489.

Fee, E.J., Shearer, J.A., DeBruyn, E.R., Schindler, E.U., 1992. Effects of Lake Size on Phytoplankton Photosynthesis. Canadian Journal of Fisheries and Aquatic Sciences 49, 2445-2459.

Feng, R., Otto-Bliesner, B.L., Fletcher, T.L., Tabor, C.R., Ballantyne, A.P., Brady, E.C., 2017. Amplified Late Pliocene terrestrial warmth in northern high latitudes from greater radiative forcing and closed Arctic Ocean gateways. Earth and Planetary Science Letters 466, 129-138.

Feng, S., Hu, Q., Huang, W., Ho, C.-H., Li, R., Tang, Z., 2014. Projected climate regime shift under future global warming from multi-model, multi-scenario CMIP5 simulations. Global and Planetary Change 112, 41-52.

Fick, S.E., Hijmans, R.J., 2017. WorldClim 2: new 1-km spatial resolution climate surfaces for global land areas. International journal of climatology 37, 4302-4315.

Florea, L., Bird, B., Lau, J.K., Wang, L., Lei, Y., Yao, T., Thompson, L.G., 2017. Stable isotopes of river water and groundwater along altitudinal gradients in the High Himalayas and the Eastern Nyainqentanghla Mountains. Journal of Hydrology: Regional Studies 14, 37-48.

Francis, J.E., Hill, R.S., 1996. Fossil plants from the Pliocene Sirius Group, Transantarctic Mountains; evidence for climate from growth rings and fossil leaves. PALAIOS 11, 389-396.

Fu, C., An, Z., Qiang, X., Bloemendal, J., Song, Y., Chang, H., 2013. Magnetostratigraphic determination of the age of ancient Lake Qinghai, and record of the East Asian monsoon since 4.63 Ma. Geology 41, 875-878.

Fu, C., Bloemendal, J., Qiang, X., Hill, M.J., An, Z., 2015. Occurrence of greigite in the Pliocene sediments of Lake Qinghai, China, and its paleoenvironmental and paleomagnetic implications. Geochemistry, Geophysics, Geosystems 16, 1293-1306.

Fu, J.-L., Qian, W.-H., 2011. The Structure of a Typical Mei-Yu Front Identified by the Equivalent Temperature. Atmospheric and Oceanic Science Letters 4, 109-113.

Füllenbach, C.S., Schöne, B.R., Mertz-Kraus, R., 2015. Strontium/lithium ratio in aragonitic shells of Cerastoderma edule (Bivalvia) — A new potential temperature proxy for brackish environments. Chemical Geology 417, 341-355.

Gao, C., McAndrews, J.H., Wang, X., Menzies, J., Turton, C.L., Wood, B.D., Pei, J., Kodors, C., 2012. Glaciation of North America in the James Bay Lowland, Canada, 3.5 Ma. Geology 40, 975-978.

Gao, Y.X., 1962. On some problems of Asian monsoon., in: Gao, Y.X. (Ed.), Some Questions about the East Asian Monsoon. Chinese Science Press, Beijing, pp. pp. 1 - 49 (in Chinese).

Garber, R.A., Friedman, G.M., 1983. Coated Grains Along the Dead Sea Shore. Springer Berlin Heidelberg, Berlin, Heidelberg, pp. 163-168.

Garzione, C.N., 2008. Surface uplift of Tibet and Cenozoic global cooling. Geology 36, 1003-1004.

Garzione, C.N., Dettman, D.L., Quade, J., DeCelles, P.G., Butler, R.F., 2000. High times on the Tibetan Plateau: Paleoelevation of the Thakkhola graben, Nepal. Geology 28, 339-342.

Garzione, C.N., Hoke, G.D., Libarkin, J.C., Withers, S., MacFadden, B., Eiler, J., Ghosh, P., Mulch, A., 2008. Rise of the Andes. Science 320, 1304-1307.

Gebelin, A., Mulch, A., Teyssier, C., Jessup, M.J., Law, R.D., Brunel, M., 2013. The Miocene elevation of Mount Everest. Geology 41, 799-802.

George, A.D., Marshallsea, S.J., Wyrowoll, K.H., Jie, C., Yanchou, L., 2001. Miocene cooling in the northern Qilian Shan, northeastern margin of the Tibetan Plateau, revealed by apatite fission-track and vitrinite-reflectance analysis. Geology 29, 939-942.

Gessner, U., Naeimi, V., Klein, I., Kuenzer, C., Klein, D., Dech, S., 2013. The relationship between precipitation anomalies and satellite-derived vegetation activity in Central Asia. Global and Planetary Change 110, 74-87.

Gordon, A.L., Fine, R.A., 1996. Pathways of water between the Pacific and Indian oceans in the Indonesian seas. Nature 379, 146-149.

Grimm, E., 1991. Tilia and Tiliagraph. Illinois State Museum, Springfield.

Grimm, E.C., 1987. CONISS: a FORTRAN 77 program for stratigraphically constrained cluster analysis by the method of incremental sum of squares. Comput. Geosci. 13, 13-35.

Grimm, G.W., Denk, T., 2012. Reliability and resolution of the coexistence approach — A revalidation using modern-day data. Review of Palaeobotany and Palynology 172, 33-47.

Guildford, S.J., Hendzel, L.L., Kling, H.J., Fee, E.J., Robinson, G.G.C., Hecky, R.E., Kasian, S.E.M., 1994. Effects of Lake Size on Phytoplankton Nutrient Status. Canadian Journal of Fisheries and Aquatic Sciences 51, 2769-2783.

Guo, Q., 2003. Interdecadal variability of East Asian summer monsoon and its impact on the climate of China. Acta Geographica Sinica 58, 569-576.

Guo, Z.T., Ruddiman, W.F., Hao, Q.Z., Wu, H.B., Qiao, Y.S., Zhu, R.X., Peng, S.Z., Wei, J.J., Yuan, B.Y., Liu, T.S., 2002. Onset of Asian desertification by 22[thinsp]Myr ago inferred from loess deposits in China. Nature 416, 159-163.

Ha, K.-J., Heo, K.-Y., Lee, S.-S., Yun, K.-S., Jhun, J.-G., 2012. Variability in the East Asian Monsoon: a review. Meteorological Applications 19, 200-215.

Haberzettl, T., Fey, M., Lücke, A., Maidana, N., Mayr, C., Ohlendorf, C., Schäbitz, F., Schleser, G.H., Wille, M., Zolitschka, B., 2005. Climatically induced lake level changes during the last two millennia as reflected in sediments of Laguna Potrok Aike, southern Patagonia (Santa Cruz, Argentina). Journal of Paleolimnology 33, 283-302.

Håkanson, L., 1982. Lake bottom dynamics and morphometry: the dynamic ratio. Water Resources Research 18, 1444-1450.

Håkanson, L., Jansson, M., 1983. Principles of lake sedimentology. Springer-Verlag Berlin.

Hammer, Ø., Harper, D., Ryan, P., 2001. PAST-Palaeontological statistics.

Hansen, B.C.S., Grimm, E.C., Watts, W.A., 2001. Palynology of the Peace Creek site, Polk County, Florida. Geological Society of America Bulletin 113, 682-692.

Hanson, A.D., 1999. Organic geochemistry and petroleum geology, tectonics and basin analysis of southern Tarim and northern Qaidam basins, northwest China. Stanford University, Stanford, p. 388.

Harper, S., 2000. Thermocline ventilation and pathways of tropical–subtropical water mass exchange. Tellus A 52, 330-345.

Haug, G.H., Ganopolski, A., Sigman, D.M., Rosell-Mele, A., Swann, G.E.A., Tiedemann, R., Jaccard, S.L., Bollmann, J., Maslin, M.A., Leng, M.J., Eglinton, G., 2005. North Pacific seasonality and the glaciation of North America 2.7 million years ago. Nature 433, 821.

Haug, G.H., Günther, D., Peterson, L.C., Sigman, D.M., Hughen, K.A., Aeschlimann, B., 2003. Climate and the Collapse of Maya Civilization. Science 299, 1731-1735.

Haug, G.H., Sigman, D.M., Tiedemann, R., Pedersen, T.F., Sarnthein, M., 1999. Onset of permanent stratification in the subarctic Pacific Ocean. Nature 401, 779.

Haug, G.H., Tiedemann, R., 1998. Effect of the formation of the Isthmus of Panama on Atlantic Ocean thermohaline circulation. Nature 393, 673-676.

Haywood, A.M., Chandler, M.A., Valdes, P.J., Salzmann, U., Lunt, D.J., Dowsett, H.J., 2009. Comparison of mid-Pliocene climate predictions produced by the HadAM3 and GCMAM3 General Circulation Models. Global and Planetary Change 66, 208-224.

Haywood, A.M., Dolan, A.M., Pickering, S.J., Dowsett, H.J., McClymont, E.L., Prescott, C.L., Salzmann, U., Hill, D.J., Hunter, S.J., Lunt, D.J., Pope, J.O., Valdes, P.J., 2013. On the identification of a Pliocene time slice for data-model comparison. Philosophical transactions. Series A, Mathematical, physical, and engineering sciences 371, 20120515.

Haywood, A.M., Dowsett, H.J., Dolan, A.M., Rowley, D., Abe-Ouchi, A., Otto-Bliesner, B., Chandler, M.A., Hunter, S.J., Lunt, D.J., Pound, M., Salzmann, U., 2016. The Pliocene Model Intercomparison (PlioMIP) Phase 2: scientific objectives and experimental design. Clim. Past 12, 663-675.

Haywood, A.M., Valdes, P.J., 2004. Modelling Pliocene warmth: contribution of atmosphere, oceans and cryosphere. Earth and Planetary Science Letters 218, 363-377.

Haywood, A.M., Valdes, P.J., Peck, V.L., 2007. A permanent El Niño–like state during the Pliocene? Paleoceanography 22.

Haywood, A.M., Valdes, P.J., Sellwood, B.W., 2000. Global scale palaeoclimate reconstruction of the middle Pliocene climate using the UKMO GCM: initial results. Global and Planetary Change 25, 239-256.

He, C., Zhou, T., Lin, A., Wu, B., Gu, D., Li, C., Zheng, B., 2015. Enhanced or Weakened Western North Pacific Subtropical High under Global Warming? Scientific reports 5, 16771.

Hedges, J.I., Clark, W.A., Quay, P.D., Richey, J.E., Devol, A.H., Santos, M., 1986. Compositions and fluxes of particulate organic material in the Amazon River1. Limnology and Oceanography 31, 717-738.

Hedges, J.I., Keil, R.G., Benner, R., 1997. What happens to terrestrial organic matter in the ocean? Organic Geochemistry 27, 195-212.

Heermance, R.V., Pullen, A., Kapp, P., Garzione, C.N., Bogue, S., Ding, L., Song, P., 2013. Climatic and tectonic controls on sedimentation and erosion during the Pliocene–Quaternary in the Qaidam Basin (China). Geological Society of America Bulletin 125, 833-856.

Hendy, I.L., Napier, T.J., Schimmelmann, A., 2015. From extreme rainfall to drought: 250 years of annually resolved sediment deposition in Santa Barbara Basin, California. Quaternary International 387, 3-12.

Herb, C., Appel, E., Voigt, S., Koutsodendris, A., Pross, J., Zhang, W., Fang, X., 2015. Orbitally tuned age model for the late Pliocene–Pleistocene lacustrine succession of drill core SG-1 from the western Qaidam Basin (NE Tibetan Plateau). Geophysical Journal International 200, 35-51.

Herb, C., Koutsodendris, A., Zhang, W., Appel, E., Fang, X., Voigt, S., Pross, J., 2017. Late Plio-Pleistocene humidity fluctuations in the western Qaidam Basin (NE Tibetan Plateau) revealed by an integrated magnetic–palynological record from lacustrine sediments. Quaternary Research 84, 457-466.

Herb, C., Zhang, W., Koutsodendris, A., Appel, E., Fang, X., Pross, J., 2013. Environmental implications of the magnetic record in Pleistocene lacustrine sediments of the Qaidam Basin, NE Tibetan Plateau. Quaternary International 313–314, 218-229.

Herbert, T.D., Peterson, L.C., Lawrence, K.T., Liu, Z., 2010. Tropical Ocean Temperatures Over the Past 3.5 Million Years. Science 328, 1530-1534.

Herczeg, A.L., Smith, A.K., Dighton, J.C., 2001. A 120 year record of changes in nitrogen and carbon cycling in Lake Alexandrina, South Australia: C:N, δ15N and δ13C in sediments. Applied Geochemistry 16, 73-84.

Herzschuh, U., 2007. Reliability of pollen ratios for environmental reconstructions on the Tibetan Plateau. Journal of Biogeography 34, 1265-1273.

Heusser, L.E., Morley, J.J., 1996. Pliocene climate of Japan and environs between 4.8 and 2.8 Ma: A joint pollen and marine faunal study. Marine Micropaleontology 27, 85-106.

Hijmans, R., Cameron, S., Parra, J., Jones, P., Jarvis, A., Richardson, K., 2005. WorldClim. Global climate data. Version 1.4 (release 3).

Hill, D.J., Dolan, A.M., Haywood, A.M., Hunter, S.J., Stoll, D.K., 2010. Sensitivity of the Greenland Ice Sheet to Pliocene sea surface temperatures. Stratigraphy 7, 111-121.

Hilton, J., Lishman, J.P., Allen, P.V., 1986. The dominant processes of sediment distribution and focusing in a small, eutrophic, monomictic lake. Limnology and Oceanography 31, 125-133.

Hodell, D.A., Channell, J.E.T., 2016. Mode transitions in Northern Hemisphere glaciation: co-evolution of millennial and orbital variability in Quaternary climate. Clim. Past 12, 1805-1828.

Hoke, G.D., Liu-Zeng, J., Hren, M.T., Wissink, G.K., Garzione, C.N., 2014. Stable isotopes reveal high southeast Tibetan Plateau margin since the Paleogene. Earth and Planetary Science Letters 394, 270-278.

Hong, Y.T., Hong, B., Lin, Q.H., Shibata, Y., Hirota, M., Zhu, Y.X., Leng, X.T., Wang, Y., Wang, H., Yi, L., 2005. Inverse phase oscillations between the East Asian and Indian Ocean summer monsoons during the last 12000 years and paleo-El Niño. Earth and Planetary Science Letters 231, 337-346.

Honjo, S., 1982. Seasonality and Interaction of Biogenic and Lithogenic Particulate Flux at the Panama Basin. Science 218, 883-884.

Hoorn, C., Guerrero, J., Sarmiento, G.A., Lorente, M.A., 1995. Andean tectonics as a cause for changing drainage patterns in Miocene northern South America. Geology 23, 237-240.

Hou, X., 2001. Vegetation atlas of China. Chinese Academy of Science, the editorial board of vegetation map of China, 113-124.

Hsü, J., 1976. On the palaeobotanical evidence for continental drift and Himalayan uplift.

Hu, R., Piotrowski, A.M., Bostock, H.C., Crowhurst, S., Rennie, V., 2016a. Variability of neodymium isotopes associated with planktonic foraminifera in the Pacific Ocean during the Holocene and Last Glacial Maximum. Earth and Planetary Science Letters 447, 130-138.

Hu, X., Garzanti, E., Wang, J., Huang, W., An, W., Webb, A., 2016b. The timing of India-Asia collision onset – Facts, theories, controversies. Earth-Science Reviews 160, 264-299.

Huang, B., Piper, J.D.A., Peng, S., Liu, T., Li, Z., Wang, Q., Zhu, R., 2006. Magnetostratigraphic study of the Kuche Depression, Tarim Basin, and Cenozoic uplift of the Tian Shan Range, Western China. Earth and Planetary Science Letters 251, 346-364.

Huang, B.C., Chen, J.S., Yi, Z.Y., 2010. Paleomagnetic discussion of when and where India and Asia initially collided. Chinese Journal of Geophysics (Acta Geophysica Sinica) 53, 2045-2058.

Huang, X., Xue, J., Zhang, J., Qin, Y., Meyers, P.A., Wang, H., 2012. Effect of different wetness conditions on Sphagnum lipid composition in the Erxianyan peatland, central China. Organic Geochemistry 44, 1-7.

Ineson, S., Scaife, A.A., Knight, J.R., Manners, J.C., Dunstone, N.J., Gray, L.J., Haigh, J.D., 2011. Solar forcing of winter climate variability in the Northern Hemisphere. Nature Geosci 4, 753-757.

IPCC, I.P.o.C.C., 2007. Climate Change 2007: The physical science basis, in: Solomon, S., Qin, D., Manning, M., Chen, Z., Marquis, M., Averyt, K.B., Tignor, M., Miller, H.L. (Eds.), Contribution of Working Group I to the Fourth Assessment Report of the Intergovernmental Panel on Climate Change. Cambridge University Press, Cambridge, U.K./New York.

Jacobson, G.L., Bradshaw, R.H.W., 1981. The Selection of Sites for Paleovegetational Studies. Quaternary Research 16, 80-96.

Jansen, E., Fronval, T., Rack, F., Channell, J.E.T., 2000. Pliocene-Pleistocene ice rafting history and cyclicity in the Nordic Seas during the last 3.5 Myr. Paleoceanography 15, 709-721.

Jansen, E., Sjøholm, J., 1991. Reconstruction of glaciation over the past 6 Myr from ice-borne deposits in the Norwegian Sea. Nature 349, 600.

Ji, S., Nie, J., Breecker, D.O., Luo, Z., Song, Y., 2017. Intensified aridity in northern China during the middle Piacenzian warm period. Journal of Asian Earth Sciences 147, 222-225.

Jian, Z.M., Wang, P.X., Saito, Y., Wang, J.L., Pflaumann, U., Oba, T., Cheng, X.R., 2000. Holocene variability of the Kuroshio Current in the Okinawa Trough, northwestern Pacific Ocean. Earth and Planetary Science Letters 184, 305-319.

Jiang, H., Ding, Z., 2009. Spatial and temporal characteristics of Neogene palynoflora in China and its implication for the spread of steppe vegetation. Journal of Arid Environments 73, 765-772.

Jin, L., Chen, F., Morrill, C., Otto-Bliesner, B.L., Rosenbloom, N., 2012. Causes of early Holocene desertification in arid central Asia. Clim Dyn 38, 1577-1591.

Jin, Z., Li, F., Cao, J., Wang, S., Yu, J., 2006. Geochemistry of Daihai Lake sediments, Inner Mongolia, north China: Implications for provenance, sedimentary sorting, and catchment weathering. Geomorphology 80, 147-163.

Johnson, T.C., Brown, E.T., Shi, J., 2011. Biogenic silica deposition in Lake Malawi, East Africa over the past 150,000years. Palaeogeography, Palaeoclimatology, Palaeoecology 303, 103-109.

Jolly-Saad, M.C., Bonnefille, R., 2012. Lower Pliocene Fossil Wood from the Middle Awash Valley, Ethiopia. Palaeontographica Abteilung B-Palaophytologie 289, 43-73.

Juggins, S., 2009. Package 'rioja'. Analysis of Quaternary Science Data, The Comprehensive R Archive Network.

Kamae, Y., Ueda, H., 2011. Evaluation of simulated climate in lower latitude regions during the mid-Pliocene warm period using paleovegetation data. SOLA 7, 177-180.

Kar, N., Garzione, C.N., Jaramillo, C., Shanahan, T., Carlotto, V., Pullen, A., Moreno, F., Anderson, V., Moreno, E., Eiler, J., 2016. Rapid regional surface uplift of the northern Altiplano plateau revealed by multiproxy paleoclimate reconstruction. Earth and Planetary Science Letters 447, 33-47.

Karas, C., Nürnberg, D., Gupta, A.K., Tiedemann, R., Mohan, K., Bickert, T., 2009. Mid-Pliocene climate change amplified by a switch in Indonesian subsurface throughflow. Nature Geoscience 2, 434.

Karas, C., Nürnberg, D., Tiedemann, R., Garbe-Schönberg, D., 2011. Pliocene climate change of the Southwest Pacific and the impact of ocean gateways. Earth and Planetary Science Letters 301, 117-124.

Kassambara, A., Mundt, F., 2017. Package 'factoextra': Extract and Visualize the Results of multivariate Data Analyses.

Kaushal, S., Binford, M.W., 1999. Relationship between C:N ratios of lake sediments, organic matter sources, and historical deforestation in Lake Pleasant, Massachusetts, USA. Journal of Paleolimnology 22, 439-442.

Kawabe, M., Fujio, S., 2010. Pacific ocean circulation based on observation. Journal of Oceanography 66, 389-403.

Kelts, K., Hsü, K., 1978. Freshwater carbonate sedimentation, Lakes. Springer, pp. 295-323.

Kershaw, A.P., Sluiter, I.R., 1982. Late Cenozoic pollen spectra from the Atherton Tableland, Northeastern Australia. Australian Journal of Botany 30, 279-295.

Khalil, M.A.K., 1999. Non-CO2 greenhouse gases in the atmosphere. Annual Review of Energy and the Environment 24, 645-661.

Kirono, D.G.C., Tapper, N.J., McBride, J.L., 1999. Documenting Indonesian rainfall in the 1997/1998 El Nino event. Physical Geography 20, 422-435.

Klein, R., Tudhope, A.W., Chilcott, C.P., Patzold, J., Abdulkarim, Z., Fine, M., Fallick, A.E., Loya, Y., 1997. Evaluating southern Red Sea corals as a proxy record for the Asian monsoon. Earth and Planetary Science Letters 148, 381-394.

Kleiven, H.F., Jansen, E., Fronval, T., Smith, T.M., 2002. Intensification of Northern Hemisphere glaciations in the circum Atlantic region (3.5-2.4 Ma) - ice-rafted detritus evidence. Palaeogeography Palaeoclimatology Palaeoecology 184, 213-223.

Klootwijk, C.T., Gee, J.S., Peirce, J.W., Smith, G.M., McFadden, P.L., 1992. An early India-Asia contact - paleomagnetic constraints from Ninetyeast Ridge, ODP Leg 121. Geology 20, 395-398.

Komuscu, A.U., Erkan, A., Oz, S., 1998. Possible Impacts of Climate Change on Soil Moisture Availability in the Southeast Anatolia Development Project Region (GAP): An Analysis from an Agricultural Drought Perspective. Climatic Change 40, 519-545.

Kottek, M., Grieser, J., Beck, C., Rudolf, B., Rubel, F., 2006. World Map of the Köppen-Geiger climate classification updated. Meteor. Z. 15, 259-263.

Kou, X.Y., Ferguson, D.K., Xu, J.X., Wang, Y.F., Li, C.S., 2006. The reconstruction of paleovegetation and paleoclimate in the Late Pliocene of West Yunnan, China. Climatic Change 77, 431-448.

Koutsodendris, A., Sachse, D., Appel, E., Herb, C., Fischer, T., Fang, X., Pross, J., 2018. Prolonged Monsoonal Moisture Availability Preconditioned Glaciation of the Tibetan Plateau During the Mid-Pleistocene Transition. Geophysical Research Letters 45, 13,020-013,030.

Kutzbach, J.E., Guetter, P.J., Ruddiman, W.F., Prell, W.L., 1989. Sensitivity of climate to late Cenozoic uplift in Southern Asia and the American West: numerical experiments. J Geophys Res 94, 18393-18407.

Kylander, M.E., Ampel, L., Wohlfarth, B., Veres, D., 2011. High-resolution X-ray fluorescence core scanning analysis of Les Echets (France) sedimentary sequence: new insights from chemical proxies. Journal of Quaternary Science 26, 109-117.

Lamb, A.L., Wilson, G.P., Leng, M.J., 2006. A review of coastal palaeoclimate and relative sea-level reconstructions using δ13C and C/N ratios in organic material. Earth-Science Reviews 75, 29-57.

Lamy, F., Hebbeln, D., Wefer, G., 1999. High-resolution marine record of climatic change in mid-latitude Chile during the last 28,000 years based on terrigenous sediment parameters. Quaternary Research 51, 83-93.

Lancaster, N., Baas, A., 1998. Influence of vegetation cover on sand transport by wind: field studies at Owens Lake, California. Earth Surface Processes and Landforms: The Journal of the British Geomorphological Group 23, 69-82.

Laskar, J., Robutel, P., Joutel, F., Gastineau, M., Correia, A.C.M., Levrard, B., 2004. A long-term numerical solution for the insolation quantities of the Earth. A&A 428, 261-285.

Last, W.M., Schweyen, T.H., 1983. Sedimentology and geochemistry of saline lakes of the Great Plains. Hydrobiologia 105, 245-263.

Lau, K.-M., Weng, H., 2001. Coherent Modes of Global SST and Summer Rainfall over China: An Assessment of the Regional Impacts of the 1997–98 El Niño. Journal of Climate 14, 1294-1308.

Lawrence, K.T., Liu, Z., Herbert, T.D., 2006. Evolution of the Eastern Tropical Pacific Through Plio-Pleistocene Glaciation. Science 312, 79-83.

Lease, R.O., Burbank, D.W., Clark, M.K., Farley, K.A., Zheng, D., Zhang, H., 2011. Middle Miocene reorganization of deformation along the northeastern Tibetan Plateau. Geology 39, 359-362.

Leduc, G., Vidal, L., Tachikawa, K., Bard, E., 2010. Changes in Eastern Pacific ocean ventilation at intermediate depth over the last 150kyrBP. Earth and Planetary Science Letters 298, 217-228.

Lenters, J.D., Kratz, T.K., Bowser, C.J., 2005. Effects of climate variability on lake evaporation: Results from a long-term energy budget study of Sparkling Lake, northern Wisconsin (USA). Journal of Hydrology 308, 168-195.

Leroy, S., Dupont, L., 1994. Development of vegetation and continental aridity in northwestern Africa during the late Pliocene - the pollen record of ODP Site-658. Palaeogeography Palaeoclimatology Palaeoecology 109, 295-316.

Leroy, S.A.G., Dupont, L.M., 1997. Marine palynology of the ODP site 658 (N-W Africa) and its contribution to the stratigraphy of Late Pliocene. Geobios 30, 351-359.

Levine, M.A., Whalen, S.C., 2001. Nutrient limitation of phytoplankton production in Alaskan Arctic foothill lakes. Hydrobiologia 455, 189-201.

Li, F., Rousseau, D.-D., Wu, N., Hao, Q., Pei, Y., 2008. Late Neogene evolution of the East Asian monsoon revealed by terrestrial mollusk record in Western Chinese Loess Plateau: From winter to summer dominated sub-regime. Earth and Planetary Science Letters 274, 439-447.

Li, J.-F., Hu, Y.-Q., Ferguson, D.K., Wang, Y.-F., Li, C.-S., 2010. An Early Pliocene lake and its surrounding vegetation in Zhejiang, East China. Journal of Paleolimnology 43, 751-769.

Li, J.-J., Fang, X.-M., Van der Voo, R., Zhu, J.-J., Mac Niocaill, C., Cao, J.-X., Zhong, W., Chen, H.-L., Wang, J., Wang, J.-M., Zhang, Y.-C., 1997. Late Cenozoic magnetostratigraphy (11 – 0 Ma) of the Dongshanding and Wangjiashan sections in the Longzhong Basin, western China. Geologie en Mijnbouw 76, 121-134.

Li, J., Li, B., Wang, F., Zhang, Q., Wen, S., Zhang, B., 1981. The process of the uplift of the Qinghai-Xizang Plateau, Geological and Ecological Studies in Qinghai-Xizang Plateau, 1, 111–118. Science Press, Beijing.

Li, J.F., Ferguson, D.K., Yang, J., Feng, G.P., Ablaev, A.G., Wang, Y.F., Li, C.S., 2009. Early Miocene vegetation and climate in Weichang District, North China. Palaeogeography Palaeoclimatology Palaeoecology 280, 47-63.

Li, L., Garzione, C.N., Pullen, A., Chang, H., 2016. Early–middle Miocene topographic growth of the northern Tibetan Plateau: Stable isotope and sedimentation evidence from the southwestern Qaidam basin. Palaeogeography, Palaeoclimatology, Palaeoecology 461, 201-213.

Li, M.-m., Liu, A.-t., Zou, C.-j., Xu, W.-d., Shimizu, H., Wang, K.-y., 2012. An overview of the “Three-North” Shelterbelt project in China. Forestry Studies in China 14, 70-79.

Li, S.-P., Li, J.-F., Ferguson, D.K., Wang, N.-W., He, X.-X., Yao, J.-X., 2014. Palynological analysis of the late Early Pleistocene sediments from Queque Cave in Guangxi, South China. Quaternary International 354, 24-34.

Li, X.-Y., Xu, H.-Y., Sun, Y.-L., Zhang, D.-S., Yang, Z.-P., 2007. Lake-Level Change and Water Balance Analysis at Lake Qinghai, West China during Recent Decades. Water Resources Management 21, 1505-1516.

Li, X., Fang, X., Wu, F., Miao, Y., 2011. Pollen evidence from Baode of the northern Loess Plateau of China and strong East Asian summer monsoons during the Early Pliocene. Chin.Sci.Bull. 56, 64-69.

Li, X., Jiang, D., Tian, Z., Yang, Y., 2018a. Mid-Piacenzian global land monsoon from PlioMIP1 simulations. Palaeogeography, Palaeoclimatology, Palaeoecology 512, 56-70.

Li, X.Q., Li, C.S., Lu, H.Y., Dodson, J.R., Wang, Y.F., 2004. Paleovegetation and paleoclimate in middle–late Pliocene, Shanxi, central China. Palaeogeography, Palaeoclimatology, Palaeoecology 210, 57-66.

Li, Z., Wang, F., Wang, X., Li, B., Chen, F., 2018b. A multi-proxy climatic record from the central Tengger Desert, southern Mongolian Plateau: Implications for the aridification of inner Asia since the late Pliocene. Journal of Asian Earth Sciences 160, 27-37.

Li, Z., Yao, T., Tian, L., 2006. Variation of delta 18O in precipitation in annual timescale with moisture transport in Delingha region. Earth Science Frontiers 13, 330.

Lisiecki, L.E., Raymo, M.E., 2005. A Pliocene-Pleistocene stack of 57 globally distributed benthic δ18O records. Paleoceanography 20, 1-17.

Liu, D., Fang, X., Gao, J., Wang, Y., Zhang, W., Miao, Y., Liu, Y., Zhang, Y., 2009. Cenozoic stratigraphy deformation history in the central and eastern of Qaidam Basin by the balance section restoration and its implication. Acta Geologica Sinica-English Edition 83, 359-371.

Liu, G., Leopold, E.B., Liu, Y., Wang, W., Yu, Z., Tong, G., 2002a. Palynological record of Pliocene climate events in North China. Review of Palaeobotany and Palynology 119, 335-340.

Liu, J., Li, J.J., Song, C.H., Yu, H., Peng, T.J., Hui, Z.C., Ye, X.Y., 2016. Palynological evidence for late Miocene stepwise aridification on the northeastern Tibetan Plateau. Climate of the Past 12, 1473-1484.

Liu, L., Chen, J., Chen, Y., Ji, J., Lu, H., 2002b. Variation of Zr/Rb ratios on the Loess Plateau of Central China during the last 130000 years and its implications for winter monsoon. Chin.Sci.Bull. 47, 1298-1302.

Liu, T., Li, T.-T., Wang, Z., Li, Z., 2019. Palynological record of Holocene climate change from a Sphagnum peat mire on Qizimei Mountain, Central China. Palynology, 1-8.

Liu, T., Menglin, D., Derbyshire, E., 1996. Gravel deposits on the margins of the Qinghai-Xizang Plateau, and their environmental significance. Palaeogeography, Palaeoclimatology, Palaeoecology 120, 159-170.

Liu, W., Liu, Z., An, Z., Sun, J., Chang, H., Wang, N., Dong, J., Wang, H., 2014. Late Miocene episodic lakes in the arid Tarim Basin, western China. Proceedings of the National Academy of Sciences 111, 16292-16296.

Liu, X., Lu, R., Du, J., Lyu, Z., Wang, L., Gao, S., Wu, Y., 2018. Evolution of Peatlands in the Mu Us Desert, Northern China, Since the Last Deglaciation. Journal of Geophysical Research: Earth Surface 123, 252-261.

Loch, R.J., 2000. Effects of vegetation cover on runoff and erosion under simulated rain and overland flow on a rehabilitated site on the Meandu Mine, Tarong, Queensland. Soil Research 38, 299-312.

Lu, F., An, Z., Chang, H., Dodson, J., Qiang, X., Yan, H., Dong, J., Song, Y., Fu, C., Li, X., 2017. Climate change and tectonic activity during the early Pliocene Warm Period from the ostracod record at Lake Qinghai, northeastern Tibetan Plateau. Journal of Asian Earth Sciences 138, 466-476.

Lu, H., Wu, N., Yang, X., Shen, C., Zhu, L., Wang, L., Li, Q., Xu, D., Tong, G., Sun, X., 2008. Spatial pattern of Abies and Picea surface pollen distribution along the elevation gradient in the Qinghai–Tibetan Plateau and Xinjiang, China. Boreas 37, 254-262.

Lu, Y., Fang, X.M., Appel, E., Wang, J.Y., Herb, C., Han, W.X., Wu, F.L., Song, C.H., 2015. A 7.3-1.6 Ma grain size record of interaction between anticline uplift and climate change in the western Qaidam Basin, NE Tibetan Plateau. Sedimentary Geology 319, 40-51.

Lunt, D.J., Haywood, A.M., Schmidt, G.A., Salzmann, U., Valdes, P.J., Dowsett, H.J., 2010. Earth system sensitivity inferred from Pliocene modelling and data. Nature Geosci 3, 60-64.

Lunt, D.J., Haywood, A.M., Schmidt, G.A., Salzmann, U., Valdes, P.J., Dowsett, H.J., Loptson, C.A., 2012. On the causes of mid-Pliocene warmth and polar amplification. Earth and Planetary Science Letters 321, 128-138.

Lutz, B.P., 2011. Shifts in North Atlantic planktic foraminifer biogeography and subtropical gyre circulation during the mid-Piacenzian warm period. Marine Micropaleontology 80, 125-149.

Ma, Y., Wu, F., Fang, X., Li, J., An, Z., Wang, W., 2005a. Pollen record from red clay sequence in the central Loess Plateau between 8.10 and 2.60 Ma. Chin.Sci.Bull. 50, 2234-2243.

Ma, Y.Z., Fang, X.M., Li, J.J., Wu, F.L., Zhang, J., 2005b. The vegetation and climate change during Neocene and Early Quaternary in Jiuxi Basin, China. Science in China Series D-Earth Sciences 48, 676-688.

Machlus, M., Enzel, Y., Goldstein, S., S, M., Stein, M., 2000. Reconstruction of low-stands of lake Lisan between 55 and 35 kyr. Quarternary International 73/74, 137-144.

Maher, B.A., Thompson, R., Zhou, L.P., 1994. Spatial and temporal reconstructions of changes in the Asian palaeomonsoon: A new mineral magnetic approach. Earth and Planetary Science Letters 125, 461-471.

Mai, H.D., 1995. Tertiäre Vegetationsgeschichte Europas. Gustav Fischer Verlag, Jena Stuttgart New York.

Mángano, M.G., Buatois, L.A., Wu, X., Sun, J., Zhang, G., 1994. Sedimentary facies, depositional processes and climatic controls in a Triassic Lake, Tanzhuang Formation, western Henan Province, China. Journal of Paleolimnology 11, 41-65.

Marcarelli, A.M., Wurtsbaugh, W.A., Griset, O., 2006. Salinity controls phytoplankton response to nutrient enrichment in the Great Salt Lake, Utah, USA. Canadian Journal of Fisheries and Aquatic Sciences 63, 2236-2248.

Marshall, L.G., Webb, S.D., Sepkoski, J.J., Raup, D.M., 1982. Mammalian Evolution and the Great American Interchange. Science 215, 1351-1357.

Martinez-Boti, M.A., Foster, G.L., Chalk, T.B., Rohling, E.J., Sexton, P.F., Lunt, D.J., Pancost, R.D., Badger, M.P.S., Schmidt, D.N., 2015. Plio-Pleistocene climate sensitivity evaluated using high-resolution CO_2 records. Nature 518, 49-54.

Maussion, F., Scherer, D., Mölg, T., Collier, E., Curio, J., Finkelnburg, R., 2014. Precipitation Seasonality and Variability over the Tibetan Plateau as Resolved by the High Asia Reanalysis. Journal of Climate 27, 1910-1927.

Max, L., Rippert, N., Lembke-Jene, L., Mackensen, A., Nürnberg, D., Tiedemann, R., 2017. Evidence for enhanced convection of North Pacific Intermediate Water to the low-latitude Pacific under glacial conditions. Paleoceanography 32, 41-55.

McBride, J.L., Nicholls, N., 1983. Seasonal Relationships between Australian Rainfall and the Southern Oscillation. Monthly Weather Review 111, 1998-2004.

McClymont, E.L., Elmore, A.C., Kender, S., Leng, M.J., Greaves, M., Elderfield, H., 2016. Pliocene-Pleistocene evolution of sea surface and intermediate water temperatures from the southwest Pacific. Paleoceanography 31, 895-913.

McCreary, J.P., Miyama, T., Furue, R., Jensen, T., Kang, H.-W., Bang, B., Qu, T., 2007. Interactions between the Indonesian Throughflow and circulations in the Indian and Pacific Oceans. Progress in Oceanography 75, 70-114.

McKay, R., Naish, T., Carter, L., Riesselman, C., Dunbar, R., Sjunneskog, C., Winter, D., Sangiorgi, F., Warren, C., Pagani, M., Schouten, S., Willmott, V., Levy, R., DeConto, R., Powell, R.D., 2012. Antarctic and Southern Ocean influences on Late Pliocene global cooling. Proceedings of the National Academy of Sciences of the United States of America 109, 6423-6428.

McLennan, S.M., Hemming, S., McDaniel, D.K., Hanson, G.N., 1993. Geochemical approaches to sedimentation, provenance, and tectonics, in: Johnsson, M.J., Basu, A. (Eds.), Processes Controlling the Composition of Clastic Sediments. Geological Society of America.

McManus, J.F., Anderson, R.F., Broecker, W.S., Fleisher, M.Q., Higgins, S.M., 1998. Radiometrically determined sedimentary fluxes in the sub-polar North Atlantic during the last 140,000 years. Earth and Planetary Science Letters 155, 29-43.

Meehl, G.A., Arblaster, J.M., Tebaldi, C., 2005. Understanding future patterns of increased precipitation intensity in climate model simulations. Geophysical Research Letters 32.

Metcalfe, S.E., Jones, M.D., Davies, S.J., Noren, A., MacKenzie, A., 2010. Climate variability over the last two millennia in the North American Monsoon region, recorded in laminated lake sediments from Laguna de Juanacatlán, Mexico. The Holocene 20, 1195-1206.

Métivier, F., Gaudemer, Y., Tapponnier, P., Meyer, B., 1998. Northeastward growth of the Tibet plateau deduced from balanced reconstruction of two depositional areas: The Qaidam and Hexi Corridor basins, China. Tectonics 17, 823-842.

Meyers, P.A., 1994. Preservation of elemental and isotopic source identification of sedimentary organic matter. Chemical Geology 114, 289-302.

Meyers, P.A., Ishiwatari, R., 1995. Organic Matter Accumulation Records in Lake Sediments, in: Lerman, A., Imboden, D.M., Gat, J.R. (Eds.), Physics and Chemistry of Lakes. Springer Berlin Heidelberg, Berlin, Heidelberg, pp. 279-328.

Miao, Y., Fang, X., Herrmann, M., Wu, F., Zhang, Y., Liu, D., 2011. Miocene pollen record of KC-1 core in the Qaidam Basin, NE Tibetan Plateau and implications for evolution of the East Asian monsoon. Palaeogeography, Palaeoclimatology, Palaeoecology 299, 30-38.

Miao, Y.F., Fang, X.M., Wu, F.L., Cai, M.T., Song, C.H., Meng, Q.Q., Xu, L., 2013. Late Cenozoic continuous aridification in the western Qaidam Basin: evidence from sporopollen records. Climate of the Past 9, 1863-1877.

Miller, G.H., Brigham-Grette, J., Alley, R.B., Anderson, L., Bauch, H.A., Douglas, M.S.V., Edwards, M.E., Elias, S.A., Finney, B.P., Fitzpatrick, J.J., Funder, S.V., Herbert, T.D., Hinzman, L.D., Kaufman, D.S., MacDonald, G.M., Polyak, L., Robock, A., Serreze, M.C., Smol, J.P., Spielhagen, R., White, J.W.C., Wolfe, A.P., Wolff, E.W., 2010. Temperature and precipitation history of the Arctic. Quaternary Science Reviews 29, 1679-1715.

Miller, K.G., Wright, J.D., Browning, J.V., Kulpecz, A., Kominz, M., Naish, T.R., Cramer, B.S., Rosenthal, Y., Peltier, W.R., Sosdian, S., 2012. High tide of the warm Pliocene: Implications of global sea level for Antarctic deglaciation. Geology 40, 407-410.

Milton, S., Wickham, H., 2016. Package 'magrittr': A Forward-Pipe Operator for R.

Mingram, J., Schettler, G., Nowaczyk, N., Luo, X., Lu, H., Liu, J., Negendank, J.F.W., 2004. The Huguang maar lake—a high-resolution record of palaeoenvironmental and palaeoclimatic changes over the last 78,000 years from South China. Quaternary International 122, 85-107.

Molnar, P., England, P., Martinod, J., 1993. Mantle dynamics, uplift of the Tibetan Plateau, and the Indian monsoon. Reviews of Geophysics 31, 357-396.

Montes, C., Cardona, A., Jaramillo, C., Pardo, A., Silva, J.C., Valencia, V., Ayala, C., Pérez-Angel, L.C., Rodriguez-Parra, L.A., Ramirez, V., Niño, H., 2015. Middle Miocene closure of the Central American Seaway. Science 348, 226-229.

Moreno, A., Valero-Garcés, B.L., Jiménez-Sánchez, M., Domínguez-Cuesta, M.J., Mata, M.P., Navas, A., González-Sampériz, P., Stoll, H., Farias, P., Morellón, M., Corella, J.P., Rico, M., 2010. The last deglaciation in the Picos de Europa National Park (Cantabrian Mountains, northern Spain). Journal of Quaternary Science 25, 1076-1091.

Mosbrugger, V., Utescher, T., 1997. The coexistence approach—a method for quantitative reconstructions of Tertiary terrestrial palaeoclimate data using plant fossils. Palaeogeography, Palaeoclimatology, Palaeoecology 134, 61-86.

Moy, C.M., Seltzer, G.O., Rodbell, D.T., Anderson, D.M., 2002. Variability of El Niño/Southern Oscillation activity at millennial timescales during the Holocene epoch. Nature 420, 162.

Naafs, B.D.A., Hefter, J., Acton, G., Haug, G.H., Martínez-Garcia, A., Pancost, R., Stein, R., 2012. Strengthening of North American dust sources during the late Pliocene (2.7 Ma). Earth and Planetary Science Letters 317, 8-19.

Nagashima, K., Tada, R., Tani, A., Sun, Y., Isozaki, Y., Toyoda, S., 2011. Millennial-scale oscillations of the westerly jet path during the last glacial period. J Asian Earth Sci 40.

Naish, T., Powell, R., Levy, R., Wilson, G., Scherer, R., Talarico, F., Krissek, L., Niessen, F., Pompilio, M., Wilson, T., Carter, L., DeConto, R., Huybers, P., McKay, R., Pollard, D., Ross, J., Winter, D., Barrett, P., Browne, G., Cody, R., Cowan, E., Crampton, J., Dunbar, G., Dunbar, N., Florindo, F., Gebhardt, C., Graham, I., Hannah, M., Hansaraj, D., Harwood, D., Helling, D., Henrys, S., Hinnov, L., Kuhn, G., Kyle, P., Laufer, A., Maffioli, P., Magens, D., Mandernack, K., McIntosh, W., Millan, C., Morin, R., Ohneiser, C., Paulsen, T., Persico, D., Raine, I., Reed, J., Riesselman, C., Sagnotti, L., Schmitt, D., Sjunneskog, C., Strong, P., Taviani, M., Vogel, S., Wilch, T., Williams, T., 2009. Obliquity-paced Pliocene West Antarctic ice sheet oscillations. Nature 458, 322-U384.

Nelson, C.H., 1982. Modern shallow-water graded sand layers from storm surges, Bering Shelf; a mimic of Bouma sequences and turbidite systems. Journal of Sedimentary Research 52, 537-545.

Ni, J., 2001. A biome classification of China based on plant functional types and the BIOME3 model. Folia Geobotanica 36, 113-129.

Ni, J., Cao, X., Jeltsch, F., Herzschuh, U., 2014. Biome distribution over the last 22,000yr in China. Palaeogeography, Palaeoclimatology, Palaeoecology 409, 33-47.

Ni, J., Herzschuh, U., 2011. Simulating Biome Distribution on the Tibetan Plateau Using a Modified Global Vegetation Model. Arctic Antarctic and Alpine Research 43, 429-441.

Ni, J., Sykes, M.T., Prentice, I.C., Cramer, W., 2000. Modelling the vegetation of China using the process-based equilibrium terrestrial biosphere model BIOME3. Global Ecology and Biogeography 9, 463-479.

Nicholls, N., Della-Marta, P., Collins, D., 2004. 20 th century changes in temperature and rainfall in New South Wales. Australian Meteorological Magazine 53, 263-268.

Nie, J., King, J.W., Fang, X., 2008. Link between benthic oxygen isotopes and magnetic susceptibility in the red-clay sequence on the Chinese Loess Plateau. Geophysical Research Letters 35, 1-5.

Nie, J., Stevens, T., Song, Y., King, J.W., Zhang, R., Ji, S., Gong, L., Cares, D., 2014. Pacific freshening drives Pliocene cooling and Asian monsoon intensification. Scientific reports 4, 5474.

Nogués-Bravo, D., Araújo, M.B., Errea, M.P., Martínez-Rica, J.P., 2007. Exposure of global mountain systems to climate warming during the 21st Century. Global Environmental Change 17, 420-428.

Olsen, P., 1985. Constraints on the formation of lacustrine microlaminated sediments.

Olsen, P., 1990. Tectonic, Climatic, and Biotic Modulation of Lacustrine Ecosystems-Examples from Newark Supergroup of Eastern North America, in: Katz, B. (Ed.), Lacustrine Basin Exploration: Case Studies and Modern Analogs. American Association Petroleum Geologists Memoir, pp. 209-224.

Pagani, M., 2002. The alkenone-CO_2 proxy and ancient atmospheric carbon dioxide. Philosophical Transactions of the Royal Society of London Series a-Mathematical Physical and Engineering Sciences 360, 609-632.

Pagani, M., Liu, Z., LaRiviere, J., Ravelo, A.C., 2010. High Earth-system climate sensitivity determined from Pliocene carbon dioxide concentrations. Nature Geosci 3, 27-30.

Panitz, S., Salzmann, U., Risebrobakken, B., De Schepper, S., Pound, M.J., 2016. Climate variability and long-term expansion of peatlands in Arctic Norway during the late Pliocene (ODP Site 642, Norwegian Sea). Clim. Past 12, 1043-1060.

Patterson, M.O., McKay, R., Naish, T., Escutia, C., Jimenez-Espejo, F.J., Raymo, M.E., Meyers, S.R., Tauxe, L., Brinkhuis, H., Scientists, I.E., 2014. Orbital forcing of the East Antarctic ice sheet during the Pliocene and Early Pleistocene. Nature Geosci 7, 841-847.

Philander, S.G., Fedorov, A.V., 2003. Role of tropics in changing the response to Milankovich forcing some three million years ago. Paleoceanography 18, 1-12.

Piovano, E.L., Ariztegui, D., Moreira, S.D., 2002. Recent environmental changes in Laguna Mar Chiquita (central Argentina): a sedimentary model for a highly variable saline lake. Sedimentology 49, 1371-1384.

Potter, P.E., Maynard, J.B., Depetris, P.J., 2005. Mud and mudstones: Introduction and overview. Springer Science & Business Media.

Prahl, F.G., Ertel, J.R., Goni, M.A., Sparrow, M.A., Eversmeyer, B., 1994. Terrestrial organic carbon contributions to sediments on the Washington margin. Geochimica et Cosmochimica Acta 58, 3035-3048.

Prairie, Y.T., Duarte, C.M., Kalff, J., 1989. Unifying nutrient–chlorophyll relationships in lakes. Canadian Journal of Fisheries and Aquatic Sciences 46, 1176-1182.

Prell, W.L., Kutzbach, J.E., 1992. Sensitivity of the Indian monsoon to forcing parameters and implications for its evolution. Nature 360, 647-652.

Prentice, C., 1988. Records of vegetation in time and space: the principles of pollen analysis, in: Huntley, B., Webb, T. (Eds.), Vegetation history. Springer Netherlands, Dordrecht, pp. 17-42.

Prentice, C., Berglund, B.E., Olsson, T., 1987. Quantitative forest-composition sensing characteristics of pollen samples from Swedish lakes. Boreas 16, 43-54.

Prentice, I.C., 1980. Multidimensional scaling as a research tool in quaternary palynology: A review of theory and methods. Review of Palaeobotany and Palynology 31, 71-104.

Prescott, C.L., Haywood, A.M., Dolan, A.M., Hunter, S.J., Pope, J.O., Pickering, S.J., 2014. Assessing orbitally-forced interglacial climate variability during the mid-Pliocene Warm Period. Earth and Planetary Science Letters 400, 261-271.

Pueyo, J.J., Sáez, A., Giralt, S., Valero-Garcés, B.L., Moreno, A., Bao, R., Schwalb, A., Herrera, C., Klosowska, B., Taberner, C., 2011. Carbonate and organic matter sedimentation and isotopic signatures in Lake Chungará, Chilean Altiplano, during the last 12.3kyr. Palaeogeography, Palaeoclimatology, Palaeoecology 307, 339-355.

Pullen, A., Kapp, P., McCallister, A.T., Chang, H., Gehrels, G., Garzione, C.N., Heermance, R.V., Ding, L., 2011. Qaidam Basin and northern Tibetan Plateau as dust sources for the Chinese Loess Plateau and paleoclimatic implications. Geology 39, 1031-1034.

Quade, J., Breecker, D.O., Daëron, M., Eiler, J., 2011. The paleoaltimetry of Tibet: An isotopic perspective. American Journal of Science 311, 77-115.

Ramage, C.S., 1972. Monsoon Meteorology. Academic Press.

Ravelo, A.C., Andreasen, D.H., Lyle, M., Olivarez Lyle, A., Wara, M.W., 2004. Regional climate shifts caused by gradual global cooling in the Pliocene epoch. Nature 429, 263-267.

Raymo, M., Ruddiman, W.F., Clement, B., 1986. Pliocene-Pleistocene Paleoceanography of the North Atlantic at Deep Sea Drilling Project Site 609. Initial reports DSDP, Leg 94, Norfolk, Virginia to St. John's, Newfoundland. Part 2 94, 895-901.

Rea, D.K., Snoeckx, H., Joseph, L.H., 1998. Late Cenozoic Eolian deposition in the North Pacific: Asian drying, Tibetan uplift, and cooling of the northern hemisphere. Paleoceanography 13, 215-224.

Retallack, G.J., Krull, E.S., Bockheim, J.G., 2001. New grounds for reassessing palaeoclimate of the Sirius Group, Antarctica. Journal of the Geological Society 158, 925-935.

Riebe, C.S., Kirchner, J.W., Finkel, R.C., 2004. Erosional and climatic effects on long-term chemical weathering rates in granitic landscapes spanning diverse climate regimes. Earth and Planetary Science Letters 224, 547-562.

Rippert, N., Max, L., Mackensen, A., Cacho, I., Povea, P., Tiedemann, R., 2017. Alternating Influence of Northern Versus Southern-Sourced Water Masses on the Equatorial Pacific Subthermocline During the Past 240 ka. Paleoceanography 32, 1256-1274.

Rodgers, K.B., Latif, M., Legutke, S., 2000. Sensitivity of equatorial Pacific and Indian Ocean watermasses to the position of the Indonesian Throughflow. Geophysical Research Letters 27, 2941-2944.

Rodríguez, R., Mabres, A., Luckman, B., Evans, M., Masiokas, M., Ektvedt, T.M., 2005. “El Niño” events recorded in dry-forest species of the lowlands of northwest Peru. Dendrochronologia 22, 181-186.

Rohling, E.J., Foster, G.L., Grant, K.M., Marino, G., Roberts, A.P., Tamisiea, M.E., Williams, F., 2014. Sea-level and deep-sea-temperature variability over the past 5.3 million years. Nature 508, 477.

Rosén, P., Segerström, U., Eriksson, L., Renberg, I., 2003. Do Diatom, Chironomid, and Pollen Records Consistently Infer Holocene July Air Temperature? A Comparison Using Sediment Cores from Four Alpine Lakes in Northern Sweden AU. Arctic, Antarctic, and Alpine Research 35, 279-290.

Rossby, C.-G., 1939. Relation between variations in the intensity of the zonal circulation of the atmosphere and the displacements of the semi-permanent centers of action. J. Mar. Res. 2, 38-55.

Rousseau, D.D., Taoufiq, N.B., Petit, C., Farjanel, G., Meon, H., Puissegur, J.J., 1992. Continental Late Pliocene paleoclimatic history recorded in the Bresse Basin (France). Palaeogeography Palaeoclimatology Palaeoecology 95, 253-261.

Roxy, M.K., Ritika, K., Terray, P., Murtugudde, R., Ashok, K., Goswami, B.N., 2015. Drying of Indian subcontinent by rapid Indian Ocean warming and a weakening land-sea thermal gradient. Nature Communications 6, 7423.

Salzmann, U., Dolan, A.M., Haywood, A.M., Chan, W.-L., Voss, J., Hill, D.J., Abe-Ouchi, A., Otto-Bliesner, B., Bragg, F.J., Chandler, M.A., Contoux, C., Dowsett, H.J., Jost, A., Kamae, Y., Lohmann, G., Lunt, D.J., Pickering, S.J., Pound, M.J., Ramstein, G., Rosenbloom, N.A., Sohl, L., Stepanek, C., Ueda, H., Zhang, Z., 2013. Challenges in quantifying Pliocene terrestrial warming revealed by data-model discord. Nature Clim. Change 3, 969-974.

Salzmann, U., Haywood, A.M., Lunt, D.J., Valdes, P.J., Hill, D.J., 2008. A new global biome reconstruction and data-model comparison for the Middle Pliocene. Global Ecology and Biogeography 17, 432-447.

Salzmann, U., Williams, M., Haywood, A.M., Johnson, A.L.A., Kender, S., Zalasiewicz, J., 2011. Climate and environment of a Pliocene warm world. Palaeogeography, Palaeoclimatology, Palaeoecology 309, 1-8.

Sarkar, A., Ramesh, R., Somayajulu, B.L.K., Agnihotri, R., Jull, A.J.T., Burr, G.S., 2000. High resolution Holocene monsoon record from the eastern Arabian Sea. Earth and Planetary Science Letters 177, 209-218.

Schiemann, R., Lüthi, D., Schär, C., 2009. Seasonality and interannual variability of the Westerly jet in the Tibetan Plateau region. J Clim 22, 2940-2957.

Schimpf, D., Kilian, R., Kronz, A., Simon, K., Spötl, C., Wörner, G., Deininger, M., Mangini, A., 2011. The significance of chemical, isotopic, and detrital components in three coeval stalagmites from the superhumid southernmost Andes (53°S) as high-resolution palaeo-climate proxies. Quaternary Science Reviews 30, 443-459.

Schneider, B., Schmittner, A., 2006. Simulating the impact of the Panamanian seaway closure on ocean circulation, marine productivity and nutrient cycling. Earth and Planetary Science Letters 246, 367-380.

Schreiber, B.C., Tabakh, M.E., 2000. Deposition and early alteration of evaporites. Sedimentology 47, 215-238.

Seki, O., Foster, G.L., Schmidt, D.N., Mackensen, A., Kawamura, K., Pancost, R.D., 2010. Alkenone and boron-based Pliocene pCO(2) records. Earth and Planetary Science Letters 292, 201-211.

Seppä, H., Birks, H.J.B., Odland, A., Poska, A., Veski, S., 2004. A modern pollen–climate calibration set from northern Europe: developing and testing a tool for palaeoclimatological reconstructions. Journal of Biogeography 31, 251-267.

Shackleton, N.J., Hall, M.A., Pate, D., 1995. Pliocene stable oxygen and carbon isotope record of benthic foraminifera from ODP Site 138-846 in the eastern equatorial Pacific, Supplement to: Shackleton, NJ et al. (1995): Pliocene stable isotope stratigraphy of Site 864. In: Pisias, NG; Mayer, LA; Janecek, TR; Palmer-Julson, A; van Andel, TH (eds.), Proceedings of the Ocean Drilling Program, Scientific Results, College Station, TX (Ocean Drilling Program), 138, 337-355, https://doi.org/10.2973/odp.proc.sr.138.117.1995. PANGAEA.

Shen, J., Liu, W., Wang, S., Ryo, M., 2005. Palaeoclimatic changes in the Qinghai Lake area during the last 18,000 years. Quaternary International 136, 131-140.

Shi, N., Jia-Xin, C., Königsson, L.-K., 1993. Late Cenozoic Vegetational History and the Pliocene-Pleistocene Boundary in the Yushe Basin, S. E. Shanxi, China. Grana 32, 260-271.

Shi, Z., Liu, X., Cheng, X., 2012. Anti-phased response of northern and southern East Asian summer precipitation to ENSO modulation of orbital forcing. Quaternary Science Reviews 40, 30-38.

Shi, Z., Liu, X., Sun, Y., An, Z., Liu, Z., Kutzbach, J., 2011. Distinct responses of East Asian summer and winter monsoons to orbital forcing. Clim Past 7, 1363-1370.

Shimaraev, M.N., Granin, N.G., Zhdanov, A.A., 1993. Deep ventilation of Lake Baikal waters due to spring thermal bars. Limnology and Oceanography 38, 1068-1072.

Shotyk, W., Weiss, D., Kramers, J.D., Frei, R., Cheburkin, A.K., Gloor, M., Reese, S., 2001. Geochemistry of the peat bog at Etang de la Gruère, Jura Mountains, Switzerland, and its record of atmospheric Pb and lithogenic trace metals (Sc, Ti, Y, Zr, and REE) since 12,370 14C yr BP. Geochimica et Cosmochimica Acta 65, 2337-2360.

Sly, P., 1978. Sedimentary processes in lakes, Lakes. Springer, pp. 65-89.

Snyder, J.P., 1997. Flattening the earth: two thousand years of map projections. University of Chicago Press.

Sobel, E.R., Hilley, G.E., Strecker, M.R., 2003. Formation of internally drained contractional basins by aridity-limited bedrock incision. Journal of Geophysical Research: Solid Earth 108, 2344-2367.

Solomon, S., Qin, D., Manning, M., Averyt, K., Marquis, M., 2007. Climate change 2007-the physical science basis: Working group I contribution to the fourth assessment report of the IPCC. Cambridge university press.

Song, C., Dongling, G., Xiaomin, F., Zhijiu, C., Jijun, L., Shengli, Y., Hongbo, J., Burbank, D., Kirschvink, J.L., 2005a. Late Cenozoic high-resolution magnetostratigraphy in the Kunlun Pass Basin and its implications for the uplift of the northern Tibetan Plateau. Chin.Sci.Bull. 50, 1912-1922.

Song, M., Zhou, C., Ouyang, H., 2005b. Simulated distribution of vegetation types in response to climate change on the Tibetan Plateau. Journal of Vegetation Science 16, 341-350.

Soriano, A., Movia, C., León, R., 1983. Deserts and semideserts of Patagonia: vegetation in: West, N. (Ed.), Temperate Deserts and Semi-deserts. Elsevier, Amsterdam, pp. 423-460.

Spicer, R.A., Harris, N.B., Widdowson, M., Herman, A.B., Guo, S., Valdes, P.J., Wolfe, J.A., Kelley, S.P., 2003. Constant elevation of southern Tibet over the past 15 million years. Nature 421, 622.

Staehr, P.A., Baastrup-Spohr, L., Sand-Jensen, K., Stedmon, C., 2012. Lake metabolism scales with lake morphometry and catchment conditions. Aquatic Sciences 74, 155-169.

Stap, L.B., de Boer, B., Ziegler, M., Bintanja, R., Lourens, L.J., van de Wal, R.S.W., 2016. CO2 over the past 5 million years: Continuous simulation and new δ11B-based proxy data. Earth and Planetary Science Letters 439, 1-10.

Steph, S., Tiedemann, R., Prange, M., Groeneveld, J., Schulz, M., Timmermann, A., Nürnberg, D., Rühlemann, C., Saukel, C., Haug, G.H., 2010. Early Pliocene increase in thermohaline overturning: A precondition for the development of the modern equatorial Pacific cold tongue. Paleoceanography 25, 1-17.

Stockhecke, M., Sturm, M., Brunner, I., Schmincke, H.-U., Sumita, M., Kipfer, R., Cukur, D., Kwiecien, O., Anselmetti, F.S., 2014. Sedimentary evolution and environmental history of Lake Van (Turkey) over the past 600 000 years. Sedimentology 61, 1830-1861.

Stockmarr, J., 1971. Tablets with spores used in abolute pollen analysis: Pollen et Spores, v. 8. XIII.

Suc, J.P., Bertini, A., Combourieu-Nebout, N., Diniz, F., Leroy, S., Russo-Ermoli, E., Zheng, Z., Bessais, E., Ferrier, J., 1995. Structure of West Mediterranean vegetation and climate since 5.3 Ma. Acta Zool 38, 3-16.

Sugita, S., 1994. Pollen Representation of Vegetation in Quaternary Sediments: Theory and Method in Patchy Vegetation. Journal of Ecology 82, 881-897.

Sun, D., Bloemendal, J., Rea, D.K., Vandenberghe, J., Jiang, F., An, Z., Su, R., 2002. Grain-size distribution function of polymodal sediments in hydraulic and aeolian environments, and numerical partitioning of the sedimentary components. Sedimentary Geology 152, 263-277.

Sun, J., Gong, Z., Tian, Z., Jia, Y., Windley, B., 2015. Late Miocene stepwise aridification in the Asian interior and the interplay between tectonics and climate. Palaeogeography, Palaeoclimatology, Palaeoecology 421, 48-59.

Sun, J., Liu, T., 2006. The Age of the Taklimakan Desert. Science 312, 1621-1621.

Sun, J., Liu, W., Liu, Z., Deng, T., Windley, B.F., Fu, B., 2017. Extreme aridification since the beginning of the Pliocene in the Tarim Basin, western China. Palaeogeography, Palaeoclimatology, Palaeoecology 485, 189-200.

Sun, J., Zhang, L., Deng, C., Zhu, R., 2008. Evidence for enhanced aridity in the Tarim Basin of China since 5.3Ma. Quaternary Science Reviews 27, 1012-1023.

Sun, J., Zhang, Z., Zhang, L., 2009. New evidence on the age of the Taklimakan Desert. Geology 37, 159-162.

Sun, J., Zhu, R., An, Z., 2005. Tectonic uplift in the northern Tibetan Plateau since 13.7 Ma ago inferred from molasse deposits along the Altyn Tagh Fault. Earth and Planetary Science Letters 235, 641-653.

Sun, J.M., Zhang, Z.Q., 2008. Palynological evidence for the Mid-Miocene Climatic Optimum recorded in Cenozoic sediments of the Tian Shan Range, northwestern China. Global and Planetary Change 64, 53-68.

Sun, X., Wang, P., 2005. How old is the Asian monsoon system?—Palaeobotanical records from China. Palaeogeogr Palaeoclimatol Palaeoecol 222, 181-222.

Sun, Y., An, Z., Clemens, S.C., Bloemendal, J., Vandenberghe, J., 2010. Seven million years of wind and precipitation variability on the Chinese Loess Plateau. Earth Planet Sci Lett 297, 525-535.

Sun, Y., Ding, Y., 2011. Responses of South and East Asian summer monsoons to different land-sea temperature increases under a warming scenario. Chin.Sci.Bull. 56, 2718.

Sun, Z., Pei, J., Li, H., Xu, W., Jiang, W., Zhu, Z., Wang, X., Yang, Z., 2012. Palaeomagnetism of late Cretaceous sediments from southern Tibet: Evidence for the consistent palaeolatitudes of the southern margin of Eurasia prior to the collision with India. Gondwana Research 21, 53-63.

Tada, R., Zheng, H., Clift, P.D., 2016. Evolution and variability of the Asian monsoon and its potential linkage with uplift of the Himalaya and Tibetan Plateau. Progress in Earth and Planetary Science 3, 4.

Tang, Z., Ding, Z., White, P.D., Dong, X., Ji, J., Jiang, H., Luo, P., Wang, X., 2011. Late Cenozoic central Asian drying inferred from a palynological record from the northern Tian Shan. Earth and Planetary Science Letters 302, 439-447.

Tao, W., 2014. Aeolian desertification and its control in Northern China. International Soil and Water Conservation Research 2, 34-41.

Tapponnier, P., Peltzer, G., Armijo, R., 1986. On the mechanics of the collision between India and Asia. Geological Society, London, Special Publications 19, 113-157.

Tapponnier, P., Zhiqin, X., Roger, F., Meyer, B., Arnaud, N., Wittlinger, G., 2001. Oblique stepwise rise and growth of the Tibet plateau. Science 294, 1671-1677.

Team, Q.D., 2016. QGIS geographic information system. Open Source Geospatial Foundation Project.

Team, R.D.C., 2008. R: A language and environment for statistical computing.
. R Foundation for Statistical Computing, Vienna, Austria.

Teller, J.T., Last, W.M., 1990. Paleohydrological indicators in playas and salt lakes, with examples from Canada, Australia, and Africa. Palaeogeography, Palaeoclimatology, Palaeoecology 76, 215-240.

ter Braak, C., Juggins, S., Birks, H., van der Voet, H., 1993. Weighted Averaging Partial Least Squares regression (WA-PLS): definition and comparison with other methods for species-environment calibration, in: Patil, G.P.a.R., C.R. (Ed.), Multivariate Environmental Statistics. Elsevier, Amsterdam, pp. 525-560.

Tian, J., Wang, P.X., Cheng, X.R., 2004. Development of the East Asian monsoon and Northern Hemisphere glaciation: oxygen isotope records from the South China Sea. Quaternary Science Reviews 23, 2007-2016.

Tian, L., Masson-Delmotte, V., Stievenard, M., Yao, T., Jouzel, J., 2001. Tibetan Plateau summer monsoon northward extent revealed by measurements of water stable isotopes. Journal of Geophysical Research: Atmospheres 106, 28081-28088.

Tian, L., Yao, T., MacClune, K., White, J.W.C., Schilla, A., Vaughn, B., Vachon, R., Ichiyanagi, K., 2007. Stable isotopic variations in west China: A consideration of moisture sources. Journal of Geophysical Research: Atmospheres (1984–2012) 112.

Tian, Y., Kohn, B.P., Hu, S., Gleadow, A.J.W., 2015. Synchronous fluvial response to surface uplift in the eastern Tibetan Plateau: Implications for crustal dynamics. Geophysical Research Letters 42, 29-35.

Timmermann, A., An, S.-I., Krebs, U., Goosse, H., 2005. ENSO Suppression due to Weakening of the North Atlantic Thermohaline Circulation. Journal of Climate 18, 3122-3139.

Toggweiler, J.R., Dixon, K., Broecker, W.S., 1991. The Peru upwelling and the ventilation of the south Pacific thermocline. Journal of Geophysical Research: Oceans 96, 20467-20497.

Torrence, C., Compo, G.P., 1998. A practical guide to wavelet analysis. Bulletin of the American Meteorological society 79, 61-78.

Trenberth, K.E., Fasullo, J., Smith, L., 2005. Trends and variability in column-integrated atmospheric water vapor. Clim Dyn 24, 741-758.

Trenberth, K.E., Shea, D.J., 2005. Relationships between precipitation and surface temperature. Geophysical Research Letters 32, 1-4.

Tu, R.H., 1964. A preliminary observation on geomorphic characteristics along the Qinghai-Tibet Highway. Acta Geogr. Sin. 30, pp. 143-157.

Utescher, T., Bruch, A., Erdei, B., François, L., Ivanov, D., Jacques, F.M.B., Kern, A., Liu, C.Y., Mosbrugger, V., Spicer, R., 2014. The Coexistence Approach—Theoretical background and practical considerations of using plant fossils for climate quantification. Palaeogeography, Palaeoclimatology, Palaeoecology 410, 58–73.

Utescher, T., Mosbrugger, V., 2015. The Palaeoflora Database. , http://www.geologie.unibonn.de/Palaeoflora.

van de Wal, R.S.W., de Boer, B., Lourens, L.J., Köhler, P., Bintanja, R., 2011. Reconstruction of a continuous high-resolution CO_2 record over the past 20 million years. Clim. Past 7, 1459-1469.

Vehtari, A., Gelman, A., Gabry, J., 2017. Practical Bayesian model evaluation using leave-one-out cross-validation and WAIC. Statistics and Computing 27, 1413-1432.

Vincens, A., Buchet, G., Williamson, D., Taieb, M., 2005. A 23,000 yr pollen record from Lake Rukwa (8°S, SW Tanzania): New data on vegetation dynamics and climate in Central Eastern Africa. Review of Palaeobotany and Palynology 137, 147-162.

Vogel, H., Wessels, M., Albrecht, C., Stich, H.B., Wagner, B., 2010. Spatial variability of recent sedimentation in Lake Ohrid (Albania/Macedonia). Biogeosciences 7, 3333-3342.

Wan, C., Sun, Y., Xue, Y., Qiao, X., Jin, Y., Zhang, Y., 2014. Neogene palynological assemblages in the west slope of Songliao Basin and their geological implications. Science China Earth Sciences 57, 2486-2497.

Wan, S., Clift, P.D., Li, A., Yu, Z., Li, T., Hu, D., 2012. Tectonic and climatic controls on long-term silicate weathering in Asia since 5 Ma. Geophysical Research Letters 39, 1-5.

Wan, S., Li, A., Clift, P.D., Stuut, J.-B.W., 2007. Development of the East Asian monsoon: Mineralogical and sedimentologic records in the northern South China Sea since 20 Ma. Palaeogeography, Palaeoclimatology, Palaeoecology 254, 561-582.

Wang, B., Clemens, S.C., Liu, P., 2003. Contrasting the Indian and East Asian monsoons: implications on geologic timescales. Marine Geology 201, 5-21.

Wang, B., Lin, H., 2002. Rainy Season of the Asian–Pacific Summer Monsoon. Journal of Climate 15, 386-398.

Wang, G., Hendon, H.H., 2007. Sensitivity of Australian Rainfall to Inter–El Niño Variations. Journal of Climate 20, 4211-4226.

Wang, H., Ni, J., Prentice, I.C., 2011. Sensitivity of potential natural vegetation in China to projected changes in temperature, precipitation and atmospheric CO2. Regional Environmental Change 11, 715-727.

Wang, J., Fang, X., Appel, E., Song, C., 2012. Pliocene–Pleistocene Climate Change At the NE Tibetan Plateau Deduced From Lithofacies Variation In the Drill Core SG-1, Western Qaidam Basin, China. Journal of Sedimentary Research 82, 933-952.

Wang, J., Wang, Y.J., Liu, Z.C., Li, J.Q., Xi, P., 1999. Cenozoic environmental evolution of the Qaidam Basin and its implications for the uplift of the Tibetan Plateau and the drying of central Asia. Palaeogeography, Palaeoclimatology, Palaeoecology 152, 37-47.

Wang, L., Chen, W., 2014. An intensity index for the East Asian winter monsoon. J Clim 27, 2361-2374.

Wang, L., Lu, H.Y., Wu, N.Q., Li, J., Pei, Y.P., Tong, G.B., Peng, S.Z., 2006a. Palynological evidence for Late Miocene-Pliocene vegetation evolution recorded in the red clay sequence of the central Chinese Loess Plateau and implication for palaeoenvironmental change. Palaeogeography Palaeoclimatology Palaeoecology 241, 118-128.

Wang, N., Chang, M.-m., 2010. Pliocene cyprinids (Cypriniformes, Teleostei) from Kunlun Pass Basin, northeastern Tibetan Plateau and their bearings on development of water system and uplift of the area. Science China Earth Sciences 53, 485-500.

Wang, P., Clemens, S., Beaufort, L., Braconnot, P., Ganssen, G., Jian, Z., Kershaw, P., Sarnthein, M., 2005. Evolution and variability of the Asian monsoon system: state of the art and outstanding issues. Quaternary Science Reviews 24, 595-629.

Wang, W., Liu, X., Xu, G., Shao, X., Qin, D., Sun, W., An, W., Zeng, X., 2013. Moisture variations over the past millennium characterized by Qaidam Basin tree-ring $\delta^{18}O$. Chin.Sci.Bull. 58, 3956-3961.

Wang, X., Qiu, Z., Li, Q., Wang, B., Qiu, Z., Downs, W.R., Xie, G., Xie, J., Deng, T., Takeuchi, G.T., Tseng, Z.J., Chang, M., Liu, J., Wang, Y., Biasatti, D., Sun, Z., Fang, X., Meng, Q., 2007. Vertebrate paleontology, biostratigraphy, geochronology, and paleoenvironment of Qaidam Basin in northern Tibetan Plateau. Palaeogeography, Palaeoclimatology, Palaeoecology 254, 363-385.

Wang, X.J., Yang, M.X., Liang, X.W., Pang, G.J., Wan, G.N., Chen, X.L., Luo, X.Q., 2014. The dramatic climate warming in the Qaidam Basin, northeastern Tibetan Plateau, during 1961-2010. International Journal of Climatology 34, 1524-1537.

Wang, Y., Cheng, H., Edwards, R.L., Kong, X., Shao, X., Chen, S., 2008a. Millennial- and orbital-scale changes in the East Asian monsoon over the past 224,000 years. Nature 451.

Wang, Y., Deng, T., Biasatti, D., 2006b. Ancient diets indicate significant uplift of southern Tibet after ca. 7 Ma. Geology 34, 309-312.

Wang, Y., Liu, X., Herzschuh, U., 2010. Asynchronous evolution of the Indian and East Asian Summer Monsoon indicated by Holocene moisture patterns in monsoonal central Asia. Earth-Science Reviews 103, 135-153.

Wang, Y., Wang, X., Xu, Y., Zhang, C., Li, Q., Tseng, Z.J., Takeuchi, G., Deng, T., 2008b. Stable isotopes in fossil mammals, fish and shells from Kunlun Pass Basin, Tibetan Plateau: Paleo-climatic and paleo-elevation implications. Earth and Planetary Science Letters 270, 73-85.

Wang, Y.Q., Zhang, X.Y., Arimoto, R., 2006c. The contribution from distant dust sources to the atmospheric particulate matter loadings at XiAn, China during spring. Science of The Total Environment 368, 875-883.

Wara, M.W., Ravelo, A.C., Delaney, M.L., 2005. Permanent El Niño-Like Conditions During the Pliocene Warm Period. Science 309, 758-761.

Ward, J.H., 1963. Hierarchical Grouping to Optimize an Objective Function. Journal of the American Statistical Association 58, 236-244.

Warren, J., 1989. Evaporite sedimentology : importance in hydrocarbon accumulation / John K. Warren.

Webster, P.J., Magaña, V.O., Palmer, T.N., Shukla, J., Tomas, R.A., Yanai, M., Yasunari, T., 1998. Monsoons: Processes, predictability, and the prospects for prediction. Journal of Geophysical Research: Oceans 103, 14451-14510.

Wei, H., Fan, Q., Zhao, Y., Ma, H., Shan, F., An, F., Yuan, Q., 2015. A 94–10ka pollen record of vegetation change in Qaidam Basin, northeastern Tibetan Plateau. Palaeogeography, Palaeoclimatology, Palaeoecology 431, 43-52.

Weiss, D., Shotyk, W., Appleby, P.G., Kramers, J.D., Cheburkin, A.K., 1999. Atmospheric Pb Deposition since the Industrial Revolution Recorded by Five Swiss Peat Profiles: Enrichment Factors, Fluxes, Isotopic Composition, and Sources. Environmental Science & Technology 33, 1340-1352.

Weiss, R.F., Carmack Carmack, E.C., Koropalov, V.M., 1991. Deep-water renewal and biological production in Lake Baikal. Nature 349, 665.

Wells, M.L., Vallis, G.K., Silver, E.A., 1999. Tectonic processes in Papua New Guinea and past productivity in the eastern equatorial Pacific Ocean. Nature 398, 601.

Wen, C., Graf, H.-F., Ronghui, H., 2000. The interannual variability of East Asian Winter Monsoon and its relation to the summer monsoon. Adv. Atmos. Sci. 17, 48-60.

Wen, R.L., Xiao, J.L., Ma, Y.Z., Feng, Z.D., Li, Y.C., Xu, Q.H., 2013. Pollen-climate transfer functions intended for temperate eastern Asia. Quaternary International 311, 3-11.

Whittaker, R.H., 1975. Communities and ecosystems. Communities and ecosystems.

Wickham, H., Francois, R., Henry, L., Mueller, K., RStudio, 2019. Package 'dplyr': A Grammar of Data Manipulation.

Willard, D.A., 1994. Palynological record from the North Atlantic region at 3 Ma: vegetational distribution during a period of global warmth. Review of Palaeobotany and Palynology 83, 275-297.

Williams, M., Haywood, A.M., Harper, E.M., Johnson, A.L.A., Knowles, T., Leng, M.J., Lunt, D.J., Okamura, B., Taylor, P.D., Zalasiewicz, J., 2009. Pliocene climate and seasonality in North Atlantic shelf seas. Philosophical Transactions of the Royal Society A: Mathematical, Physical and Engineering Sciences 367, 85-108.

Wilmshurst, J.M., McGlone, M.S., 2005. Origin of pollen and spores in surface lake sediments: Comparison of modern palynomorph assemblages in moss cushions, surface soils and surface lake sediments. Review of Palaeobotany and Palynology 136, 1-15.

Woodard, S.C., Rosenthal, Y., Miller, K.G., Wright, J.D., Chiu, B.K., Lawrence, K.T., 2014. Antarctic role in Northern Hemisphere glaciation. Science 346, 847-851.

Wu, F., Fang, X., Herrmann, M., Mosbrugger, V., Miao, Y., 2011. Extended drought in the interior of Central Asia since the Pliocene reconstructed from sporopollen records. Global and Planetary Change 76, 16-21.

Wu, F., Herrmann, M., Fang, X., 2014a. Early Pliocene paleo-altimetry of the Zanda Basin indicated by a sporopollen record. Palaeogeography, Palaeoclimatology, Palaeoecology 412, 261-268.

Wu, F.Y., Ji, W.Q., Wang, J.G., Liu, C.Z., Chung, S.L., Clift, P.D., 2014b. Zircon U-Pb and Hf ISOTOPIC constraints on the onset time of India-Asia collision. American Journal of Science 314, 548-579.

Wu, N., Pei, Y., Lu, H., Guo, Z., Li, F., Liu, T., 2006. Marked ecological shifts during 6.2–2.4 Ma revealed by a terrestrial molluscan record from the Chinese Red Clay Formation and implication for palaeoclimatic evolution. Palaeogeography, Palaeoclimatology, Palaeoecology 233, 287-299.

Wu, R., 2017. Relationship between Indian and East Asian summer rainfall variations. Adv. Atmos. Sci. 34, 4-15.

Wu, R., Wang, B., 2001. Multi-stage onset of the summer monsoon over the western North Pacific. Clim Dyn 17, 277-289.

Wu, Y., Cui, Z., Liu, G., Ge, D., Yin, J., Xu, Q., Pang, Q., 2001. Quaternary geomorphological evolution of the Kunlun Pass area and uplift of the Qinghai-Xizang (Tibet) Plateau. Geomorphology 36, 203-216.

Xia, W., Zhang, N., Yuan, X., Fan, L., Zhang, B., 2001. Cenozoic Qaidam basin, China: a stronger tectonic inversed, extensional rifted basin. AAPG bulletin 85, 715-736.

Xiao, G., Guo, Z., Dupont-Nivet, G., Lu, H., Wu, N., Ge, J., 2012. Evidence for northeastern Tibetan Plateau uplift between 25 and 20 Ma in the sedimentary archive of the Xining Basin, Northwestern China. Earth Planet Sci Lett 317–318.

Xu, G., Chen, T., Liu, X., An, W., Wang, W., Yun, H., 2011. Potential linkages between the moisture variability in the northeastern Qaidam Basin, China, since 1800 and the East Asian summer monsoon as reflected by tree ring δ18O. Journal of Geophysical Research: Atmospheres 116.

Xu, H., Ai, L., Tan, L., An, Z., 2006. Stable isotopes in bulk carbonates and organic matter in recent sediments of Lake Qinghai and their climatic implications. Chemical Geology 235, 262-275.

Xu, H., Liu, X., An, Z., Hou, Z., Dong, J., Liu, B., 2010a. Spatial pattern of modern sedimentation rate of Qinghai Lake and a preliminary estimate of the sediment flux. Chin.Sci.Bull. 55, 621-627.

Xu, J.X., Ferguson, D.K., Li, C.S., Wang, Y.F., 2008. Late Miocene vegetation and climate of the Luhe region in Yunnan, southwestern China. Review of Palaeobotany and Palynology 148, 36-59.

Xu, Q., Xiao, J., Li, Y., Tian, F., Nakagawa, T., 2010b. Pollen-Based Quantitative Reconstruction of Holocene Climate Changes in the Daihai Lake Area, Inner Mongolia, China. Journal of Climate 23, 2856-2868.

Xue, F., Wang, H., He, J., 2004. Interannual Variability of Mascarene High and Australian High and Their Influences on East Asian Summer Monsoon. 気象集誌. 第2輯 82, 1173-1186.

Yan, Q., Wei, T., Zhang, Z., 2019. Reexamination of the Late Pliocene Climate over China Using a 25-km Resolution General Circulation Model. Journal of Climate 32, 897-916.

Yang, S., Jung, H.-S., Li, C., 2004. Two unique weathering regimes in the Changjiang and Huanghe drainage basins: geochemical evidence from river sediments. Sedimentary Geology 164, 19-34.

Yang, T., Ma, Y., Zhang, S., Bian, W., Yang, Z., Wu, H., Li, H., Chen, W., Ding, J., 2015. New insights into the India–Asia collision process from Cretaceous paleomagnetic and geochronologic results in the Lhasa terrane. Gondwana Research 28, 625-641.

Yang, W., Spencer, R.J., Krouse, H.R., Lowenstein, T.K., Casas, E., 1995. Stable isotopes of lake and fluid inclusion brines, Dabusun Lake, Qaidam Basin, western China:

Hydrology and paleoclimatology in arid environments. Palaeogeography, Palaeoclimatology, Palaeoecology 117, 279-290.

Yang, Y., Xiang, R., Liu, J., Fu, S., Zhou, L., Du, S., Lü, H., 2017. Changes in intermediate water conditions in the northern South China Sea using Globorotalia inflata over the last 20 ka. Journal of Quaternary Science 32, 1037-1048.

Yin, A., Dang, Y., Zhang, M., McRivette, M.W., Burgess, W.P., Chen, X., 2007. Cenozoic tectonic evolution of Qaidam basin and its surrounding regions (part 2): Wedge tectonics in southern Qaidam basin and the Eastern Kunlun Range. Geological Society of America Special Papers 433, 369-390.

Yin, A., Rumelhart, P.E., Butler, R., Cowgill, E., Harrison, T.M., Foster, D.A., 2002. Tectonic history of the Altyn Tagh fault system in northern Tibet inferred from Cenozoic sedimentaion. Geol Soc Am Bull 114.

Yu, G., Tang, L., Yang, X., Ke, X., Harrison, S.P., 2001. Modern Pollen Samples from Alpine Vegetation on the Tibetan Plateau. Global Ecology and Biogeography 10, 503-520.

Yu, K.F., Zhao, J.X., Collerson, K.D., Shi, Q., Chen, T.G., Wang, P.X., Liu, T.S., 2004. Storm cycles in the last millennium recorded in Yongshu Reef, southern South China Sea. Palaeogeography Palaeoclimatology Palaeoecology 210, 89-100.

Yuan, D.Y., Ge, W.P., Chen, Z.W., Li, C.Y., Wang, Z.C., Zhang, H.P., 2013. The growth of northeastern Tibet and its relevance to large-scale continental geodynamics: A review of recent studies. Tectonics 32.

Zachos, J., Pagani, M., Sloan, L., Thomas, E., Billups, K., 2001. Trends, rhythms, and aberrations in global climate 65 Ma to present. Science 292.

Zechmeister, M., Kürster, M., 2009. The generalised Lomb-Scargle periodogram-a new formalism for the floating-mean and Keplerian periodograms. Astronomy & Astrophysics 496, 577-584.

Zhai, P., Yu, R., Guo, Y., Li, Q., Ren, X., Wang, Y., Xu, W., Liu, Y., Ding, Y., 2016. The strong El Niño of 2015/16 and its dominant impacts on global and China's climate. Journal of Meteorological Research 30, 283-297.

Zhang, G., Buatois, L.A., Mángano, M.G., Aceñolaza, F.G., 1998. Sedimentary facies and environmental ichnology of a ?Permian playa-lake complex in western Argentina. Palaeogeography, Palaeoclimatology, Palaeoecology 138, 221-243.

Zhang, K., Zhao, Y., Yu, Z., Zhou, A., 2010. A 2700-year high resolution pollen record of climate change from varved Sugan Lake in the Qaidam Basin, northeastern Tibetan Plateau. Palaeogeography, Palaeoclimatology, Palaeoecology 297, 290-298.

Zhang, R., Sumi, A., Kimoto, M., 1996. Impact of El Niño on the East Asian Monsoon

A Diagnostic Study of the '86/87 and '91/92 Events. Journal of the Meteorological Society of Japan. Ser. II 74, 49-62.

Zhang, W., Appel, E., Fang, X., Song, C., Cirpka, O., 2012a. Magnetostratigraphy of deep drilling core SG-1 in the western Qaidam Basin (NE Tibetan Plateau) and its tectonic implications. Quaternary Research 78, 139-148.

Zhang, W., Appel, E., Fang, X., Song, C., Setzer, F., Herb, C., Yan, M., 2014. Magnetostratigraphy of drill-core SG-1b in the western Qaidam Basin (NE Tibetan Plateau) and tectonic implications. Geophysical Journal International 197, 90-118.

Zhang, W., De Vleeschouwer, D., Shen, J., Zhang, Z., Zeng, L., 2018. Orbital time scale records of Asian eolian dust from the Sea of Japan since the early Pliocene. Quaternary Science Reviews 187, 157-167.

Zhang, W.L., 2006. Cenozoic uplift of the Tibetan Plateau: evidence from high resolution magnetostratigraphy of the Qaidam Basin, PhD Thesis, Lanzhou University.

Zhang, X., Jin, L., Huang, W., Chen, F., 2016. Forcing mechanisms of orbital-scale changes in winter rainfall over northwestern China during the Holocene. The Holocene 26, 549-555.

Zhang, X., Liu, H., Baker, C., Graham, S., 2012b. Restoration approaches used for degraded peatlands in Ruoergai (Zoige), Tibetan Plateau, China, for sustainable land management. Ecological Engineering 38, 86-92.

Zhang, Z.-Y., Harrison, S.P., Mosbrugger, V., Ferguson, D.K., Paudayal, K.N., Trivedi, A., Li, C.-S., 2015. Evaluation of the realism of climate reconstruction using the Coexistence Approach with modern pollen samples from the Qinghai–Tibetan Plateau. Review of Palaeobotany and Palynology 219, 172-182.

Zhang, Z., Han, W., Fang, X., Song, C., Li, X., 2013. Late Miocene–Pleistocene aridification of Asian inland revealed by geochemical records of lacustrine-fan delta sediments from the western Tarim Basin, NW China. Palaeogeography, Palaeoclimatology, Palaeoecology 377, 52-61.

Zhang, Z., Sun, J., 2011. Palynological evidence for Neogene environmental change in the foreland basin of the southern Tianshan range, northwestern China. Global and Planetary Change 75, 56-66.

Zhao, D., Wu, S., Yin, Y., Yin, Z.-Y., 2011. Vegetation distribution on Tibetan Plateau under climate change scenario. Regional Environmental Change 11, 905-915.

Zhao, P., Zhou, Z., 2009. An East Asian subtripical summer monsoon index and its relationship to summer rainfall in China. Acta Meteorol Sin 23.

Zhao, W.W., Andreev, A.A., Wennrich, V., Tarasov, P.E., Anderson, P., Lozhkin, A.V., Melles, M., 2015. The Réunion Subchron vegetation and climate history of the northeastern Russian Arctic inferred from the Lake El'gygytgyn pollen record. Palaeogeography, Palaeoclimatology, Palaeoecology 436, 167-177.

Zhao, Y., Herzschuh, U., 2009. Modern pollen representation of source vegetation in the Qaidam Basin and surrounding mountains, north-eastern Tibetan Plateau. Vegetation History and Archaeobotany 18, 245-260.

Zhao, Y., Liu, H., Li, F., Huang, X., Sun, J., Zhao, W., Herzschuh, U., Tang, Y., 2012. Application and limitations of the Artemisia/Chenopodiaceae pollen ratio in arid and semi-arid China. The Holocene 22, 1385-1392.

Zhao, Y., Xu, Q., Huang, X., Guo, X., Tao, S., 2009. Differences of modern pollen assemblages from lake sediments and surface soils in arid and semi-arid China and their significance for pollen-based quantitative climate reconstruction. Review of Palaeobotany and Palynology 156, 519-524.

Zhao, Y., Yu, Z., Chen, F., Ito, E., Zhao, C., 2007. Holocene vegetation and climate history at Hurleg Lake in the Qaidam Basin, northwest China. Review of Palaeobotany and Palynology 145, 275-288.

Zhao, Y., Yu, Z., Chen, F., Liu, X., Ito, E., 2008. Sensitive response of desert vegetation to moisture change based on a near-annual resolution pollen record from Gahai Lake in the Qaidam Basin, northwest China. Global and Planetary Change 62, 107-114.

Zheng, D., Clark, M.K., Zhang, P., Zheng, W., Farley, K.A., 2010. Erosion, fault initiation and topographic growth of the North Qilian Shan (northern Tibetan Plateau). Geosphere 6.

Zheng, D., Zhang, P.Z., Wan, J.L., Yuan, D.Y., Li, C.Y., Yin GM, G.L.Z., 2006. Rapid exhumation at ~8 Ma on the Liupan Shan thrust fault from apatite fission-track thermochronology: implications for growth of the northeastern Tibetan Plateau margin. Earth Planet Sci Lett 248.

Zheng, H., Powell, C.M., An, Z., Zhou, J., Dong, G., 2000. Pliocene uplift of the northern Tibetan Plateau. Geology 28, 715-718.

Zheng, Z., Wei, J., Huang, K., Xu, Q., Lu, H., Tarasov, P., Luo, C., Beaudouin, C., Deng, Y., Pan, A., Zheng, Y., Luo, Y., Nakagawa, T., Li, C., Yang, S., Peng, H., Cheddadi, R., 2014. East Asian pollen database: modern pollen distribution and its quantitative relationship with vegetation and climate. Journal of Biogeography 41, 1819-1832.

Zhou, J., Xu, F., Wang, T., Cao, A., Yin, C., 2006. Cenozoic deformation history of the Qaidam Basin, NW China: Results from cross-section restoration and implications for Qinghai–Tibet Plateau tectonics. Earth and Planetary Science Letters 243, 195-210.

Zhou, S., Nakawo, M., Sakai, A., Matsuda, Y., Duan, K., Pu, J., 2007. Water isotope variations in the snow pack and summer precipitation at July 1 Glacier, Qilian Mountains in northwest China. Chin.Sci.Bull. 52, 2963-2972.

Appendix

Tab. A – 1: Sample names, core depths, real depths and ages of the SG-1b samples. Numbers in red refer to samples, which were provided by project partners from the University of Heidelberg University (Dr. Andreas Koutsodendris).

Sample Nr.	Core Depth [m]	Real Depth [m]	Age [Ma]
136.5	136.5	156.79	3.011
138	138	158.16	3.019
139.5	139.5	159.53	3.027
141	141	160.89	3.034
142.28	142.28	162.06	3.042
144	144	163.63	3.049
145.5	145.5	164.99	3.057
147	147	166.36	3.064
148.5	148.5	167.73	3.072
150	150	169.1	3.079
151.5	151.5	170.46	3.087
153	153	171.83	3.094
1	153.5	172.2879	3.097
2	154.4	173.1084	3.101
154.5	154.5	173.2	3.102
3	155.3	173.9289	3.106
48	155.75	174.3391	3.108
156	156	174.57	3.109
4	156.2	174.7493	3.110
49	156.65	175.1596	3.113
5	157.1	175.5698	3.115
157.5	157.5	175.93	3.118
50	157.55	175.98	3.119
6	158	176.3903	3.125
51	158.45	176.8005	3.131
7	158.9	177.2107	3.137
159	159	177.3	3.138
52	159.35	177.621	3.142
8	159.8	178.0312	3.148
53	160.25	178.4414	3.154

160.5	160.5	178.67	3.157
9	160.7	178.8517	3.160
54	161.15	179.2619	3.166
10	161.6	179.6721	3.172
55	162.05	180.0824	3.177
11	162.5	180.4926	3.183
56	162.95	180.9028	3.189
12	163.4	181.3131	3.195
57	163.85	181.7233	3.201
13	164.3	182.1335	3.207
58	164.75	182.5438	3.209
14	165.16	182.9175	3.211
15	166.1	183.7745	3.216
16	167	184.5949	3.221
17	167.7	185.2331	3.225
18	168.8	186.2359	3.231
19	169.7	187.0563	3.235
20	170.72	187.9862	3.241
21	171.5	188.6973	3.245
22	172.4	189.5177	3.250
23	173.36	190.3929	3.255
24	174.2	191.1587	3.259
25	175.1	191.9791	3.264
175.5	175.5	192.34	3.266
26	176.02	192.8178	3.269
59	176.45	193.2098	3.271
27	176.9	193.6201	3.273
60	177.35	194.0303	3.276
28	177.8	194.4405	3.278
61	178.23	194.8325	3.280
29	178.7	195.261	3.283
62	179.15	195.6712	3.285
30	179.6	196.0815	3.288
63	180.05	196.4917	3.290
31	180.5	196.9019	3.292

64	180.95	197.3122	3.295
32	181.4	197.7224	3.297
65	181.85	198.1326	3.300
33	182.28	198.5246	3.302
66	182.75	198.9531	3.304
34	183.2	199.3633	3.307
35	184.1	200.1881	3.311
36	185	201.0639	3.316
37	185.9	201.9397	3.322
38	186.8	202.8155	3.327
39	187.7	203.6912	3.332
40	188.6	204.567	3.339
189	189	204.96	3.342
41	189.5	205.4428	3.346
42	190.4	206.3186	3.353
190.5	190.5	206.42	3.354
43	191.3	207.1944	3.359
192	192	207.88	3.365
44	192.2	208.0702	3.366
45	193.1	208.9459	3.373
193.5	193.5	209.34	3.376
46	194	209.8217	3.380
47	194.9	210.6975	3.386
194.98	194.98	210.78	3.387
67	195.8	211.5733	3.393
196.5	196.5	212.25	3.399
68	196.7	212.4491	3.400
69	197.6	213.3249	3.407
198	198	213.71	3.410
70	198.5	214.2006	3.414
71	199.4	215.0764	3.421
199.5	199.5	215.17	3.422
72	200.3	215.9522	3.427
73	201.2	216.828	3.434
74	202.1	217.7038	3.441

75	202.98	218.5601	3.448
76	203.9	219.4553	3.455
77	204.8	220.3311	3.461
78	205.7	221.2069	3.468
79	206.6	222.0827	3.475
80	207.5	222.9585	3.482
81	208.36	223.7953	3.488
82	209.3	224.71	3.495

Tab.A – 2: Sample names and related ages from the Kunlun Pass Basin record. The samples were provided by project partners from the University of Rochester, USA (Prof. Dr. Carmala N. Garzione and Dr. Feng Cheng). Counted pollen samples are marked in bold (total 154).

Sample-Nr.	Age [Ma]	Sample-Nr.	Age [Ma]
16KL23	**0.852**	16KL80	1.162
16KL22	0.857	16KL79	1.181
16KL21	0.861	16KL78	1.201
16KL20	0.865	16KL77	1.220
16KL19	0.869	16KL76	1.240
16KL18	0.873	16KL75	1.260
16KL17	0.877	**16KL74**	**1.279**
16KL16	0.881	16KL73	1.299
16KL15	0.885	16KL72	1.318
16KL14	0.889	16KL71	1.338
16KL13	0.893	16KL70	1.358
16KL12	0.898	16KL69	1.377
16KL11	0.902	16KL68	1.397
16KL10	**0.906**	16KL67	1.416
16KL09	0.908	16KL66	1.436
16KL08	0.910	16KL65	1.456
16KL07	0.914	16KL64	1.475
16KL06	0.918	16KL63	1.485
16KL05	0.922	16KL62	1.495
16KL04	0.926	16KL61	1.504
16KL03	0.936	16KL60	1.514
16KL02	0.956	16KL59	1.524
16KL01	0.976	**16KL58**	**1.534**
16KL89	0.985	16KL57	1.544
16KL88	1.005	16KL56	1.553
16KL87	**1.025**	16KL55	1.563
16KL86	1.044	16KL54	1.573
16KL85	1.064	16KL53	1.583
16KL84	1.083	16KL52	1.593
16KL83	1.103	16KL51	1.602
16KL82	1.123	16KL50	1.612
16KL81	1.142	16KL49	1.622

16KL48	1.632	16KL149	2.061
16KL47	1.642	**16KL148**	**2.071**
16KL46	1.651	16KL147	2.081
16KL45	1.671	16KL146	2.092
16KL44	1.691	16KL145	2.102
16KL43	1.710	16KL144	2.112
16KL42	1.730	**16KL143**	**2.132**
16KL41	1.749	16KL142	2.142
16KL40	1.769	16KL141	2.152
16KL39	**1.789**	16KL140	2.163
16KL38	1.798	16KL139	2.173
16KL37	1.808	**16KL138**	**2.183**
16KL36	1.824	16KL137	2.193
16KL35	1.848	16KL136	2.203
16KL34	1.863	16KL135	2.213
16KL33	1.868	16KL134	2.223
16KL32	1.878	16KL133	2.234
16KL31	**1.884**	16KL132	2.244
16KL30	1.899	16KL131	2.254
16KL29	1.904	16KL130	2.264
16KL26	1.909	16KL129	2.274
16KL28	1.914	16KL128	2.284
16KL27	1.919	**16KL127**	**2.295**
16KL25	1.939	16KL126	2.305
16KL24	1.947	16KL125	2.315
16KL159	**1.960**	16KL124	2.325
16KL158	1.970	16KL123	2.335
16KL157	1.980	16KL122	2.345
16KL156	1.990	16KL121	2.355
16KL155	2.000	16KL120	2.366
16KL154	2.010	16KL119	2.376
16KL153	2.021	**16KL118**	**2.386**
16KL152	2.031	16KL117	2.396
16KL151	2.041	16KL116	2.406
16KL150	2.051	16KL115	2.416

16KL114	**2.426**	**16KL211**	**2.782**
16KL113	2.437	16KL210	2.792
16KL112	2.447	**16KL209**	**2.802**
16KL111	**2.457**	16KL208	2.812
16KL110	2.467	16KL207	2.822
16KL109	2.477	16KL206	2.832
16KL108	2.487	16KL205	2.842
16KL107	2.497	**16KL204**	**2.853**
16KL106	**2.508**	16KL203	2.863
16KL105	2.518	**16KL202**	**2.873**
16KL104	2.528	16KL201	2.883
16KL103	2.538	**16KL200**	**2.893**
16KL102	**2.548**	16KL199	2.903
16KL101	2.558	**16KL198**	**2.913**
16KL100	**2.568**	16KL197	2.924
16KL99	2.579	**16KL196**	**2.934**
16KL98	**2.589**	16KL195	2.944
16KL97	**2.599**	**16KL194**	**2.954**
16KL96	**2.609**	**16KL193**	**2.964**
16KL95	**2.619**	**16KL192**	**2.974**
16KL94	**2.629**	**16KL191**	**2.985**
16KL93	**2.640**	**16KL190**	**2.995**
16KL92	**2.650**	**16KL189**	**3.005**
16KL91	2.660	**16KL188**	**3.015**
16KL90	**2.670**	**16KL187**	**3.025**
16KL221	**2.680**	**16KL186**	**3.035**
16KL220	**2.690**	**16KL185**	**3.045**
16KL219	2.700	**16KL184**	**3.056**
16KL218	**2.711**	**16KL183**	**3.066**
16KL217	**2.721**	**16KL182**	**3.076**
16KL216	**2.731**	**16KL181**	**3.086**
16KL215	**2.741**	**16KL180**	**3.096**
16KL214	2.751	**16KL179**	**3.106**
16KL213	**2.761**	**16KL178**	**3.116**
16KL212	2.771	**16KL177**	**3.127**

16KL176	**3.137**	**16KL238**	**3.492**
16KL175	**3.147**	**16KL237**	**3.502**
16KL174	**3.157**	**16KL236**	**3.512**
16KL173	**3.167**	**16KL235**	**3.522**
16KL172	**3.177**	**16KL234**	**3.532**
16KL171	**3.187**	**16KL233**	**3.543**
16KL170	**3.198**	**16KL232**	**3.553**
16KL169	**3.208**	**16KL231**	**3.563**
16KL168	**3.218**	**16KL230**	**3.573**
16KL167	**3.228**	**16KL229**	**3.583**
16KL166	**3.238**	**16KL228**	**3.593**
16KL165	**3.248**	**16KL227**	**3.604**
16KL164	**3.259**	**16KL226**	**3.614**
16KL163	3.269	**16KL225**	**3.624**
16KL162	**3.279**	**16KL224**	**3.634**
16KL161	**3.289**	**16KL223**	**3.644**
16KL160/258	**3.299**	**16KL222**	**3.654**
16KL257	3.309	**16KL290**	**3.725**
16KL256	**3.319**	16KL289	3.730
16KL255	**3.330**	16KL288	3.735
16KL254	**3.340**	16KL287	3.741
16KL253	3.350	16KL286	3.746
16KL252	**3.360**	16KL285	3.751
16KL251	**3.370**	**16KL284**	**3.756**
16KL250	**3.380**	16KL283	3.761
16KL249	**3.390**	16KL282	3.766
16KL248	**3.401**	16KL281	3.776
16KL247	**3.411**	**16KL280**	**3.786**
16KL245	**3.421**	16KL279	3.796
16KL244	**3.431**	16KL278	3.806
16KL243	**3.441**	**16KL277**	**3.817**
16KL242	**3.451**	16KL276	3.827
16KL241	**3.461**	**16KL275**	**3.837**
16KL240	**3.472**	**16KL274**	**3.847**
16KL239	**3.482**	**16KL273**	**3.857**

16KL272	3.898	16KL325	4.141
16KL271	**3.908**	**16KL324**	**4.146**
16KL270	3.918	16KL323	4.151
16KL269	**3.928**	**16KL322**	**4.157**
16KL268	**3.938**	16KL321	4.162
16KL267	**3.949**	16KL320	4.167
16KL266	**3.959**	16KL319	4.172
16KL265	**3.969**	**16KL318**	**4.177**
16KL264	3.979	16KL317	4.182
16KL263	**3.989**	**16KL316**	**4.187**
16KL262	**3.999**	**16KL315**	**4.192**
16KL261	**4.009**	**16KL314**	**4.197**
16KL260	**4.020**	16KL313	4.202
16KL259	**4.030**	**16KL312**	**4.207**
16KL346	**4.035**	**16KL311**	**4.212**
16KL345	4.040	**16KL310**	**4.217**
16KL344	**4.045**	**16KL309**	**4.223**
16KL343	4.050	16KL308	4.228
16KL342	**4.055**	**16KL307**	**4.233**
16KL341	4.060	16KL306	4.238
16KL340	**4.065**	16KL305	4.243
16KL339	4.070	16KL304	4.248
16KL338	**4.075**	**16KL303**	**4.253**
16KL337	4.080	16KL302	4.258
16KL336	**4.086**	**16KL301**	**4.263**
16KL335	4.091	16KL300	4.268
16KL334	**4.096**	**16KL299**	**4.273**
16KL333	4.101	16KL298	4.278
16KL332	**4.106**	**16KL297**	**4.283**
16KL331	4.111	16KL296	4.288
16KL330	**4.116**	**16KL295**	**4.294**
16KL329	4.121	16KL294	4.299
16KL328	**4.126**	**16KL293**	**4.304**
16KL327	4.131	16KL292	4.309
16KL326	**4.136**	**16KL291**	**4.314**

Development of calibration curves for C and N

In Fig. A – 1 and A – 2 the peak area per weight carbon (nitrogen) is shown depending on the weight of carbon (nitrogen) in a standard sample. The figures show that the relationship between the weight carbon (nitrogen) and measured area per weight carbon (nitrogen) is non-linear.

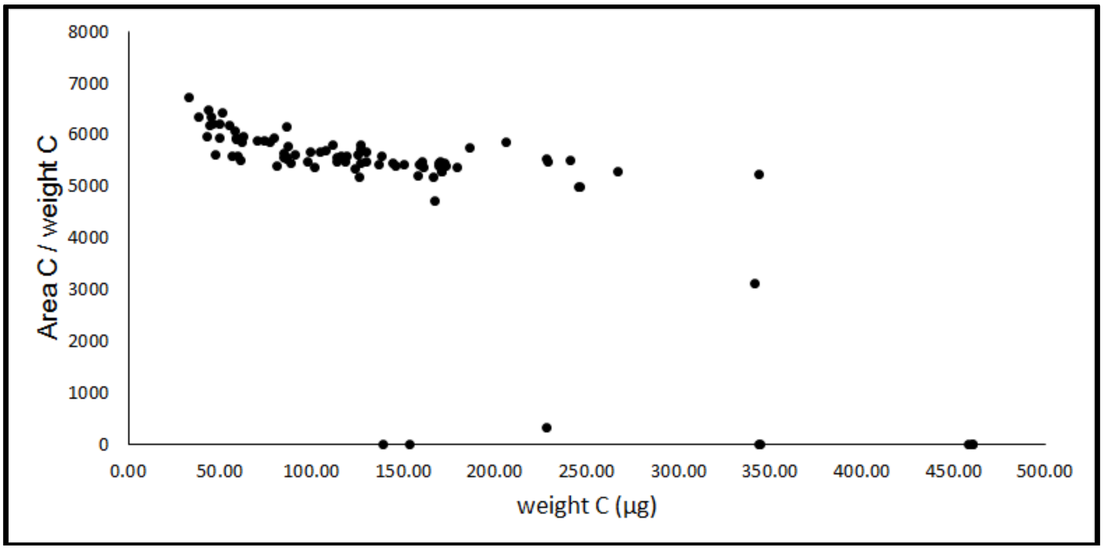

Fig. A – 1: Plot of C Area normed by weight C depending on weight C. Apart from errornous samples, the area per weight carbon does not stay constant throughout the carbon range. This suggests that a calibration function would not be linear in all ranges of detected carbon.

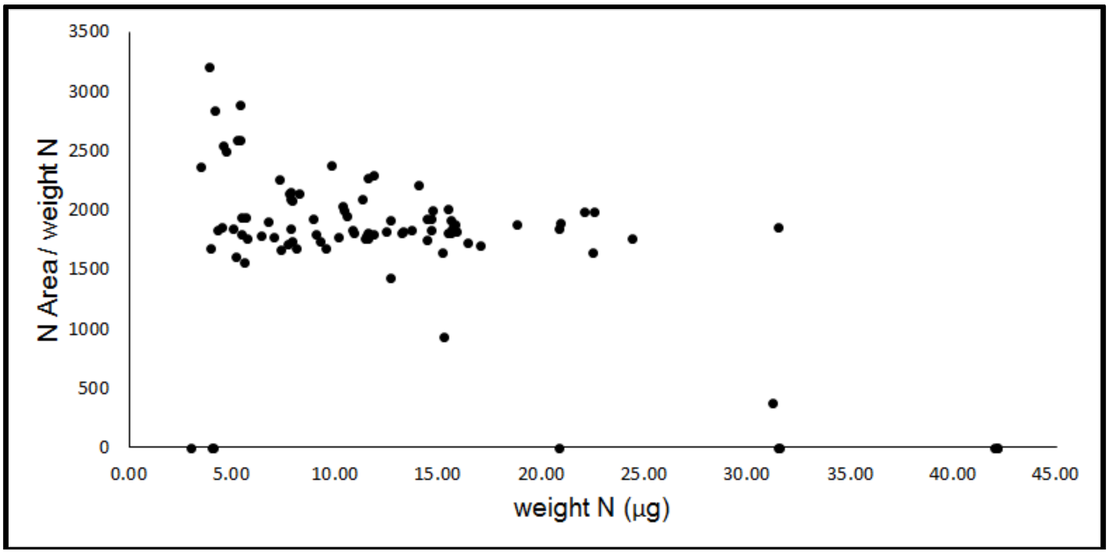

Fig. A – 2: Plot of N Area normed by weight N depending on weight N. Apart from errornous samples, the area per weight nitrogen does not stay constant throughout the nitrogen range. This suggests that a calibration function would not be linear in all ranges of detected carbon. The nitrogen plot does not show characteristic increase for low nitrogen weights compared to the carbon plot (Fig. A – 3). Instead a broad range of N area / weight N values characterise low weight N samples. This might be due to incomplete combustion of some samples.

To calibrate the carbon and nitrogen signals based on good measurements, several data points have been removed from the calibration because they either did not measure any carbon or nitrogen (Area = 0) or were too far off from the general trend.

To backtest the calibrations, C/N ratios for all standard measurements (excluding measurements in which no carbon and/or nitrogen have been detected) were calculated based on the calibration functions (Fig. A – 3). Good results were produced when the measured N area was above 10000 as suggested by the red dashed line (± 20% of the expected value). Since the samples were run in triplets, consistent results for the samples were expected.

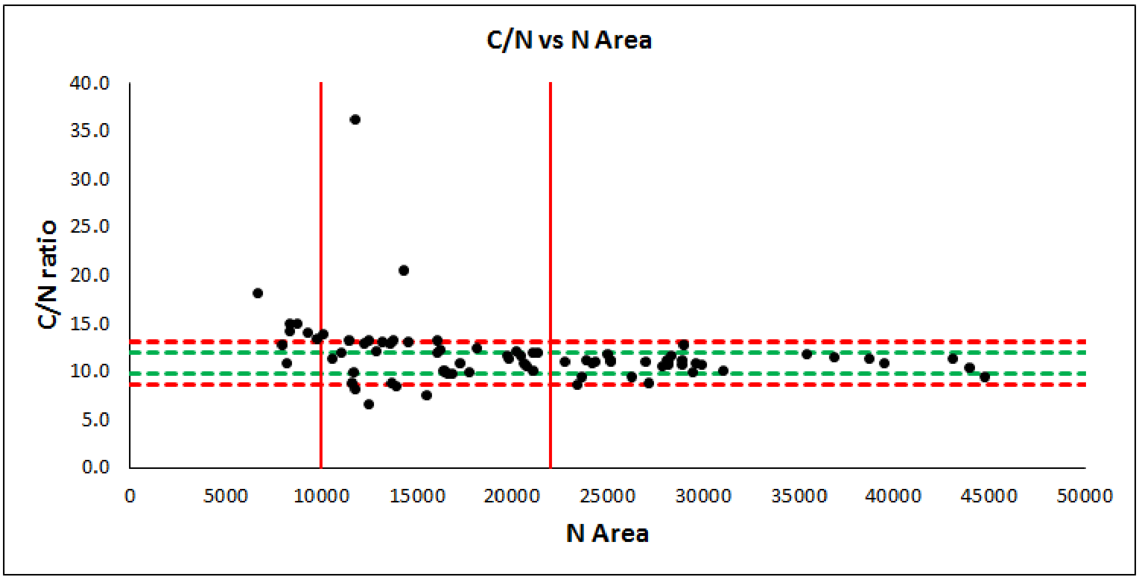

Fig. A – 3: C/N ratio of all standard samples (excluding 0 values) against N area. The figure shows that most samples are within ± 20% (red dashed line) for whole record and even within ± 10% (green dashed line) for higher N areas. The two red lines represent the change in calibration function (N area = 22000) and the lowermost area that could be trusted.

Tab. A – 3: Homogenisation of pollen taxa for the modern pollen dataset based on the work of Cao et al. (2013). Additional merging steps of taxa, which were not part of Cao et al. (2013), are marked in red. "*Artemisia* + Chenopodiaceae", "*Pedicularis*", "*Rheum* + *Rumex*", "*Rumex* + *Rheum*" were removed from the original dataset.

Taxa after Homogenisation	**Original Pollen Taxa**
Abies	*Abies*
Acer	Aceraceae, *Acer*
Alnus	*Alnus*
Anacardiaceae	Anacardiaceae
Apiaceae	Apiaceae, *Bupleurum, Umbelliferae*
Araceae	*Acorus,* Araceae
Artemisia	*Artemisia*
Asteraceae	*Anthemis, Aster, Carduoideae, Compositae, Liguliflorae, Saussurea, Serratula, Taraxacum, Ajania, Chrysantheum*
Berbericaceae	Berberidaceae, *Berberis*
Betula	*Betula,* Betulaceae
Bignoniaceae	Bignoniaceae
Brassicaceae	*Brassica,* Brassicaceae, *Cruciferae*
Calligonum	*Calligonum*
Campanulaceae	Campanulaceae
Cannabis	*Cannabis*
Capparidaceae	Capparidaceae
Carpinus	*Carpinus*
Carya	*Carya*
Caryophyllaceae	*Arenaria*, Caryophyllaceae, *Cerastium, Dianthus*
Castanea	*Castanea*
Castanopsis	*Castanopsis*
Cedrus	*Cedrus*
Chenopodiaceae	Amaranthaceae, Amaranthaceae – Chenopodiaceae, *Anabasis, Ceratoides*, Chenopodiaceae, *Chenopodium*, *Kochia, Nanophyton, Salsola*

Convolvulaceae	Convolvulaceae, *Cuscuta*
Cornaceae	Cornaceae
Corylus	*Corylus*
Crassulaceae	Crassulaceae, *Rhodiola*
Cupressaceae	Cupressaceae
Cyperaceae	Cyperaceae
Dipsacaceae	Dipsacaceae
Elaeagnus	*Elaeagnus*, Elaeagnaceae
Elaeocarpus	*Elaeocarpus*
Ephedra	*Ephedra – distachya*, Ephedraceae, *Ephedra – equisetina, Ephedra – fragilis, Ephedra*
Ericaceae	Ericaceae, *Rhododendron*
Euphorbiaceae (undiff.)	Euphorbiaceae
Fabaceae (shrub)	*Alhagi, Astragalus, Caragana, Cassia*
Fabaceae (herb)	*Oxytropis, Glycyrrhiza*
Fabaceae (undiff.)	Fabaceae, *Leguminosae*, Papillionaceae
Fagaceae	Fagaceae
Fagus	*Fagus*
Gentianaceae	*Gentianella – campestris,* Gentianaceae, *Gentiana - pneumonanthe*
Geranium	*Geranium*
Haloragidaceae	Haloragidaceae
Hedera	*Hedera*
Hippophae	*Hippophae*
Humulus	*Humulus*
Ilex	*Ilex*
Iridaceae	Iridaceae
Juglans	*Juglans*
Juniperus	*Juniperus, Sabina*
Lamiaceae	Labiatae, Lamiaceae, *Lamium, Mentha*
Larix	*Larix*

Lauraceae	Lauraceae
Liliaceae	*Allium*, Liliaceae
Linaceae	Linaceae, *Linum*
Liquidambar	*Liquidambar*
Morus	*Morus*
Nitrariaceae	*Nitraria, Peganum*
Oleaceae (undiff.)	Oleaceae
Oleaceae (temperate)	*Fraxinus*
Ostryopsis	*Ostryopsis*
Papaveraceae	Papaveraceae, *Papaver, Corydalis*
Picea	*Picea, Picea – schrenkiana,*
Pinus	Pinaceae, *Pinus – Diploxylon, Pinus – Haploxylon, Pinus*
Pistacia	*Pistacia*
Plantago	*Plantago,* Plantaginaceae
Plumbaginaceae	Plumbaginaceae
Poaceae	*Cerealia*, Graminae, Poaceae, *Stipa, Zea*
Polygalaceae	*Polygala*
Polygonaceae	*Polygonum – aviculare, Polygonum – bistorta*, Polygonaceae, *Polygonum, Polygonum – viviparum, Atraphaxis*
Populus	*Populus*
Primulaceae	*Androsace, Primula*
Pyrola	*Pyrola*
Quercus (undiff.)	*Quercus, Quercus* – deciduous,
Quercus (evergreen)	*Quercus* – evergreen
Ranunculus	*Aconitum, Caltha*, Ranunculaceae, *Ranunculus, Trollius, Pulsatilla*
Rhamnaceae	Rhamnaceae, *Rhamnus*
Rheum	*Rheum*
Rhus	*Rhus*
Rosaceae	*Potentilla*, Rosaceae, *Rosa, Sorbus, Spiraea, Sibbaldia, Sanguisorba*

Rubiaceae	Rubiaceae
Rumex	*Rumex*
Rutaceae	Rutaceae
Salix	*Salix*
Sapindaceae	Sapindaceae
Saxifragaceae	Saxifragaceae, *Saxifraga, Saxifraga – granulata, Saxifraga – oppositifolia*
Scrophulariaceae	Scrophulariaceae, *Veronica*
Solanaceae	*Lycium, Solanum*, Solanaceae
Tamaricaceae	*Reaumaria, Myricaria, Tamarix,* Tamaricaceae
Taxodiaceae	Taxodiaceae
Thalictrum	*Thalictrum*
Thymelaeceae	Thymelaeceae, *Stellera, Wikstroemia*
Tsuga	*Tsuga*
Ulmus	*Ulmus, Ulmus + Zelkova*
Urticaceae	Urticaceae, *Urtica*
Verbenaceae	Verbenaceae
Viola	*Viola*
Zygophyllaceae	Zygophyllaceae, *Zygophyllum, Tribulus*

R Code

Principle Component Analysis

```
log.xrf<-log(xrf)
xrf.pca<-prcomp(log.xrf,
center = TRUE,
scale. = TRUE)
print(xrf.pca)
summary (xrf.pca)
```

Cluster Analysis

Dendrogramm

```
res.hc<-xrf %>%
scale () %>%
dist(method = "euclidean") %>%
hclust(method = "ward.D2")
plot(res.hc)
```

Assigning cluster numbers to samples in table

```
rect.hclust(res.hc, 6)
xrf$clusternumber<-cutree(res.hc, 6)
xrf
```

Pollen – climate transfer functions

```
MWP1<-read.csv("Pollendata_MWP.csv", sep = ",")

MWP2<-read.csv("Pollendatasqrt_MWP.csv", sep = ",")

Pollen1<-read.csv("Pollendata.csv", sep = ",")

Pollen2<-read.csv("Pollendatasqrt.csv", sep = ",")

Pollensqrt<-sqrt(Pollen2)

TF1<-WAPLS(Pollen1, MWP1, npls=10)

Summary(TF1)

S<-coef(TF1)

S

C<-crossval(TF, cv.method="loo", verbose=TRUE,ngroups=10, nboot=100, h.cutoff=0, h.dist=NULL)

C
```